

Syracuse University

SURFACE

Electrical Engineering and Computer Science -
Dissertations

College of Engineering and Computer Science

5-2012

Arbitrarily Oriented Biaxially Anisotropic Media: Wave Behavior and Microstrip Antennas

Jennifer Warzala Graham
Syracuse University

Follow this and additional works at: https://surface.syr.edu/eecs_etd



Part of the [Electrical and Computer Engineering Commons](#)

Recommended Citation

Graham, Jennifer Warzala, "Arbitrarily Oriented Biaxially Anisotropic Media: Wave Behavior and Microstrip Antennas" (2012). *Electrical Engineering and Computer Science - Dissertations*. 320.
https://surface.syr.edu/eecs_etd/320

This Dissertation is brought to you for free and open access by the College of Engineering and Computer Science at SURFACE. It has been accepted for inclusion in Electrical Engineering and Computer Science - Dissertations by an authorized administrator of SURFACE. For more information, please contact surface@syr.edu.

ABSTRACT

This dissertation explores the electromagnetic behavior of arbitrarily oriented biaxially anisotropic media. An overview of wave behavior in biaxially anisotropic (or simply biaxial) media is presented. The reflection and transmission behaviors of electromagnetic waves from half-space and two-layer isotropic-biaxial interfaces are studied. The reflection and transmission coefficients are used in the formulation of eigenvector dyadic Green's functions. These Green's functions are employed in full-wave analyses of rectangular microstrip antennas printed on biaxial substrates.

The general characteristics of electrically biaxially anisotropic (biaxial) media are presented including permittivity tensors, optic axes, orientation of the medium, and birefringence. After a detailed discussion of wave propagation, wave behavior at isotropic-biaxial interfaces is investigated. The reflection and transmission of electromagnetic waves incident upon half-space and two-layer interfaces, at which the waves may be incident from either the isotropic region or the biaxial region, are investigated. The biaxial medium considered may be aligned with the principal coordinate system or may be arbitrarily oriented. Critical angle and Brewster angle effects are analyzed for the half-space case. Once the wave behavior is well understood, the eigenvector dyadic Green's function is presented for two-layer geometries involving isotropic and biaxially anisotropic media. The symmetrical property of the dyadic Green's function is derived and used to generate an unknown Green's function from a known Green's function for the two-layer geometry of interest. This new Green's function is used to model rectangular microstrip antennas.

Following the investigation of reflection and transmission, rectangular microstrip antennas are analyzed using the eigenvector dyadic Green's function and the method of moments. Galerkin's method is used to evaluate current distributions on gap-fed dipole antennas and probe-fed patch antennas. The resulting current distributions are used to compute antenna parameters such as input impedance, resonant length and principal polarization radiation patterns. For the patch antennas, impedance bandwidth and cross-polarization patterns are also investigated. Results are presented for biaxially anisotropic substrates of varying thickness, permittivities, and orientations, providing the understanding of the complex behaviors of microstrip antennas printed on biaxially anisotropic substrates.

**ARBITRARILY ORIENTED BIAXIALLY ANISOTROPIC MEDIA:
WAVE BEHAVIOR AND MICROSTRIP ANTENNAS**

By

Jennifer Warzala Graham

B.S. Syracuse University, 2000

M.S. Syracuse University, 2004

DISSERTATION

*Submitted in partial fulfillment of the requirements for the degree of Doctor of
Philosophy in Electrical and Computer Engineering in the Graduate School of Syracuse
University*

May 2012

Copyright © Jennifer Warzala Graham May 2012

All Rights Reserved

ACKNOWLEDGEMENTS

First and foremost I would like to acknowledge and thank my advisor Dr. Jay Kyoon Lee. He has been a constant teacher and mentor not only during my doctoral studies but throughout my academic career. I have great appreciation for all of his help and guidance throughout my higher education. I would also like to thank my reader Dr. Harvey Schuman. Harvey's advice throughout the antenna analysis and review of this dissertation provided valuable and practical inputs. Thanks also go to my dissertation defense committee, Dr. Thong Q. Dang, Dr. Ercument Arvas, Dr. Joseph R. Mautz and Dr. Prasanta K. Ghosh for their review of this work. I would also like to acknowledge Dr. Gregory F. Pettis for his help at the start of this process.

Finally I would like to thank my family for their love and support; especially my parents for always backing me up, my husband Tim for his encouragement and my wonderful children Calvin and Alice.

CONTENTS

ACKNOWLEDGEMENTS	v
LIST OF FIGURES	viii
LIST OF TABLES	xiv
1 INTRODUCTION.....	1
1.1 Research Objectives.....	1
1.2 Previous Work.....	2
1.2.1 Wave Behavior in Anisotropic Materials	2
1.2.2 Microstrip Antennas.....	5
1.3 Electromagnetic Definitions for Isotropic and Biaxial Media	8
1.3.1 Permittivity Tensor	10
1.3.1.1 Permittivity Tensor Rotations.....	12
1.4 Chapter Overview.....	14
2 WAVE BEHAVIOR IN LAYERED BIAxIAL MEDIA	16
2.1 Birefringence	16
2.1.1 Propagation Vectors.....	16
2.1.1.1 Unbounded Media.....	17
2.1.1.2 Layered Media	21
2.1.2 Electric Field Vectors	27
2.2 Reflection and Transmission.....	29
2.2.1 Half Space Reflection and Transmission Coefficients	31
2.2.1.1 Wave Incident from Isotropic Region 0.....	31
2.2.1.2 Wave Incident from Biaxial Region 1	59
2.2.2 Two Layer Coefficients	87
2.2.2.1 Evaluation of Two Layer Coefficients.....	89
3 EIGENVECTOR DYADIC GREEN'S FUNCTION	96
3.1 Formulation of Dyadic Green's Functions	96
3.2 Symmetrical Property of Dyadic Green's Function	98
3.2.1 Application of Symmetrical Property of DGF.....	102

4	PRINTED RECTANGULAR MICROSTRIP ANTENNAS	107
4.1	Solution Techniques.....	108
4.1.1	Method of Moments.....	108
4.1.1.1	Variational Methods.....	108
4.1.1.2	Basis Functions	112
4.2	Reaction Formulation.....	113
4.2.1	Reaction Equation Derivation.....	113
4.2.1.1	Currents.....	116
4.2.1.2	Induced Field Integral.....	121
4.2.1.3	Excitation Integral.....	125
4.2.2	Numerical Integration.....	130
4.3	Microstrip Dipole Antennas.....	132
4.3.1	Dipole with Delta Gap Source	132
4.3.1.1	Modified Reaction Equation	133
4.3.1.2	Analysis.....	134
4.4	Rectangular Microstrip Patch Antenna.....	152
4.4.1	Reaction Equation.....	153
4.4.2	Basis Function Convergence.....	153
4.4.3	Performance Analysis	158
4.4.3.1	Input Impedance, Resonant Length and Impedance Bandwidth	159
4.4.3.2	Radiation Behavior	173
5	CONCLUSIONS AND FUTURE WORK.....	180
	BIBLIOGRAPHY	185
	VITA.....	189

LIST OF FIGURES

Figure 1-1: Rotation diagrams	13
Figure 2-1: Wave vector surface: unrotated biaxial medium $(\epsilon_x, \epsilon_y, \epsilon_z) = (2, 8, 4)$, plotted over $0 \leq \theta \leq \pi, 0 \leq \varphi \leq \pi$	19
Figure 2-2: Wave vector surface: unrotated biaxial medium $(\epsilon_x, \epsilon_y, \epsilon_z) = (2, 8, 4)$, plotted over $0 \leq \theta \leq \pi, \pi/9 \leq \varphi \leq \pi/3$	21
Figure 2-3: Booker quartic root assignment for biaxial medium, k_z vs. k_y (permittivity tensor $(\epsilon_x, \epsilon_y, \epsilon_z) = (2, 4, 8)$, rotated by $(\psi_1, \psi_2) = (30^\circ, 75^\circ)$).....	24
Figure 2-4: Booker quartic root assignment for biaxial medium, k_z vs. k_x (permittivity tensor $(\epsilon_x, \epsilon_y, \epsilon_z) = (2, 4, 8)$, rotated by $(\psi_1, \psi_2) = (30^\circ, 75^\circ)$).....	24
Figure 2-5: Wave vector surface: wave vectors computed using Booker quartic (permittivity tensor $(\epsilon_x, \epsilon_y, \epsilon_z) = (2, 4, 8)$, rotated by $(\psi_1, \psi_2) = (30^\circ, 75^\circ)$)	25
Figure 2-6: Wave vector surface showing umbilical point and optic axis 2: wave vectors computed using Booker quartic (permittivity tensor $(\epsilon_x, \epsilon_y, \epsilon_z) = (2, 4, 8)$, rotated by $(\psi_1, \psi_2) = (30^\circ, 75^\circ)$).....	25
Figure 2-7: Umbilical point at optic axis 1, $(\epsilon_x, \epsilon_y, \epsilon_z) = (2, 4, 8)$, $(\psi_1, \psi_2) = (30^\circ, 75^\circ)$	26
Figure 2-8: Umbilical point at optic axis 2, $(\epsilon_x, \epsilon_y, \epsilon_z) = (2, 4, 8)$, $(\psi_1, \psi_2) = (30^\circ, 75^\circ)$	26
Figure 2-9: TE wave incident upon isotropic-biaxial interface	31
Figure 2-10: TM wave incident upon isotropic-biaxial interface	35
Figure 2-11: Diagram of plane and angle of incidence for wave incident from region 0	38
Figure 2-12: Reflection and transmission characteristics in uniaxial limit	39
Figure 2-13: Reflection and transmission in uniaxial limit – tilted permittivity tensor	40
Figure 2-14: Half-space reflection and transmission coefficients for incident wave from isotropic medium to unrotated biaxial medium $(\epsilon_x, \epsilon_y, \epsilon_z) = (2, 5, 8)$	42
Figure 2-15: Power conservation for wave incident from region 0	45
Figure 2-16: Half-space reflection and transmission coefficients for incident wave from isotropic medium to biaxial medium $((\epsilon_x, \epsilon_y, \epsilon_z) = (2, 5, 8), (\psi_1, \psi_2) = (45^\circ, 45^\circ))$	46
Figure 2-17: Half-space co-polarized reflection coefficients for incident wave from isotropic medium to biaxial medium $((\epsilon_x, \epsilon_y, \epsilon_z) = (2, 5, 8), (\psi_1=0, \psi_2 \text{ varied}))$	47
Figure 2-18: Reflection coefficients and imaginary transmission coefficients from isotropic-uniaxial interface	50

Figure 2-19: Solution to Booker quartic for uniaxial medium.....	51
Figure 2-20: Co-polarized reflection coefficients from Silicon-PTFE cloth boundary	52
Figure 2-21: Booker quartic solutions in PTFE cloth	52
Figure 2-22: Critical angle for wave incident from Silicon to PTFE cloth as ψ_2 is varied for incident angle ϕ_i of 0° (a), 25° (b), and 90° (c).....	54
Figure 2-23: Critical angle for wave incident from Silicon to PTFE cloth as ψ_1 is varied for incident angle ϕ_i of 0° (a), 25° (b), and 90° (c).....	55
Figure 2-24: Brewster angle as ψ_1 is varied for ψ_2 of 0° (a) and 45° (b). Biaxial permittivity tensor $(\epsilon_x, \epsilon_y, \epsilon_z) = (3, 4, 5)$	57
Figure 2-25: Brewster angle as ψ_2 is varied for ψ_1 of 0° (a) and 45° (b). Biaxial permittivity tensor $(\epsilon_x, \epsilon_y, \epsilon_z) = (3, 4, 5)$	57
Figure 2-26: Brewster angle as ψ_1 is varied for ψ_2 of 0° (a) and 45° (b). Biaxial permittivity tensor $(\epsilon_x, \epsilon_y, \epsilon_z) = (2, 5, 8)$	58
Figure 2-27: Brewster angle as ψ_2 is varied for ψ_1 of 0° (a) and 45° (b). Biaxial permittivity tensor $(\epsilon_x, \epsilon_y, \epsilon_z) = (2, 5, 8)$	59
Figure 2-28: a-wave incident upon biaxial- isotropic interface	59
Figure 2-29: b-wave incident upon biaxial- isotropic interface	62
Figure 2-30: a- or b-wave incident upon biaxial-perfect electric conductor interface	63
Figure 2-31: Diagram of plane and angle of incidence for wave incident from region 1	65
Figure 2-32: Reflection coefficients a-wave upward incident from rotated biaxial medium to air	68
Figure 2-33: Transmitted electric field magnitude for a-wave upward incident from rotated biaxial medium to air ..	69
Figure 2-34: Reflection coefficients b-wave incident from biaxial medium to air	70
Figure 2-35: Transmitted electric field magnitude for b-wave upward incident from rotated biaxial medium to air.	70
Figure 2-36: Reflection coefficients for a-wave upward incident upon biaxial-air half-space. Biaxial parameters: $(\epsilon_x, \epsilon_y, \epsilon_z) = (2, 5, 8), (\psi_1, \psi_2) = (0^\circ, 0^\circ)$	72
Figure 2-37: Transmission coefficients for a-wave upward incident upon biaxial-air half-space. Biaxial parameters: $(\epsilon_x, \epsilon_y, \epsilon_z) = (2, 5, 8), (\psi_1, \psi_2) = (0^\circ, 0^\circ)$	73
Figure 2-38: Transmitted Poynting vector for a-wave incident from biaxial medium to air. Biaxial parameters: $(\epsilon_x, \epsilon_y, \epsilon_z) = (2, 5, 8), (\psi_1, \psi_2) = (0^\circ, 0^\circ)$	73

Figure 2-39: Power conservation for a-wave incident from biaxial medium to air. Biaxial parameters: $(\epsilon_x, \epsilon_y, \epsilon_z) = (2, 5, 8)$, $(\psi_1, \psi_2) = (0^\circ, 0^\circ)$.	75
Figure 2-40: Reflection coefficients for a-wave upward incident upon biaxial-air half-space. Biaxial parameters: $(\epsilon_x, \epsilon_y, \epsilon_z) = (2, 5, 8)$, $(\psi_1, \psi_2) = (15^\circ, 35^\circ)$.	76
Figure 2-41: Real and imaginary reflection coefficients for a-wave upward incident upon biaxial-air half-space. Biaxial parameters: $(\epsilon_x, \epsilon_y, \epsilon_z) = (2, 5, 8)$, $(\psi_1, \psi_2) = (15^\circ, 35^\circ)$.	76
Figure 2-42: Transmission coefficients for a-wave upward incident upon biaxial-air half-space. Biaxial parameters: $(\epsilon_x, \epsilon_y, \epsilon_z) = (2, 5, 8)$, $(\psi_1, \psi_2) = (15^\circ, 35^\circ)$.	77
Figure 2-43: Transmitted Poynting vector for a-wave incident from biaxial medium to air. Biaxial parameters: $(\epsilon_x, \epsilon_y, \epsilon_z) = (2, 5, 8)$, $(\psi_1, \psi_2) = (15^\circ, 35^\circ)$.	78
Figure 2-44: Transmitted and reflected power ratios for a-wave upward incident from rotated biaxial medium to air	78
Figure 2-45: Reflection coefficients for b-wave upward incident upon biaxial-air half-space. Biaxial parameters: $(\epsilon_x, \epsilon_y, \epsilon_z) = (2, 5, 8)$, $(\psi_1, \psi_2) = (0^\circ, 0^\circ)$.	79
Figure 2-46: Transmission coefficients for b-wave upward incident upon biaxial-air half-space. Biaxial parameters: $(\epsilon_x, \epsilon_y, \epsilon_z) = (2, 5, 8)$, $(\psi_1, \psi_2) = (0^\circ, 0^\circ)$.	80
Figure 2-47: Transmitted Poynting vector for b-wave incident from biaxial medium to air. Biaxial parameters: $(\epsilon_x, \epsilon_y, \epsilon_z) = (2, 5, 8)$, $(\psi_1, \psi_2) = (0^\circ, 0^\circ)$.	81
Figure 2-48: Power conservation for b-wave incident from biaxial medium to air. Biaxial parameters: $(\epsilon_x, \epsilon_y, \epsilon_z) = (2, 5, 8)$, $(\psi_1, \psi_2) = (0^\circ, 0^\circ)$.	82
Figure 2-49: Reflection coefficients for b-wave upward incident upon biaxial-air half-space. Biaxial parameters: $(\epsilon_x, \epsilon_y, \epsilon_z) = (2, 5, 8)$, $(\psi_1, \psi_2) = (15^\circ, 35^\circ)$.	83
Figure 2-50: Real and imaginary reflection coefficients for b-wave upward incident upon biaxial-air half-space. Biaxial parameters: $(\epsilon_x, \epsilon_y, \epsilon_z) = (2, 5, 8)$, $(\psi_1, \psi_2) = (15^\circ, 35^\circ)$.	84
Figure 2-51: Transmission coefficients for b-wave upward incident upon biaxial-air half-space. Biaxial parameters: $(\epsilon_x, \epsilon_y, \epsilon_z) = (2, 5, 8)$, $(\psi_1, \psi_2) = (15^\circ, 35^\circ)$.	85
Figure 2-52: Transmitted Poynting vector for b-wave incident from biaxial medium to air. Biaxial parameters: $(\epsilon_x, \epsilon_y, \epsilon_z) = (2, 5, 8)$, $(\psi_1, \psi_2) = (15^\circ, 35^\circ)$.	85
Figure 2-53: Transmitted and reflected power ratios for b-wave upward incident from rotated biaxial medium to air	86
Figure 2-54: Incident, transmitted and reflected waves for two layer problem.	88

Figure 2-55: Two-layer coefficients for wave incident from the isotropic medium unrotated biaxial substrate	90
Figure 2-56: Power conservation for two-layer system	91
Figure 2-57: Two-layer co-polarized reflection coefficients for wave incident from the isotropic medium (region 0); rotated biaxial substrate $(\psi_1, \psi_2) = (30^\circ, 75^\circ)$	92
Figure 2-58: Two-layer cross-polarized reflection coefficients for wave incident from the isotropic medium (region 0); rotated biaxial substrate $(\psi_1, \psi_2) = (30^\circ, 75^\circ)$	92
Figure 2-59: Two-layer co-polarized reflection coefficients for wave incident from the isotropic medium (region 0) with biaxial substrate height of $0.02\lambda_0$	93
Figure 2-60: Two-layer co-polarized reflection coefficients for wave incident from the isotropic medium (region 0) with biaxial substrate height of $1.2\lambda_0$	94
Figure 2-61: Two-layer co-polarized reflection coefficients for wave incident from the isotropic medium (region 0) with rotated biaxial substrates of varying heights	95
Figure 3-1: Two layer geometry used in Green's function formulation	97
Figure 4-1: Rectangular microstrip antenna diagram	107
Figure 4-2: Patch antenna integrand example (a) vs. k_y , (b) vs. k_x	131
Figure 4-3: Current distribution for half wave gap-fed dipole: $N = 6, 12, 18$ and 24 expansion functions with biaxial permittivity $(\epsilon_x, \epsilon_y, \epsilon_z) = (2, 5, 8)$ and no rotation	136
Figure 4-4: Input impedance for gap-fed dipole with width of $0.001\lambda_0$ printed on an isotropic substrate with $\epsilon_r =$ 2.45 , height $= 0.2\lambda_0$	139
Figure 4-5: Input impedance for gap-fed dipole printed on a biaxial substrate with permittivity $(\epsilon_x, \epsilon_y, \epsilon_z) = (2, 5, 8)$ and no rotation and height $0.2\lambda_0$	140
Figure 4-6: Input impedance for gap-fed dipole printed on a biaxial substrate with permittivity $(\epsilon_x, \epsilon_y, \epsilon_z) = (2, 5, 8)$ rotated by $\psi_1 = 30^\circ$ $\psi_2 = 75^\circ$ and height $0.2\lambda_0$	141
Figure 4-7: Radiation pattern of half-wave dipole printed on isotropic substrate of height $0.2\lambda_0$ ($\epsilon_r=2.35$)	147
Figure 4-8: Radiation pattern of half-wave dipole printed on isotropic substrate of height $0.975\lambda_0$ ($\epsilon_r=2.35$)	148
Figure 4-9: Radiation pattern of half-wave dipole printed on isotropic substrate of height $1.05\lambda_0$ ($\epsilon_r = 2.35$)	149
Figure 4-10: Patterns for dipole printed on isotropic substrates of varying heights – from [47] P. B. Katehi and N. G. Alexopoulos, "On the effect of substrate thickness and permittivity on printed circuit dipole properties", <i>IEEE Trans. Ant. Prop.</i> vol. 31, no. 1, pp. 34-39, January 1983.	149
Figure 4-11: Directive gain for gap-fed dipole with biaxial permittivity $(\epsilon_x, \epsilon_y, \epsilon_z) = (5, 3, 4)$ as height is varied... ..	150

Figure 4-12: Directive gain for resonant half wavelength gap-fed dipole printed on a biaxial substrate with permittivity $(\epsilon_x, \epsilon_y, \epsilon_z) = (2, 5, 8)$	151
Figure 4-13: Directive gain for resonant half wavelength gap-fed dipole printed on PTFE cloth.....	151
Figure 4-14: Rectangular Microstrip Patch Antenna Geometry	152
Figure 4-15: Current coefficients along the length of a rectangular microstrip antenna ($W/L=1.5$) on rotated biaxial substrate (a) real, (b) imaginary	155
Figure 4-16: Input impedance behavior for $M=1$ and N is increased from 10 to 14	156
Figure 4-17: Input impedance behavior for $N=12$ and M is increased from 1 to 4.....	157
Figure 4-18: Radiation patterns for $N=12$ and M is increased from 1 to 4 (a) principal polarization (b) cross polarization.....	158
Figure 4-19: Input impedance for isotropic microstrip antenna (a) prior to probe reactance compensation, (b) with probe reactance compensation	164
Figure 4-20: Input impedance for microstrip patch antenna with width of $0.23\lambda_0$ printed on uniaxial substrate with height of $0.02\lambda_0$. (a) positive uniaxial: $(\epsilon_x, \epsilon_y, \epsilon_z) = (6, 6, 10.2)$, (b) negative uniaxial: $(\epsilon_x, \epsilon_y, \epsilon_z) = (13, 13, 10.2)$	165
Figure 4-21: Resonant length of probe fed patch antennas on uniaxial (one isotropic) substrates of varying heights	166
Figure 4-22: Input impedance (a) and return loss (b) of rectangular patch printed on unrotated biaxial substrate (2, 5, 8) of height $0.02\lambda_0$	169
Figure 4-23: Input impedance (a) and return loss (b) of rectangular patch printed on rotated ($\psi_1 = 30^\circ$ $\psi_2 = 75^\circ$) biaxial substrate of height $0.02\lambda_0$	169
Figure 4-24: Input impedance (a) and return loss (b) of rectangular patch printed on PTFE cloth of height $0.02\lambda_0$ 170	
Figure 4-25: Input impedance (a) and return loss (b) of rectangular patch printed on isotropic substrate ($\epsilon_r = 8$) of height $0.02\lambda_0$	170
Figure 4-26: Radiation patterns, unrotated biaxial substrate with permittivity $(\epsilon_x, \epsilon_y, \epsilon_z) = (2, 5, 8)$ and varied height (a) principal polarization, (b) cross polarization	175
Figure 4-27: Radiation patterns, substrate with isotropic permittivity $\epsilon_r = 8$ and varied height (a) principal polarization, (b) cross polarization.....	176
Figure 4-28: Radiation patterns, substrate thickness $0.02\lambda_0$, varied isotropic permittivity (a) principal polarization, (b) cross polarization.....	177

Figure 4-29: Radiation patterns, biaxial substrate with permittivity $(\epsilon_x, \epsilon_y, \epsilon_z) = (2, 5, 8)$ and two rotations (a) principal polarization, (b) cross polarization.....178

Figure 4-30: Radiation patterns, biaxial PTFE cloth substrate with two rotations (a) principal polarization, (b) cross polarization.....179

LIST OF TABLES

Table 1-1: Examples of Biaxial Media	11
Table 2-1: Booker Quartic Root Assignment Summary	23
Table 2-2: Half-Space Configurations	31
Table 4-1: Resonant Lengths for Microstrip Dipoles Printed on Biaxial Substrates ($W=0.001\lambda_0$)	141
Table 4-2: Half-Wave Resonant Lengths of Rectangular Microstrip Patch Antennas	170

1 INTRODUCTION

1.1 Research Objectives

This work investigates wave phenomena in arbitrarily oriented biaxially anisotropic media and the behavior of microstrip antennas on biaxial substrates. Pettis' extensive work [1] solved the problems of Hertzian dipoles positioned in and above a biaxial slab, an infinite transmission line printed on a biaxial substrate and a microstrip dipole antenna printed on a biaxial substrate. To arrive at solutions of these problems, Pettis studied propagation characteristics, Green's functions and singularities inherent in this type of media.

We intend to gain greater understanding of the wave behavior in this medium by studying reflection and transmission from isotropic-anisotropic interfaces. We then use the reflection and transmission coefficients in the eigenvector dyadic Green's functions to study microstrip antennas. We again solve the gap-fed microstrip dipole problem using the eigenvector dyadic Green's function, rather than the transition matrix dyadic Green's function (as was done by Pettis [1]). Finally, we solve the probe-fed rectangular microstrip patch antenna.

The motivation for studying biaxial materials is twofold. First, there are several naturally occurring materials with biaxial properties. When we ignore this biaxial nature, we are unable to accurately predict the behavior of circuits using these materials. However, more interesting is the current research in material science. Material scientists are working on ways to engineer new materials. Much of this research has been fueled by electromagnetic interests in left-handed materials that have negative permittivity and/or permeability as well as other metamaterials. Some studies have shown these materials to have biaxial properties. Secondly, if

we understand biaxial media and show a real benefit, the technology is developing to make the requisite materials a reality. Thus this research aims to be the next step to showing the usefulness of engineered biaxial substrates.

1.2 Previous Work

Considerable work has been done in the study of anisotropic materials. This section reviews what has been done and highlights places where additional contributions can be made, specifically in the study of biaxially anisotropic materials.

1.2.1 Wave Behavior in Anisotropic Materials

Wave propagation and the reflection and transmission of electromagnetic waves from an interface are fundamental to the study of electromagnetics. Most electromagnetics texts contain detailed study of these phenomena when the interface is between two isotropic materials. In his text, Kong [2] handles this problem for isotropic and uniaxial media. While the analysis of wave propagation and reflection and transmission does not directly lend itself to application, it is essential to the understanding of the physics of any electromagnetic problem.

Many authors have studied reflection and transmission in complex materials. Bianisotropic media (in which there is cross-coupling between electric and magnetic fields [2]) has garnered particular attention [3]-[7]. In [3] Tsalamengas provides a formulation to compute the reflection and transmission of an arbitrarily polarized wave incident upon a general bianisotropic slab. This slab is described by four tensors, with no limitations on the tensors themselves. Therefore, this formulation could be used to evaluate reflection and transmission coefficients of an arbitrarily oriented biaxial slab. However, we have only one tensor and this

formulation is unnecessary. Further, Tsalamengas does not analyze the results or provide numerical examples. In [4] Semchenko and Khakhomov derive and compute reflection and transmission coefficients for unrotated uniaxial bianisotropic material and explore the varying incident wave polarizations. Yun Hee Lee [5] studied wave behavior in tilted and untilted uniaxial media including a detailed study of reflection and transmission from an isotropic-uniaxial interface. In [6] Rikte et al. present the coordinate free reflection and transmission dyads for the two-layer problems of 1) a general bianisotropic medium with an isotropic (vacuum) half-space on both sides and 2) a bianisotropic slab with a PEC (perfect electrical conductor) backplane (reflection dyad only). In [7] the most general bianisotropic material is considered by He et al. such that permittivity and permeability tensors may be in general biaxial and/or chiral. A 2x2 matrix is used without formulating the fields explicitly in each region. This provides good numerical results, but is not as good for studying the waves at the surface.

Metamaterials, recently a hot research area, have also been studied for their reflective and refractive characteristics. Grzegorzczuk et al. ([8, 9]) provide an extensive study of the behavior of waves incident upon metamaterial layers. Their work is particularly relevant because they first consider a general bianisotropic medium (with biaxial permittivity and permeability tensors), and then apply the properties of left-handed materials. Therefore, their formulation is general but their results are specific to negative epsilon materials. In fact, the inclusions used to create negative epsilon (or mu) materials make the material anisotropic in general so it is important to understand the anisotropic behaviors.

Researchers have also considered reflection and transmission from biaxial boundaries. Stamnes and Sithambaranathan [10] considered reflection and refraction from a

plane interface separating an isotropic and a biaxial medium. In their paper, they consider only the unrotated biaxial medium with a diagonal permittivity tensor. Further, they do not present numerical results but rather the formulation of the resulting fields when a plane TE (transverse electric) or TM (transverse magnetic) wave is incident on the interface. Abdulhalim [11] presents a 2×2 matrix approach to solving for reflection and transmission coefficients from biaxial boundaries but does not present any numerical results. Landry [12, 13] studies transmission and reflection at planar interface between arbitrarily oriented biaxial media. He formulates reflection and transmission coefficients using characteristic angles. The formulation is based on an interface between two arbitrarily oriented biaxial slabs; however, the resulting analysis includes the special case where one of the slabs is isotropic. Landry considers wave incident upon the boundary from each side (downward and upward incident). His analysis includes a brief discussion of Brewster angle and critical angle.

While Landry's analysis of reflection and transmission from an arbitrarily oriented biaxial slab is fairly complete, his formulation is considerably different from our formulation. We are using a form based on components of the propagation vector as this is how we use the coefficients when computing the Green's function. Further, he studied the reflection and transmission of the incident wave in an isotropic region in terms of polarization angle. We are more interested in considering that wave as either TE (transverse electric) or TM (transverse magnetic). Finally, when he considered the layered problem, he analyzed reflection and transmission as a series of bounces. We formulate the total upward and downward propagating waves to obtain overall reflection and transmission coefficients. We also hope to more clearly define the waves inside the biaxial medium. Landry does consider the two polarizations, but

describes them only as “associated with inner surface” or “associated with outer surface.” Finally, we perform a more in-depth study of the Brewster angle effect and critical angle effect as material parameters are varied.

1.2.2 Microstrip Antennas

Microstrip circuits are ubiquitous in modern technology. Any printed wire above some grounded substrate acts as a microstrip line. They are present everywhere from computer chips to complex radar beamformers. Initially, microstrip circuits were designed and analyzed for isotropic substrates. However, as research progressed it was found that many manmade and natural substrates are not isotropic. In 1985, Alexopoulos [14] detailed known anisotropies and provided analysis of integrated microstrip circuits on anisotropic substrates using existing empirical, quasi-static and dynamic solution methods. Alexopoulos had two primary motivations for studying the behavior of microstrip lines on anisotropic materials. The first motivation stems from the fact that variations in the permittivity of a dielectric within an individual slab or between different batches were known to produce errors and hinder circuit repeatability. In fact, he showed that significant errors (over 8% for thin lines) in the computation of effective permittivity exist if anisotropy is ignored. Secondly, Alexopoulos believed that in some applications, “anisotropy serves to improve circuit performance.” This sentiment is shared by many material researchers trying to create substrates that will provide some special circuit performance. In [14] Alexopoulos considered primarily uniaxially anisotropic substrates. Later, Tsalamengas et al. [15] investigated propagation modes in microstrip lines printed on anisotropic substrates with general electric and magnetic anisotropies. The substrates were described by 3x3 permittivity and permeability tensors with no restrictions

on their elements. In our analysis, we are considering only electrically biaxial substrates. Therefore, only the permittivity of the medium is a 3×3 tensor. The medium is magnetically isotropic. Further, as will be shown, there are restrictions on the elements. We consider a diagonal biaxial permittivity tensor that is then rotated, so the elements of the 3×3 tensor are related by these rotation angles. In his dissertation Pettis [1] considered microstrip lines on arbitrarily oriented biaxial substrates, the same type of medium we are studying here.

While the research into microstrip lines printed on anisotropic substrates laid the ground work for all other microstrip circuits, in this work, we are primarily concerned with microstrip antennas. Microstrip antennas have been of interest for well over 50 years and can be printed on almost any substrate in a wide variety of shapes. They are used to make low profile conformal arrays and used in small personal electronics such as cell phones and wireless internet devices. In 1981, Carver and Mink [16] summarized over 25 years of work to date and researchers have continued to study these types of antennas for 30 more years. At the time of Carver and Mink's report [16] research had primarily focused on microstrip dipoles and conformal antennas printed on isotropic substrates. Early investigations of microstrip dipoles include radiation properties [17] and mutual impedance [18]. Uzunoglu et al. [17] studied radiation properties of microstrip dipoles. They used the Green's function for a horizontal Hertzian dipole on a grounded substrate combined with an assumed sinusoidal current distribution to compute the input impedance using variation methods. Alexopoulos and Rana [18] used the same method to compute the mutual impedance between microstrip dipoles in broadside, collinear and echelon configurations.

Many researchers studied the more general rectangular patch problem. As with microstrip line research, the baseline research was for antennas printed on isotropic substrates. Early research into microstrip patch antennas includes input impedance, mutual coupling [19] and resonant frequencies [20]. Pozar [19] uses a method of moments approach to compute both input impedance and mutual coupling of rectangular microstrip antennas in which a coaxial probe type feed is used. In the moment method computation, an idealized probe feed is used. To account for the probe self-inductance, an inductance term is added to the input impedance. Bailey and Deshpande [20] compute resonant frequency of microstrip antennas using a method based on the cavity model with the “grounded dielectric being approximated by an effective dielectric constant.” As bandwidth of an antenna is a concern for any application, Kara [21] presents simple closed-form equations for calculating the bandwidth of probe-fed rectangular microstrip antennas. Kara’s formulas are based on the cavity model and transmission line model and are valid for various substrate thicknesses and permittivities. Continued efforts produced detailed research into how to feed rectangular microstrip patch antennas [22], [23], and [24]. From this base, applications were considered including arrays of microstrip antennas [25].

As research progressed, anisotropic substrates were considered. Pozar was one of the first researchers to consider the rectangular microstrip patch on a uniaxial substrate [26]. Pozar computes both radiation and scattering from a microstrip patch on an electrically uniaxial substrate and compares these results to the same patch on an isotropic substrate. He formulates the characteristic Green’s function in the spectral domain and then uses the moment method to compute radiated power, power delivered to surface waves and radar cross section. He uses a feed model similar to the one used in [19]. As with antennas on isotropic substrates, researchers

sought solutions for parameters of interest for microstrip antennas on uniaxial substrates. Wong et al. [27] computed the resonant frequency of a rectangular patch using Galerkin's method with sinusoidal basis functions. Resonant frequency and half-power bandwidth are compared for isotropic, positive uniaxial (anisotropic ratio = $\epsilon_x/\epsilon_z < 1$) and negative uniaxial (anisotropic ratio > 1) substrates. The results show that both resonant frequency and half-power bandwidth increase on a positive uniaxial substrate and decrease on a negative uniaxial substrate. Broadband tapered microstrip patch antennas printed on uniaxial dielectric substrates are considered in [28]. Full-wave spectral domain formulation by means of Galerkin's method is used along with the transmission line method to compute bandwidth. It is found that linear variations in substrate height produce great influence on the bandwidth of microstrip antennas. Other authors considered microstrip patches printed on layers of uniaxial materials with the possibility of having uniaxial overlays [29] and [30]. These papers compute the input impedance and resonant frequency of the microstrip patch, respectively.

1.3 Electromagnetic Definitions for Isotropic and Biaxial Media

The fundamental equations describing behavior of electromagnetic waves in a biaxially anisotropic medium (or simply called *biaxial*) are more complex than the isotropic equations we are familiar with. In isotropic media, the constitutive relations that relate the electric flux density (\bar{D}) to the electric field intensity (\bar{E}) and the magnetic flux density (\bar{B}) to the magnetic field intensity (\bar{H}) are given by

$$\bar{D} = \epsilon\bar{E}; \quad \bar{B} = \mu\bar{H} \tag{1.3.1}$$

The permittivity of the medium (ϵ) describes the medium's electrical properties and the permeability (μ) describes its magnetic properties.

If the medium is biaxially anisotropic, the permittivity and permeability of medium take on a tensor form, changing (1.3.1) from a set of vector equations to a set of matrix equations. These equations can be written as

$$\bar{D} = \bar{\epsilon}E = \epsilon_o \bar{\epsilon}_r E \quad (1.3.2)$$

and

$$\bar{B} = \bar{\mu}H = \mu_o \bar{\mu}_r H \quad (1.3.3)$$

where $\bar{\epsilon}_r$ and $\bar{\mu}_r$ are relative permittivity and permeability tensors, respectively.

The change in constitutive relations will also affect Maxwell's equations in the medium. The time-harmonic forms of Maxwell's equations for isotropic media are given by

$$\nabla \times \bar{E} = i\omega\mu\bar{H} \quad (1.3.4)$$

$$\nabla \times \bar{H} = -i\omega\epsilon\bar{E} + \bar{J} \quad (1.3.5)$$

$$\nabla \cdot \bar{D} = \rho_v \quad (1.3.6)$$

$$\nabla \cdot \bar{B} = 0 \quad (1.3.7)$$

Equations (1.3.4) through (1.3.7) assume $e^{-i\omega t}$ time-harmonic variation. This is consistent with the convention used in the optics community as well as the convention used by Pettis. We are choosing this convention as well to readily compare our result with Pettis'.

In this work, we consider an electrically biaxial material. Therefore, the permittivity takes on the tensor form while the permeability will remain scalar. In fact we are assuming that

the permeability is equal to the permeability of free space. Given this assumption, Maxwell's equations in the media we are considering become

$$\nabla \times \bar{E} = i\omega\mu\bar{H} \quad (1.3.8)$$

$$\nabla \times \bar{H} = -i\omega\epsilon_o\bar{\epsilon}_r\bar{E} + \bar{J} \quad (1.3.9)$$

$$\nabla \cdot \bar{D} = \rho_v \quad (1.3.10)$$

$$\nabla \cdot \bar{B} = 0 \quad (1.3.11)$$

1.3.1 Permittivity Tensor

The defining property of electrically biaxial media is the permittivity tensor. Isotropic materials have a single permittivity. Uniaxially anisotropic materials have two different permittivity values. Uniaxial materials have the same permittivity along two dimensions and a different permittivity along the third dimension. The axis along the direction of the unique permittivity value is called the *optic axis*. An unrotated uniaxial permittivity tensor can be written as

$$\bar{\epsilon} = \begin{bmatrix} \epsilon & 0 & 0 \\ 0 & \epsilon & 0 \\ 0 & 0 & \epsilon_z \end{bmatrix} \quad (1.3.12)$$

The permittivity shown in (1.3.12) represents an unrotated uniaxial medium with optic axis along the z-direction.

Biaxially anisotropic materials have three unique values in the permittivity tensor and they have two optic axes. An unrotated biaxial permittivity tensor is given by

$$\epsilon_{||} = \begin{bmatrix} \epsilon_x & 0 & 0 \\ 0 & \epsilon_y & 0 \\ 0 & 0 & \epsilon_z \end{bmatrix} \quad (1.3.13)$$

where $\epsilon_x \neq \epsilon_y \neq \epsilon_z$. Equation (1.3.13) represents a biaxial medium whose principal axes are aligned with the Cartesian coordinate system. If, however, the biaxial medium was arbitrarily oriented with respect to the coordinate system, the permittivity tensor would not be as simple. We can obtain the tensor for an arbitrarily oriented biaxial medium by applying rotations to the tensor in equation (1.3.13). Some man-made and natural materials known to be biaxially anisotropic are shown in Table 1-1.

Table 1-1: Examples of Biaxial Media

Medium	ϵ_x	ϵ_y	ϵ_z
Extrinsically Biaxial (man-made materials) [31]			
PTFE cloth	2.45	2.89	2.95
Glass cloth	5.56	6.24	6.64
Intrinsically Biaxial (naturally occurring crystals) [32]			
Borax	2.093	2.158	2.167
Epsom Salt	2.053	2.117	2.134
Mica	2.442	2.547	2.563
Perovskite	5.290	5.476	5.664
Topaz	2.220	2.280	2.310

1.3.1.1 Permittivity Tensor Rotations

In our formulation we use the same tensor rotations used by Mudaliar and Lee [34]. Let us assume the permittivity tensor shown in (1.3.13) have principal axes x'', y'', z'' and we want to transform the tensor to the system coordinates x, y, z . Throughout this research, we consider the biaxial medium in a layered geometry. We define the layering such that one of the principal axes lies in the plane of the boundary. We chose the x'' axis to be in this plane. We then define the reference coordinate system such that the z -axis is perpendicular to the planar interface. The orientation of the medium coordinate system with respect to the reference coordinate system can then be defined by 2 rotation angles.

We begin by performing a counter-clockwise transformation about the x'' axis by an angle ψ_1 as shown in Figure 1-1 (a). The rotation matrix for the ψ_1 rotation is given by

$$R_1 = \begin{bmatrix} 1 & 0 & 0 \\ 0 & \cos \psi_1 & \sin \psi_1 \\ 0 & -\sin \psi_1 & \cos \psi_1 \end{bmatrix} \quad (1.3.14)$$

The resulting tensor now has principal axes x', y', z' . We then transform this tensor about the z' axis by an angle ψ_2 as shown in Figure 1-1 (b) and described by

$$R_2 = \begin{bmatrix} \cos \psi_2 & \sin \psi_2 & 0 \\ -\sin \psi_2 & \cos \psi_2 & 0 \\ 0 & 0 & 1 \end{bmatrix} \quad (1.3.15)$$

The resulting permittivity tensor has undergone a total rotation R computed by

$$R = R_2 \cdot R_1 = \begin{bmatrix} \cos \psi_2 & \sin \psi_2 \cos \psi_1 & \sin \psi_2 \sin \psi_1 \\ -\sin \psi_2 & \cos \psi_2 \cos \psi_1 & \cos \psi_2 \sin \psi_1 \\ 0 & -\sin \psi_1 & \cos \psi_1 \end{bmatrix} \quad (1.3.16)$$

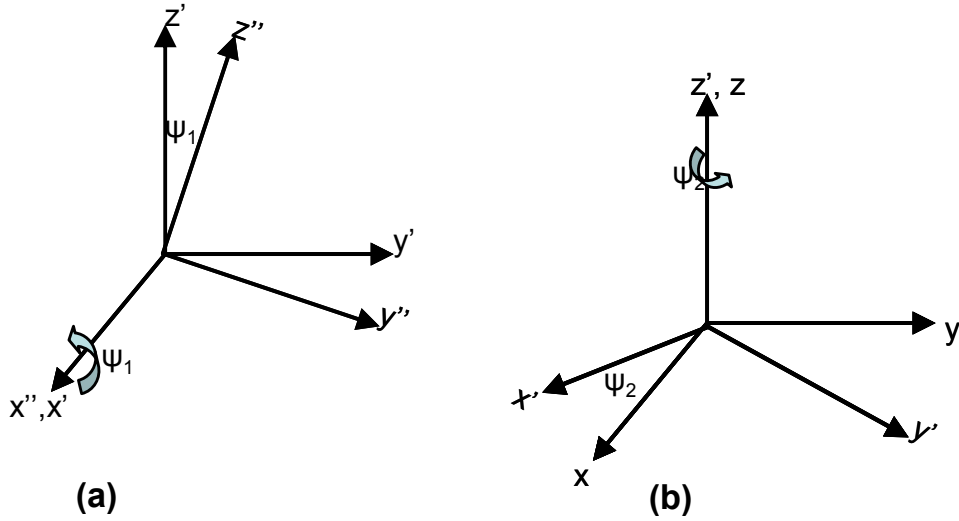


Figure 1-1: Rotation diagrams

to get to the laboratory coordinate system x, y, z . The permittivity tensor now is the full matrix

$$\underline{\underline{\epsilon}}_r = \begin{bmatrix} \epsilon_{xx} & \epsilon_{xy} & \epsilon_{xz} \\ \epsilon_{yx} & \epsilon_{yy} & \epsilon_{yz} \\ \epsilon_{zx} & \epsilon_{zy} & \epsilon_{zz} \end{bmatrix} \quad (1.3.17)$$

where

$$\begin{aligned}
\varepsilon_{xx} &= \varepsilon_x \cos^2 \psi_2 + (\varepsilon_y \cos^2 \psi_1 + \varepsilon_z \sin^2 \psi_1) \sin^2 \psi_2 \\
\varepsilon_{xy} &= (-\varepsilon_x + \varepsilon_y \cos^2 \psi_1 + \varepsilon_z \sin^2 \psi_1) \sin \psi_2 \cos \psi_2 \\
\varepsilon_{xz} &= (\varepsilon_z - \varepsilon_y) \sin \psi_1 \cos \psi_1 \sin \psi_2 \\
\varepsilon_{yy} &= \varepsilon_x \sin^2 \psi_2 + (\varepsilon_y \cos^2 \psi_1 + \varepsilon_z \sin^2 \psi_1) \cos^2 \psi_2 \\
\varepsilon_{yz} &= (\varepsilon_z - \varepsilon_y) \sin \psi_1 \cos \psi_1 \cos \psi_2 \\
\varepsilon_{zz} &= \varepsilon_y \sin^2 \psi_1 + \varepsilon_z \cos^2 \psi_1 \\
\varepsilon_{yx} &= \varepsilon_{xy} \\
\varepsilon_{zx} &= \varepsilon_{xz} \\
\varepsilon_{zy} &= \varepsilon_{yz}
\end{aligned} \tag{1.3.18}$$

1.4 Chapter Overview

The objectives of this research are to gain better understanding of electromagnetic wave characteristics in biaxially anisotropic media and to understand how microstrip antennas behave when printed on biaxial substrates. In Chapter 2, we study wave behavior in biaxial media including birefringence and reflection and transmission behaviors. Biaxial media with varying permittivities and rotation angles are used. The study of birefringence includes details of how propagation roots are assigned to the two characteristic waves. In the analysis of reflection and transmission, we consider half-space and two-layer geometries with waves impinging from either isotropic or biaxial media. Phenomena such as the Brewster angle effect and critical angle are then considered and conclusions about how waves behave at biaxial interfaces are made.

In Chapter 3 we introduce the eigenvector dyadic Green's function (E-DGF) and discuss our rationale for using this Green's function to model microstrip antennas. We also

apply the symmetric property of the dyadic Green's function (DGF) to obtain an unknown Green's function needed in our Method of Moments solution.

In Chapter 4 we analyze microstrip antennas printed on biaxially anisotropic substrates using the Method of Moments. First, we model gap-fed dipole antennas using the E-DGF and show that our results agree with published results including those presented by Pettis [1]. The largest contribution of this work is the study of the patch antenna on biaxially anisotropic substrates. This antenna has never been modeled before. The Method of Moments is used to compute unknown currents on the patch antenna excited by a coaxial probe source. These currents are then used to evaluate antenna performance. The analysis focuses on the input impedance and radiation behaviors. Input impedance is used to compute the resonant length and impedance bandwidth of the antennas. The principal and cross polarization radiation patterns are also analyzed. Antenna performance is evaluated as the relative permittivities and rotations of the biaxial medium are changed. The patch antenna and substrate dimensions are changed as well. With this body of results, we make some conclusions about the performance of probe-fed rectangular microstrip antennas printed on biaxial substrates.

Finally, in Chapter 5, we conclude. We summarize our findings and provide some context for our conclusions. We also provide some ideas for future work in this area.

2 WAVE BEHAVIOR IN LAYERED BIAxIAL MEDIA

Waves in biaxially anisotropic media behave differently than waves in isotropic or even uniaxially anisotropic media. In this chapter, we investigate this unique wave behavior. We first analyze propagation in biaxial media and birefringence. Then we analyze reflection and transmission characteristics for both half-space and two layer interfaces.

2.1 Birefringence

Born and Wolf [35] defined birefringence as the phenomenon in which a single incident wave will give rise to two refracted waves. In biaxially anisotropic media birefringence is observed. For a given wave incident upon the biaxial medium, two wave-normal directions exist resulting in four distinct refracted waves. Birefringence can be observed via analysis of the propagation vectors in biaxial media. The two characteristic waves observed in a biaxially anisotropic medium are called the *a-wave* and the *b-wave* [34].

2.1.1 Propagation Vectors

Propagation vectors are crucial to understanding birefringence. The propagation vectors of the a- and b-waves are given by

$$\bar{k}^a = \hat{x}k_x + \hat{y}k_y + \hat{z}k_z^{au} \quad (2.1.1)$$

$$\bar{k}^a = \hat{x}k_x + \hat{y}k_y + \hat{z}k_z^{ad} \quad (2.1.2)$$

$$\bar{k}^b = \hat{x}k_x + \hat{y}k_y + \hat{z}k_z^{bu} \quad (2.1.3)$$

$$\bar{k}^b = \hat{x}k_x + \hat{y}k_y + \hat{z}k_z^{bd} \quad (2.1.4)$$

where k -vectors are used for upward propagating waves (propagating in the $+z$ direction) and κ -vectors are for downward propagating waves. Note that there are four distinct values for k_z in this region: two for each a-wave and two for each b-wave. A single fourth order equation, known as the Booker quartic, provides the solutions for these propagation constants. In the following sections we will solve the Booker quartic for unbounded biaxial media and layered media.

2.1.1.1 Unbounded Media

Consider an unbounded region of biaxial media. We are interested in the propagation vectors in this region to help understand birefringence. The propagation vectors (\bar{k}) in biaxial media are governed by the fourth order dispersion relation [1]

$$k^2(\bar{k} \cdot \bar{\bar{\epsilon}}_r \cdot \bar{k}) + \bar{k} \cdot \left[\text{adj}(\bar{\bar{\epsilon}}_r) - (\text{adj}(\bar{\bar{\epsilon}}_r))_I \bar{I} \right] \cdot \bar{k} k_0^2 + |\bar{\bar{\epsilon}}_r| k_0^4 = 0 \quad (2.1.5)$$

where k_0 is the free-space wave number (propagation constant in free-space) and the subscript t indicates that the trace of the matrix is computed. If we factor out the magnitude of vector \bar{k} , we obtain the *Booker quartic*

$$k^4(\hat{k} \cdot \bar{\bar{\epsilon}}_r \cdot \hat{k}) + k^2(\hat{k} \cdot \left[\text{adj}(\bar{\bar{\epsilon}}_r) - (\text{adj}(\bar{\bar{\epsilon}}_r))_I \bar{I} \right] \cdot \hat{k} k_0^2) + |\bar{\bar{\epsilon}}_r| k_0^4 = 0 \quad (2.1.6)$$

where \hat{k} is a unit vector (magnitude of 1) in the direction of the propagation vector \bar{k} .

For the unrotated case equation (2.1.6) is a biquadratic equation in k . For each direction of propagation, there are four wave numbers or propagation constants. Two will represent upward propagating waves while two represent downward propagating waves. We call the two characteristic waves *a-wave* and *b-wave*. Solutions to the biquadratic are given by

$$k = \pm \sqrt{-\frac{B}{2A} \pm \frac{\sqrt{B^2 - 4AC}}{2A}} \quad (2.1.7)$$

where

$$\begin{aligned} A &= (\hat{k} \cdot \bar{\bar{\epsilon}}_r \cdot \hat{k}) \\ B &= \left(\hat{k} \cdot \left[\text{adj}(\bar{\bar{\epsilon}}_r) - (\text{adj}(\bar{\bar{\epsilon}}_r))_t \bar{\bar{I}} \right] \cdot \hat{k} k_0^2 \right) \\ C &= |\bar{\bar{\epsilon}}_r| k_0^4 \end{aligned} \quad (2.1.8)$$

As defined by Pettis [1], we choose the solutions associated with the positive sign under the radical to be the b-wave propagation constants. Thus, the solutions associated with the negative sign under the radical are the a-wave propagation constants. While there are two solutions for each wave, they are not unique; one solution having the opposite sign of the other. When the medium is rotated, this is not the case and in fact the upward and downward components for a given wave will not have the same magnitude.

The solutions represent two surfaces which we refer to as *wave vector surfaces*. If we choose the direction of propagation, we can solve for the propagation constant for each wave and both for each chosen direction. We will follow the technique used by Pettis [1] and define \hat{k} in terms of spherical coordinates then sweep over the angular dimensions θ and ϕ .

First, consider the same simple unrotated case that Pettis considered. We will use the same material parameters used by Pettis to compare results. The relative permittivity tensor for this medium is given by

$$\epsilon_r = \begin{bmatrix} 2 & & \\ & 8 & \\ & & 4 \end{bmatrix} \quad (2.1.9)$$

To plot the wave vector surface, we first choose the direction (θ and ϕ) to compute \hat{k} which is then used to compute k_a and k_b . This propagation constant (k_a or k_b) is then used to compute the associated k_x , k_y , and k_z for the a-wave and b-wave. Half of the resulting a- and b-wave vector surfaces (angular sweep $0 \leq \theta \leq \pi$, $0 \leq \phi \leq \pi$) are shown in Figure 2-1. The inner surface is the a-wave vector surface and the outer surface is the b-wave vector surface. The intersecting line is one of the *optic axes*. We can see from this plot that the optic axis intersects the wave vector surfaces at some point. We can further see that the b-wave wave vector surface is at a local minimum at the point of intersection.

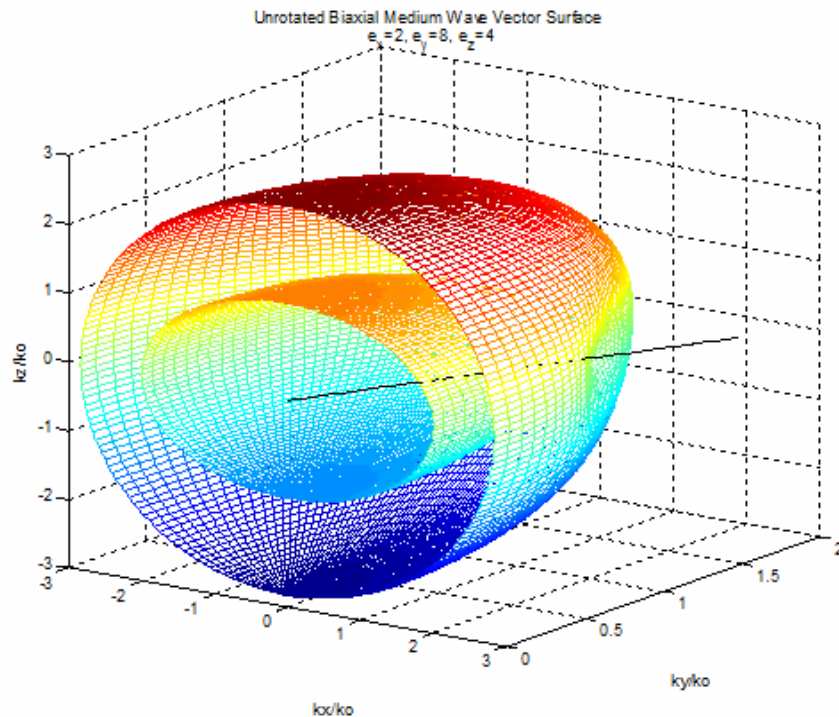


Figure 2-1: Wave vector surface: unrotated biaxial medium $(\epsilon_x, \epsilon_y, \epsilon_z) = (2, 8, 4)$, plotted over $0 \leq \theta \leq \pi$, $0 \leq \phi \leq \pi$

We can gain more insight about this point of intersection from Figure 2-2. In this figure we have plotted the surfaces over a more limited sweep ($0 \leq \theta \leq \pi$, $\pi/9 \leq \varphi \leq \pi/3$) to see more detail. First, we note that Figure 2-1 and Figure 2-2 agree with the results presented by Pettis [1]. We can also see that not only is the b-wave surface at a minimum, but the a-wave and b-wave surfaces are touching. This point is termed the *umbilical point* [1]. The behavior of the wave at this point is significant. The two propagation constants approach the same value when the propagation vectors are parallel to the optic axis (i.e. when they are intersecting). When this occurs, the wave will behave as if the medium is isotropic [36]. The medium is named *biaxial* because it has *two optic axes*. We derive explicit equations for the optic axes in Section 2.1.2. Also note that we treat the region for which k_z becomes imaginary when considering layered media.

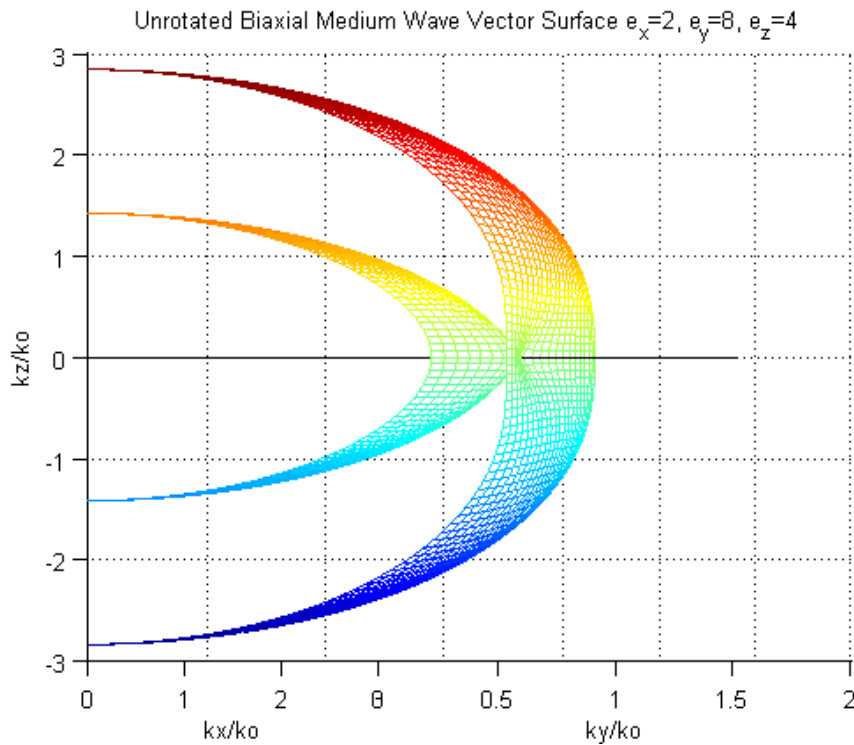


Figure 2-2: Wave vector surface: unrotated biaxial medium $(\epsilon_x, \epsilon_y, \epsilon_z) = (2, 8, 4)$, plotted over $0 \leq \theta \leq \pi$, $\pi/9 \leq \phi \leq \pi/3$

The unbounded unrotated problem is easily understood because the roots of the dispersion relation are simple to compute and assign. Studying the wave vector surfaces of the unbounded region gives us insight into how the wave behaves in the medium and provides a comparison for the layered problem. While we approach the unbounded and layered problems differently, the wave should propagate the same way in the biaxial medium for both cases. Now we turn to the layered case to formulate our propagation vector solutions.

2.1.1.2 Layered Media

Bounded electromagnetic problems present additional constraints on the assignment of the propagation vector in each region. The phase matching boundary condition on electromagnetic waves requires that the tangential components of the propagation vector be continuous across layer boundaries. In the geometry we are interested in this means that k_x and k_y are continuous. Whether we are considering reflection and transmission problems or source specific problems involving the Green's functions, the transverse components are fixed and common to all of the propagation vectors. Therefore, for layered problems we want to compute k_z in the biaxial medium given k_x and k_y to evaluate the electric field vectors. We will use the *Booker quartic* equation derived by Pettis [1] for k_z , given by

$$\epsilon_{zz}k_z^4 + \Delta k_z^3 + \Sigma k_z^2 + Xk_z + \Gamma = 0 \quad (2.1.10)$$

where the coefficients ϵ_{zz} , Δ , Σ , X , and Γ are defined by Pettis [1, Appendix I]. The solution of this Booker quartic yields four unique roots for k_z : two roots correspond to the upward propagating waves and two to the downward propagating waves. Of the two upward one will be

for the b-wave (k_z^{bu}) and one for the a-wave (k_z^{au}). Similarly, there will be one downward propagating b-wave root (k_z^{bd}) and one downward propagating a-wave root (k_z^{ad}). The way we assign these roots is important in understanding the way the a- and b-waves propagate.

We can see from Figure 2-1 that when all four roots are real, the magnitude k is larger for the b-wave than the a-wave. With the transverse components common to both waves the magnitude of k_z^b is greater than the magnitude of k_z^a for four real roots. However, when k_x and k_y get large, as they will when computing the Green's function, the roots become complex and their assignment is less intuitive.

If we track the four roots, we start with the k_z^a being smaller than the k_z^b roots. This means that the real a-wave roots approach zero before the real b-wave roots do as k_ρ (or $\sqrt{k_x^2 + k_y^2}$) increases. As k_ρ increases beyond some point, the a-wave roots will become complex. This will happen before the b-wave roots become complex. Increase k_ρ further and all four roots will be complex. In this case, the a-wave propagation constant will be larger (although complex) than the b-wave propagation constant because the imaginary part is greater for the a-wave.

In defining the orientation of a biaxial medium (with rotated permittivity tensor) Pettis used three rotation angles. Three angles are necessary for the unbounded biaxial medium to be arbitrarily oriented, however in the bounded case, two angles are sufficient as the normal to the boundary is fixed by the geometry. Therefore, we will use the two angle orientation of the biaxial medium discussed in Chapter 1.

The unrotated permittivity tensor is similar to the one given by equation (2.1.9) only we switch ϵ_y and ϵ_z resulting in

$$\bar{\epsilon}_r = \begin{bmatrix} 2 & & \\ & 4 & \\ & & 8 \end{bmatrix} \quad (2.1.11)$$

This permittivity tensor is put under a rotation of $(\psi_1 \ \psi_2) = (30^\circ, 75^\circ)$. We first look at the behavior of the Booker quartic roots for a fixed k_x ($k_x = 0.5k_0$) as k_y is varied. The resulting plot of the propagation constant in the k_y - k_z plane is shown in Figure 2-3. In Figure 2-3, we see that for small values of k_y , all the roots are purely real. As k_y reaches approximately $1.75k_0$, we see that k_a is no longer purely real. The real part of k_z^{au} and k_z^{ad} converge to zero as the imaginary components grow from zero. As k_y approaches $3k_0$, we see that all four roots are complex. The real parts of k_z^{bu} and k_z^{bd} converge to zero and the imaginary parts grow from zero. We also note that when the roots are purely real, k_z^b is greater than k_z^a . However, when the roots become complex the imaginary part of k_z^a is greater than the imaginary part of k_z^b . The logic for assigning the roots is summarized in Table 2-1.

Table 2-1: Booker Quartic Root Assignment Summary

Root Type	Action	Assignment
4 purely real roots	Sort (descending) on real roots	$k_z^{bu}, k_z^{au}, k_z^{ad}, k_z^{bd}$
2 purely real roots 2 complex roots	Two real roots: k_z^b roots Two complex roots: k_z^a roots	Larger real root is k_z^{bu} , smaller is k_z^{bd} Larger complex root is k_z^{au} , smaller is k_z^{ad}
4 complex roots	Sort (descending) on imaginary parts of roots	$k_z^{au}, k_z^{bu}, k_z^{bd}, k_z^{ad}$

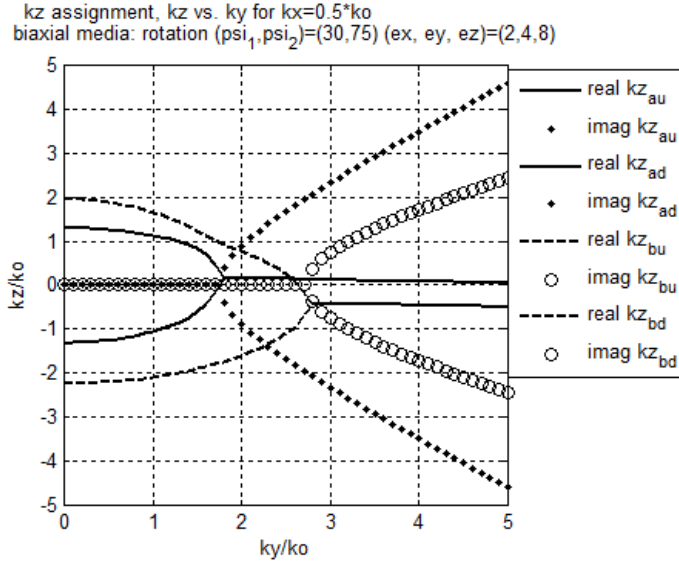


Figure 2-3: Booker quartic root assignment for biaxial medium, k_z vs. k_y (permittivity tensor $(\epsilon_x, \epsilon_y, \epsilon_z) = (2, 4, 8)$, rotated by $(\psi_1, \psi_2) = (30^\circ, 75^\circ)$)

Using the root assignment rules shown in Table 2-1, we also show the k_z roots plotted as k_x is varied in Figure 2-4. Here, we choose to fix k_y at k_0 and therefore the roots become complex at a lower value of k_x than was observed for k_y in Figure 2-3.

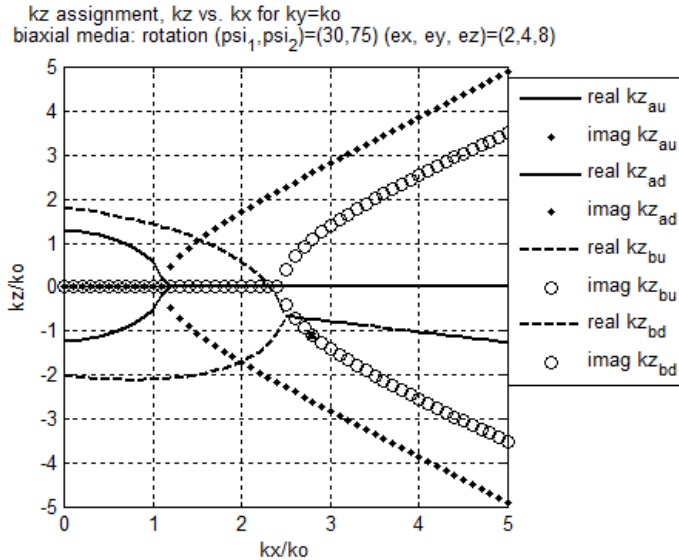


Figure 2-4: Booker quartic root assignment for biaxial medium, k_z vs. k_x (permittivity tensor $(\epsilon_x, \epsilon_y, \epsilon_z) = (2, 4, 8)$, rotated by $(\psi_1, \psi_2) = (30^\circ, 75^\circ)$)

We can also plot the wave vector surface for this medium. The a- and b-wave vector surfaces are plotted as k_x and k_y are varied. These wave vector surfaces are shown in Figures 2-5 through 2-8.

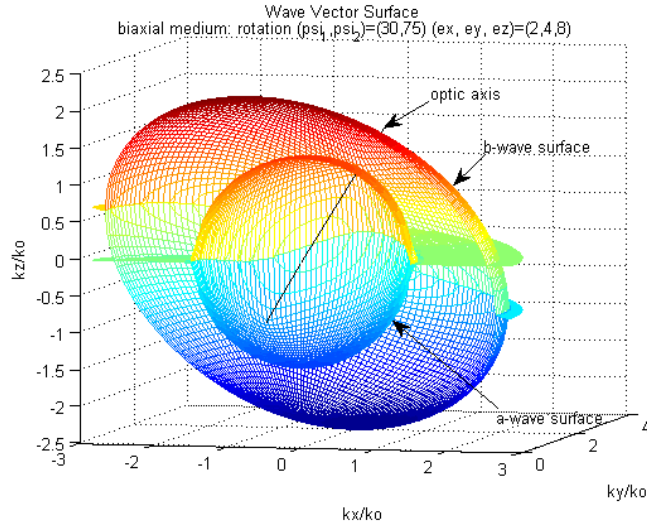


Figure 2-5: Wave vector surface: wave vectors computed using Booker quartic (permittivity tensor $(\epsilon_x, \epsilon_y, \epsilon_z) = (2, 4, 8)$, rotated by $(\psi_1 \psi_2) = (30^\circ, 75^\circ)$)

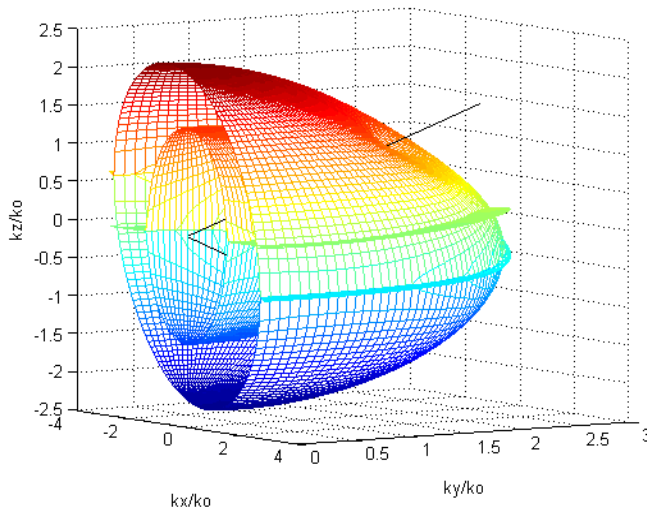


Figure 2-6: Wave vector surface showing umbilical point and optic axis 2: wave vectors computed using Booker quartic (permittivity tensor $(\epsilon_x, \epsilon_y, \epsilon_z) = (2, 4, 8)$, rotated by $(\psi_1 \psi_2) = (30^\circ, 75^\circ)$)

In Figure 2-5 and Figure 2-6 the entire wave vector surface is shown. It is difficult to clearly see the umbilical point and optic axes in these plots. Figure 2-7 and Figure 2-8 more clearly illustrate the behavior around the umbilical point by limiting the angular sweep of the wave vector surfaces.

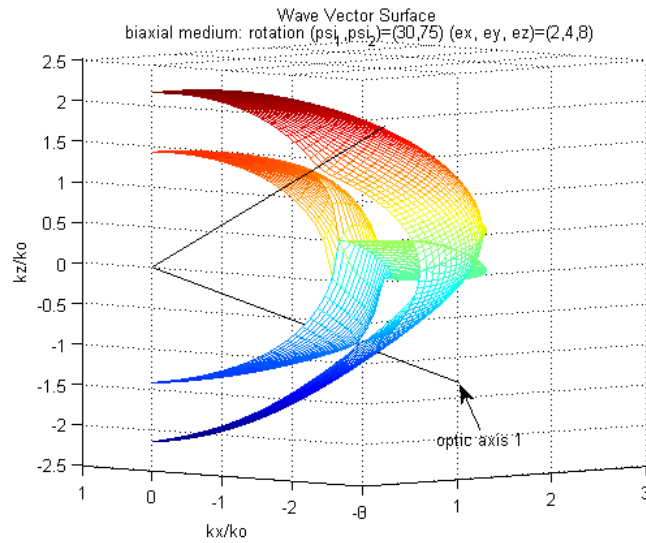


Figure 2-7: Umbilical point at optic axis 1, $(\epsilon_x, \epsilon_y, \epsilon_z) = (2, 4, 8)$, $(\psi_1, \psi_2) = (30^\circ, 75^\circ)$

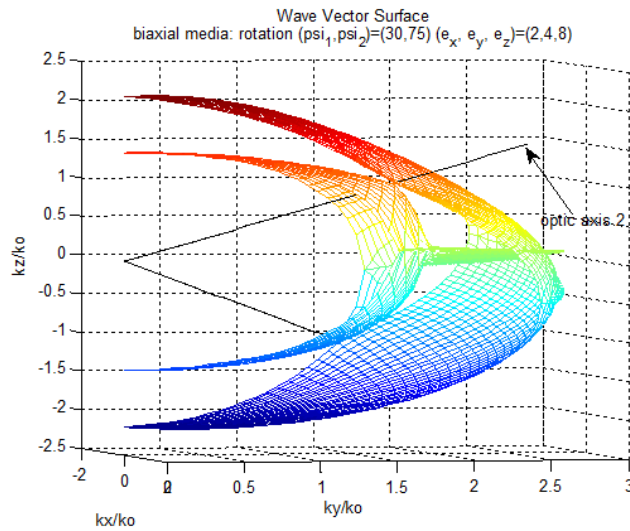


Figure 2-8: Umbilical point at optic axis 2, $(\epsilon_x, \epsilon_y, \epsilon_z) = (2, 4, 8)$, $(\psi_1, \psi_2) = (30^\circ, 75^\circ)$

The complex k_z values represent evanescent waves in the medium. It is as if a wave is incident from some angle beyond 90° and the inverse sine of k_z is greater than one. When we evaluate the Green's function (discussed in Chapter 3), we perform a doubly infinite integral over k_x and k_y so the assignment of k_z from the Booker quartic becomes important in this complex region.

2.1.2 Electric Field Vectors

We define the electric field vectors as is done by Mudaliar and Lee [34]. The electric field vectors used by Pettis are equivalent and are derived in detail in Appendix E and Chapter 2 of his dissertation [1]. As discussed, we have two waves traveling in the biaxial medium, the a-wave and the b-wave and we want to compute the unit vector associated with each of them. Each unit vector is defined as

$$\hat{a}^+ = \left(v^{\alpha a}\right)^{-1/2} \bar{\bar{\chi}} \cdot \hat{\alpha}^+ \quad (2.1.12)$$

$$\hat{a}^- = \left(v^{\alpha d}\right)^{-1/2} \bar{\bar{\chi}} \cdot \hat{\alpha}^- \quad (2.1.13)$$

$$\hat{b}^+ = \left(v^{\beta a}\right)^{-1/2} \bar{\bar{\chi}} \cdot \hat{\beta}^+ \quad (2.1.14)$$

$$\hat{b}^- = \left(v^{\beta d}\right)^{-1/2} \bar{\bar{\chi}} \cdot \hat{\beta}^- \quad (2.1.15)$$

where $\bar{\bar{\chi}}$ is defined such that the elements χ_{ij} is the ij^{th} element of the matrix $\bar{\bar{\epsilon}}^{-1}$ and v is a normalization factor defined by

$$v^{iu} = \hat{i}^+ \cdot \bar{\bar{\chi}}^2 \cdot \hat{i}^+ \quad i = \alpha \text{ or } \beta \quad (2.1.16)$$

$$v^{id} = \hat{i}^- \cdot \bar{\bar{\chi}}^2 \cdot \hat{i}^- \quad i = \alpha \text{ or } \beta \quad (2.1.17)$$

The $\hat{\alpha}$ and $\hat{\beta}$ in equations (2.1.12) through (2.1.17) are the unit vectors of the two characteristic displacement vectors in the medium. We compute these unit vectors using

$$\hat{\alpha}^+ = \frac{1}{h^{au}} \left[\frac{\hat{k}_a \times \hat{o}_1}{|\hat{k}_a \times \hat{o}_1|} + \frac{\hat{k}_a \times \hat{o}_2}{|\hat{k}_a \times \hat{o}_2|} \right] \quad (2.1.18)$$

$$\hat{\alpha}^- = \frac{1}{h^{ad}} \left[\frac{\hat{\kappa}_a \times \hat{o}_1}{|\hat{\kappa}_a \times \hat{o}_1|} + \frac{\hat{\kappa}_a \times \hat{o}_2}{|\hat{\kappa}_a \times \hat{o}_2|} \right] \quad (2.1.19)$$

$$\hat{\beta}^+ = \frac{1}{h^{bu}} \left[\frac{\hat{k}_b \times (\hat{k}_b \times \hat{o}_1)}{|\hat{k}_b \times \hat{o}_1|} + \frac{\hat{k}_b \times (\hat{k}_b \times \hat{o}_2)}{|\hat{k}_b \times \hat{o}_2|} \right] \quad (2.1.20)$$

$$\hat{\beta}^- = \frac{1}{h^{bd}} \left[\frac{\hat{\kappa}_b \times (\hat{\kappa}_b \times \hat{o}_1)}{|\hat{\kappa}_b \times \hat{o}_1|} + \frac{\hat{\kappa}_b \times (\hat{\kappa}_b \times \hat{o}_2)}{|\hat{\kappa}_b \times \hat{o}_2|} \right] \quad (2.1.21)$$

where h is a normalization factor for the displacement unit vectors, \hat{k} and $\hat{\kappa}$ are propagation unit vectors as defined by equations (2.1.1) through (2.1.4) and the \hat{o} terms are the unit vectors in the direction of the optic axes as discussed in the previous section (and shown in the wave vector surfaces). We compute h for each field vector using

$$h^{iu} = \sqrt{2} \left[1 + \frac{(\hat{k}_i \times \hat{o}_1) \cdot (\hat{k}_i \times \hat{o}_2)}{|\hat{k}_i \times \hat{o}_1| |\hat{k}_i \times \hat{o}_2|} \right]^{1/2}, \quad i = a, b \quad (2.1.22)$$

$$h^{id} = \sqrt{2} \left[1 + \frac{(\hat{\kappa}_i \times \hat{o}_1) \cdot (\hat{\kappa}_i \times \hat{o}_2)}{|\hat{\kappa}_i \times \hat{o}_1| |\hat{\kappa}_i \times \hat{o}_2|} \right]^{1/2}, \quad i = a, b \quad (2.1.23)$$

We also need to compute the unit vectors \hat{o}_1 and \hat{o}_2 . Mudaliar and Lee assumed $\epsilon_x < \epsilon_y < \epsilon_z$. However we are interested in a more general formulation. Continuing the notation, we define constants g_1 and g_2 by

$$g_1 = \left[\frac{\varepsilon_{\max} (\varepsilon_{mid} - \varepsilon_{\min})}{\varepsilon_{mid} (\varepsilon_{\max} - \varepsilon_{\min})} \right]^{\frac{1}{2}} \quad (2.1.24)$$

$$g_2 = \left[\frac{\varepsilon_{\min} (\varepsilon_{\max} - \varepsilon_{mid})}{\varepsilon_{mid} (\varepsilon_{\max} - \varepsilon_{\min})} \right]^{\frac{1}{2}} \quad (2.1.25)$$

where ε_{\max} is the maximum permittivity value, ε_{\min} is the minimum and ε_{mid} is the middle value. Note that when $\varepsilon_x < \varepsilon_y < \varepsilon_z$, g_1 and g_2 reduce to the same expressions given by Mudaliar and Lee. The first optic axis in the biaxial coordinate system is constructed by placing g_1 at the coordinate associated with ε_{\min} and g_2 at the coordinate associated with ε_{\max} . The second optic axis is constructed the same way only $-g_1$ is used. We then obtain the optic axes for any arbitrarily oriented biaxial medium by applying the rotation matrix R (equation (1.3.16)) to both unrotated optic axes. The resulting the optic axes in an arbitrarily oriented biaxial medium are given by

$$\begin{cases} \hat{o}_1 \\ \hat{o}_2 \end{cases} = \hat{x}(\pm g_1 \cos \psi_2 + g_2 \sin \psi_1 \sin \psi_2) + \hat{y}(\mp g_1 \sin \psi_2 + g_2 \sin \psi_1 \cos \psi_2) + \hat{z}g_2 \cos \psi_1 \quad (2.1.26)$$

Note that equation (2.1.26) is the same equation presented by Mudaliar and Lee except for the correction to the z term; in their paper, the g_2 multiplier on the z term is left out.

2.2 Reflection and Transmission

The most extensive work on reflection and transmission from arbitrarily oriented biaxial media is presented by Landry [12]. In his work, he studies half space reflection and transmission characteristics for biaxial-biaxial, isotropic-biaxial and biaxial-isotropic configurations. He also studies 2-layered and multi-layered problems. Landry's approach is

considerably different than the approach presented here. In his study of the half-space problems, he computes the direction and magnitude of the reflected and refracted waves separately. In his analysis of the 2-layered problem, Landry studies each bounce the incident wave undergoes and uses that to compute reflection and transmission coefficients. The multi-layered problem is treated similarly.

In our approach, we expand the plane waves in each medium then apply the boundary conditions. We use the material parameters to determine the directions of each expansion wave then apply boundary conditions to solve for the magnitude. We apply this treatment to both the half-space and 2-layered problems. This is a familiar and straightforward formulation. Another difference is that we define the electric field vectors in each medium based on the known material parameters (permittivity matrix and rotation matrix) while Landry uses the refractive index and a set of angles to define the relationship between the wave vector and fields. Landry uses a formulation more commonly used in the physics and optics communities and not familiar to most electrical engineers. Finally, we expand upon his research by analyzing the Brewster angle effect and critical angle as functions of permittivity and rotation angles.

We begin by defining the half-space reflection and transmission coefficients for the case of each incident wave on either side of an isotropic-biaxial boundary. We use these results to analyze the critical angle. We then go on to formulate the 2-layer problem with a wave incident from one isotropic layer onto the biaxial layer. We use these results to analyze the Brewster angle effect.

2.2.1 Half Space Reflection and Transmission Coefficients

2.2.1.1 Wave Incident from Isotropic Region 0

In general, the study of half-space (one interface) reflection and transmission problems can be broken down into four main configurations as noted by Pettis [1, Appendix G]. These configurations are listed in Table 2-2 below.

Table 2-2: Half-Space Configurations

Case	Configuration
1	horizontal or vertical wave downward incident on isotropic-biaxial interface
2	a-wave or b-wave upward incident on biaxial-isotropic interface
3	a-wave or b-wave downward incident on biaxial-isotropic interface
4	horizontal or vertical wave upward incident on isotropic-biaxial interface

To derive the half-space reflection and transmission coefficients, we formulate the fields in each region of interest, then apply the boundary conditions. Note that this derivation follows Pettis' work.

2.2.1.1.1 Horizontally polarized wave downward incident upon isotropic-biaxial interface

A horizontally polarized (or TE) wave downward incident on the isotropic-biaxial interface (region 0 – region 1) will give rise to two reflected waves (one horizontally polarized and one vertically polarized in the isotropic region) and two transmitted waves (an a-wave and a b-wave in the biaxial medium). This behavior is depicted in Figure 2-9.

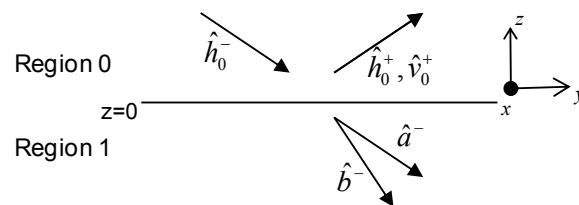


Figure 2-9: TE wave incident upon isotropic-biaxial interface

We must formulate the fields in each region to solve for the half-space coefficients.

Based on Figure 2-9 we can write the electric fields in each region as

$$\bar{E}_0(\bar{r}) = \hat{h}_0^- e^{i\bar{k}_0 \cdot \bar{r}} + \hat{h}_0^+ R_{hh}^{01} e^{i\bar{k}_0 \cdot \bar{r}} + \hat{v}_0^+ R_{hv}^{01} e^{i\bar{k}_0 \cdot \bar{r}} \quad (2.2.1)$$

$$\bar{E}_1(\bar{r}) = \hat{a}^- X_{ha}^{01} e^{i\bar{k}_a \cdot \bar{r}} + \hat{b}^- X_{hb}^{01} e^{i\bar{k}_b \cdot \bar{r}} \quad (2.2.2)$$

We are defining the reflection coefficients, R_{ij}^{mn} , such that m is the incident region, n is the transmission region, i is the incident wave polarization and j is the reflected wave polarization.

The transmission coefficients, X_{ij}^{mn} , are defined the same way with j as the transmitted wave polarization. The electric field unit vectors are defined such that \hat{h} is the horizontally polarized (or TE) wave unit vector, \hat{v} is the vertically polarized (or TM) wave unit vector, \hat{a} is the a-wave electric field unit vector and \hat{b} is the b-wave electric field unit vector. We define \hat{h} and \hat{v} in the same manner as Kong [2] and use the equations he presented to calculate the unit vectors. The superscript on the unit vectors indicate whether the wave is upward propagating (positive sign) and downward propagating (negative sign). Finally, the subscript on the isotropic unit vectors indicates which region the unit vector is in to differentiate when we consider the 2-layered problem.

Given these fields, we can evaluate the unknown reflection and transmission coefficients by applying the boundary conditions at the interface. For each half-space problem, we put the interface at $z=0$ and assume there are no sources along the interface. The boundary conditions at this interface are given by

$$\hat{z} \times \bar{E}_0(\bar{r}) = \hat{z} \times \bar{E}_1(\bar{r}), \quad \text{at } z = 0 \quad (2.2.3)$$

$$\hat{z} \times \bar{H}_0(\bar{r}) = \hat{z} \times \bar{H}_1(\bar{r}) \longrightarrow \hat{z} \times \nabla \times \bar{E}_0(\bar{r}) = \hat{z} \times \nabla \times \bar{E}_1(\bar{r}), \quad \text{at } z = 0 \quad (2.2.4)$$

We begin by applying the electric field boundary condition (equation (2.2.3)) to the formulated fields. Taking the cross product of the z unit vector with the E-field in region 0 and region 1, respectively, results in

$$\hat{z} \times \bar{E}_0(\bar{r}_{z=0}) = e^{i(k_x x + k_y y)} \left[(-\hat{x}h_{0y}^- + \hat{y}h_{0x}^-) + R_{hh}^{01}(-\hat{x}h_{0y}^+ + \hat{y}h_{0x}^+) + R_{hv}^{01}(-\hat{x}v_{0y}^+ + \hat{y}v_{0x}^+) \right] \quad (2.2.5)$$

$$\hat{z} \times \bar{E}_1(\bar{r}_{z=0}) = e^{i(k_x x + k_y y)} \left[X_{ha}^{01}(-\hat{x}a_y^- + \hat{y}a_x^-) + X_{hb}^{01}(-\hat{x}b_y^- + \hat{y}b_x^-) \right] \quad (2.2.6)$$

where the electric field unit vectors (\hat{h} , \hat{v} , \hat{a} and \hat{b}) have been decomposed. The first numerical subscript on h and v indicates the region in which the vector exists; the alphabetical subscript indicates the component of the vector and the superscript indicates whether the vector is downward (-) or upward (+) propagating. Setting (2.2.5) equal to (2.2.6) per the electric field boundary condition we obtain

$$(-\hat{x}h_{0y}^- + \hat{y}h_{0x}^-) + R_{hh}^{01}(-\hat{x}h_{0y}^+ + \hat{y}h_{0x}^+) + R_{hv}^{01}(-\hat{x}v_{0y}^+ + \hat{y}v_{0x}^+) = X_{ha}^{01}(-\hat{x}a_y^- + \hat{y}a_x^-) + X_{hb}^{01}(-\hat{x}b_y^- + \hat{y}b_x^-) \quad (2.2.7)$$

By grouping the x-directed components and the y-directed components and rearranging terms, we obtain two equations

$$-R_{hh}^{01}h_{oy}^+ - R_{hv}^{01}v_{0y}^+ + X_{ha}^{01}a_y^- + X_{hb}^{01}b_y^- = h_{oy}^- \quad (2.2.8)$$

$$-R_{hh}^{01}h_{ox}^+ - R_{hv}^{01}v_{0x}^+ + X_{ha}^{01}a_x^- + X_{hb}^{01}b_x^- = h_{ox}^- \quad (2.2.9)$$

This results in two equations for four unknown coefficients. The other two equations come from the magnetic field boundary condition shown in equation (2.2.4). We note that for plane wave propagation, the curl operator can be replaced by the propagation constant cross product. Specifically

$$\nabla \times \bar{E} \xrightarrow{\text{plane wave}} \begin{cases} i\bar{k} \times \bar{E} & \text{upward propagation} \\ i\bar{k} \times \bar{E} & \text{downward propagation} \end{cases} \quad (2.2.10)$$

Now, applying equation (2.2.10) to the electric field in region 0 we obtain

$$\hat{z} \times (\bar{k} \times \bar{E}_0(\bar{r}_{z=0})) = e^{i(k_x x + k_y y)} \left\{ \begin{aligned} & \left[\hat{x}(k_x h_{0z}^- + k_{0z} h_{0x}^-) + \hat{y}(k_y h_{0z}^- + k_{0z} h_{0y}^-) \right] \\ & + R_{hh}^{01} \left[\hat{x}(k_x h_{0z}^+ - k_{0z} h_{0x}^+) + \hat{y}(k_y h_{0z}^+ - k_{0z} h_{0y}^+) \right] \\ & + R_{hv}^{01} \left[\hat{x}(k_x v_{0z}^+ - k_{0z} v_{0x}^+) + \hat{y}(k_y v_{0z}^+ - k_{0z} v_{0y}^+) \right] \end{aligned} \right\} \quad (2.2.11)$$

Applying the same equation to the field in region 1, we obtain

$$\hat{z} \times (\bar{k} \times \bar{E}_1(\bar{r}_{z=0})) = e^{i(k_x x + k_y y)} \left\{ \begin{aligned} & \left[X_{ha}^{01} \left[\hat{x}(k_x a_z^- - k_z^{ad} a_x^-) + \hat{y}(k_y a_z^- - k_z^{ad} a_y^-) \right] \right] \\ & + X_{hb}^{01} \left[\hat{x}(k_x b_z^- - k_z^{bd} b_x^-) + \hat{y}(k_y b_z^- - k_z^{bd} b_y^-) \right] \end{aligned} \right\} \quad (2.2.12)$$

Setting the right hand sides of equations (2.2.11) and (2.2.12) equal (thus applying the boundary condition), results in

$$\left\{ \begin{aligned} & \left[\hat{x}(k_x h_{0z}^- + k_{0z} h_{0x}^-) + \hat{y}(k_y h_{0z}^- + k_{0z} h_{0y}^-) \right] \\ & + R_{hh}^{01} \left[\hat{x}(k_x h_{0z}^+ - k_{0z} h_{0x}^+) + \hat{y}(k_y h_{0z}^+ - k_{0z} h_{0y}^+) \right] \\ & + R_{hv}^{01} \left[\hat{x}(k_x v_{0z}^+ - k_{0z} v_{0x}^+) + \hat{y}(k_y v_{0z}^+ - k_{0z} v_{0y}^+) \right] \end{aligned} \right\} = \left\{ \begin{aligned} & \left[X_{ha}^{01} \left[\hat{x}(k_x a_z^- - k_z^{ad} a_x^-) + \hat{y}(k_y a_z^- - k_z^{ad} a_y^-) \right] \right] \\ & + X_{hb}^{01} \left[\hat{x}(k_x b_z^- - k_z^{bd} b_x^-) + \hat{y}(k_y b_z^- - k_z^{bd} b_y^-) \right] \end{aligned} \right\} \quad (2.2.13)$$

We now combine like components and rearrange remaining terms as we did with equation (2.2.7) to obtain the two remaining equations

$$\begin{aligned} & -R_{hh}^{01}(k_x h_{0z}^+ - k_{0z} h_{0x}^+) - R_{hv}^{01}(k_x v_{0z}^+ - k_{0z} v_{0x}^+) + X_{ha}^{01}(k_x a_z^- - k_z^{ad} a_x^-) + X_{hb}^{01}(k_x b_z^- - k_z^{bd} b_x^-) \\ & = (k_x h_{0z}^- + k_{0z} h_{0x}^-) \\ & -R_{hh}^{01}(k_y h_{0z}^+ - k_{0z} h_{0y}^+) - R_{hv}^{01}(k_y v_{0z}^+ - k_{0z} v_{0y}^+) + X_{ha}^{01}(k_y a_z^- - k_z^{ad} a_y^-) + X_{hb}^{01}(k_y b_z^- - k_z^{bd} b_y^-) \\ & = (k_y h_{0z}^- + k_{0z} h_{0y}^-) \end{aligned} \quad (2.2.14)$$

We can write the four equations in matrix form

$$\begin{bmatrix} -h_{0y}^+ & -v_{0y}^+ & a_y^- & b_y^- \\ -h_{0x}^+ & -v_{0x}^+ & a_x^- & b_x^- \\ -(k_x h_{0z}^+ - k_{0z} h_{0x}^+) & -(k_x v_{0z}^+ - k_{0z} v_{0x}^+) & (k_x a_z^- - k_z^{ad} a_x^-) & (k_x b_z^- - k_z^{bd} b_x^-) \\ -(k_y h_{0z}^+ - k_{0z} h_{0y}^+) & -(k_y v_{0z}^+ - k_{0z} v_{0y}^+) & (k_y a_z^- - k_z^{ad} a_y^-) & (k_y b_z^- - k_z^{bd} b_y^-) \end{bmatrix} \begin{bmatrix} R_{hh}^{01} \\ R_{hv}^{01} \\ X_{ha}^{01} \\ X_{hb}^{01} \end{bmatrix} = \begin{bmatrix} h_{0y}^- \\ h_{0x}^- \\ (k_x h_{0z}^- + k_{0z} h_{0x}^-) \\ (k_y h_{0z}^- + k_{0z} h_{0y}^-) \end{bmatrix} \quad (2.2.15)$$

The matrix equation in (2.2.15) can be solved to determine the half-space reflection and transmission coefficients for a horizontally polarized incident wave.

2.2.1.1.2 Vertically polarized wave downward incident upon isotropic-biaxial interface

The next reflection and transmission condition we consider is a vertically polarized (TM) wave downward incident on the same isotropic-biaxial interface. This incident wave will also give rise to two reflected waves and two transmitted waves. This behavior is depicted in Figure 2-10.

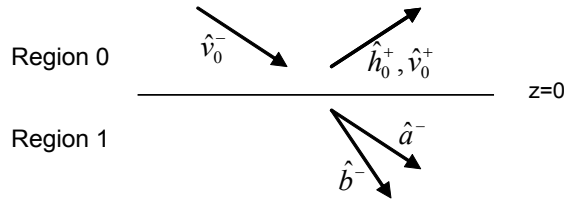


Figure 2-10: TM wave incident upon isotropic-biaxial interface

Again, we formulate the fields in each region to solve for the half-space coefficients.

The electric fields in region 0 and region 1 respectively are given by

$$\bar{E}_0(\vec{r}) = \hat{v}_0^- e^{i\vec{k}_0 \cdot \vec{r}} + \hat{h}_0^+ R_{vh}^{01} e^{i\vec{k}_0 \cdot \vec{r}} + \hat{v}_0^+ R_{vv}^{01} e^{i\vec{k}_0 \cdot \vec{r}} \quad (2.2.16)$$

$$\bar{E}_1(\bar{r}) = \hat{a}^- X_{va}^{01} e^{i\bar{k}_a \cdot \bar{r}} + \hat{b}^- X_{vb}^{01} e^{i\bar{k}_b \cdot \bar{r}} \quad (2.2.17)$$

Observing equations (2.2.16) and (2.2.17), we see that the fields in each region are similar to the fields in the previous case. Applying the boundary conditions in equations (2.2.3) and (2.2.4), and performing the same algebraic procedure we did in the previous section, we obtain the four equations

$$\begin{aligned} -R_{vh}^{01} h_{0y}^+ - R_{vv}^{01} v_{0y}^+ + X_{va}^{01} a_y^- + X_{vb}^{01} b_y^- &= v_{0y}^- \\ -R_{vh}^{01} h_{0x}^+ - R_{vv}^{01} v_{0x}^+ + X_{va}^{01} a_x^- + X_{vb}^{01} b_x^- &= v_{0x}^- \\ -R_{vh}^{01} (k_x h_{0z}^+ - k_{0z} h_{0x}^+) - R_{vv}^{01} (k_x v_{0z}^+ - k_{0z} v_{0x}^+) + X_{va}^{01} (k_x a_z^- - k_z^{ad} a_x^-) + X_{vb}^{01} (k_x b_z^- - k_z^{bd} b_x^-) &= (k_x v_{0z}^- + k_{0z} v_{0x}^-) \\ -R_{vh}^{01} (k_y h_{0z}^+ - k_{0z} h_{0y}^+) - R_{vv}^{01} (k_y v_{0z}^+ - k_{0z} v_{0y}^+) + X_{va}^{01} (k_y a_z^- - k_z^{ad} a_y^-) + X_{vb}^{01} (k_y b_z^- - k_z^{bd} b_y^-) &= (k_y v_{0z}^- + k_{0z} v_{0y}^-) \end{aligned} \quad (2.2.18)$$

We can write the four equations in matrix form

$$\begin{bmatrix} -h_{0y}^+ & -v_{0y}^+ & a_y^- & b_y^- \\ -h_{0x}^+ & -v_{0x}^+ & a_x^- & b_x^- \\ -(k_x h_{0z}^+ - k_{0z} h_{0x}^+) & -(k_x v_{0z}^+ - k_{0z} v_{0x}^+) & (k_x a_z^- - k_z^{ad} a_x^-) & (k_x b_z^- - k_z^{bd} b_x^-) \\ -(k_y h_{0z}^+ - k_{0z} h_{0y}^+) & -(k_y v_{0z}^+ - k_{0z} v_{0y}^+) & (k_y a_z^- - k_z^{ad} a_y^-) & (k_y b_z^- - k_z^{bd} b_y^-) \end{bmatrix} \begin{bmatrix} R_{vh}^{01} \\ R_{vv}^{01} \\ X_{va}^{01} \\ X_{vb}^{01} \end{bmatrix} = \begin{bmatrix} v_{0y}^- \\ v_{0x}^- \\ (k_x v_{0z}^- + k_{0z} v_{0x}^-) \\ (k_y v_{0z}^- + k_{0z} v_{0y}^-) \end{bmatrix} \quad (2.2.19)$$

This matrix equation can be solved numerically to obtain the half-space coefficients associated with the TM wave downward incident on the isotropic-biaxial interface.

2.2.1.1.3 Evaluation of Reflection and Transmission of Wave Incident from Region 0

Now we want analyze how the reflection and transmission coefficients behave. First, we define the angle of incidence for the half space problem such that \hat{z} is normal to the boundary. The incident wave propagation vector can have any orientation. We define the incident propagation vector as

$$\bar{k} = \hat{x}k_x + \hat{y}k_y + \hat{z}k_z \quad (2.2.20)$$

where each component is computed using

$$\begin{aligned} k_x &= k_0 \sin \theta \cos \phi \\ k_y &= k_0 \sin \theta \sin \phi \\ k_z &= k_0 \cos \theta \end{aligned} \quad (2.2.21)$$

The plane of incidence is defined by ϕ . When ϕ is zero, the wave is incident from the x - z plane and when ϕ is 90° , the wave is incident from the y - z plane. Intermediate values of ϕ will describe some intermediate plane of incidence. The angle of incidence in the prescribed plane is given by θ . The reflection and transmission coefficients are calculated and displayed as function of θ . The plane of incidence and angle of incidence are shown in Figure 2-11. Due to the phase matching condition, k_x and k_y are continuous across the boundary. We will use k_x and k_y as described by equation (2.2.21) to compute the two k_z values in region 1 using the Booker quartic.

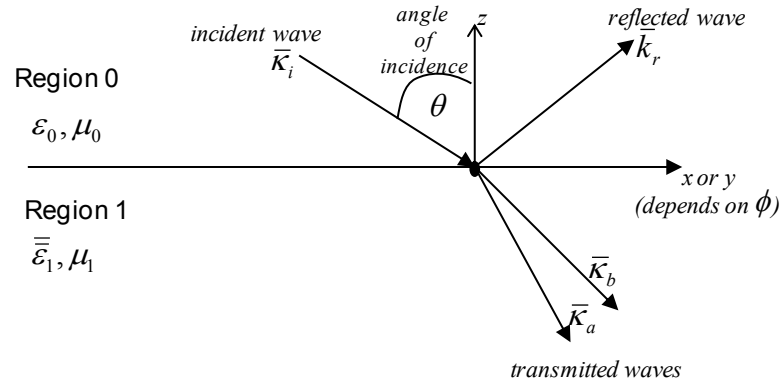
Plane of Incidence

Figure 2-11: Diagram of plane and angle of incidence for wave incident from region 0

We begin this analysis by studying reflection and transmission characteristics in the uniaxial limit. In his dissertation [5, Chapter 2] Yun Hee Lee studied reflection and transmission from uniaxial media. Two waves propagate in uniaxial media: the ordinary wave and the extraordinary wave. The ordinary wave behaves like a wave in isotropic media with a spherical wave vector surface. The extraordinary wave has an ellipsoidal wave vector surface. If the medium is positive uniaxial ($\epsilon_z > \epsilon_x$) the wave vector surface of the ordinary wave is inside the wave vector surface of the extraordinary wave. If the medium is negative uniaxial ($\epsilon_z < \epsilon_x$), this condition is reversed. Considering our biaxial formulation in the uniaxial limit, the a-wave will act as the ordinary wave and the b-wave will act as the extraordinary wave in a positive uniaxial medium. If the medium is negative uniaxial the a-wave will be the extraordinary wave and the b-wave the ordinary wave.

With this knowledge of uniaxial media, we show that our reflection and transmission formulation reduces to the uniaxial case by computing the coefficients for the same interface

considered by Lee [5, Chapter 2]. A 13GHz wave is incident from air to the uniaxial medium with unrotated relative permittivity tensor given by

$$\epsilon_{||} = \begin{bmatrix} 4.32 + i0.01 & & \\ & 4.32 + i0.01 & \\ & & 4.43 + i0.03 \end{bmatrix} \quad (2.2.22)$$

In the first case we consider, this uniaxial medium is unrotated. The reflection and transmission coefficients are computed and plotted versus angle of incidence (θ_i) in the $\phi_i = 70^\circ$ plane and shown in Figure 2-12.

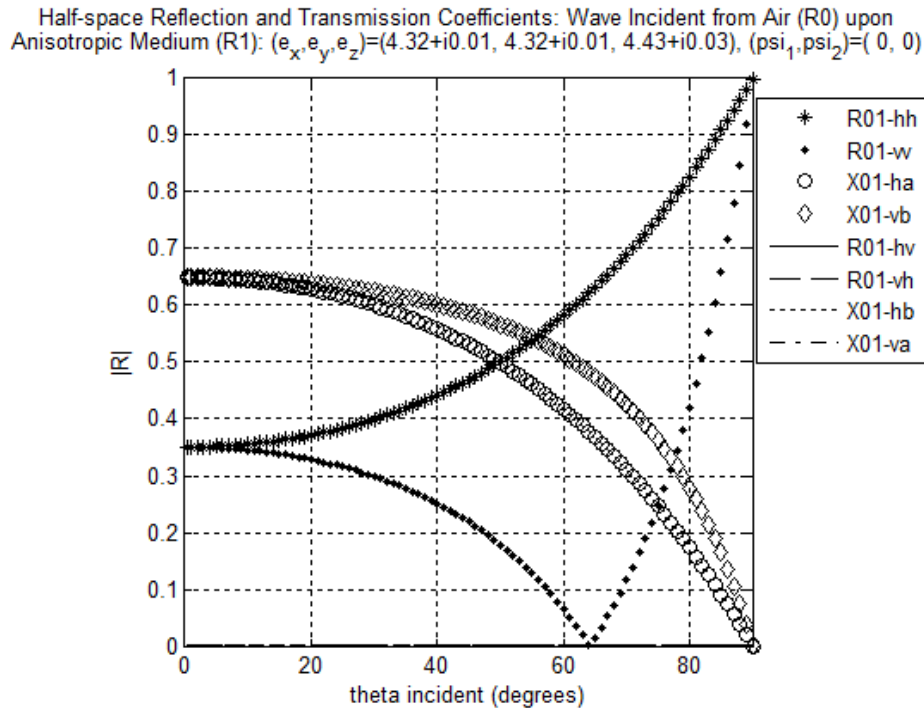


Figure 2-12: Reflection and transmission characteristics in uniaxial limit

The figure shows that the cross-polarization terms are approximately zero. The horizontal reflection coefficient is always greater than the vertical reflection coefficient and the

vertically polarized wave experiences zero reflection (Brewster angle) at approximately 64° . We also observe that when the incident wave is horizontally polarized, the transmitted wave is “*a*” polarized. In this positive uniaxial medium the *a*-wave acts like the ordinary wave. Also, when the incident wave is vertically polarized, the transmitted wave is “*b*” polarized where the *b*-wave acts like the extraordinary wave. These results agree exactly with the results presented in Lee’s dissertation.

Yun Hee Lee also considered the tilted uniaxial medium. In the tilted medium case, the permittivity tensor is rotated about the *x*-axis with respect to the primary coordinate system. In our definition, this is a ψ_1 rotation. Keeping all parameters the same as in Figure 2-12, we apply a 30° rotation (or tilt) and plot the results in Figure 2-13.

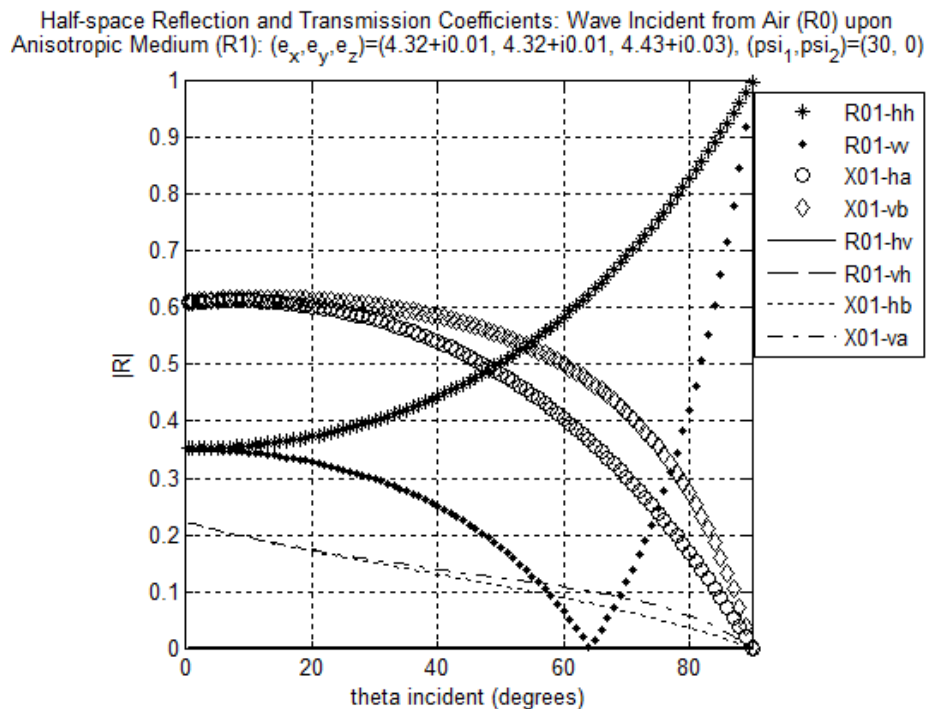


Figure 2-13: Reflection and transmission in uniaxial limit – tilted permittivity tensor

First, we observe that the cross polarized reflection coefficients are still approximately zero but the cross-polarized transmission coefficients are not. When the horizontally polarized wave is incident both the a-wave (ordinary) and b-wave (extraordinary) are excited. Similarly when the vertically polarized wave is incident, both anisotropic waves are excited. The co-polarized reflection coefficients are the same with the same Brewster angle. These results agree with those presented by Lee [5, Chapter 2].

Having shown that we accurately compute reflection and transmission coefficients in the uniaxial limit, we return to the biaxial half-space case. In this first half-space problem, we consider the plane of incidence to be the y - z plane ($\phi=90^\circ$). The isotropic medium is again air and the biaxial medium is unrotated with relative permittivity tensor

$$\bar{\bar{\epsilon}}_r = \begin{bmatrix} 2 & & \\ & 5 & \\ & & 8 \end{bmatrix} \quad (2.2.23)$$

The reflection and transmission coefficients are plotted against angle of incidence in Figure 2-14. Considering first the co-polarized reflection coefficients, we observe that at smaller angles, the vertically polarized wave is reflected more strongly than the horizontally polarized wave. For angles greater than approximately 40° , this behavior is reversed and the horizontally polarized wave is reflected more strongly. This is in contrast with the typical behavior at an isotropic-isotropic half space boundary where the horizontally polarized wave is reflected more strongly for all incident angles. We can also observe the Brewster angle effect. At an incident angle just above 60° , the vertically polarized wave has zero reflection and only the horizontally polarized wave is reflected. The Brewster angle effect will be discussed in more detail in Section 2.2.1.1.5. For this case, the cross-polarized reflection coefficients (R_{hv} and R_{vh}) are

nearly zero. This is consistent with the behavior at an isotropic-isotropic interface. Analyzing the transmission coefficients we observe that when the horizontally polarized wave is incident, the energy is transmitted to the a-wave but not the b-wave as X_{hb} is approximately zero. Similarly, the vertically polarized wave transmits into the b-wave with X_{va} approximately zero. The X_{ha} and X_{vb} behave like co-polarized transmission coefficients while X_{hb} and X_{va} behave like cross-polarized transmission coefficients. In this manner, the a-wave is acting like a horizontally polarized wave and the b-wave is acting like a vertically polarized wave for the given medium parameters.

Half-space Reflection and Transmission Coefficients: Wave Incident from Air (R0) upon Anisotropic Medium (R1): $(\epsilon_x, \epsilon_y, \epsilon_z) = (2.00 + i0.00, 5.00 + i0.00, 8.00 + i0.00)$, $(\psi_1, \psi_2) = (0, 0)$

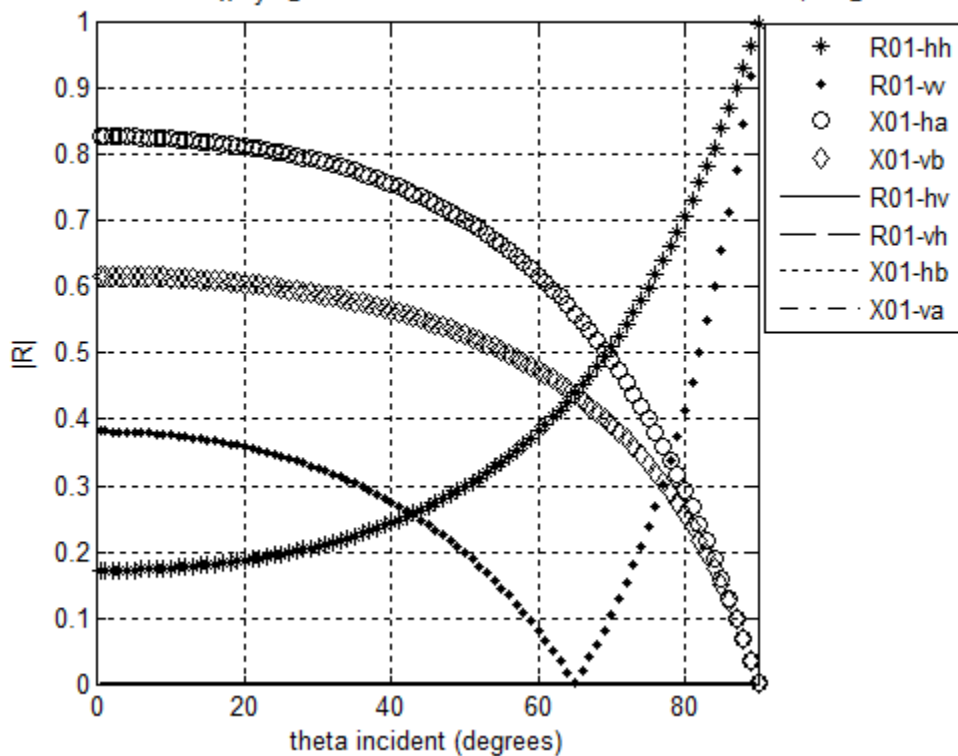


Figure 2-14: Half-space reflection and transmission coefficients for incident wave from isotropic medium to unrotated biaxial medium $(\epsilon_x, \epsilon_y, \epsilon_z) = (2, 5, 8)$.

The calculated reflection and transmission coefficients can be verified by formulating the waves in each region and showing that power is conserved. To observe power conservation, we must calculate the time average Poynting vectors of the incident, reflected and transmitted waves. We will derive the expressions for the Poynting vectors assuming a horizontally polarized incident wave. The time average Poynting vector of the incident wave is given by

$$\langle \bar{S}_i \rangle = \frac{1}{2} \text{Re} \{ \bar{E}_i \times \bar{H}_i^* \} \quad (2.2.24)$$

where

$$\bar{E}_i = \hat{h}_0^- E_0 e^{i\bar{k}_0 \cdot \bar{r}} \quad (2.2.25)$$

$$\bar{H}_i = \frac{\bar{k}_0 \times \bar{E}_i}{\omega \mu_0} = \bar{k}_0 \times \hat{h}_0^- \frac{E_0}{\omega \mu_0} e^{i\bar{k}_0 \cdot \bar{r}} \quad (2.2.26)$$

By substituting equations (2.2.25) and (2.2.26) into equation (2.2.24), the expression for the time average Poynting vector is

$$\langle \bar{S}_i \rangle = \frac{1}{2} \frac{|E_0|^2}{\omega \mu_0} \text{Re} \left\{ \hat{h}_0^- \times (\bar{k}_0 \times \hat{h}_0^-)^* \right\} \quad (2.2.27)$$

Similarly, we can formulate the reflected and transmitted waves to compute their time average Poynting vectors. It can be shown that the time average Poynting vector of the reflected wave is

$$\langle \bar{S}_r \rangle = \frac{1}{2} \frac{|E_0|^2}{\omega \mu_0} \text{Re} \left\{ \begin{aligned} & \hat{h}_0^+ \times (\bar{k}_0 \times \hat{h}_0^+)^* |R_{hh}^{01}|^2 + \hat{h}_0^+ \times (\bar{k}_0 \times \hat{v}_0^+)^* R_{hh}^{01} (R_{hv}^{01})^* \\ & + \hat{v}_0^+ \times (\bar{k}_0 \times \hat{h}_0^+)^* R_{hv}^{01} (R_{hh}^{01})^* + \hat{v}_0^+ \times (\bar{k}_0 \times \hat{v}_0^+)^* |R_{hv}^{01}|^2 \end{aligned} \right\} \quad (2.2.28)$$

and the transmitted wave is

$$\langle \bar{S}_i \rangle = \frac{1}{2} \frac{|E_0|^2}{\omega \mu_0} \operatorname{Re} \left\{ \begin{aligned} & \hat{a}^- \times (\bar{\kappa}_a \times \hat{a}^-)^* |X_{ha}^{01}|^2 + \hat{a}^- \times (\bar{\kappa}_b \times \hat{b}^-)^* X_{ha}^{01} (X_{hb}^{01})^* e^{i(\bar{\kappa}_a - \bar{\kappa}_b) \bar{r}} \\ & + \hat{b}^- \times (\bar{\kappa}_a \times \hat{a}^-)^* X_{hb}^{01} (X_{ha}^{01})^* e^{i(\bar{\kappa}_b - \bar{\kappa}_a) \bar{r}} + \hat{b}^- \times (\bar{\kappa}_b \times \hat{b}^-)^* |X_{hb}^{01}|^2 \end{aligned} \right\} \quad (2.2.29)$$

Power conservation is proved by showing that the z-directed components of all of the Poynting vectors entering and leaving the interface are equal [2]. We show this using the power reflection and transmission coefficients given by

$$r = \frac{-\hat{z} \cdot \langle \bar{S}_r \rangle}{\hat{z} \cdot \langle \bar{S}_i \rangle} \quad (2.2.30)$$

and

$$t = \frac{\hat{z} \cdot \langle \bar{S}_t \rangle}{\hat{z} \cdot \langle \bar{S}_i \rangle} \quad (2.2.31)$$

respectively [2]. If power is conserved the sum of these coefficients is equal to 1. In Figure 2-15 we show that the sum of the power reflection and transmission coefficients is 1 for the horizontally polarized wave incident and the vertically polarized wave incident. Therefore, power is conserved and the calculated coefficients are verified.

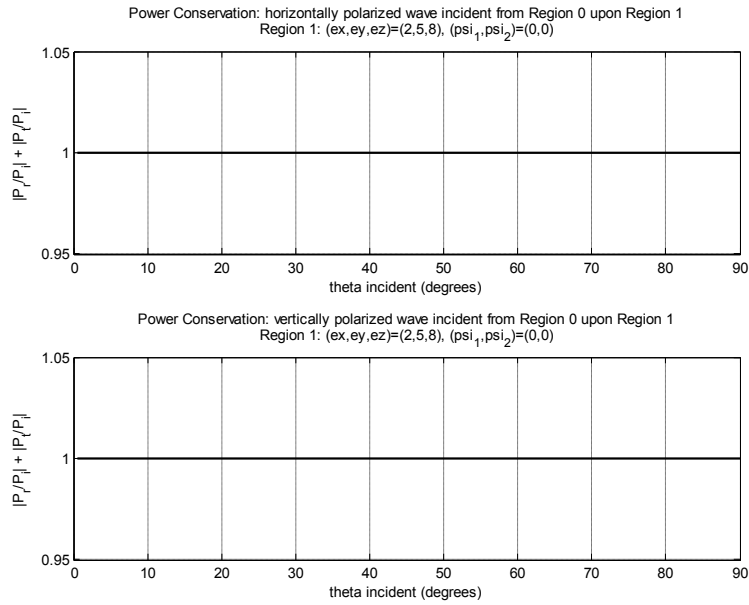


Figure 2-15: Power conservation for wave incident from region 0

We have considered the half-space reflection and transmission behavior when the biaxial medium is unrotated. Now, we'd like to consider the same phenomena when region 2 is rotated such that ψ_1 and ψ_2 are 45° . Given this new biaxial medium, we first consider the copolarized reflection coefficients shown in Figure 2-16. Here we see that the behavior has changed. For all incident angles, the horizontally polarized wave is reflected more strongly than the vertically polarized wave. Also of interest are the cross-polarized reflection coefficients which are no longer zero. They are still small, but when the biaxial medium is rotated, there is some cross-polarized reflection into the isotropic region. This means that a horizontally polarized wave will reflect both horizontally and vertically polarized waves. This behavior is not observed at an isotropic-isotropic boundary. Finally, we observe that the transmission coefficients are also affected by this rotation. Energy is transmitted to both the a-wave and b-wave when either the horizontally polarized wave or vertically polarized wave is incident. When

the biaxial medium was unrotated, we saw that the horizontally polarized wave transmitted into only the a-wave and the vertically polarized wave transmitted only into the b-wave. Now, both biaxial waves are generated from either polarization. We can conclude then a wave incident upon a rotated biaxial medium from an isotropic medium it will generate two transmitted and two reflected waves.

Half-space Reflection and Transmission Coefficients: Wave Incident from Air (R0) upon Anisotropic Medium (R1): $(\epsilon_x, \epsilon_y, \epsilon_z) = (2.00 + i0.00, 5.00 + i0.00, 8.00 + i0.00)$, $(\psi_1, \psi_2) = (45, 45)$

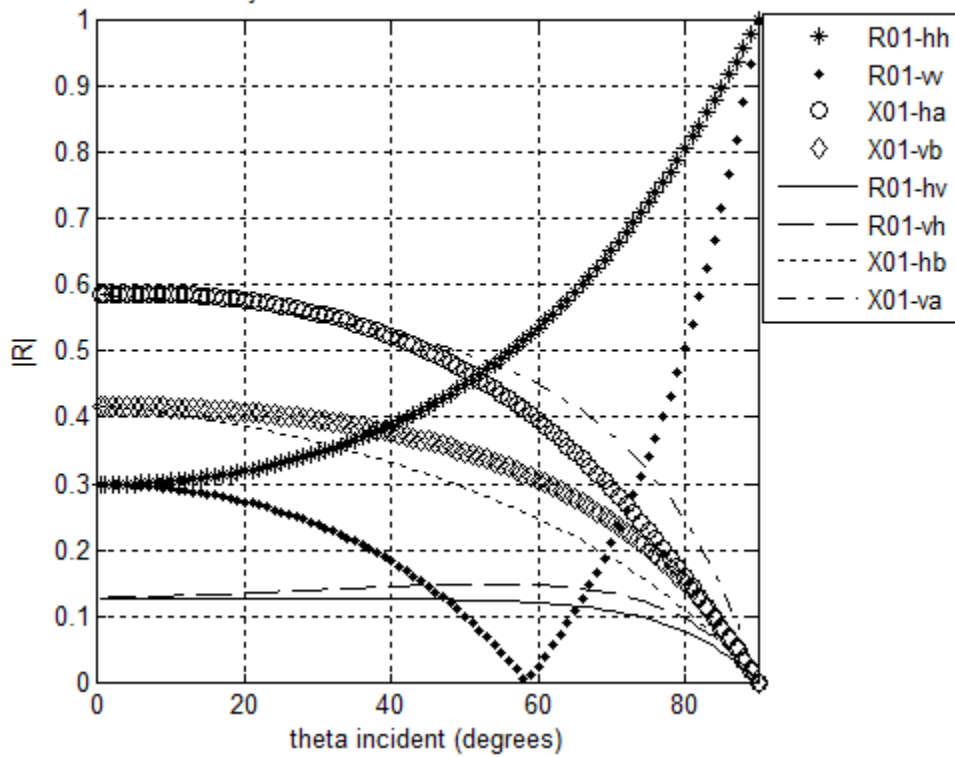


Figure 2-16: Half-space reflection and transmission coefficients for incident wave from isotropic medium to biaxial medium $((\epsilon_x, \epsilon_y, \epsilon_z) = (2, 5, 8), (\psi_1, \psi_2) = (45^\circ, 45^\circ))$.

In the unrotated case, we observed the unique behavior of the horizontally polarized wave being reflected less than the vertically polarized wave. When the medium was rotated, this

behavior is no longer present. We now analyze this behavior in more detail. First, we rotate by ψ_1 . As ψ_1 increases from 0° , R_{hh} is not significantly changed while R_{vv} increases thus enhancing the unique behavior. However, when we increase ψ_2 we see more significant results. As ψ_2 increases from 0° R_{hh} increases and R_{vv} decreases. When ψ_2 reaches 45° R_{hh} and R_{vv} are equal at an incidence angle of 0° and diverge as the angle of incidence increases. When ψ_2 increases beyond 45° , the difference between R_{hh} and R_{vv} at low angle increases with R_{hh} always greater than R_{vv} . This behavior is shown in Figure 2-17.

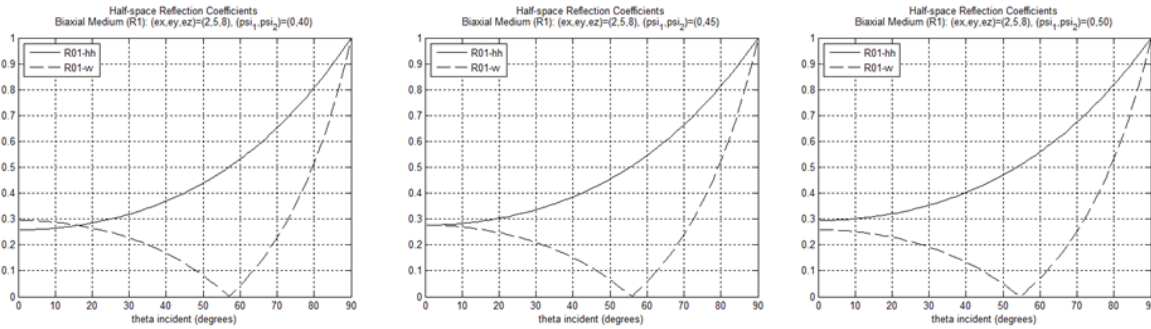


Figure 2-17: Half-space co-polarized reflection coefficients for incident wave from isotropic medium to biaxial medium ($(\epsilon_x, \epsilon_y, \epsilon_z) = (2, 5, 8)$, ($\psi_1=0$, ψ_2 varied))

The half-space reflection behavior changes when we move the angle of incidence to the x - z plane ($\phi_i=0$). In this plane, when the biaxial medium is unrotated, R_{hh} is greater than R_{vv} for all incident angles. As ψ_2 increases from 0° R_{hh} decreases and R_{vv} increases. When ψ_2 reaches 45° R_{hh} and R_{vv} are equal at zero incident angle and for ψ_2 greater than 45° , R_{hh} is less than R_{vv} at low incident angles. Again changing ψ_1 results in less overall change, but in this plane, this ψ_1 has a greater impact on R_{hh} than R_{vv} .

2.2.1.1.4 Critical Angle Analysis

The critical angle is related to the phenomenon of total internal reflection. When the angle of incidence is larger than the critical angle, we have total reflection [2]. Total internal reflection is an important practical phenomenon as it is used to implement dielectric waveguides such as fiber optic cables. This phenomenon occurs when the transmitted wave becomes evanescent. Evanescence occurs when the propagation vector becomes imaginary so as the wave travels into the transmission medium, it decays as $e^{\alpha z}$, where α is the imaginary part of the propagation vector for the wave traveling in the $-z$ direction. Therefore, the critical angle is the angle of incidence for which the propagation vector becomes imaginary.

The critical angle effect is only observed when a wave is propagating from a denser to less dense medium. First, we consider the critical angle in the uniaxial limit. In his dissertation, Y. H. Lee [5] computes the critical angle for the ordinary and extraordinary wave when the wave is downward incident from an isotropic medium to a uniaxial medium. For the ordinary wave to experience total internal reflection (or zero real transmittance to the ordinary wave), $\epsilon_0 > \epsilon_x$ and the angle of incidence must be greater than or equal to the critical angle given by

$$\theta_c = \sin^{-1} \sqrt{\frac{\epsilon_x}{\epsilon_0}} \quad (2.2.32)$$

The extraordinary wave can experience total internal reflection can occur if one of two sets of conditions applies. These conditions are based on the modified permittivities derived by Lee [5] and presented here

$$\varepsilon_+ = \frac{\varepsilon_x \varepsilon_z}{\varepsilon_x \cos^2 \phi_i + \varepsilon_{22} \sin^2 \phi_i} \quad (2.2.33)$$

$$\varepsilon_- = \frac{\varepsilon_z \varepsilon_{33}}{\varepsilon_{33} \cos^2 \phi_i + \varepsilon_z \sin^2 \phi_i} \quad (2.2.34)$$

The extraordinary wave can experience total internal reflection if $(\varepsilon_x - \varepsilon_z) \sin \phi_i > 0$ and $\varepsilon_0 > \varepsilon_+$. If these conditions are met, the critical angle for the extraordinary wave is given by

$$\theta_c = \sin^{-1} \sqrt{\frac{\varepsilon_+}{\varepsilon_0}} \quad (2.2.35)$$

The extraordinary wave can also experience total internal reflection if $(\varepsilon_x - \varepsilon_z) \sin \phi_i < 0$ and $\varepsilon_0 > \varepsilon_-$. Under these conditions the critical angle is given by

$$\theta_c = \sin^{-1} \sqrt{\frac{\varepsilon_-}{\varepsilon_0}} \quad (2.2.36)$$

As an example we consider the same case presented by Lee [5]. The incident isotropic region has a relative permittivity (ε_r) of 6. The uniaxial relative permittivity tensor is given by

$$\bar{\bar{\varepsilon}}_r = \begin{bmatrix} 4 & & \\ & 4 & \\ & & 3 \end{bmatrix} \quad (2.2.37)$$

and a 30° rotation is applied. The incident wave has frequency 13GHz and is incident from $\phi_i = 60^\circ$. Lee computes an ordinary wave critical angle of 54.7° and an extraordinary wave critical angle of 46.4° . We will use our computations to analyze this interface. Applying our biaxial

definitions to this medium, the ordinary wave will be the b-wave and the extraordinary wave will be the a-wave. The resulting reflection coefficients are shown in Figure 2-18. We observe *elbows* at each critical angle. The imaginary part of X_{va} becomes large at the first critical angle (associated with the a-wave or extraordinary wave) and the imaginary part of X_{hb} becomes large at the second critical angle (associated with the b-wave or ordinary wave). We can gain further insight into the critical angle observing the solutions to the Booker Quartic. In this medium, the real part of k_{za} becomes a minimum at the a-wave critical angle and k_{zb} reaches its minimum at the b-wave critical angle. This behavior is shown in Figure 2-19.

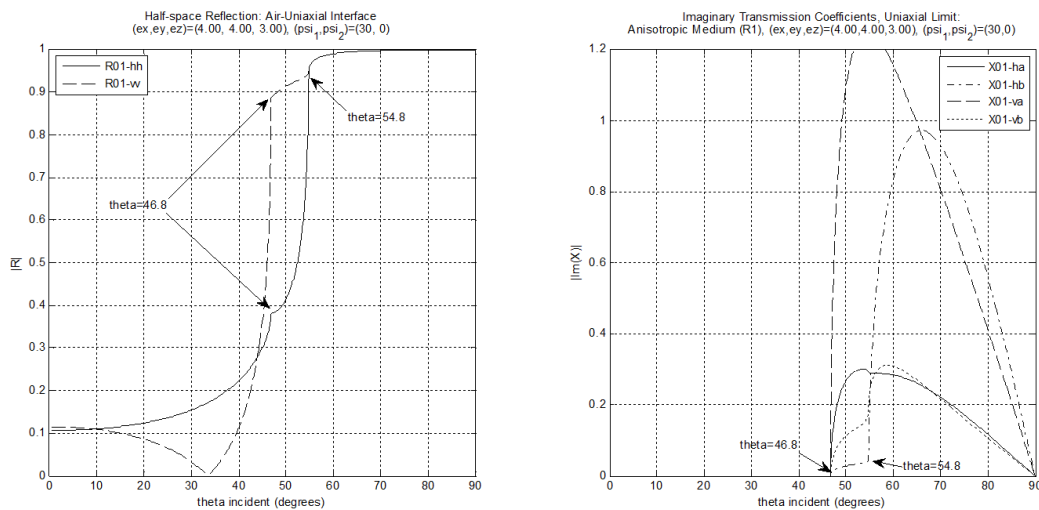


Figure 2-18: Reflection coefficients and imaginary transmission coefficients from isotropic-uniaxial interface

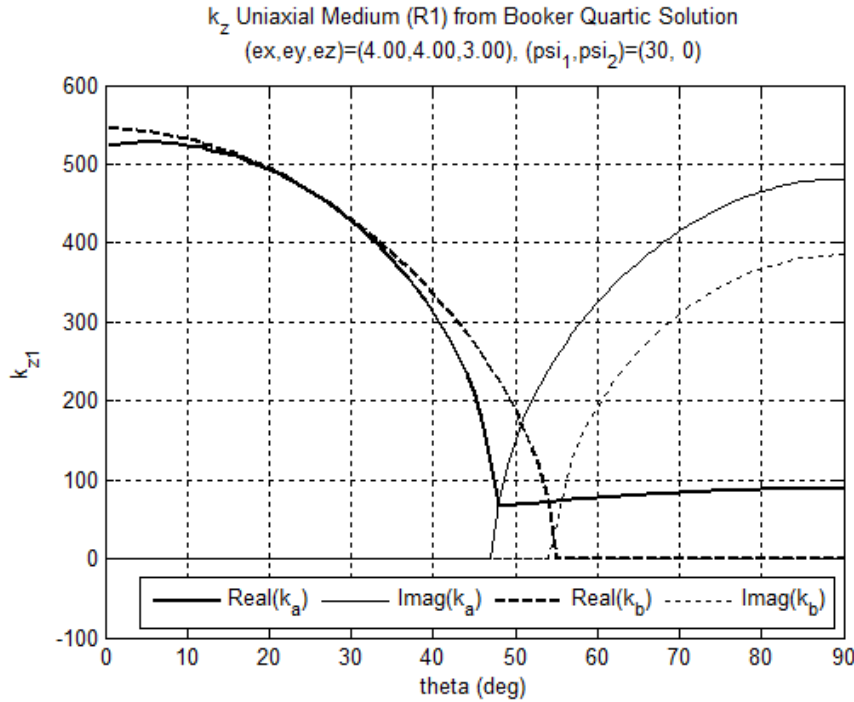


Figure 2-19: Solution to Booker quartic for uniaxial medium

After we have shown agreement of the critical angle behavior in the uniaxial limit, we turn our analysis back to the biaxial interface. We have chosen a boundary between two real materials to demonstrate the critical angle effect. The incident wave is propagating in Silicon which has a relative permittivity of approximately 12. The transmission medium is PTFE cloth (Teflon), which is biaxially anisotropic with relative permittivity tensor

$$\bar{\bar{\epsilon}}_r = \begin{bmatrix} 2.45 & & \\ & 2.89 & \\ & & 2.95 \end{bmatrix} \quad (2.2.38)$$

The co-polarized half-space reflection coefficients from the silicon-PTFE cloth are shown in Figure 2-20. In this figure, the reflection coefficients go to 1 at approximately 30°. This is the phenomenon of total internal reflection.

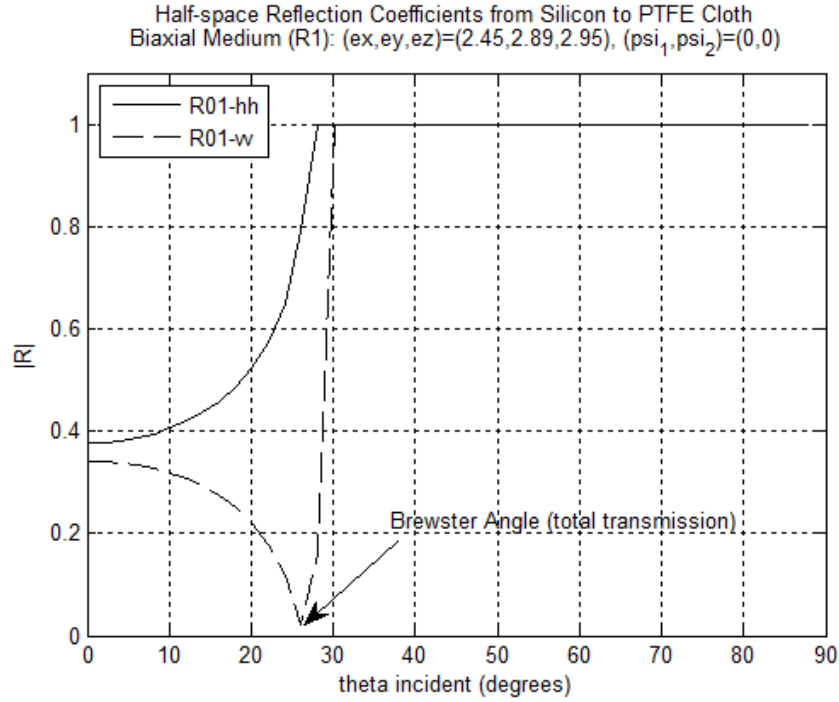


Figure 2-20: Co-polarized reflection coefficients from Silicon-PTFE cloth boundary

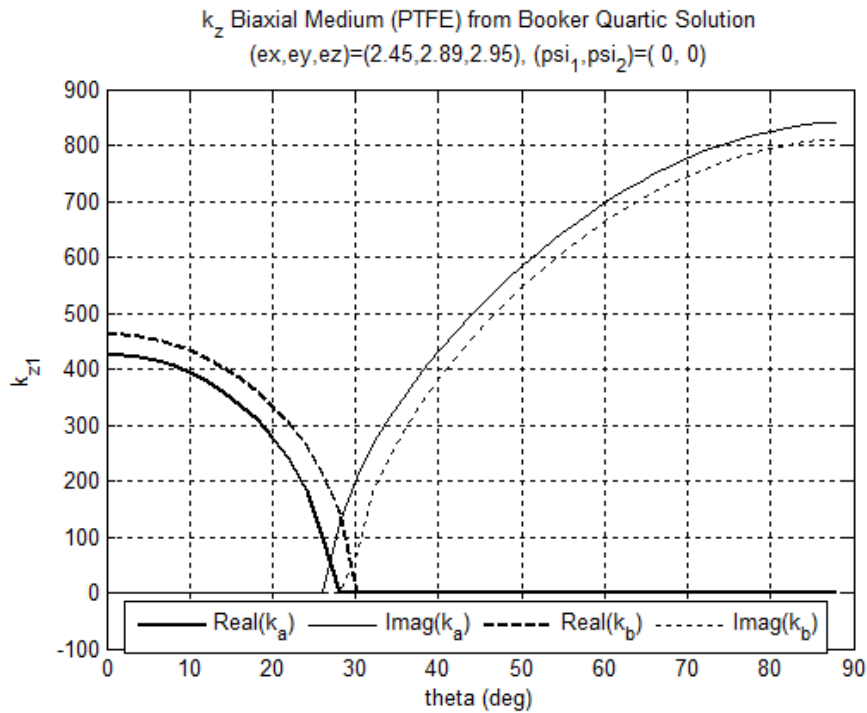


Figure 2-21: Booker quartic solutions in PTFE cloth

To better understand the conditions that lead to total internal reflection, we again examine the solutions to the Booker quartic (k_z values) versus angle of incidence in Figure 2-21 in the PTFE cloth. Here we see that at the same incident angle (approximately 30°) k_z becomes imaginary. The normal to the boundary is the z -direction so when the z component of the propagation vector becomes imaginary, the wave in that medium will be evanescent and no real power will transmit.

Figure 2-20 clearly showed the critical angle effect. When we consider an isotropic-isotropic interface the critical angle is calculated simply using Snell's law. Grzegorzczuk et al. [9] show that in the x - z plane ($\varphi_i = 0$) for an unrotated biaxial medium, the critical angle for the horizontal polarization can be computed by

$$\theta_c^{hh} = \sin^{-1} \left(\sqrt{\frac{\epsilon_{1y} \mu_{1z}}{\epsilon_0 \mu_0}} \right) \quad (2.2.39)$$

The equation for the critical angle for the vertical component can be found by duality which results in

$$\theta_c^{vv} = \sin^{-1} \left(\sqrt{\frac{\epsilon_{1z} \mu_{1y}}{\epsilon_0 \mu_0}} \right) \quad (2.2.40)$$

In our analysis, we found that the angle computed in equation (2.2.39) corresponds to the angle where k_z for the a-wave becomes imaginary. Similarly, the angle computed in equation (2.2.40) is the angle for which the b-wave propagation constant becomes imaginary. In our notation, we denote these angles θ_c^{ha} and θ_c^{vb} respectively. Using (2.2.39) and (2.2.40), the horizontal polarization critical angle is 29.4° and vertical polarization critical angle is 29.7° , which agrees with our computed values for the unrotated medium as shown in Figure 2-22(a) and Figure 2-23(a).

We are also interested in the behavior of the critical angle as the permittivity tensor is rotated. In the first case, permittivity rotations are about the z -axis (ψ_2) with no rotation about the x -axis ($\psi_1=0$) in a plane of incidence described by ϕ_i of 0° (x - z plane), 25° and 90° (y - z plane). The results (in Figure 2-22 (a), (b), and (c)) show that when the medium is rotated about the z -axis, the critical angle varies by less than 5° . When the plane of incidence is changed, the critical angle behavior changes but the peak-to-peak variation over ψ_2 does not change.

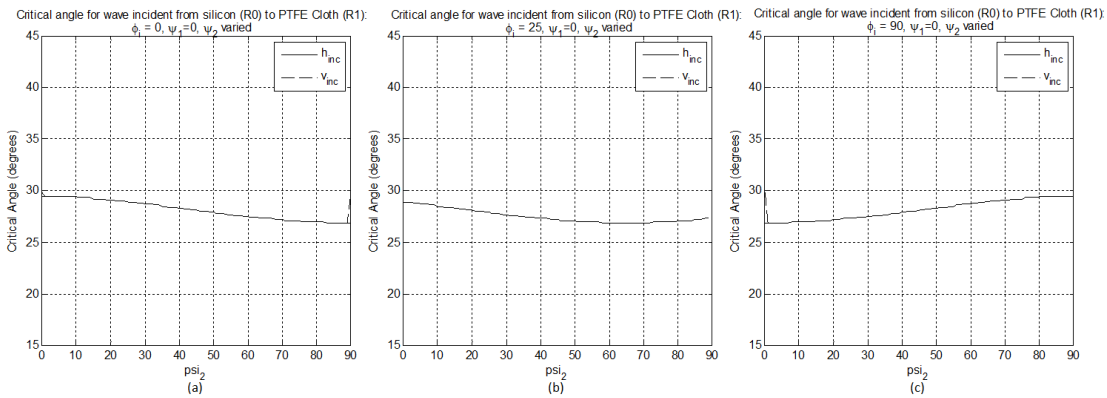


Figure 2-22: Critical angle for wave incident from Silicon to PTFE cloth as ψ_2 is varied for incident angle ϕ_i of 0° (a), 25° (b), and 90° (c).

In the second case, we consider rotations about the x -axis (ψ_1) with no rotation about the z -axis ($\psi_2=0$) and the same incidence planes. The results for this case are shown in Figure 2-23 (a), (b), and (c). We observe that when the medium is rotated about the x -axis, the critical angle varies by less than 1° when ϕ_i is 25° and not at all for other incident planes. When the wave is incident from the y - z plane ($\phi_i=90^\circ$), we see that the horizontal and vertical waves have significantly different critical angles, a behavior not observed in previous cases. To investigate this phenomenon, we computed critical angles for ϕ_i close to 90° and found that it is only observed when ϕ_i is equal to 90° .

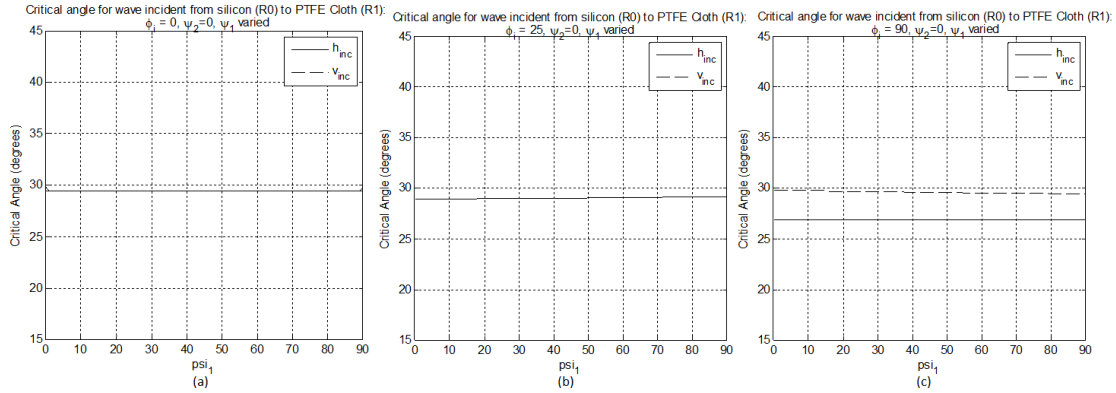


Figure 2-23: Critical angle for wave incident from Silicon to PTFE cloth as ψ_1 is varied for incident angle ϕ_i of 0° (a), 25° (b), and 90° (c).

2.2.1.1.5 Brewster Angle Effect

We are also interested in studying the Brewster angle effect. The Brewster angle is defined as the angle of incidence for which there is no reflected power. At an isotropic-isotropic half-space boundary, the vertically polarized (transverse magnetic) wave generally experiences zero reflection at some angle. The horizontally polarized (transverse electric) wave generally reflects more than the vertical wave and has non-zero reflection for all angles. The result is that when an unpolarized wave (with both vertical and horizontal polarizations present) is incident upon a boundary at the Brewster angle the reflected electromagnetic wave will be linearly polarized (with horizontal polarization). The most common application of this effect is polarized sunglasses in which the lenses filter out the horizontal polarization reducing the dominant component of reflected sunlight (glare). A less common application is in the use of Brewster window lasers. In this application, the horizontally polarized wave is filtered out using a Brewster window resulting in vertically polarized laser light.

The Brewster angle has not been extensively studied for arbitrarily oriented biaxial media. We can see the Brewster angle effect in Figure 2-14 and Figure 2-16. Figure 2-14

shows that for an incident angle of approximately 62° , only the horizontally polarized wave is reflected; the vertically polarized wave is not reflected at all (reflection coefficient goes to zero). The Brewster angle for this unrotated biaxial substrate is approximately 62° . When we rotated the medium as shown in Figure 2-16, the Brewster angle is approximately 57° . Thus we conclude that the Brewster angle depends on rotation of the permittivity tensor.

We are also interested in how the Brewster angle behaves for a different substrate. In this analysis we look at how changes to both the orientation of the biaxial layer and the permittivity of the biaxial layer affect the Brewster angle. We consider the incident wave in the y - z plane from air incident on the biaxial medium with permittivity tensor

$$\bar{\bar{\epsilon}}_r = \begin{bmatrix} 3 & & \\ & 4 & \\ & & 5 \end{bmatrix} \quad (2.2.41)$$

and a fixed value of ψ_2 while we vary ψ_1 . As shown in Figure 2-24, the Brewster angle at this interface is between 60° and 65° as ψ_1 is varied for $\psi_2=0^\circ$ (a) and $\psi_2=45^\circ$ (b). Changing the z -axis rotation from 0° to 45° did not change the Brewster angle trend; it only shifted it down slightly. We also consider the case where ψ_1 is fixed and ψ_2 is varied (Figure 2-25). We see that the peak-to-peak variation is similar to what we observed when ψ_1 was varied except the Brewster angle decreases as ψ_2 increases and changing ψ_1 from 0° to 45° shifts the trend upward slightly. We can conclude from this analysis that the Brewster angle for this permittivity tensor will increase as ψ_1 increases and decrease as ψ_2 increases.

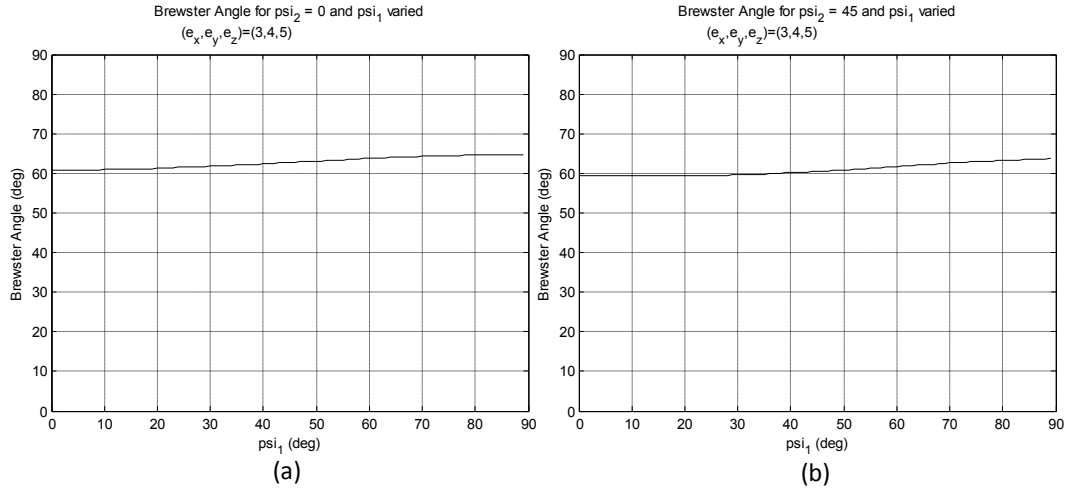


Figure 2-24: Brewster angle as ψ_1 is varied for ψ_2 of 0° (a) and 45° (b). Biaxial permittivity tensor $(\epsilon_x, \epsilon_y, \epsilon_z) = (3, 4, 5)$.

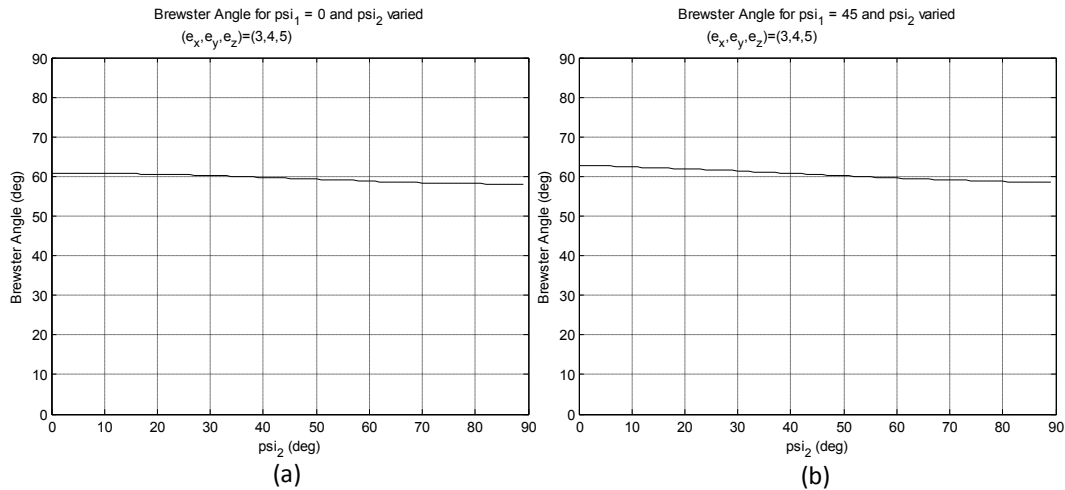


Figure 2-25: Brewster angle as ψ_2 is varied for ψ_1 of 0° (a) and 45° (b). Biaxial permittivity tensor $(\epsilon_x, \epsilon_y, \epsilon_z) = (3, 4, 5)$.

The results for this first permittivity tensor tell us something about how the Brewster angle behaves as the optic axes of the medium are rotated with respect to the layers. We also want to understand how the Brewster angle behaves for a medium with stronger biaxial characteristics. In order to gain this understanding we change our permittivity tensor to the

tensor shown in equation (2.2.23). As we did with the previous permittivity tensor, we will first look at the Brewster angle as a function of ψ_1 rotation angle for fixed ψ_2 angles and then fix ψ_1 and compute the Brewster angle as a function of ψ_2 .

We compute the Brewster angles for the same rotations that were analyzed previously and show the results in Figure 2-26 and Figure 2-27. The first thing to note is that the variation over ψ_1 is more affected by a change in ψ_2 in this medium (Figure 2-26). When ψ_2 is 0° , the total variation is less than 10° (a) but when ψ_2 is 45° , the peak-to-peak variation is approximately 15° . As ψ_2 is varied (Figure 2-27), we see a peak to peak variation of approximately 15° for both ψ_1 values (0° (a) and 45° (b)). We can conclude that for this permittivity tensor ψ_2 rotations have a more significant impact than ψ_1 rotations and the total variation in Brewster angle is greater for this stronger biaxial medium than it was for the previous medium.

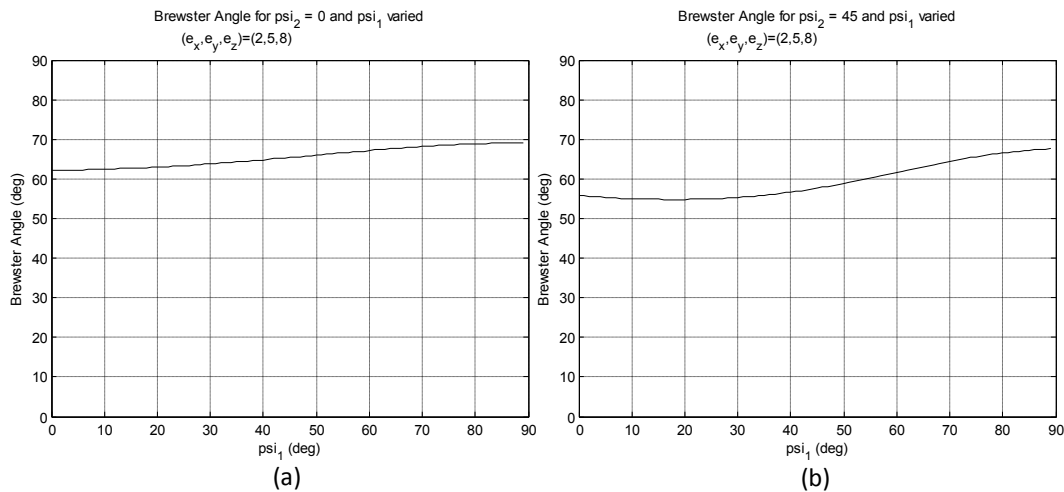


Figure 2-26: Brewster angle as ψ_1 is varied for ψ_2 of 0° (a) and 45° (b). Biaxial permittivity tensor $(\epsilon_x, \epsilon_y, \epsilon_z) = (2, 5, 8)$.

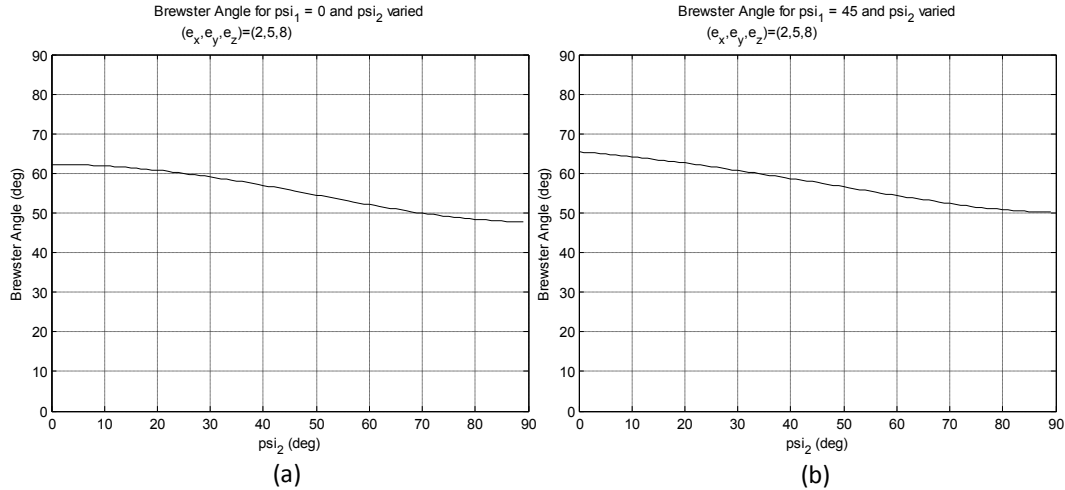


Figure 2-27: Brewster angle as ψ_2 is varied for ψ_1 of 0° (a) and 45° (b). Biaxial permittivity tensor $(\epsilon_x, \epsilon_y, \epsilon_z) = (2, 5, 8)$.

2.2.1.2 Wave Incident from Biaxial Region 1

2.2.1.2.1 a-wave upward incident upon biaxial-isotropic interface

The third configuration from Table 2-2 is the case of an upward propagating a-wave incident from region 1 upon region 0. This incident wave will generate two downward propagating reflected waves (an a-wave and a b-wave in the biaxial medium) and two upward propagating transmitted waves (one horizontally polarized and one vertically polarized in the isotropic region). This phenomenon is depicted in Figure 2-28.

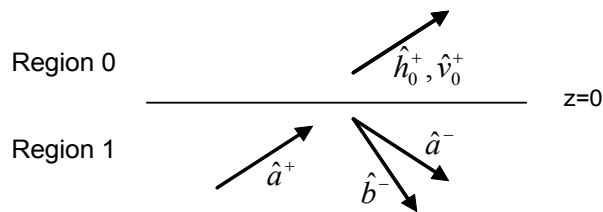


Figure 2-28: a-wave incident upon biaxial- isotropic interface

As done in previous sections, the first step is to formulate the fields in each region to solve for the half-space coefficients. Based on Figure 2-28 we can write

$$\bar{E}_1(\bar{r}) = \hat{a}^+ e^{i\bar{k}_a \cdot \bar{r}} + \hat{a}^- R_{aa}^{10} e^{i\bar{k}_a \cdot \bar{r}} + \hat{b}^- R_{ab}^{10} e^{i\bar{k}_b \cdot \bar{r}} \quad (2.2.42)$$

$$\bar{E}_0(\bar{r}) = \hat{h}_0^+ X_{ah}^{10} e^{i\bar{k}_0 \cdot \bar{r}} + \hat{v}_0^+ X_{av}^{10} e^{i\bar{k}_0 \cdot \bar{r}}$$

The four unknown coefficients are evaluated by applying the boundary conditions on the electric fields and magnetic fields. Next we must evaluate the cross product of the normal with the electric fields in regions one and zero. These cross products are given by

$$-\hat{z} \times \bar{E}_1(\bar{r}_{z=0}) = e^{i(k_x x + k_y y)} \left[(\hat{x} a_y^+ - \hat{y} a_x^+) + R_{aa}^{10} (\hat{x} a_y^- - \hat{y} a_x^-) + R_{ab}^{10} (\hat{x} b_y^- - \hat{y} b_x^-) \right] \quad (2.2.43)$$

$$-\hat{z} \times \bar{E}_0(\bar{r}_{z=0}) = e^{i(k_x x + k_y y)} \left[X_{ah}^{10} (\hat{x} h_{0y}^+ - \hat{y} h_{0x}^+) + X_{av}^{10} (\hat{x} v_{0y}^+ - \hat{y} v_{0x}^+) \right] \quad (2.2.44)$$

To satisfy the electric field boundary condition, we set (2.2.43) equal to (2.2.44) yielding

$$(\hat{x} a_y^- - \hat{y} a_x^+) + R_{aa}^{10} (\hat{x} a_y^- - \hat{y} a_x^-) + R_{ab}^{10} (\hat{x} b_y^- - \hat{y} b_x^-) = X_{ah}^{10} (\hat{x} h_{0y}^+ - \hat{y} h_{0x}^+) + X_{av}^{10} (\hat{x} v_{0y}^+ - \hat{y} v_{0x}^+) \quad (2.2.45)$$

As done previously, we combine like components and rearranging resulting terms. For this case, the two equations obtained from the electric field boundary condition are

$$-R_{aa}^{10} a_y^- - R_{ab}^{10} b_y^- + X_{ah}^{10} h_{0y}^+ + X_{av}^{10} v_{0y}^+ = a_y^+ \quad (2.2.46)$$

$$-R_{aa}^{10} a_x^- - R_{ab}^{10} b_x^- + X_{ah}^{10} h_{0x}^+ + X_{av}^{10} v_{0x}^+ = a_x^+$$

We repeat the process with magnetic field boundary condition. Evaluating the curl using the propagation constant cross product, the tangential magnetic field in region 0 is given by

$$-\hat{z} \times (\bar{k} \times \bar{E}_1(\bar{r}_{z=0})) = e^{i(k_x x + k_y y)} \left\{ \begin{array}{l} -[\hat{x}(k_x a_z^+ - k_z^{au} a_x^+) + \hat{y}(k_y a_z^+ + k_z^{au} a_y^+)] \\ -R_{aa}^{10} [\hat{x}(k_x a_z^- - k_z^{ad} a_x^-) + \hat{y}(k_y a_z^- - k_z^{ad} a_y^-)] \\ -R_{ab}^{10} [\hat{x}(k_x b_z^- - k_z^{bd} b_x^-) + \hat{y}(k_y b_z^- - k_z^{bd} b_y^-)] \end{array} \right\} \quad (2.2.47)$$

and the tangential magnetic field in region 1 is given by

$$-\hat{z} \times (\bar{k} \times \bar{E}_1(\bar{r}_{z=0})) = e^{i(k_x x + k_y y)} \left\{ \begin{array}{l} -X_{ah}^{10} [\hat{x}(k_x h_{0z}^+ - k_{0z} h_{0x}^+) + \hat{y}(k_y h_{0z}^+ - k_{0z} h_{0y}^+)] \\ -X_{av}^{10} [\hat{x}(k_x v_{0z}^+ - k_{0z} v_{0x}^+) + \hat{y}(k_y v_{0z}^+ - k_{0z} v_{0y}^+)] \end{array} \right\} \quad (2.2.48)$$

If we set the right hand sides of equations (2.2.47) and (2.2.48) to be equal, combine like components, and rearrange remaining terms the two resulting equations are

$$\begin{aligned} & -R_{aa}^{10}(k_x a_z^- - k_z^{ad} a_x^-) - R_{ab}^{10}(k_x b_z^- - k_z^{bd} b_x^-) + X_{ah}^{10}(k_x h_{0z}^+ - k_{0z} h_{0x}^+) + X_{av}^{10}(k_x v_{0z}^+ - k_{0z} v_{0x}^+) \\ & \quad = (k_x a_z^+ + k_z^{au} a_x^+) \\ & -R_{aa}^{10}(k_y a_z^- - k_z^{ad} a_y^-) - R_{ab}^{10}(k_y b_z^- - k_z^{bd} b_y^-) + X_{ah}^{10}(k_y h_{0z}^+ - k_{0z} h_{0y}^+) + X_{av}^{10}(k_y v_{0z}^+ - k_{0z} v_{0y}^+) \\ & \quad = (k_y a_z^+ + k_z^{au} a_y^+) \end{aligned} \quad (2.2.49)$$

Again, we write the four equations in matrix form

$$\begin{bmatrix} -a_y^- & -b_y^- & h_{oy}^+ & v_{oy}^+ \\ -a_x^- & -b_x^- & h_{ox}^+ & v_{ox}^+ \\ -(k_x a_z^- - k_z^{ad} a_x^-) & -(k_x b_z^- - k_z^{bd} b_x^-) & (k_x h_{0z}^+ - k_{0z} h_{0x}^+) & (k_x v_{0z}^+ - k_{0z} v_{0x}^+) \\ -(k_y a_z^- - k_z^{ad} a_y^-) & -(k_y b_z^- - k_z^{bd} b_y^-) & (k_y h_{0z}^+ - k_{0z} h_{0y}^+) & (k_y v_{0z}^+ - k_{0z} v_{0y}^+) \end{bmatrix} \begin{bmatrix} R_{aa}^{10} \\ R_{ab}^{10} \\ X_{ah}^{10} \\ X_{av}^{10} \end{bmatrix} = \begin{bmatrix} a_y^+ \\ a_x^+ \\ (k_x a_z^+ - k_z^{au} a_x^+) \\ (k_y a_z^+ - k_z^{au} a_y^+) \end{bmatrix} \quad (2.2.50)$$

This matrix can be solved numerically to obtain the half-space reflection and transmission coefficients for this configuration.

2.2.1.2.2 b-wave upward incident upon biaxial- isotropic interface

The fourth case to consider is when an upward propagating b-wave is incident from region 1 upon region 0. This phenomenon is depicted in Figure 2-29.

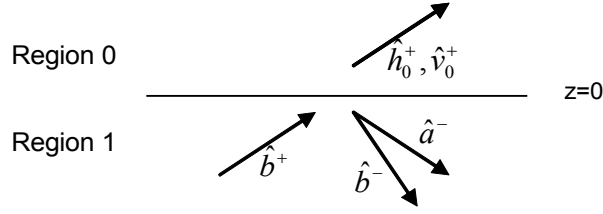


Figure 2-29: b-wave incident upon biaxial- isotropic interface

Based on Figure 2-29 we can write the electric fields in each region as

$$\bar{E}_1(\bar{r}) = \hat{b}^+ e^{i\bar{k}_a \cdot \bar{r}} + \hat{a}^- R_{ba}^{10} e^{i\bar{k}_a \cdot \bar{r}} + \hat{b}^- R_{bb}^{10} e^{i\bar{k}_b \cdot \bar{r}} \quad (2.2.51)$$

$$\bar{E}_0(\bar{r}) = \hat{h}_0^+ X_{bh}^{10} e^{i\bar{k}_0 \cdot \bar{r}} + \hat{v}_0^+ X_{bv}^{10} e^{i\bar{k}_0 \cdot \bar{r}} \quad (2.2.52)$$

Again, we apply the boundary conditions and derive four equations for the four unknowns. We can write the four equations in the matrix form

$$\begin{bmatrix} -a_y^- & -b_y^- & h_{oy}^+ & v_{oy}^+ \\ -a_x^- & -b_x^- & h_{ox}^+ & v_{ox}^+ \\ -(k_x a_z^- - k_z^{ad} a_x^-) & -(k_x b_z^- - k_z^{bd} b_x^-) & (k_x h_{oz}^+ - k_{0z} h_{0x}^+) & (k_x v_{oz}^+ - k_{0z} v_{0x}^+) \\ -(k_y a_z^- - k_z^{ad} a_y^-) & -(k_y b_z^- - k_z^{bd} b_y^-) & (k_y h_{oz}^+ - k_{0z} h_{0y}^+) & (k_y v_{oz}^+ - k_{0z} v_{0y}^+) \end{bmatrix} \begin{bmatrix} R_{ba}^{10} \\ R_{bb}^{10} \\ X_{bh}^{10} \\ X_{bv}^{10} \end{bmatrix} = \begin{bmatrix} b_y^+ \\ b_x^+ \\ (k_x b_z^+ - k_z^{bu} b_x^+) \\ (k_y b_z^+ - k_z^{bu} b_y^+) \end{bmatrix} \quad (2.2.53)$$

2.2.1.2.3 a- and b-waves downward incident upon biaxial-conductor interface

Lastly, we consider the case where a downward propagating is incident from region 1 upon region 2, the *perfect electric conductor* (PEC). Each incident wave will generate two

upward propagating transmitted waves; however, there will be no transmitted fields as there are no fields in a perfect conductor. This case is depicted in Figure 2-30.

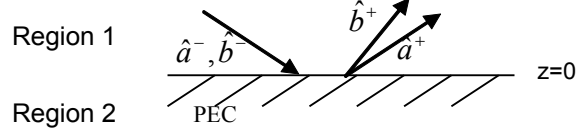


Figure 2-30: a- or b-wave incident upon biaxial-perfect electric conductor interface

As done in previous sections, the first step is to formulate the fields in each region to solve for the half-space coefficients. We first consider the case when the incident wave is the a-wave. Formulating the fields to be consistent with Figure 2-30 results in

$$\bar{E}_1(\bar{r}) = \hat{a}^- e^{i\bar{k}_a \cdot \bar{r}} + \hat{a}^+ R_{aa}^{12} e^{i\bar{k}_a \cdot \bar{r}} + \hat{b}^+ R_{ab}^{12} e^{i\bar{k}_b \cdot \bar{r}} \quad (2.2.54)$$

$$\bar{E}_2(\bar{r}) = 0 \quad (2.2.55)$$

For this problem we do not know the current on the conductor. We cannot assume it is zero as we did when we had a non-conducting boundary. Therefore, we cannot use the magnetic field boundary condition. However, we only have two unknowns and can obtain two equations from the electric field boundary condition to evaluate the two unknowns. The electric field boundary condition at the perfect conductor interface is given by

$$\hat{z} \times \bar{E}_1(\bar{r}) = \hat{z} \times \bar{E}_2(\bar{r}) = 0, \quad \text{at } z = 0 \quad (2.2.56)$$

If we substitute the expression for $\bar{E}_1(\bar{r})$ into equation (2.2.56) we obtain

$$e^{i(k_x x + k_y y)} \left[(-\hat{x}a_y^- + \hat{y}a_x^-) + R_{aa}^{12} (-\hat{x}a_y^+ + \hat{y}a_x^+) + R_{ab}^{12} (-\hat{x}b_y^+ + \hat{y}b_x^+) \right] = 0 \quad (2.2.57)$$

For equation (2.2.57) to hold for all k_x and k_y then the sum (inside the square brackets) must be equal to zero. If we combine like terms, we obtain two equations for the two unknowns. This set of equations can be written as the matrix equation

$$\begin{bmatrix} a_y^+ & b_y^+ \\ a_x^+ & b_x^+ \end{bmatrix} \begin{bmatrix} R_{aa}^{12} \\ R_{ab}^{12} \end{bmatrix} = \begin{bmatrix} -a_y^- \\ -a_x^- \end{bmatrix} \quad (2.2.58)$$

The same boundary conditions can be used to generate a similar set of equations when the b-wave is incident upon the perfect electrical conductor. The resulting set of equations is given by the matrix

$$\begin{bmatrix} a_y^+ & b_y^+ \\ a_x^+ & b_x^+ \end{bmatrix} \begin{bmatrix} R_{ba}^{12} \\ R_{bb}^{12} \end{bmatrix} = \begin{bmatrix} -b_y^- \\ -b_x^- \end{bmatrix} \quad (2.2.59)$$

2.2.1.2.4 Evaluation of Reflection and Transmission of Wave Upward Incident from Region 1

Now we want to repeat the analysis in Section 2.2.1.1.3 for a wave incident from region 1. We once again choose the plane of incidence to be the x - z plane, setting ϕ equal to zero, thus making k_y zero. The angle of incidence in the prescribed plane is given by θ . The plane of incidence and angle of incidence are shown in Figure 2-31.

Plane of Incidence

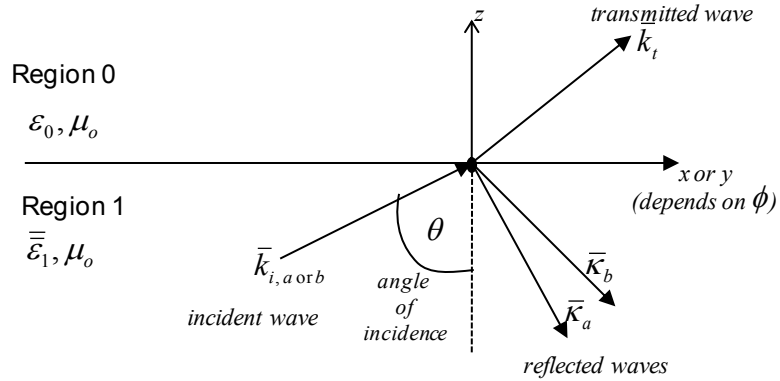


Figure 2-31: Diagram of plane and angle of incidence for wave incident from region 1

The definition of the propagation vectors is not as straightforward when the wave is incident from the biaxial medium. We can define a direction of propagation as a unit vector

$$\hat{k} = -\hat{x} \sin \theta \cos \phi + \hat{y} \sin \theta \sin \phi + \hat{z} \cos \theta \quad (2.2.60)$$

However, to compute the four k_z values, we need k_x and k_y in the medium. We need to know the wave number *in the medium* to compute the propagation vector from the direction given in (2.2.60). When the wave was incident from region 0 (isotropic) we multiplied the direction unit vector by the wave number k_0 . In the biaxial medium, we do not know the wave number explicitly until we solve the Booker quartic, but we need k_x and k_y to solve the Booker quartic for k_z . However, if the direction of propagation is known, our task is not so difficult because k_a (wave number for the a-wave) and k_b (wave number for the b-wave) can be computed using the biquadratic solution in equation (2.1.7) which comes directly from the wave equation. When the medium is unrotated the solutions are valid for both upward and downward propagating waves. However, when the medium is rotated, all four k_z 's are unique (given the same k_x and k_y) so the

solution is only valid for the wave propagating in the pre-determined direction. We set the direction of propagation of the incident wave by the angles of incidence so the biquadratic can be used to compute the wave number of the incident wave then we can use this to compute the four k_z values at the boundary. If we assume the a-wave is incident, then the method we employ is:

1. Compute the wave number for the a-wave (k_a) from the biquadratic solution
2. Use this k_a to obtain the k_x and k_y inputs to the Booker quartic
3. Compute k_z^{au} , k_z^{ad} and k_z^{bd} using the Booker quartic

This issue of defining the propagation vector raises many questions about how we define propagation problems in a biaxial medium. We cannot simply define a wave number with only the frequency and material parameters as we would in an isotropic medium. We also cannot simply define the polarization of the wave. We cannot fix the polarization direction of the electric field then change the direction of propagation while satisfying Maxwell's equations. As already discussed these definitions become more difficult when the medium is rotated. While the governing equations throughout this text hold no matter how we define our incident wave, our understanding of the results is affected. If our "wave number" multiplier to the direction of propagation is not correct, the angles of incidence will not be true. Throughout the rest of this section we choose to compute k_a and k_b using

$$k_a = \sqrt{-\frac{B}{2A} - \frac{\sqrt{B^2 - 4AC}}{2A}} \quad (2.2.61)$$

$$k_b = \sqrt{-\frac{B}{2A} + \frac{\sqrt{B^2 - 4AC}}{2A}} \quad (2.2.62)$$

when the a-wave or b-wave is incident. Then the propagation vector for the incident wave is given by

$$\hat{k}_i^j = -\hat{x}k_i \sin \theta \cos \phi + \hat{y}k_i \sin \theta \sin \phi + \hat{z}k_z^j \quad (2.2.63)$$

where i is the wave polarization (a-wave or b-wave) and j is the direction (upward or downward). It is also important to note that we must treat the a-wave incident and b-wave incident problems separately as there is no single wave number in this medium.

We begin by analyzing the same interface considered by Landry and Maldonado [13]. Landry considers the biaxial-isotropic half-space as a special case. The biaxial relative permittivity tensor under consideration is

$$\bar{\bar{\epsilon}} = \begin{bmatrix} 1.2^2 & 0 & 0 \\ 0 & 1.7^2 & 0 \\ 0 & 0 & 2.2^2 \end{bmatrix} \quad (2.2.64)$$

Landry defined three counter clockwise rotations, first around the z-axis (ψ_0), then around the x-axis (ψ_1) and finally again around the z-axis (ψ_2). We modified our equations to accommodate this additional z-axis rotation (ψ_0) and set $\psi_0 = \psi_1 = 75^\circ$ and $\psi_2 = -75^\circ$. The wave is incident in the x - z plane ($\phi_i = 0^\circ$) while the angle of incidence ranges from -25° to 25° (where the negative angles are equivalent to $\phi_i = 180^\circ$). Note, this modification only affects the permittivity tensor and is used to generate the same tensor Landry used to verify our reflection and transmission computations

The half-space reflection coefficients for the upward incident a-wave (Figure 2-32), exactly match those published by Landry and Maldonado [13].

Half-space Reflection Coefficients: a-wave Incident from Biaxial Medium (R1) to Air (R0)
to compare to Landry and Maldonado paper

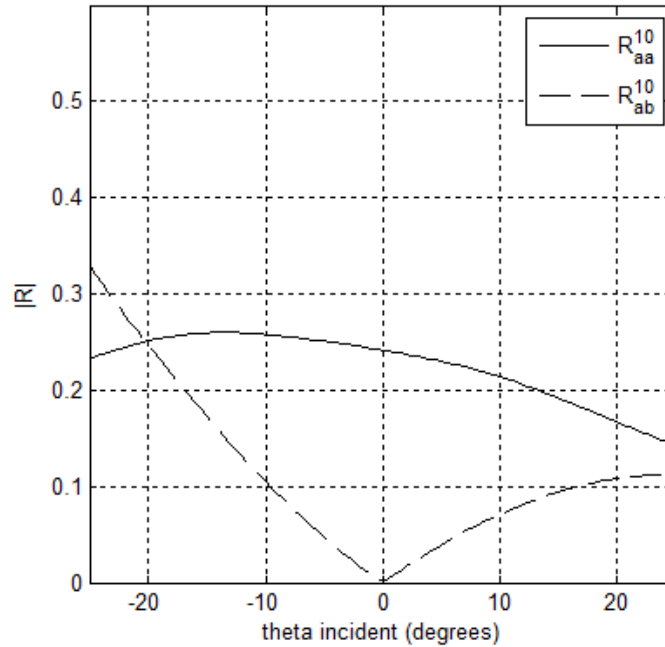


Figure 2-32: Reflection coefficients a-wave upward incident from rotated biaxial medium to air

We observe that an incident a-wave will reflect both an a-wave and a b-wave back into the biaxial medium unless it is normal incidence (theta equal to zero). We also see that the reflection coefficients are not symmetric about the normal incidence point. This is due to the rotation of the permittivity matrix and it means that the reflection behavior is different in the x - z ($\varphi_i = 0^\circ$) plane and the $-x$ - z plane ($\varphi_i = 180^\circ$). The magnitude of the transmitted electric field (Figure 2-33) also exactly matches the result published by Landry and Maldonado. Here we again observe that the transmitted field strength is not symmetric about $\theta = 0^\circ$.

Half-space Transmission: a-wave Incident from Biaxial Medium (R1) to Air (R0)
to compare to Landry and Maldonado paper

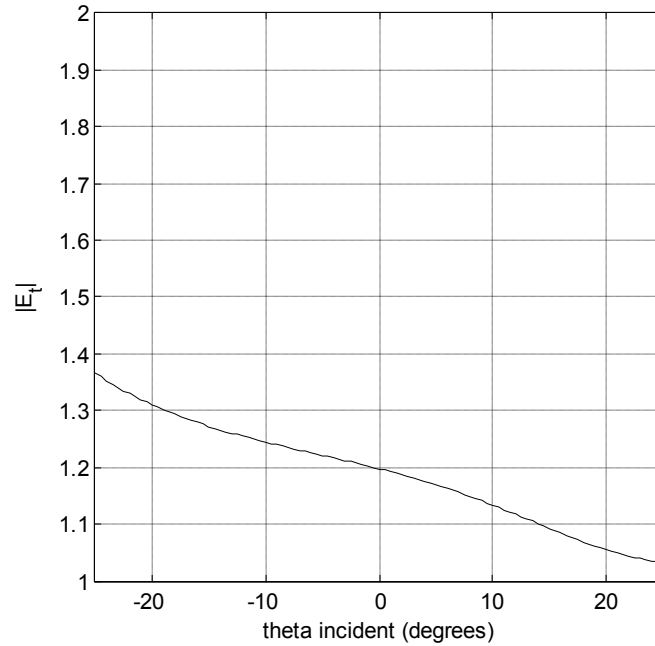


Figure 2-33: Transmitted electric field magnitude for a-wave upward incident from rotated biaxial medium to air

The half-space reflection coefficients and magnitude of the transmitted field for the upward incident b-wave (Figure 2-34 and Figure 2-35, respectively) again exactly match those published by Landry and Maldonado [13]. We observe the same type of asymmetry with respect to θ we saw in the case of the a-wave incident. We also see that the reflection is stronger when the b-wave is incident and that the reflection of the a-wave goes to zero at -25° . This is associated with the critical angle at this interface. Critical angle will be analyzed more thoroughly later in this section. We also note that the transmitted field strength of the transmitted wave is stronger for the b-wave as compared to the a-wave.

Half-Space Reflection Coefficients: b-Wave Incident from Biaxial Medium (R1) to Air (R0)
to compare to Landry and Maldonado paper

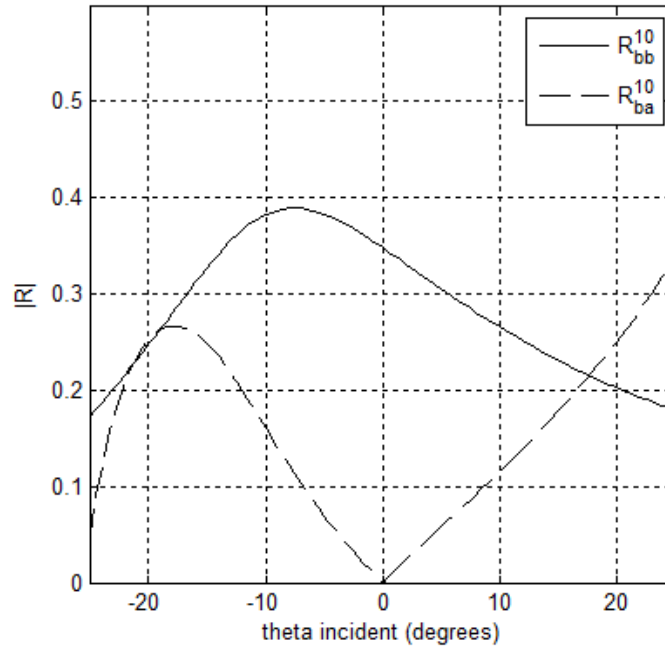


Figure 2-34: Reflection coefficients b-wave incident from biaxial medium to air

Half-space Transmission: b-wave Incident from Biaxial Medium (R1) to Air (R0)
to compare to Landry and Maldonado paper

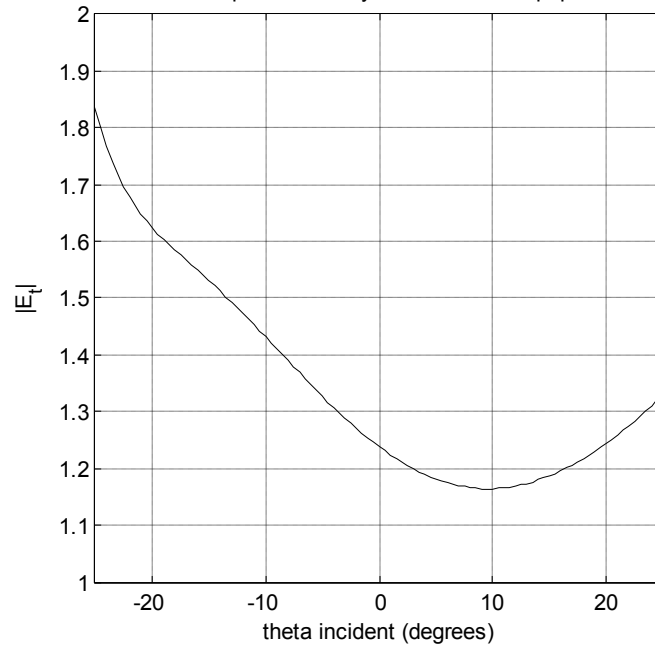


Figure 2-35: Transmitted electric field magnitude for b-wave upward incident from rotated biaxial medium to air

Now we would like to consider the co-polarized half space reflection coefficients for the biaxial-isotropic interface for a different biaxial media using our own permittivity definitions. The isotropic medium is again air and the biaxial medium has a permittivity tensor with relative permittivities of $\epsilon_x=2$, $\epsilon_y=5$, and $\epsilon_z=8$. Here, the plane of incidence has changed such that φ is now 0° . As we did in the previous analysis, we start with an unrotated biaxial medium. As discussed previously in this section, to make sense of the incident wave definitions, we consider the b-wave incidence and a-wave incidence separately and start with the a-wave. The reflection coefficients are plotted against angle of incidence in Figure 2-36. We observe total internal reflection with R_{aa} equal to 1 above the critical angle of 37.5° . The Brewster angle effect is also evident where R_{aa} goes to zero at an incident angle of 28° . Finally, the cross-polarized reflection coefficients R_{ab} is approximately zero, a behavior observed at an isotropic-isotropic boundary.

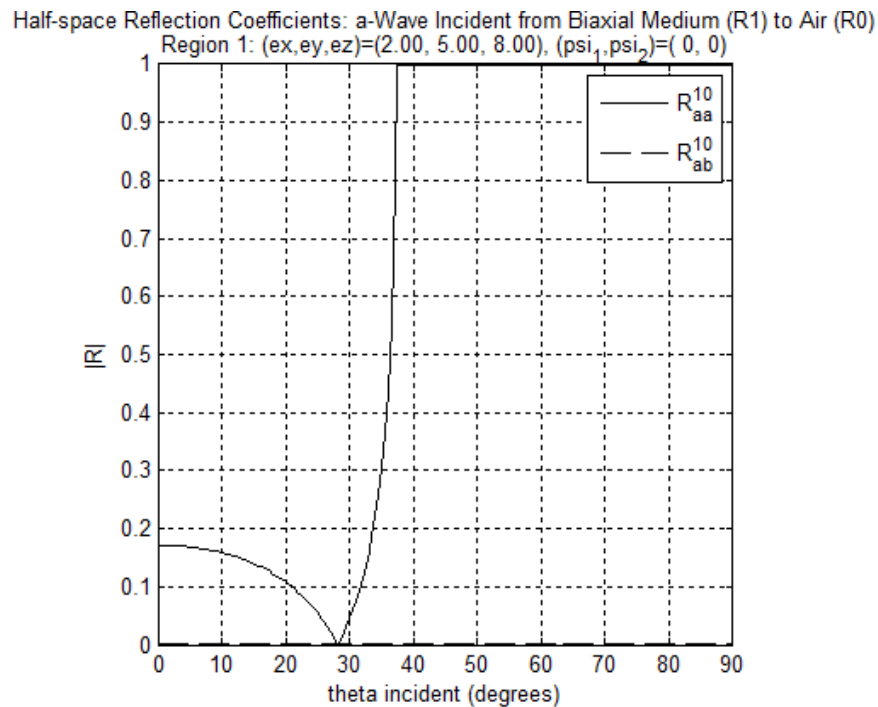


Figure 2-36: Reflection coefficients for a-wave upward incident upon biaxial-air half-space. Biaxial parameters: $(\epsilon_x, \epsilon_y, \epsilon_z) = (2, 5, 8)$, $(\psi_1, \psi_2) = (0^\circ, 0^\circ)$.

Next, we look at the half-space transmission coefficients shown in Figure 2-37 (recall the plane of incidence is $\varphi = 0^\circ$). Here we see that when the a-wave is incident, the energy is transmitted to the vertically polarized wave and X_{av} behaves like co-polarized transmission coefficient. There is no energy transmitted to the horizontally polarized wave as X_{ah} behaves like a cross-polarized transmission coefficient with values close to zero. This polarization pairing is opposite of what we observed when the incident wave was from region 0 (in Figure 2-14). If the plane of incidence is changed, such that $\varphi = 90^\circ$, the a-wave is transmitted to the h-wave, as it was for the same plane of incidence when the wave was incident from region 0. The reason for this behavior is that the horizontally polarized and vertically polarized waves are defined with reference to the plane of incidence whereas the a- and b-waves are defined with respect to the medium coordinate system. Therefore, when the plane of incidence changes the isotropic wave that couples to the biaxial wave also changes. We also observe that the imaginary part of the co-polarized transmission coefficient becomes non-zero beyond the critical angle. This behavior results in an evanescent wave in region 0 that decays rapidly as it propagates and is the cause of total internal reflection. To further illustrate the phenomenon of total internal reflection, we plot the real and imaginary part of the Poynting vector in Figure 2-38. We see that the imaginary part is zero up to the critical angle and non-zero beyond the critical angle. The real part demonstrates the opposite behavior.

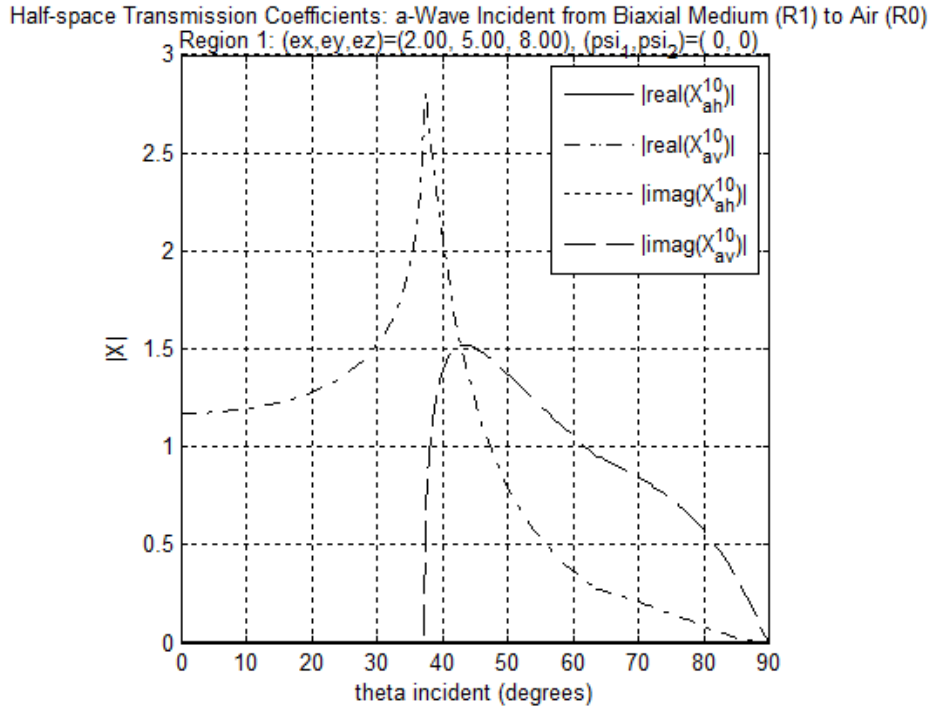


Figure 2-37: Transmission coefficients for a-wave upward incident upon biaxial-air half-space. Biaxial parameters: $(\epsilon_x, \epsilon_y, \epsilon_z) = (2, 5, 8)$, $(\psi_1, \psi_2) = (0^\circ, 0^\circ)$.

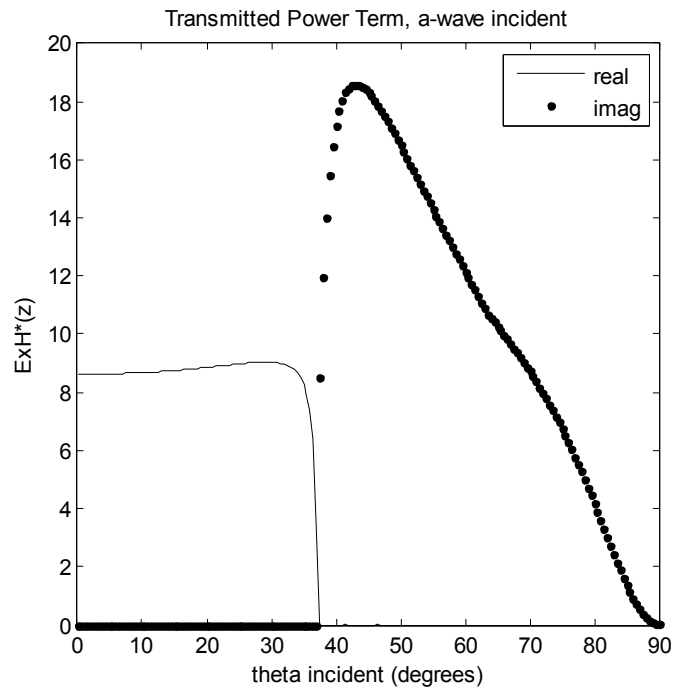


Figure 2-38: Transmitted Poynting vector for a-wave incident from biaxial medium to air. Biaxial parameters: $(\epsilon_x, \epsilon_y, \epsilon_z) = (2, 5, 8)$, $(\psi_1, \psi_2) = (0^\circ, 0^\circ)$.

Again, we verify our result by showing that power is conserved. Therefore, we need to formulate time average Poynting vectors for the incident, reflected and transmitted waves.

Considering the case when the a-wave is incident, the incident time average Poynting vector is

$$\langle \bar{S}_i \rangle = \frac{1}{2} \frac{|E_0|^2}{\omega \mu_0} \operatorname{Re} \left\{ \hat{a}^+ \times (\bar{k}_a \times \hat{a}^+)^* \right\} \quad (2.2.65)$$

Similarly, it can be shown that the time average Poynting vector of the reflected wave is

$$\langle \bar{S}_r \rangle = \frac{1}{2} \frac{|E_0|^2}{\omega \mu_0} \operatorname{Re} \left\{ \begin{aligned} & \hat{a}^- \times (\bar{k}_a \times \hat{a}^-)^* |R_{aa}^{10}|^2 + \hat{a}^- \times (\bar{k}_b \times \hat{b}^-)^* R_{aa}^{10} (R_{ab}^{10})^* e^{i(\bar{k}_a - \bar{k}_b) \cdot \bar{r}} \\ & + \hat{b}^- \times (\bar{k}_a \times \hat{a}^-)^* R_{ab}^{10} (R_{aa}^{10})^* e^{i(\bar{k}_b - \bar{k}_a) \cdot \bar{r}} + \hat{b}^- \times (\bar{k}_b \times \hat{b}^-)^* |R_{ab}^{10}|^2 \end{aligned} \right\} \quad (2.2.66)$$

and the transmitted wave is

$$\langle \bar{S}_t \rangle = \frac{1}{2} \frac{|E_0|^2}{\omega \mu_0} \operatorname{Re} \left\{ \begin{aligned} & \hat{h}_0^+ \times (\bar{k}_0 \times \hat{h}_0^+)^* |X_{ah}^{10}|^2 + \hat{h}_0^+ \times (\bar{k}_0 \times \hat{v}^+)^* X_{ah}^{10} (X_{av}^{10})^* \\ & + \hat{v}^+ \times (\bar{k}_0 \times \hat{h}_0^+)^* X_{av}^{10} (X_{ah}^{10})^* + \hat{v}^+ \times (\bar{k}_0 \times \hat{v}^+)^* |X_{av}^{10}|^2 \end{aligned} \right\} \quad (2.2.67)$$

As detailed previously, we prove that power is conserved by showing that the power reflection and transmission coefficients (given in equations (2.2.30) and (2.2.31)) add to one. In Figure 2-39 we show that the sum of the power reflection and transmission coefficients is in fact one for the a-wave incident. Therefore, power is conserved.

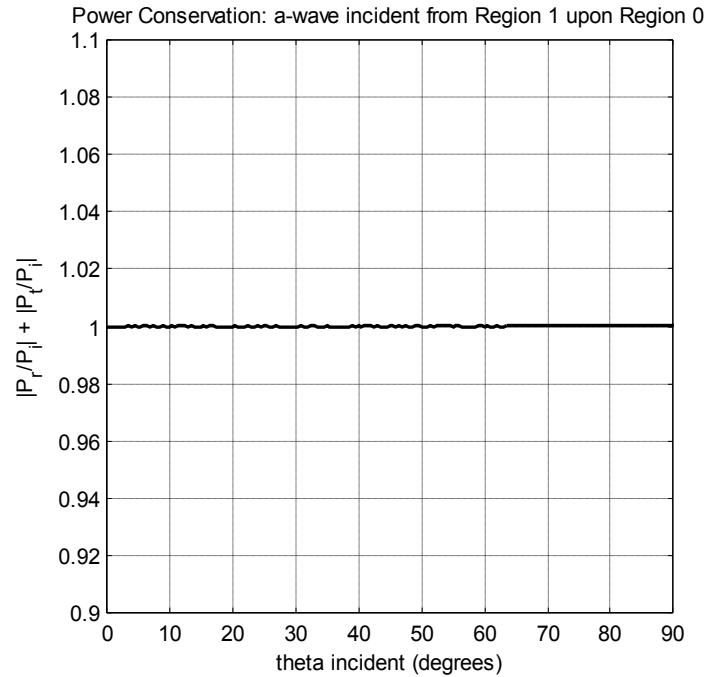


Figure 2-39: Power conservation for a-wave incident from biaxial medium to air. Biaxial parameters: $(\epsilon_x, \epsilon_y, \epsilon_z) = (2, 5, 8)$, $(\psi_1, \psi_2) = (0^\circ, 0^\circ)$.

Now we consider the same biaxial medium but we rotated the permittivity tensor around the x -axis by 15° (ψ_1) and around the z -axis by 35° (ψ_2). The resulting reflection coefficients are shown in Figure 2-40. We observe that depending on the angle of incidence, either biaxial polarization may be reflected more strongly. Also, we do not clearly see the total internal reflection as we did for the unrotated case. As the angle of incidence approaches 40° , the absolute value of R_{ab} rises dramatically to 0.7 with an absolute value of R_{aa} at approximately 0.45. To better understand what is happening to the reflection coefficients, we also break them out into their real and imaginary parts in Figure 2-41. In this plot we see that beyond 40° , the imaginary parts of both reflection coefficients become non-zero. We will see in our transmission and power analyses that 40° is the critical angle under this rotation. In the previous unrotated case the critical angle was 37.5° so the critical angle is affected by rotation.

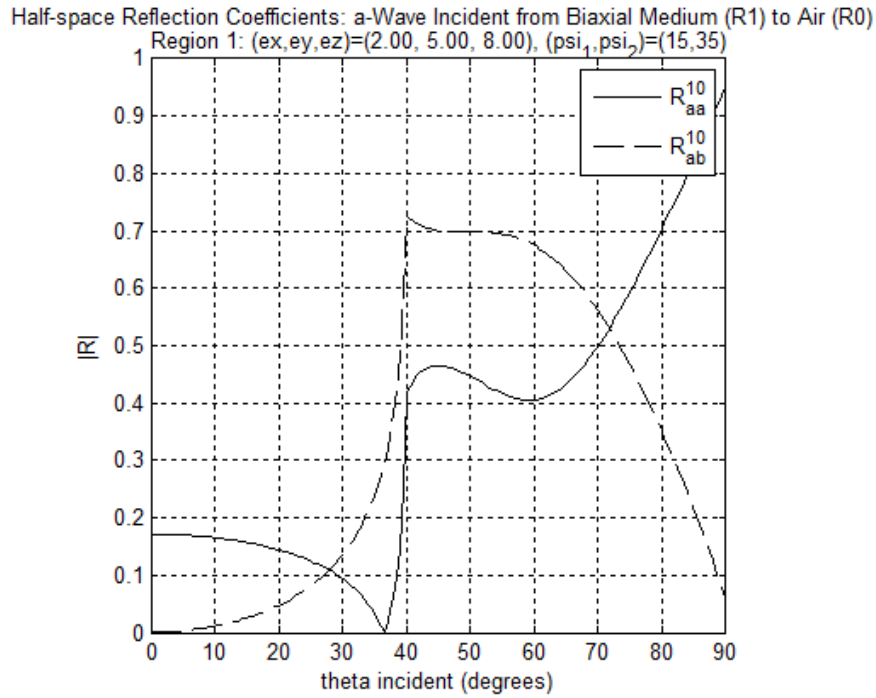


Figure 2-40: Reflection coefficients for a-wave upward incident upon biaxial-air half-space. Biaxial parameters: $(\epsilon_x, \epsilon_y, \epsilon_z) = (2, 5, 8)$, $(\psi_1, \psi_2) = (15^\circ, 35^\circ)$.

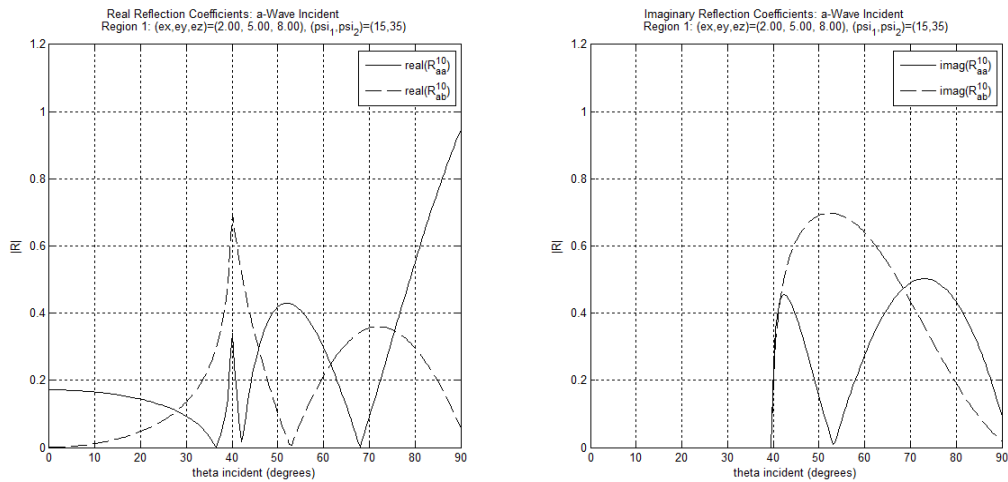


Figure 2-41: Real and imaginary reflection coefficients for a-wave upward incident upon biaxial-air half-space. Biaxial parameters: $(\epsilon_x, \epsilon_y, \epsilon_z) = (2, 5, 8)$, $(\psi_1, \psi_2) = (15^\circ, 35^\circ)$.

In Figure 2-42 we plot the transmission coefficients for the rotated half-space problem. When the medium is rotated, energy is transmitted to both the horizontally polarized and vertically polarized waves in the isotropic region. This transmission is purely real until the angle of incidence reaches 40° . Beyond this critical angle, the transmission coefficients both become complex resulting in two evanescent waves and total internal reflection. The Poynting vector of the transmitted wave also shows that the critical angle occurs at 40° (Figure 2-43). This figure also shows that the real and imaginary parts of the transmitted wave are both approximately zero at 52.5° . Finally, we analyze the real transmitted and reflected power ratios in Figure 2-44 and show that the total reflected power ratio goes to one at 40° , verifying that 40° is the critical angle even if no one reflection coefficient is equal to 1. This plot also verifies that power is conserved, showing that the sum of the two ratios is 1 for all angles of incidence.

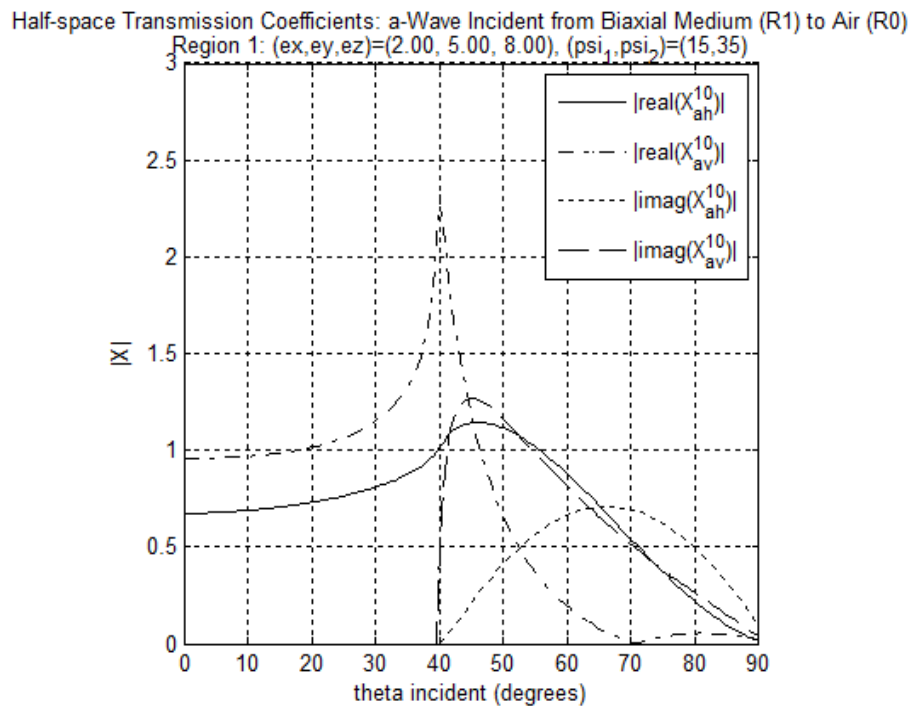


Figure 2-42: Transmission coefficients for a-wave upward incident upon biaxial-air half-space. Biaxial parameters: $(\epsilon_x, \epsilon_y, \epsilon_z) = (2, 5, 8)$, $(\psi_1, \psi_2) = (15^\circ, 35^\circ)$.

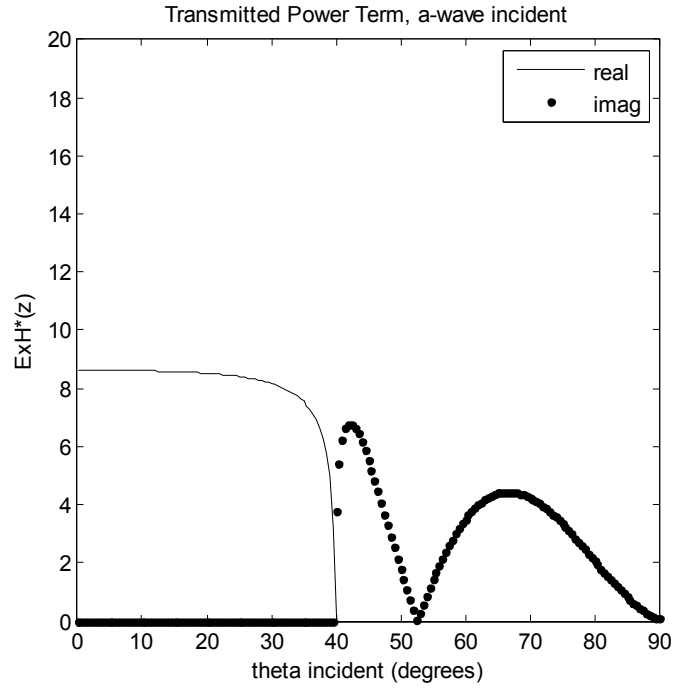


Figure 2-43: Transmitted Poynting vector for a-wave incident from biaxial medium to air. Biaxial parameters: $(\epsilon_x, \epsilon_y, \epsilon_z) = (2, 5, 8)$, $(\psi_1, \psi_2) = (15^\circ, 35^\circ)$.

Transmitted and Reflected Power Ratio: a-Wave Incident from Biaxial Medium (R1) to Air (R0)
 Region 1: $(\epsilon_x, \epsilon_y, \epsilon_z) = (2.00, 5.00, 8.00)$, $(\psi_1, \psi_2) = (15, 35)$

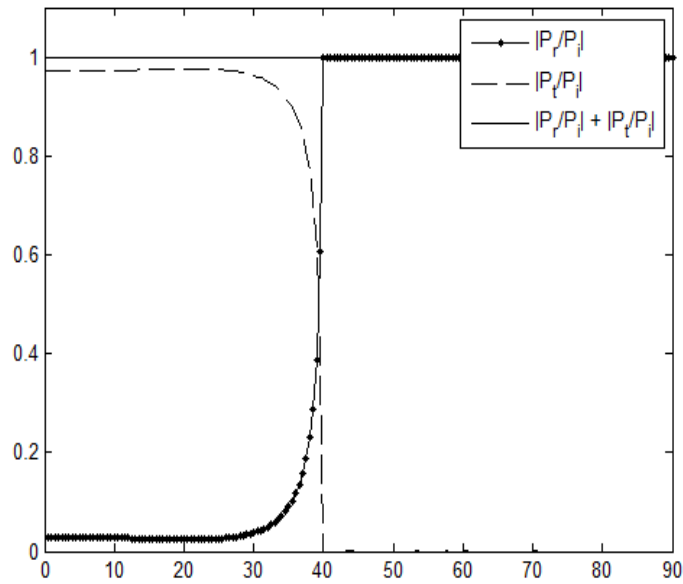


Figure 2-44: Transmitted and reflected power ratios for a-wave upward incident from rotated biaxial medium to air

Consider now the b-wave incident from the same biaxial medium considered in the a-wave incidence analysis with $\varphi = 0^\circ$. We begin again with the unrotated case. The reflection coefficients are plotted against angle of incidence (Figure 2-45). We observe total internal reflection above the critical angle of 27° . The cross-polarized reflection coefficients R_{ba} is approximately zero just as we observed when the wave was incident from the isotropic region. The b-wave does not experience the Brewster effect as R_{bb} never goes to zero; the b-wave is reflected for all incidence angles.

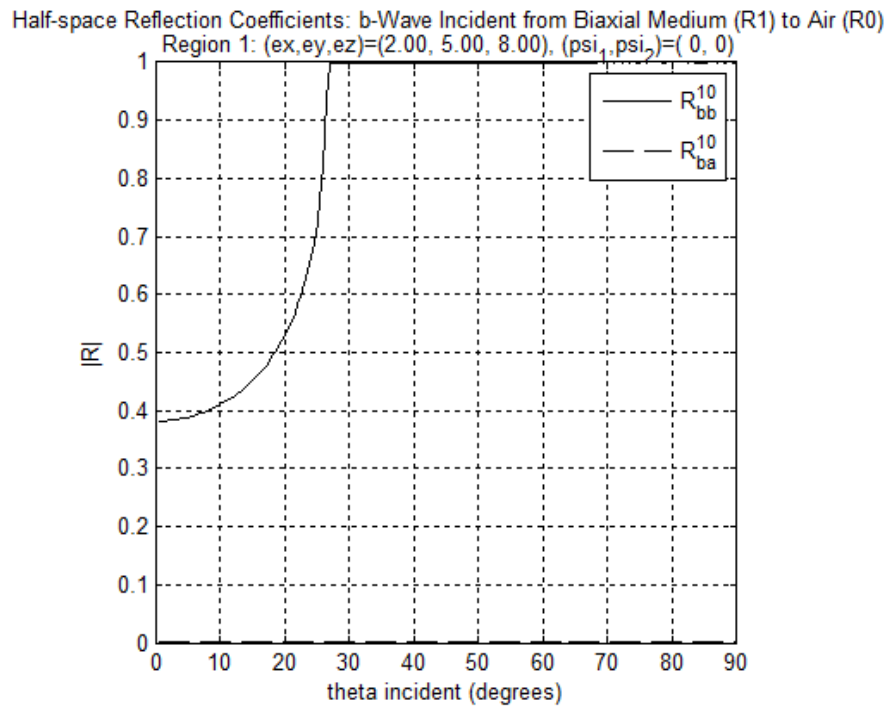


Figure 2-45: Reflection coefficients for b-wave upward incident upon biaxial-air half-space. Biaxial parameters: $(\epsilon_x, \epsilon_y, \epsilon_z) = (2, 5, 8)$, $(\psi_1, \psi_2) = (0^\circ, 0^\circ)$.

Next, we look at the half-space transmission coefficients shown in Figure 2-46. Here we see that when the b-wave is incident, the energy is transmitted to the horizontally polarized wave and X_{bh} behaves like co-polarized transmission coefficient. There is no energy transmitted

to the vertically polarized wave as X_{bv} is approximately zero. We also observe that the imaginary part of X_{bh} becomes non-zero beyond the critical angle. This behavior results in an evanescent wave in region zero that decays rapidly as it propagates and is the cause of total internal reflection. To further illustrate the phenomenon of total internal reflection, we plot the real and imaginary part of the Poynting vector in Figure 2-47. We see that the imaginary part is zero up to the critical angle and non-zero beyond the critical angle. The real part has opposite behavior.

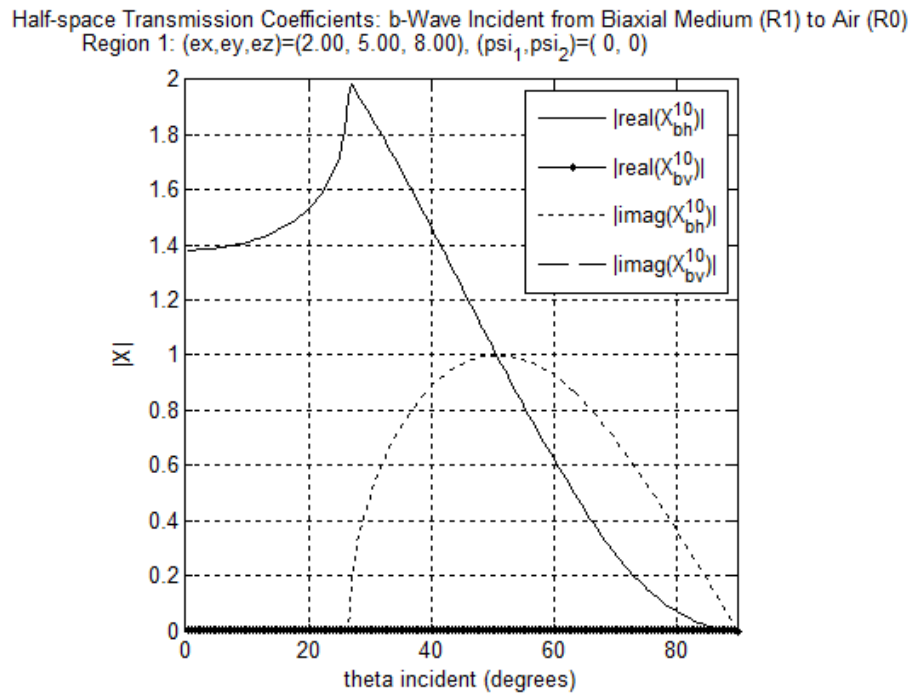


Figure 2-46: Transmission coefficients for b-wave upward incident upon biaxial-air half-space. Biaxial parameters: $(\epsilon_x, \epsilon_y, \epsilon_z) = (2, 5, 8)$, $(\psi_1, \psi_2) = (0^\circ, 0^\circ)$.

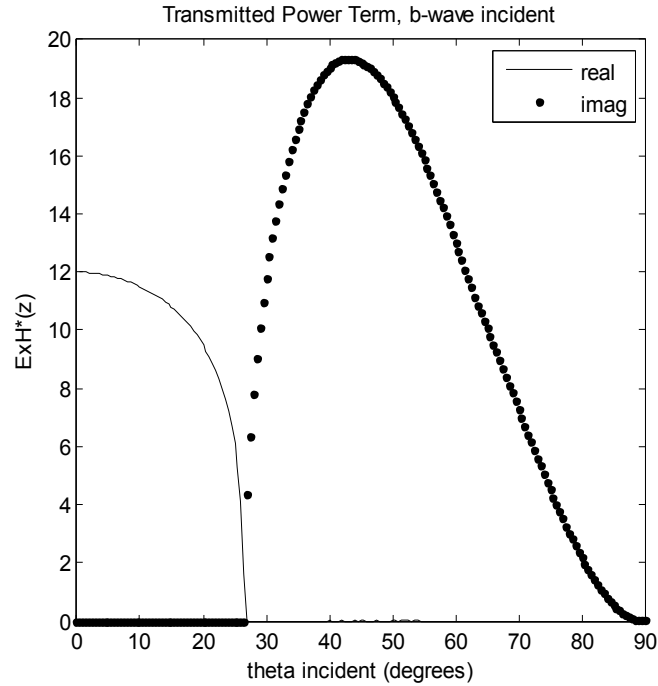


Figure 2-47: Transmitted Poynting vector for b-wave incident from biaxial medium to air. Biaxial parameters: $(\epsilon_x, \epsilon_y, \epsilon_z) = (2, 5, 8)$, $(\psi_1, \psi_2) = (0^\circ, 0^\circ)$.

Again, we want to verify our results showing that power is conserved. Therefore, we formulate time average Poynting vectors for the incident, reflected and transmitted waves when the b-wave is incident in the same manner as for the a-wave incident. As we did previously, we prove that power is conserved by showing that the power reflection and transmission coefficients (given in equations (2.2.30) and (2.2.31)) add to one. In this way Figure 2-48 shows that power is conserved when the b-wave is incident.

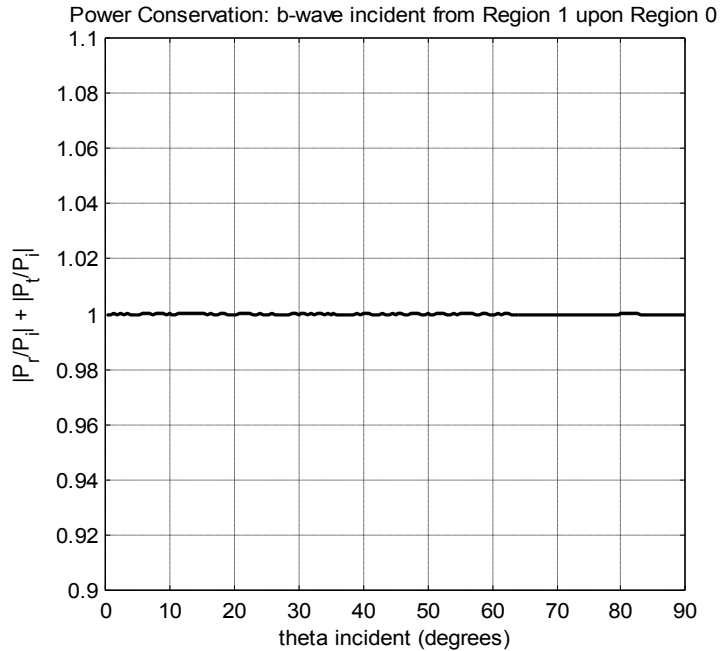


Figure 2-48: Power conservation for b-wave incident from biaxial medium to air. Biaxial parameters: $(\epsilon_x, \epsilon_y, \epsilon_z) = (2, 5, 8)$, $(\psi_1, \psi_2) = (0^\circ, 0^\circ)$.

Now that we have observed reflection and transmission characteristics for a b-wave incident from an unrotated biaxial layer, we will analyze the same behaviors if we rotate the biaxial permittivity tensor. Again, we choose rotation angles ψ_1 and ψ_2 of 15° and 35° respectively. First, we analyze the reflection coefficients (Figure 2-49). We see that the cross-polarized reflection coefficient is significant. In fact, we see that the absolute value of both reflection coefficients become greater than one for some incident angles. The first incident angle that this behavior is demonstrated is at 25.5° where the absolute value R_{ba} increases sharply to almost 1.2. Figure 2-49 also shows the absolute value of the reflection coefficients are greater than 1. Figure 2-50 shows that the imaginary part of R_{ba} becomes non-zero (and large) at this same angle which contributes to the large absolute value. We will see when we analyze the transmission characteristics that 25.5° is the critical angle for this case. Again this is a change

from the unrotated case in which the critical angle was 27° . Rotating the biaxial medium (by $\psi_1=15^\circ$ and $\psi_2=35^\circ$) results in a larger critical angle for a-wave incidence and a smaller critical angle for b-wave incidence. Figure 2-49 shows that the absolute value of the co-polarized reflection coefficient (R_{bb}) also increases sharply at an incident angle of 47° which is where the imaginary part becomes non-zero (Figure 2-50).

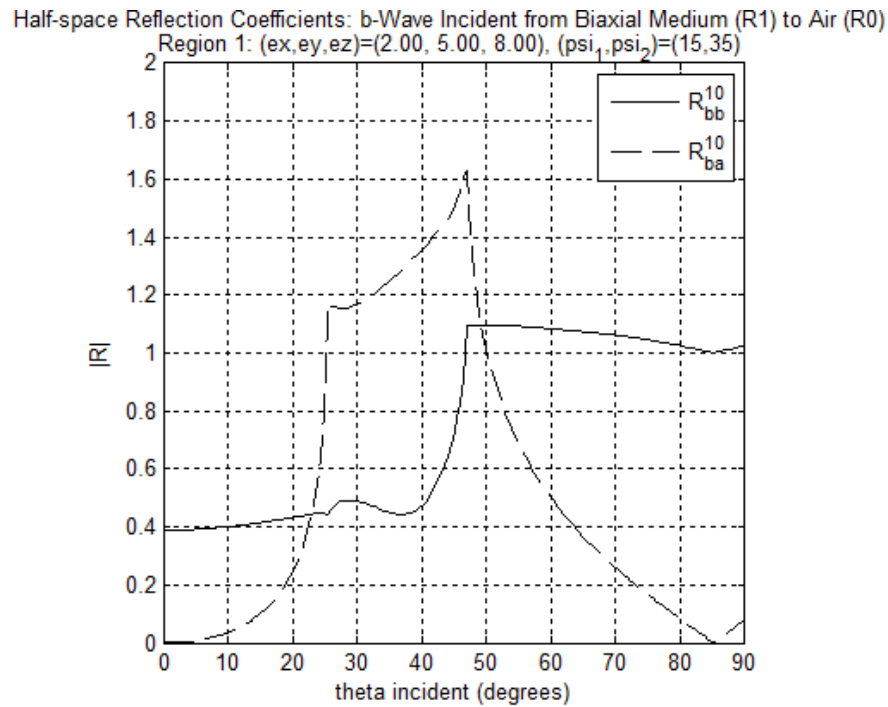


Figure 2-49: Reflection coefficients for b-wave upward incident upon biaxial-air half-space. Biaxial parameters: $(\epsilon_x, \epsilon_y, \epsilon_z) = (2, 5, 8)$, $(\psi_1, \psi_2) = (15^\circ, 35^\circ)$.

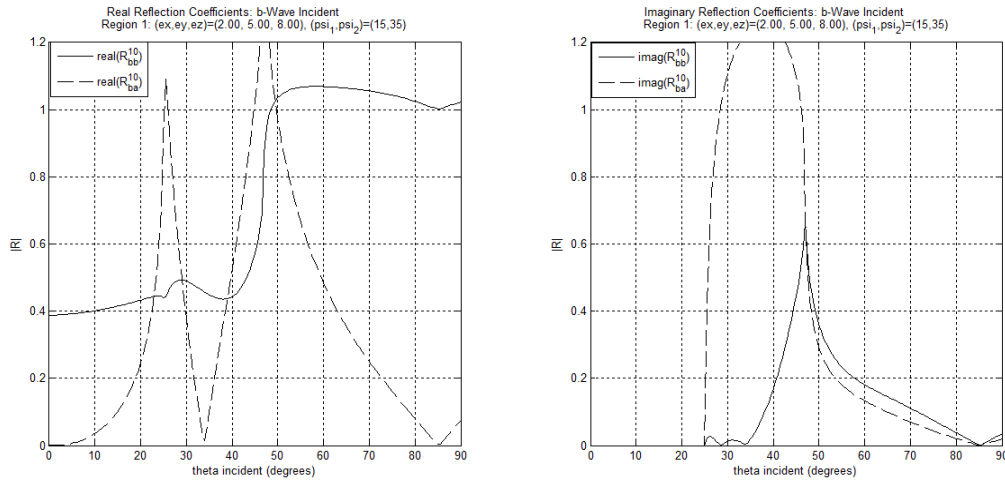


Figure 2-50: Real and imaginary reflection coefficients for b-wave upward incident upon biaxial-air half-space. Biaxial parameters: $(\epsilon_x, \epsilon_y, \epsilon_z) = (2, 5, 8)$, $(\psi_1, \psi_2) = (15^\circ, 35^\circ)$.

The transmission coefficients in Figure 2-51 show that energy is transmitted to both the horizontally polarized and vertically polarized waves in the isotropic region when the b-wave is incident. This transmission is purely real until the angle of incidence reaches 25.5° . Beyond this critical angle, the transmission coefficients both become complex resulting in two evanescent waves and total internal reflection. The Poynting vector of the transmitted wave also shows that the critical angle occurs at 25.5° (Figure 2-52). When the b-wave is incident, we do not observe an angle beyond the critical angle where both the real and imaginary parts of the transmitted wave go to zero. This is in contrast to what we observed when the a-wave was incident.

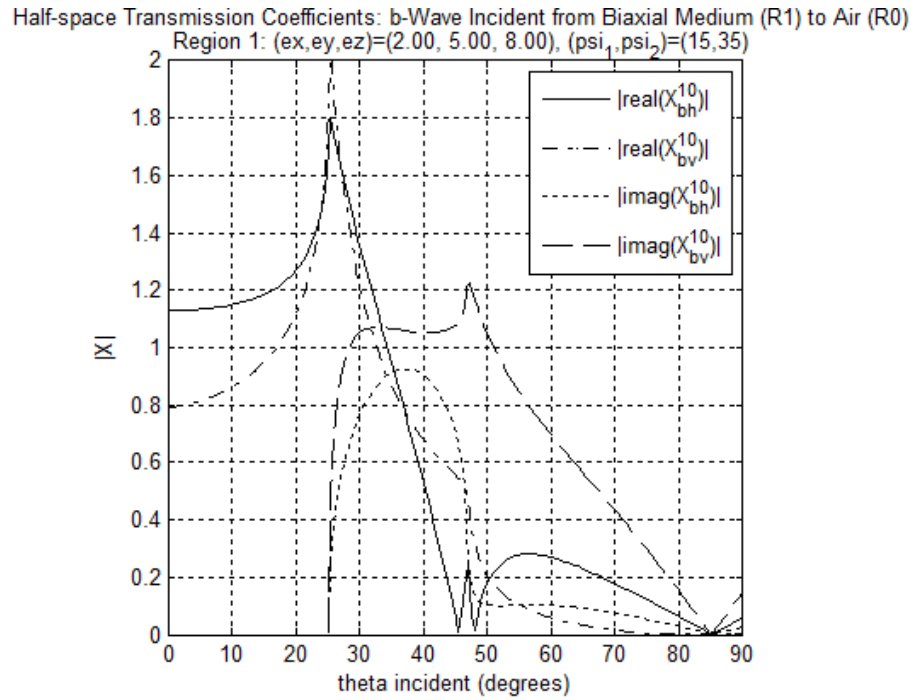


Figure 2-51: Transmission coefficients for b-wave upward incident upon biaxial-air half-space. Biaxial parameters: $(\epsilon_x, \epsilon_y, \epsilon_z) = (2, 5, 8)$, $(\psi_1, \psi_2) = (15^\circ, 35^\circ)$.

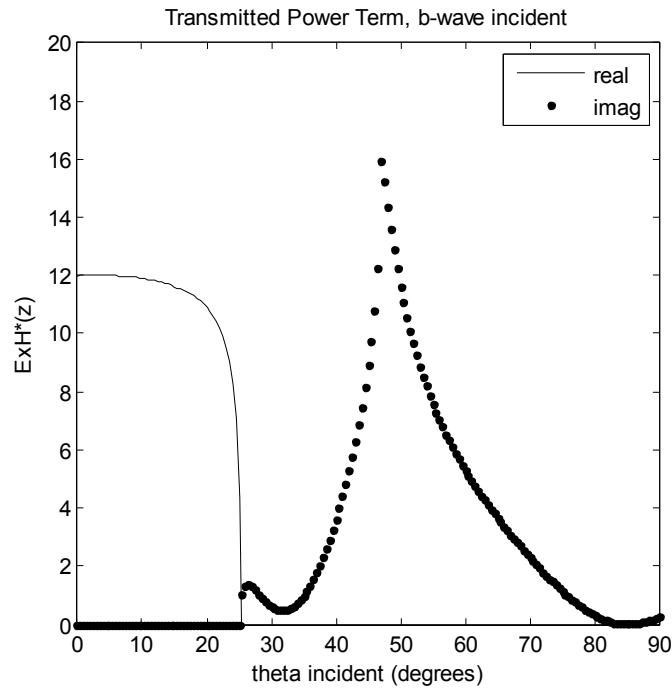


Figure 2-52: Transmitted Poynting vector for b-wave incident from biaxial medium to air. Biaxial parameters: $(\epsilon_x, \epsilon_y, \epsilon_z) = (2, 5, 8)$, $(\psi_1, \psi_2) = (15^\circ, 35^\circ)$.

Finally, we analyze the real transmitted and reflected power ratios. We observed that the absolute values of the reflection coefficients were greater than one for some angles (Figure 2-49). However, when we analyze the power ratios in Figure 2-53, we see that the reflected power ratio never exceeds 1 and in fact is equal to 1 beyond the critical angle. Figure 2-53 also verifies that power is conserved, showing that the sum of the two ratios is 1 for all angles of incidence.

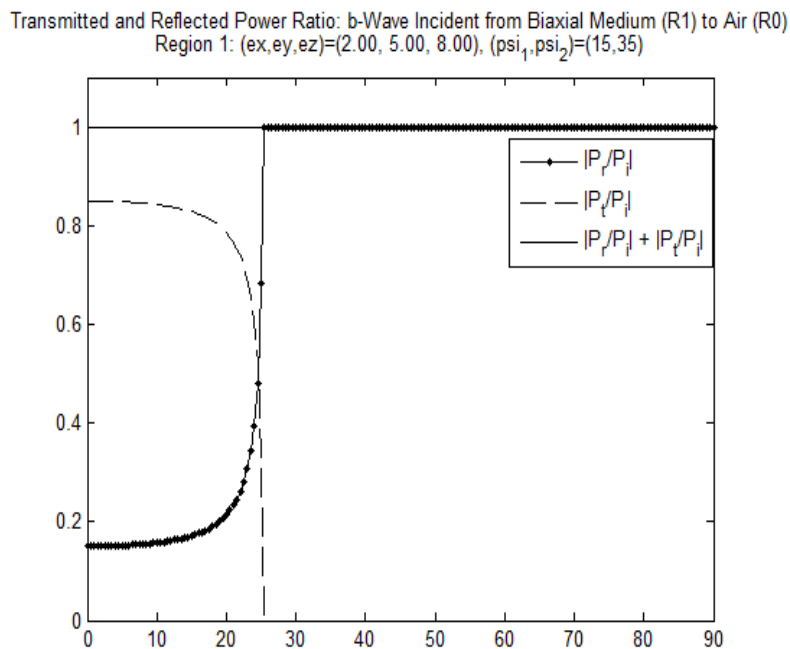


Figure 2-53: Transmitted and reflected power ratios for b-wave upward incident from rotated biaxial medium to air

2.2.2 Two Layer Coefficients

We can use the half-space coefficients derived previously to define two-layer coefficients. First, we use the half-space coefficients to define four half-space matrices. We note that in our derivation of half-space coefficients, we assumed all boundaries were at $z = 0$. However, for the two layer problem the second boundary (between region 1 and region 2) is located at $z = -h$. Therefore, a phase shift related to this z transformation will have to be added to the region 1 – region 2 coefficients. The resulting half-space matrices are given by

$$\overline{\overline{R}}_{01}^{(z=0)} = \begin{bmatrix} R_{hh}^{01} & R_{vh}^{01} \\ R_{hv}^{01} & R_{vv}^{01} \end{bmatrix} \quad (2.2.68)$$

$$\overline{\overline{X}}_{01}^{(z=0)} = \begin{bmatrix} X_{ha}^{01} & X_{va}^{01} \\ X_{hb}^{01} & X_{vb}^{01} \end{bmatrix} \quad (2.2.69)$$

$$\overline{\overline{X}}_{10}^{(z=0)} = \begin{bmatrix} X_{ah}^{01} & X_{bh}^{01} \\ X_{av}^{01} & X_{bv}^{01} \end{bmatrix} \quad (2.2.70)$$

$$\overline{\overline{R}}_{10}^{(z=0)} = \begin{bmatrix} R_{aa}^{10} & R_{ba}^{10} \\ R_{ab}^{10} & R_{bb}^{10} \end{bmatrix} \quad (2.2.71)$$

$$\overline{\overline{R}}_{12}^{(z=-h)} = \begin{bmatrix} R_{aa}^{12} e^{i(k_z^{au} - k_z^{ad})h} & R_{ba}^{12} e^{i(k_z^{au} - k_z^{bd})h} \\ R_{ab}^{12} e^{i(k_z^{bu} - k_z^{ad})h} & R_{bb}^{12} e^{i(k_z^{bu} - k_z^{bd})h} \end{bmatrix} \quad (2.2.72)$$

We define the upward and downward propagating waves in each region as Pettis did [1]. These waves are shown in Figure 2-54.

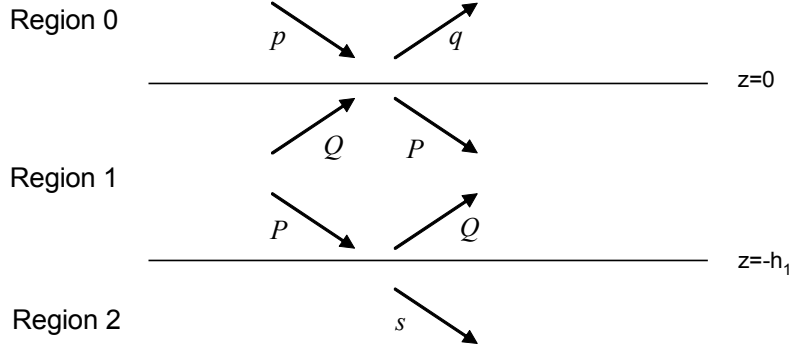


Figure 2-54: Incident, transmitted and reflected waves for two layer problem.

We want to describe all of our two-layer coefficients as if a downward wave is incident from region 0 (the p-wave). We can then write each remaining wave in terms of the half-space matrices in equations (2.2.68) through (2.2.72). The resulting equations are

$$q = \left[\bar{\bar{R}}_{01}^{(0)} + \bar{\bar{X}}_{10}^{(0)} \bar{\bar{R}}_{12}^{(-h)} \left[\bar{\bar{I}} - \bar{\bar{R}}_{10}^{(0)} \bar{\bar{R}}_{12}^{(-h)} \right]^{-1} \bar{\bar{X}}_{01}^{(0)} \right] p \quad (2.2.73)$$

$$P = \left[\bar{\bar{I}} - \bar{\bar{R}}_{10}^{(0)} \bar{\bar{R}}_{12}^{(-h)} \right]^{-1} \bar{\bar{X}}_{01}^{(0)} p \quad (2.2.74)$$

$$Q = \bar{\bar{R}}_{12}^{(-h)} \left[\bar{\bar{I}} - \bar{\bar{R}}_{10}^{(0)} \bar{\bar{R}}_{12}^{(-h)} \right]^{-1} \bar{\bar{X}}_{01}^{(0)} p \quad (2.2.75)$$

$$s = \bar{\bar{X}}_{12}^{(-h)} \left[\bar{\bar{I}} - \bar{\bar{R}}_{10}^{(0)} \bar{\bar{R}}_{12}^{(-h)} \right]^{-1} \bar{\bar{X}}_{01}^{(0)} p \quad (2.2.76)$$

We consider overall reflection and transmission coefficients for this geometry with the wave incident from region 0. From equation (2.2.73) we define the overall reflection coefficient as

$$R = \left[\bar{\bar{R}}_{01}^{(0)} + \bar{\bar{X}}_{10}^{(0)} \bar{\bar{R}}_{12}^{(-h)} \left[\bar{\bar{I}} - \bar{\bar{R}}_{10}^{(0)} \bar{\bar{R}}_{12}^{(-h)} \right]^{-1} \bar{\bar{X}}_{01}^{(0)} \right] \quad (2.2.77)$$

From equation (2.2.76) we define the overall transmission coefficient as

$$X = \bar{\bar{X}}_{12}^{(-h)} \left[\bar{\bar{I}} - \bar{\bar{R}}_{10}^{(0)} \bar{\bar{R}}_{12}^{(-h)} \right]^{-1} \bar{\bar{X}}_{01}^{(0)} \quad (2.2.78)$$

2.2.2.1 Evaluation of Two Layer Coefficients

In this section, we analyze the two-layer coefficient in the same manner as detailed in Section 2.2.1 for the half-space coefficients. The biaxial layer (region1) has a thickness of $0.4\lambda_0$ (where λ_0 is the free-space wavelength) and is situated between two isotropic regions both with permittivity and permeability of ϵ_0 and μ_0 respectively (air). In this analysis the biaxial medium has permittivity given by

$$\underline{\underline{\epsilon}}_r = \begin{bmatrix} 3 & & \\ & 4 & \\ & & 5 \end{bmatrix} \quad (2.2.79)$$

The first case we consider is the unrotated case in the x - z plane ($\varphi=0^\circ$). The two layer reflection and transmission coefficients are shown in Figure 2-55. The co-polarized reflection coefficients show that for all incident angles, the horizontal polarization is reflected more strongly, as is normally observed at an isotropic boundary. This is the same behavior discussed (but not shown) at the isotropic-biaxial half-space interface when the wave is incident from the x - z plane. The cross-polarized reflection coefficients are approximately zero. Therefore, we observe similar behavior at the two-layer interface, with a different biaxial permittivity tensor, as we did in the half-space case. We also see that the vertically polarized wave undergoes zero reflection at the Brewster angle of 57.5° . Figure 2-55 also shows the calculated transmission coefficients. The co-polarized transmission coefficients have an inverse relationship to the reflection coefficients. We also see that the cross polarized transmission coefficients are also approximately zero. Once again, this is the same type of behavior observed in the half-space analysis where the a-wave acted as if it were co-polarized with the horizontal polarization and the b-wave co-polarized with the vertical polarization. Finally, as a means of verifying our

results we compute the power reflection and transmission coefficients to prove that power is conserved. Figure 2-56 verifies that the sum of the two coefficients is one, proving that power is conserved and the calculated coefficients are verified.

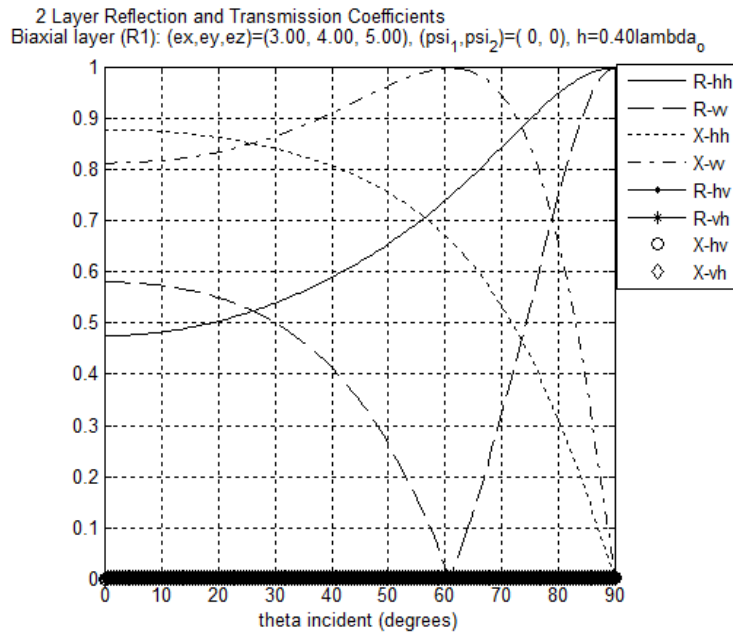


Figure 2-55: Two-layer coefficients for wave incident from the isotropic medium unrotated biaxial substrate

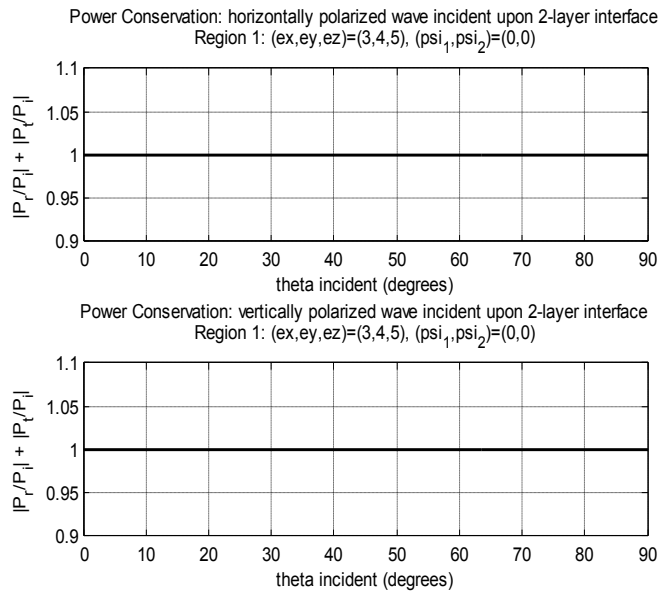


Figure 2-56: Power conservation for two-layer system

Once again we rotate the biaxial medium and observe the changes to the reflection and transmission coefficients. In this case, we consider the same phenomena when region 1 is rotated by $\psi_1 = 30^\circ$ and $\psi_2 = 75^\circ$. Given this new biaxial medium, we first look at the co-polarized reflection coefficients shown in Figure 2-57. We observe that when the permittivity tensor is rotated, the vertically polarized wave is reflected more strongly than the horizontally polarized wave for small incident angles and that this behavior is reversed for larger incident angles. This behavior was discussed in the half-space problem where we observed this behavior with a rotation of 45° or more around the z -axis (ψ_2). Also, there is no true Brewster angle. The vertically polarized reflection coefficient has a minimum around 61° but does not go to zero. This is true in general of 2-layer problems. The co-polarized transmission coefficients have an inverse relationship to the co-polarized reflection coefficients. We also can see in Figure 2-58 that cross-polarized coefficients are non-zero. Note that the transmission coefficients overlap.

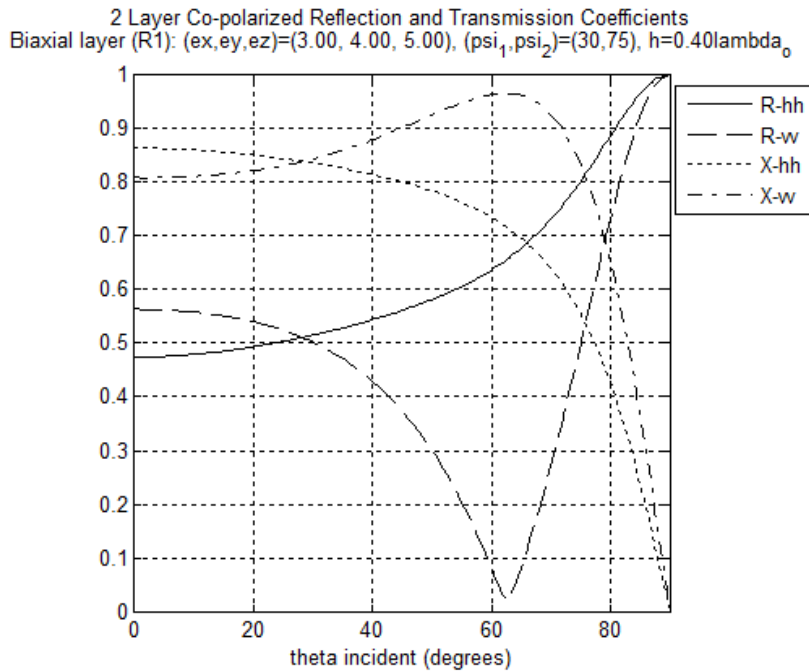


Figure 2-57: Two-layer co-polarized reflection coefficients for wave incident from the isotropic medium (region 0); rotated biaxial substrate $(\psi_1, \psi_2) = (30^\circ, 75^\circ)$

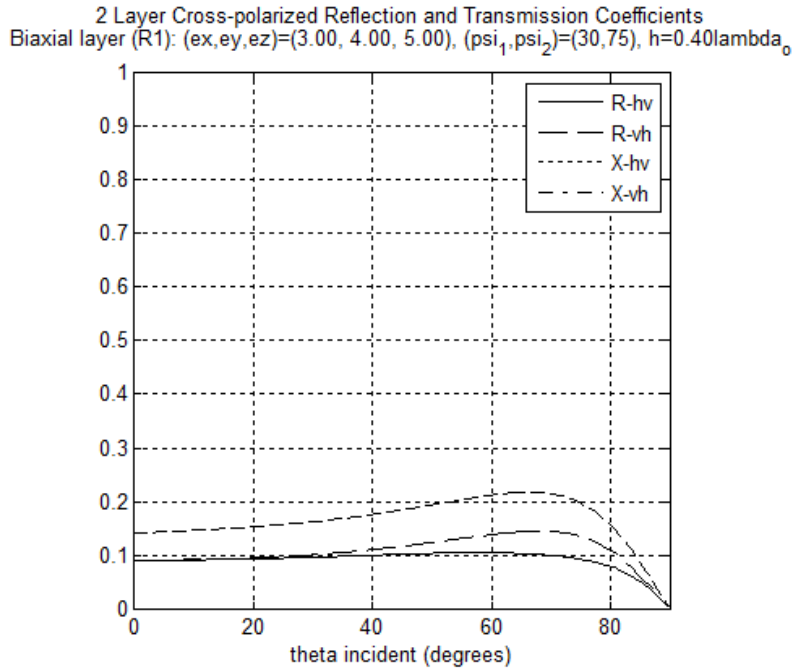


Figure 2-58: Two-layer cross-polarized reflection coefficients for wave incident from the isotropic medium (region 0); rotated biaxial substrate $(\psi_1, \psi_2) = (30^\circ, 75^\circ)$

The two-layer reflection and transmission analysis is not complete unless we analyze the effect of thickness (or height) of the biaxial layer. We consider the same unrotated biaxial medium with results shown in Figure 2-55, this time with thicknesses of $0.02\lambda_0$ and $1.2\lambda_0$. First, we consider the case of the very thin substrate (thickness is very small, $0.02\lambda_0$). The vertically polarized reflection coefficient (R_{vv}) is always less than the horizontally polarized coefficient (R_{hh}). The Brewster angle is the same as it was when the layer was $0.4\lambda_0$ thick (57.5°). The transmission coefficients are nearly 1 for low angles and zero for large incident angles and the cross-polarized coefficients are all approximately zero.

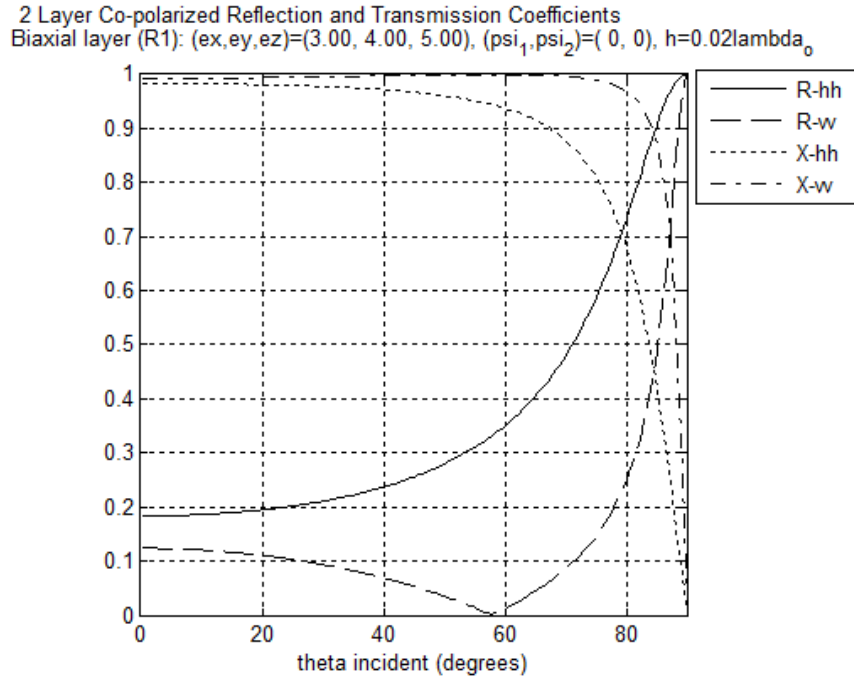


Figure 2-59: Two-layer co-polarized reflection coefficients for wave incident from the isotropic medium (region 0) with biaxial substrate height of $0.02\lambda_0$

When substrate is very thick ($1.2\lambda_0$) the vertically polarized reflection coefficient (R_{vv}) is still always less than the horizontally polarized coefficient (R_{hh}) and the cross-polarized coefficients are still nearly zero. Interestingly with this thick layer, we see what looks like two Brewster angles. One is at approximately the same angle observed at other thicknesses (57.5°), but there is another Brewster angle at 37.5° . This behavior is primarily due to the thickness of the layer as it may be observed when a thick middle layer is isotropic.

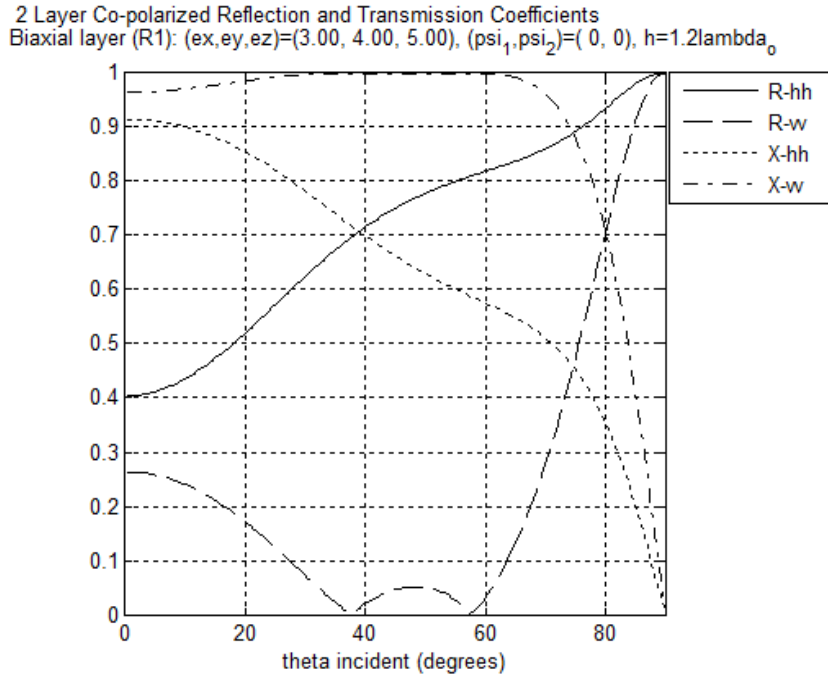


Figure 2-60: Two-layer co-polarized reflection coefficients for wave incident from the isotropic medium (region 0) with biaxial substrate height of $1.2\lambda_0$

For completeness, we also want to consider the effect of varying the height of the biaxial layer when the medium is rotated. The results are shown in Figure 2-61. For all three heights, the cross-polarized reflection and transmission coefficients are significantly larger than in the unrotated case. As the height increases, these cross-polarized coefficients increase and may be greater than the co-polarized terms when the height is $1.2\lambda_0$. Not only do the cross-pol terms increase, but the minimum reflection coefficient for the vertically polarized wave is not zero. Finally, we observe that when the height of the anisotropic layer is $1.2\lambda_0$, both the horizontally and vertically polarized waves experience a type of Brewster angle effect.

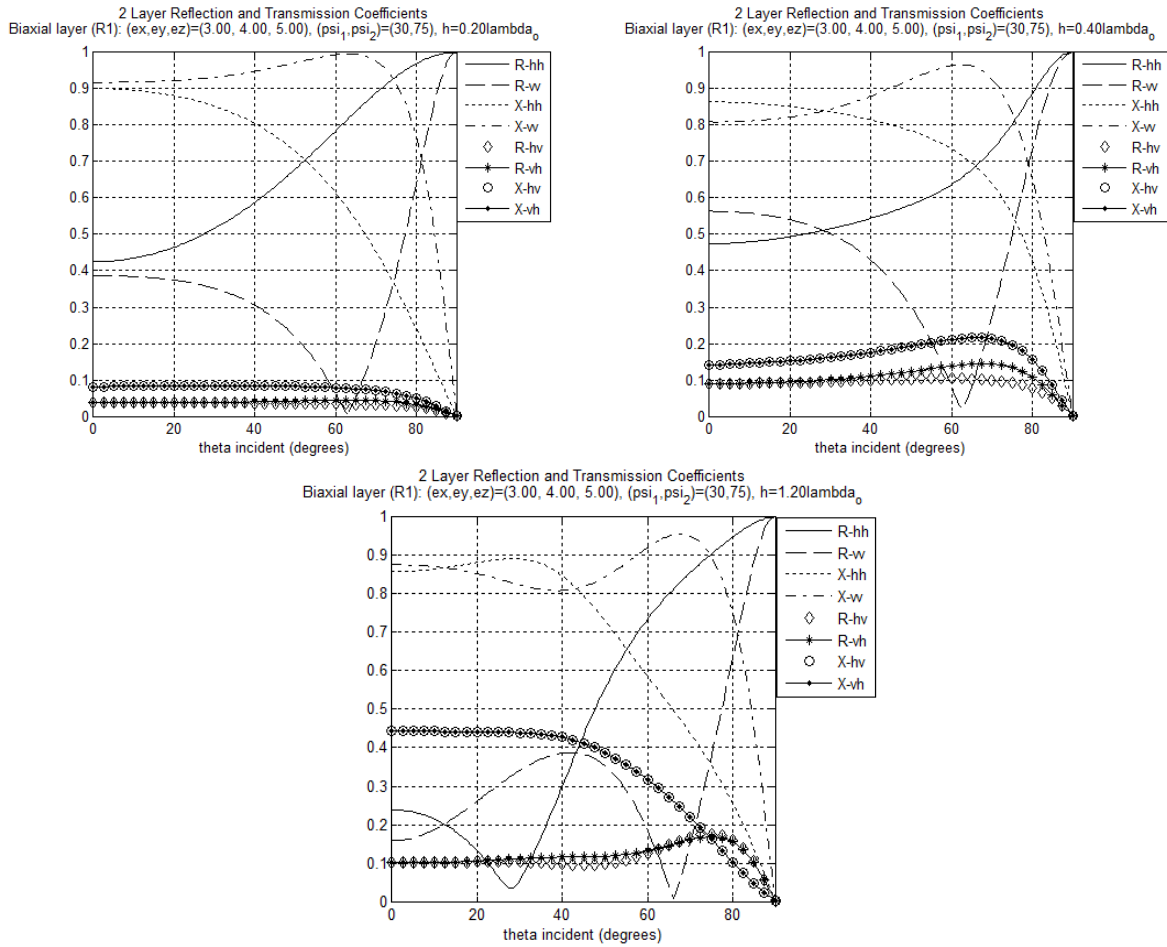


Figure 2-61: Two-layer co-polarized reflection coefficients for wave incident from the isotropic medium (region 0) with rotated biaxial substrates of varying heights

3 EIGENVECTOR DYADIC GREEN'S FUNCTION

In this work, we will be using the eigenvector dyadic Green's function (E-DGF) to compute the electric fields generated by a current in the presence of a biaxially anisotropic medium. Pettis used the transition matrix dyadic Green's function (T-DGF). There are benefits to using each and we have chosen the E-DGF for two reasons. First, the E-DGF is more general than the T-DGF. Once formulated, the source can be located anywhere within the specified region whereas the T-DGF requires that the source be placed on a boundary surface. This is a powerful property of the E-DGF. For example, the E-DGF can handle a z-directed source that extends through the entire region which allows us to model a coaxial probe feed. The T-DGF would not be able to handle this source as the current is (1) not tangential to the boundary and (2) exists within the layer, not solely on the surface. Further, the E-DGF applies to the solution of a stripline problem since the source may be embedded in the substrate. If using the T-DGF, one would have to re-formulate a stripline problem with another layer. The second reason for using the E-DGF formulation (as discussed in the next section) is that it is rooted in the fundamental physical properties of the problem. It is based on half-space or two-layer reflection coefficients and the electric field vectors (eigenvectors) of the media. Understanding the E-DGF provides greater insight into the physical behavior of the waves generated in and around the biaxial medium.

3.1 Formulation of Dyadic Green's Functions

In this work, we propose to use the eigenvector dyadic Green's function (E-DGF) to compute electric field quantities. Lee and Kong [33] derived the unbounded eigenvector dyadic Green's function (E-DGF) for uniaxial media. Based on this work, Mudaliar and Lee [34]

formulated of the E-DGF for unbounded and two-layer biaxial geometries. In this work, we use the two-layer Green's function from [34] and have adopted the layer conventions from the Mudaliar and Lee paper: region 0 is the isotropic medium above the biaxial layer, region 1 is the biaxial medium, and region 2 is another isotropic region below the biaxial layer. This two-layer geometry is shown in Figure 3-1.

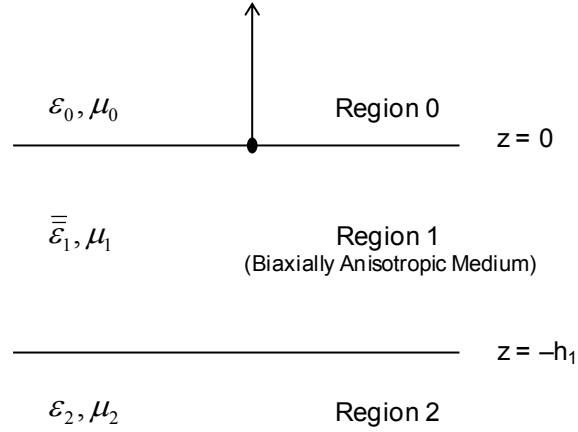


Figure 3-1: Two layer geometry used in Green's function formulation

Given this geometry, the E-DGF equations for a source in region 0 are [34]

$$\overline{\overline{G}}_e^{(0,0)}(\vec{r}, \vec{r}') = \frac{i}{8\pi^2} \int_{-\infty}^{\infty} d^2\vec{k}_\rho \frac{1}{k_{0z}} e^{-i\vec{k}_0 \cdot \vec{r}'} \left\{ \begin{aligned} & \left[\hat{h}_0^- e^{i\vec{k}_0 \cdot \vec{r}} + R_{hh} \hat{h}_0^+ e^{i\vec{k}_0 \cdot \vec{r}} + R_{hv} \hat{v}_0^+ e^{i\vec{k}_0 \cdot \vec{r}} \right] \hat{h}_0^- \\ & + \left[\hat{v}_0^- e^{i\vec{k}_0 \cdot \vec{r}} + R_{vh} \hat{h}_0^+ e^{i\vec{k}_0 \cdot \vec{r}} + R_{vv} \hat{v}_0^+ e^{i\vec{k}_0 \cdot \vec{r}} \right] \hat{v}_0^- \end{aligned} \right\}, \quad (3.1.1)$$

$$0 < z < z'$$

$$\overline{\overline{G}}_e^{(1,0)}(\vec{r}, \vec{r}') = \frac{i}{8\pi^2} \int_{-\infty}^{\infty} d^2\vec{k}_\rho \frac{1}{k_{0z}} e^{-i\vec{k}_0 \cdot \vec{r}'} \left\{ \begin{aligned} & \left[A_{ha} \hat{a}^- e^{i\vec{k}_1^a \cdot \vec{r}} + B_{ha} \hat{a}^+ e^{i\vec{k}_1^a \cdot \vec{r}} + A_{hb} \hat{b}^- e^{i\vec{k}_1^b \cdot \vec{r}} + B_{hb} \hat{b}^+ e^{i\vec{k}_1^b \cdot \vec{r}} \right] \hat{h}_0^- \\ & + \left[A_{va} \hat{a}^- e^{i\vec{k}_1^a \cdot \vec{r}} + B_{va} \hat{a}^+ e^{i\vec{k}_1^a \cdot \vec{r}} + A_{vb} \hat{b}^- e^{i\vec{k}_1^b \cdot \vec{r}} + B_{vb} \hat{b}^+ e^{i\vec{k}_1^b \cdot \vec{r}} \right] \hat{v}_0^- \end{aligned} \right\}, \quad (3.1.2)$$

$$-h_1 < z < 0$$

$$\overline{\overline{G}}_e^{(2,0)}(\vec{r}, \vec{r}') = \frac{i}{8\pi^2} \int_{-\infty}^{\infty} d^2\vec{k}_\rho \frac{1}{k_{0z}} e^{-i\vec{k}_0 \cdot \vec{r}'} \left\{ \begin{array}{l} [X_{hh}\hat{h}_2^- e^{i\vec{k}_2 \cdot \vec{r}} + X_{hv}\hat{v}_2^- e^{i\vec{k}_2 \cdot \vec{r}}] \hat{h}_0^- \\ + [X_{vh}\hat{h}_2^- e^{i\vec{k}_2 \cdot \vec{r}} + X_{vv}\hat{v}_2^- e^{i\vec{k}_2 \cdot \vec{r}}] \hat{v}_0^- \end{array} \right\}, \quad (3.1.3)$$

z < -h₁

Equations (3.1.1) through (3.1.3) depend on the propagation vectors (discussed in Section 2.1.1), the two layer reflection and transmission coefficients (R_{ij} , X_{ij} , A_{ij} , and B_{ij}), and the electric field unit vectors (discussed in Section 2.1.2). The two layer coefficients come from equations (2.2.73) through (2.2.76). For example, the matrix multiplier in equation (2.2.73) gives us R_{ij} . Similarly, the A matrix comes from equation (2.2.74); the B matrix from (2.2.75)

and the X matrix from (2.2.76). Note that $\int_{-\infty}^{\infty} d^2\vec{k}_\rho = \int_{-\infty}^{\infty} \int_{-\infty}^{\infty} dk_x dk_y$.

3.2 Symmetrical Property of Dyadic Green's Function

When solving new electromagnetic problems using dyadic Green's function (DGF) techniques, we often do not have the appropriate Green's functions at our disposal. This is true in our case as only three of the nine possible E-DGFs have been solved. We know the E-DGF to compute the field in region 1 given a source in region 0. However, to study antenna problems of interest, we would like to know the field in region 0 given a source in region 1. Fortunately, we can utilize the symmetric property of the DGF to transform a known Green's function into the Green's function needed to solve the problem. First, we will derive the symmetric property of the DGF. We will then use this property to derive the Green's function needed.

C. T. Tai [37] derived symmetrical property of dyadic Green's Function (DGF) for free space problems, half-space problems and bounded half-space problems including conductor backed dielectric applications. He did not consider the general 2-layer problem or anisotropic

materials (all materials were assumed isotropic). J. K. Lee [38] considered this case and derived the symmetrical property of the DGF for the 2-layer problem with an anisotropic medium in the middle layer, which we rederive here. First, we define the inhomogeneous wave equations for DGFs given a source in each region. Next, we apply electromagnetic boundary conditions at each interface then generate suitable integrals via application of the dyadic-dyadic Green's theorem of the second kind. Finally, the resulting integrals are simplified using distribution theory and appropriate vector identities in order to derive the desired symmetry relation for the dyadic Green's function.

First, we define inhomogeneous wave equations for the Green's functions for a source in region 0 as

$$\begin{aligned}
\nabla \times \nabla \times \overline{\overline{G}}^{(0,0)}(\vec{r}, \vec{r}_0) - \omega^2 \mu_0 \varepsilon_0 \overline{\overline{G}}^{(0,0)}(\vec{r}, \vec{r}_0) &= \overline{\overline{I}} \delta(\vec{r} - \vec{r}_0), & z \geq 0 \\
\nabla \times \nabla \times \overline{\overline{G}}^{(1,0)}(\vec{r}, \vec{r}_0) - \omega^2 \mu_1 \varepsilon_1 \overline{\overline{G}}^{(1,0)}(\vec{r}, \vec{r}_0) &= 0, & -h_1 \leq z \leq 0 \\
\nabla \times \nabla \times \overline{\overline{G}}^{(2,0)}(\vec{r}, \vec{r}_0) - \omega^2 \mu_2 \varepsilon_2 \overline{\overline{G}}^{(2,0)}(\vec{r}, \vec{r}_0) &= 0, & z \leq -h_1
\end{aligned} \tag{3.2.1}$$

where the first numerical superscript on the DGF denotes the field region and the second numerical superscript is the source region. Similarly, the inhomogeneous wave equations for Green's functions with source in region 1 are given by

$$\begin{aligned}
\nabla \times \nabla \times \overline{\overline{G}}^{(0,1)}(\vec{r}, \vec{r}_1) - \omega^2 \mu_0 \varepsilon_0 \overline{\overline{G}}^{(0,1)}(\vec{r}, \vec{r}_1) &= 0, & z \geq 0 \\
\nabla \times \nabla \times \overline{\overline{G}}^{(1,1)}(\vec{r}, \vec{r}_1) - \omega^2 \mu_1 \varepsilon_1 \overline{\overline{G}}^{(1,1)}(\vec{r}, \vec{r}_1) &= \overline{\overline{I}} \delta(\vec{r} - \vec{r}_1), & -h_1 \leq z \leq 0 \\
\nabla \times \nabla \times \overline{\overline{G}}^{(2,1)}(\vec{r}, \vec{r}_1) - \omega^2 \mu_2 \varepsilon_2 \overline{\overline{G}}^{(2,1)}(\vec{r}, \vec{r}_1) &= 0, & z \leq -h_1
\end{aligned} \tag{3.2.2}$$

Next, we define electromagnetic boundary conditions in terms of the dyadic Green's functions. We will apply the boundary conditions at $z = 0$ which relates the tangential field components to a source in region 0 by

$$\begin{aligned}\hat{z} \times \overline{\overline{G}}^{(0,0)}(\vec{r}, \vec{r}_0) &= \hat{z} \times \overline{\overline{G}}^{(1,0)}(\vec{r}, \vec{r}_0) \\ \hat{z} \times \frac{1}{\mu_0} \nabla \times \overline{\overline{G}}^{(0,0)}(\vec{r}, \vec{r}_0) &= \hat{z} \times \frac{1}{\mu_1} \nabla \times \overline{\overline{G}}^{(1,0)}(\vec{r}, \vec{r}_0)\end{aligned}\quad (3.2.3)$$

If the source is in region 1 the boundary conditions can be written as

$$\begin{aligned}\hat{z} \times \overline{\overline{G}}^{(0,1)}(\vec{r}, \vec{r}_1) &= \hat{z} \times \overline{\overline{G}}^{(1,1)}(\vec{r}, \vec{r}_1) \\ \hat{z} \times \frac{1}{\mu_0} \nabla \times \overline{\overline{G}}^{(0,1)}(\vec{r}, \vec{r}_1) &= \hat{z} \times \frac{1}{\mu_1} \nabla \times \overline{\overline{G}}^{(1,1)}(\vec{r}, \vec{r}_1)\end{aligned}\quad (3.2.4)$$

Next, we want to relate the Green's functions for a source in region 0 to the Green's functions for a source in region 1. We will do that via the application of the vector Green's theorem. To generate integrals via application of the vector Green's theorem we need to define a set of vector functions in each region. We define the vectors as

$$\begin{aligned}\overline{P}_0 &= \overline{\overline{G}}^{(0,0)}(\vec{r}, \vec{r}_0) \cdot \vec{a} \\ \overline{Q}_0 &= \overline{\overline{G}}^{(0,1)}(\vec{r}, \vec{r}_1) \cdot \vec{b}\end{aligned}\quad (3.2.5)$$

$$\begin{aligned}\overline{P}_1 &= \overline{\overline{G}}^{(1,0)}(\vec{r}, \vec{r}_0) \cdot \vec{a} \\ \overline{Q}_1 &= \overline{\overline{G}}^{(1,1)}(\vec{r}, \vec{r}_1) \cdot \vec{b}\end{aligned}\quad (3.2.6)$$

$$\begin{aligned}\overline{P}_2 &= \overline{\overline{G}}^{(2,0)}(\vec{r}, \vec{r}_0) \cdot \vec{a} \\ \overline{Q}_2 &= \overline{\overline{G}}^{(2,1)}(\vec{r}, \vec{r}_1) \cdot \vec{b}\end{aligned}\quad (3.2.7)$$

where \vec{a} and \vec{b} are arbitrary point source vectors, in region 0 and 1 respectively, post-multiplying the dyadic Green's functions. Vectors \overline{P}_i and \overline{Q}_i are the resulting vectors in each

region from this post multiplication. We now apply the vector Green's theorem to each set of two functions resulting in

$$\iiint_V [\bar{P}_i \cdot \nabla \times \nabla \times \bar{Q}_i - \bar{Q}_i \cdot \nabla \times \nabla \times \bar{P}_i] dV = \oiint_S (\bar{Q}_i \times \nabla \times \bar{P}_i - \bar{P}_i \times \nabla \times \bar{Q}_i) \cdot d\bar{s} \quad i = 0,1,2 \quad (3.2.8)$$

The volume refers to the region in which the field exists (denoted by subscript i) and the closed surface is the surface bounding that volume. We apply the integral to all three sets of vector relationships. We then simplify the integrals using common vector identities and the boundary conditions defined in (3.2.3) and (3.2.4) to show

$$\bar{a} \cdot \frac{1}{\mu_0} \bar{G}^{(0,1)}(\bar{r}_0, \bar{r}_1) \cdot \bar{b} = \bar{b} \cdot \frac{1}{\mu_1} \bar{G}^{(1,0)}(\bar{r}_1, \bar{r}_0) \cdot \bar{a} \quad (3.2.9)$$

This relationship in (3.2.9) must hold for any arbitrary vectors \bar{a} and \bar{b} . If this condition holds, then

$$\frac{1}{\mu_0} \bar{G}^{(0,1)}(\bar{r}_0, \bar{r}_1) = \frac{1}{\mu_1} [\bar{G}^{(1,0)}(\bar{r}_1, \bar{r}_0)]^T \quad (3.2.10)$$

Equation (3.2.10) is the symmetrical property of the dyadic Green's function for 2-layer anisotropic geometry. If all media are non-magnetic then

$$\bar{G}^{(0,1)}(\bar{r}_0, \bar{r}_1) = [\bar{G}^{(1,0)}(\bar{r}_1, \bar{r}_0)]^T \quad (3.2.11)$$

In this derivation, the most critical assumption is that the anisotropic medium is reciprocal. Consider some general bianisotropic medium whose fields are related by

$$\begin{aligned} \bar{D} &= \bar{\epsilon} \cdot \bar{E} + \bar{\xi} \cdot \bar{H} \\ \bar{B} &= \bar{\mu} \cdot \bar{H} + \bar{\zeta} \cdot \bar{E} \end{aligned} \quad (3.2.12)$$

Kong [2] defines the medium as reciprocal if

$$\begin{aligned}
\bar{\bar{\epsilon}} &= \bar{\bar{\epsilon}}^T \\
\bar{\bar{\mu}} &= \bar{\bar{\mu}}^T \\
\bar{\bar{\zeta}} &= -\bar{\bar{\zeta}}^T
\end{aligned} \tag{3.2.13}$$

We considered an electrically anisotropic medium (condition 1). In general, for the symmetric property of the DGF to hold, the medium should be reciprocal. Uniaxial and biaxial media are reciprocal, so we can use this property for our purposes. However, gyrotropic media are not reciprocal so an alternate form of the symmetrical property would need to be derived. We are not handling gyrotropic media here, so this alternate form is not needed.

3.2.1 Application of Symmetrical Property of DGF

We are interested in computing the electric fields in region 0 given a source in region 1. In (3.1.2), we have the eigenvector dyadic Green's function for the field in region 1 given a source in region 0. We can apply the symmetrical property of the DGF from equation (3.2.10) to obtain the required Green's function.

We begin by taking the DGF in equation (3.1.2) and placing the unprimed (field) position vector (\bar{r}) in region 1 and the primed (source) position vector (\bar{r}') in region 0. This manipulation results in

$$\begin{aligned}
\bar{\bar{G}}_e^{(1,0)}(\bar{r}_1, \bar{r}'_0) = & \\
\frac{i}{8\pi^2} \int_{-\infty}^{\infty} d^2\bar{k}_\rho \frac{1}{k_{0z}} e^{-i\bar{k}_0 \cdot \bar{r}'_0} & \left\{ \begin{aligned} & \left[A_{ha} \hat{a}^- e^{i\bar{k}_1^a \cdot \bar{r}_1} + B_{ha} \hat{a}^+ e^{i\bar{k}_1^a \cdot \bar{r}_1} + A_{hb} \hat{b}^- e^{i\bar{k}_1^b \cdot \bar{r}_1} + B_{hb} \hat{b}^+ e^{i\bar{k}_1^b \cdot \bar{r}_1} \right] \hat{h}_0^- \\ & + \left[A_{va} \hat{a}^- e^{i\bar{k}_1^a \cdot \bar{r}_1} + B_{va} \hat{a}^+ e^{i\bar{k}_1^a \cdot \bar{r}_1} + A_{vb} \hat{b}^- e^{i\bar{k}_1^b \cdot \bar{r}_1} + B_{vb} \hat{b}^+ e^{i\bar{k}_1^b \cdot \bar{r}_1} \right] \hat{v}_0^- \end{aligned} \right\} \tag{3.2.14}
\end{aligned}$$

where $\int_{-\infty}^{\infty} d^2\bar{k}_\rho = \int_{-\infty}^{\infty} \int_{-\infty}^{\infty} dk_x dk_y$. Now, we must take the transpose of (3.2.14)

$$\begin{aligned} \left[\overline{\overline{G}}_e^{(1,0)}(\vec{r}_1, \vec{r}_0) \right]^T = \\ \frac{i}{8\pi^2} \int_{-\infty}^{\infty} d^2 \bar{k}_\rho \frac{1}{k_{0z}} e^{-i\bar{k}_0 \cdot \vec{r}_0} \left\{ \hat{h}_0^- \left[A_{ha} \hat{a}^- e^{i\bar{k}_1^a \cdot \vec{r}_1} + B_{ha} \hat{a}^+ e^{i\bar{k}_1^a \cdot \vec{r}_1} + A_{hb} \hat{b}^- e^{i\bar{k}_1^b \cdot \vec{r}_1} + B_{hb} \hat{b}^+ e^{i\bar{k}_1^b \cdot \vec{r}_1} \right] \right. \\ \left. + \hat{v}_0^- \left[A_{va} \hat{a}^- e^{i\bar{k}_1^a \cdot \vec{r}_1} + B_{va} \hat{a}^+ e^{i\bar{k}_1^a \cdot \vec{r}_1} + A_{vb} \hat{b}^- e^{i\bar{k}_1^b \cdot \vec{r}_1} + B_{vb} \hat{b}^+ e^{i\bar{k}_1^b \cdot \vec{r}_1} \right] \right\} \end{aligned} \quad (3.2.15)$$

From equation (3.2.10), we know that this gives us the eigenvector dyadic Green's function for the field in region 0 given a source in region 1. Using our primed and unprimed notation for source and field regions, respectively, equation (3.2.15) can be written as

$$\begin{aligned} \overline{\overline{G}}_e^{(0,1)}(\vec{r}, \vec{r}') = \\ \frac{i}{8\pi^2} \int_{-\infty}^{\infty} d^2 \bar{k}_\rho \frac{1}{k_{0z}} e^{-i\bar{k}_0 \cdot \vec{r}} \left\{ \hat{h}_0^- \left[A_{ha} \hat{a}^- e^{i\bar{k}_1^a \cdot \vec{r}'} + B_{ha} \hat{a}^+ e^{i\bar{k}_1^a \cdot \vec{r}'} + A_{hb} \hat{b}^- e^{i\bar{k}_1^b \cdot \vec{r}'} + B_{hb} \hat{b}^+ e^{i\bar{k}_1^b \cdot \vec{r}'} \right] \right. \\ \left. + \hat{v}_0^- \left[A_{va} \hat{a}^- e^{i\bar{k}_1^a \cdot \vec{r}'} + B_{va} \hat{a}^+ e^{i\bar{k}_1^a \cdot \vec{r}'} + A_{vb} \hat{b}^- e^{i\bar{k}_1^b \cdot \vec{r}'} + B_{vb} \hat{b}^+ e^{i\bar{k}_1^b \cdot \vec{r}'} \right] \right\} \end{aligned} \quad (3.2.16)$$

This form is mathematically correct; however, it is not physically meaningful. The source in region 1 would generate an upward propagating field in region 0, but in this form we have a downward propagating wave in that isotropic region. To write (3.2.16) in a more physically meaningful form we make the change of variables

$$\begin{aligned} k_x &\rightarrow -k_x \\ k_y &\rightarrow -k_y \\ d\bar{k}_\rho &= dk_x dk_y \rightarrow (-dk_x)(-dk_y) = d\bar{k}_\rho \end{aligned} \quad (3.2.17)$$

In his thesis Pettis [1, Appendix M] derived relationships for the electric field vectors and the propagation vectors under the same change of variables. The electric field vectors in region 0 are given by

$$\begin{aligned} \hat{h}_0^-(-k_x, -k_y) &= -\hat{h}_0^+(k_x, k_y) \\ \hat{v}_0^-(-k_x, -k_y) &= \hat{v}_0^+(k_x, k_y) \end{aligned} \quad (3.2.18)$$

Under the same change of variables, the electric field vectors in region 1 are given by

$$\begin{aligned}
\hat{a}^-(-k_x, -k_y) &= -\hat{a}^+(k_x, k_y) \\
\hat{a}^+(-k_x, -k_y) &= -\hat{a}^-(k_x, k_y) \\
\hat{b}^-(-k_x, -k_y) &= \hat{b}^+(k_x, k_y) \\
\hat{b}^+(-k_x, -k_y) &= \hat{b}^-(k_x, k_y)
\end{aligned} \tag{3.2.19}$$

Finally, the propagation vectors can simply be rewritten

$$\begin{aligned}
\bar{k}_0(-k_x, -k_y) &= -k_x \hat{x} - k_y \hat{y} + k_{0z} \hat{z} = -\bar{k}_0(k_x, k_y) \\
\bar{k}_0(-k_x, -k_y) &= -k_x \hat{x} - k_y \hat{y} - k_{0z} \hat{z} = -\bar{k}_0(k_x, k_y) \\
\bar{k}_1^j(-k_x, -k_y) &= -k_x \hat{x} - k_y \hat{y} + k_{1z}^{ju}(-k_x, -k_y) \hat{z} = -\bar{k}_1^j(k_x, k_y), \quad j = a, b \\
\bar{k}_1^j(-k_x, -k_y) &= -k_x \hat{x} - k_y \hat{y} + k_{1z}^{jd}(-k_x, -k_y) \hat{z} = -\bar{k}_1^j(k_x, k_y), \quad j = a, b
\end{aligned} \tag{3.2.20}$$

where the superscript j indicates whether the a- or b-wave is propagating in region 1. The relationships shown in equation (3.2.20) were confirmed numerically for several biaxial tensors under multiple rotations. Making all of the substitutions related to the k_x and k_y change of variables into equation (3.2.16) results in

$$\begin{aligned}
\bar{\bar{G}}_e^{(0,1)}(\bar{r}, \bar{r}') &= \frac{i}{8\pi^2} \int_{-\infty}^{\infty} d^2 \bar{k}_\rho \frac{1}{k_{0z}} e^{i\bar{k}_0 \cdot \bar{r}} \\
&\left\{ -\hat{h}_0^+ \left[-A_{ha}(-k_x, -k_y) \hat{a}^+ e^{-i\bar{k}_1^a \cdot \bar{r}'} - B_{ha}(-k_x, -k_y) \hat{a}^- e^{-i\bar{k}_1^a \cdot \bar{r}'} + A_{hb}(-k_x, -k_y) \hat{b}^+ e^{-i\bar{k}_1^b \cdot \bar{r}'} + B_{hb}(-k_x, -k_y) \hat{b}^- e^{-i\bar{k}_1^b \cdot \bar{r}'} \right] \right. \\
&\left. + \hat{v}_0^+ \left[-A_{va}(-k_x, -k_y) \hat{a}^+ e^{-i\bar{k}_1^a \cdot \bar{r}'} - B_{va}(-k_x, -k_y) \hat{a}^- e^{-i\bar{k}_1^a \cdot \bar{r}'} + A_{vb}(-k_x, -k_y) \hat{b}^+ e^{-i\bar{k}_1^b \cdot \bar{r}'} + B_{vb}(-k_x, -k_y) \hat{b}^- e^{-i\bar{k}_1^b \cdot \bar{r}'} \right] \right\}
\end{aligned} \tag{3.2.21}$$

If we rearrange the terms

$$\begin{aligned} \overline{\overline{G}}_e^{(0,1)}(\vec{r}, \vec{r}') = \frac{i}{8\pi^2} \int_{-\infty}^{\infty} d^2 \bar{k}_\rho \frac{1}{k_{0z}} e^{i\bar{k}_0 \cdot \vec{r}} \\ \left\{ \begin{aligned} & \left[A_{ha}(-k_x, -k_y) \hat{h}_0^+ - A_{va}(-k_x, -k_y) \hat{v}_0^+ \right] \hat{a}^+ e^{-i\bar{k}_1^a \cdot \vec{r}'} \\ & + \left[B_{ha}(-k_x, -k_y) \hat{h}_0^+ - B_{va}(-k_x, -k_y) \hat{v}_0^+ \right] \hat{a}^- e^{-i\bar{k}_1^a \cdot \vec{r}'} \\ & + \left[-A_{hb}(-k_x, -k_y) \hat{h}_0^+ + A_{vb}(-k_x, -k_y) \hat{v}_0^+ \right] \hat{b}^+ e^{-i\bar{k}_1^b \cdot \vec{r}'} \\ & + \left[-B_{hb}(-k_x, -k_y) \hat{h}_0^+ + B_{vb}(-k_x, -k_y) \hat{v}_0^+ \right] \hat{b}^- e^{-i\bar{k}_1^b \cdot \vec{r}'} \end{aligned} \right\} \end{aligned} \quad (3.2.22)$$

The equation is nearly consistent with the physics of a source in region 1. The only additional manipulation involves simplifying the coefficients A and B and making the notation consistent with conventions previously used. We define a set of primed coefficients (as did Pettis [1]) as

$$\begin{aligned} A_{ha}(-k_x, -k_y) &= A'_{ah}(k_x, k_y) & A_{va}(-k_x, -k_y) &= -A'_{av}(k_x, k_y) \\ B_{ha}(-k_x, -k_y) &= B'_{ah}(k_x, k_y) & B_{va}(-k_x, -k_y) &= -B'_{av}(k_x, k_y) \\ A_{hb}(-k_x, -k_y) &= -A'_{bh}(k_x, k_y) & A_{vb}(-k_x, -k_y) &= A'_{bv}(k_x, k_y) \\ B_{hb}(-k_x, -k_y) &= -B'_{bh}(k_x, k_y) & B_{vb}(-k_x, -k_y) &= B'_{bv}(k_x, k_y) \end{aligned} \quad (3.2.23)$$

These new coefficients are then substituted into the Green's function in equation (3.2.22). The result is a Green's function for computing electric fields in the isotropic region 0 when a source is in region 1 in a physically meaningful form; this form is given by

$$\begin{aligned} \overline{\overline{G}}_e^{(0,1)}(\vec{r}, \vec{r}') = \frac{i}{8\pi^2} \int_{-\infty}^{\infty} d^2 \bar{k}_\rho \frac{1}{k_{0z}} \left\{ \begin{aligned} & \left[A'_{ah}(k_x, k_y) \hat{h}_0^+ e^{i\bar{k}_0 \cdot \vec{r}} + A'_{av}(k_x, k_y) \hat{v}_0^- e^{i\bar{k}_0 \cdot \vec{r}} \right] \hat{a}^+ e^{-i\bar{k}_1^a \cdot \vec{r}'} \\ & + \left[B'_{ah}(k_x, k_y) \hat{h}_0^+ e^{i\bar{k}_0 \cdot \vec{r}} + B'_{av}(k_x, k_y) \hat{v}_0^- e^{i\bar{k}_0 \cdot \vec{r}} \right] \hat{a}^- e^{-i\bar{k}_1^a \cdot \vec{r}'} \\ & + \left[A'_{bh}(k_x, k_y) \hat{h}_0^+ e^{i\bar{k}_0 \cdot \vec{r}} + A'_{bv}(k_x, k_y) \hat{v}_0^+ e^{i\bar{k}_0 \cdot \vec{r}} \right] \hat{b}^+ e^{-i\bar{k}_1^b \cdot \vec{r}'} \\ & + \left[B'_{bh}(k_x, k_y) \hat{h}_0^+ e^{i\bar{k}_0 \cdot \vec{r}} + B'_{bv}(k_x, k_y) \hat{v}_0^+ e^{i\bar{k}_0 \cdot \vec{r}} \right] \hat{b}^- e^{-i\bar{k}_1^b \cdot \vec{r}'} \end{aligned} \right\} \end{aligned} \quad (3.2.24)$$

The symmetrical property of the DGF is a powerful tool in obtaining unknown Green's functions from known Green's functions. In this section, we use the property to derive the E-DGF for the fields in region 0 given a source in region 1. The property could also be used to obtain the Green's function for the field above a source when only the Green's function for fields below the

source is known. This property is a valuable tool in solving new, complex electromagnetic problems and will be used later in this work to compute fields generated by a probe-fed microstrip patch antenna.

4 PRINTED RECTANGULAR MICROSTRIP ANTENNAS

A significant contribution of this work is the study of rectangular microstrip antennas printed on arbitrarily oriented biaxial substrates as shown in Figure 4-1. The rectangular patch antenna has some width (W) in the y -dimension and some length (L) in the x -dimension and is infinitely thin (in the z -direction although depicted with some thickness for illustrative purposes only). Before treating this general case, we address the dipole problem in which the width of the antenna is much smaller than the length. Note that we continue with our notation in which the biaxial substrate is region 1 and the isotropic region above the antenna is region 0. The conductor ground for the substrate is region 2 and considered a perfect conductor for this problem. Further note that we are considering non-magnetic materials all with permeability μ_0 .

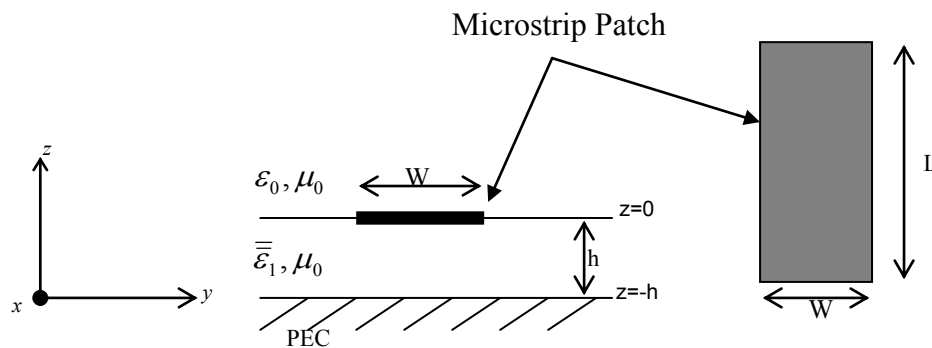


Figure 4-1: Rectangular microstrip antenna diagram

We begin by discussing solution techniques and our choice of the Method of Moments (MoM). We then derive a reaction equation for a general probe-fed rectangular microstrip antenna. We use this reaction equation to solve two microstrip antenna problems: the delta-gap fed dipole antenna and the coaxial probe fed rectangular patch antenna.

4.1 Solution Techniques

4.1.1 Method of Moments

4.1.1.1 Variational Methods

Many physical phenomena are governed by differential equations. In general, the solution to this class of problem requires integrating the differential equation. However, when this integration becomes very complicated, we can employ variational methods to find a function that will give us the minimum of a related integral [40]. Variational methods are common to both the method of moments and the finite element method used to solve electromagnetic problems [40]. Therefore, a study of variational methods is important in this research to ensure that an appropriate method is chosen for the solution of the microstrip patch problem.

The set of problems solved using variational methods are deterministic, meaning that for a given known source, there is one unique solution [41]. The deterministic equation we wish to solve is a simple inhomogeneous operator equation that can be written as

$$L(f) = g \quad (4.1.1)$$

where L is a linear operator, f is some unknown function and g is a known source function [41]. The goal is to find f . For some physical problems f can be found directly. However, for many electromagnetic problems, we cannot find f analytically so we need a computational method to find an approximation of f . To use a variational method we must define the inner product. The definition used by Sadiku [40] is given by

$$\langle a, b \rangle = \int_{\Omega} ab^* d\Omega \quad (4.1.2)$$

which satisfies the conditions set out by Harrington [41].

The function f is approximated with basis functions such that the approximation (\tilde{f}) is given by

$$\tilde{f} = \sum_{n=1}^N a_n u_n \quad (4.1.3)$$

where each u_n is a known basis function and each a_n is an unknown constant. The objective of the variational method then is to solve for the unknown coefficients when sufficient N is used to approximate the original function. If the solution method is appropriate for the problem, the error between the approximate solution and the actual solution will decrease as N increases to some limit.

The method of moments is based on an indirect variational method or *weighted residual method*. This *residual* represents the difference between the exact solution (the excitation g) and the operator L acting upon the approximate solution. The residual is given by

$$R = L(\tilde{f} - f) = L(\tilde{f}) - g \quad (4.1.4)$$

Note that while we do not know the exact solution f , we can still know the error because we know the excitation. In the weighted residual method a weighting function is chosen to minimize the residual.

$$\langle w_m, R \rangle = 0 \quad (4.1.5)$$

Substituting the expression for R from equation (4.1.4) and performing some manipulations, we have

$$\begin{aligned}\langle w_m, R \rangle &= \langle w_m, L(\tilde{f}) - g \rangle = 0 \\ \langle w_m, L(\tilde{f}) \rangle &= \langle w_m, g \rangle\end{aligned}\tag{4.1.6}$$

Then, by applying equation (4.1.3) we obtain

$$\begin{aligned}\left\langle w_m, \sum_{n=1}^N a_n L u_n \right\rangle &= \langle w_m, g \rangle \\ \sum_{n=1}^N a_n^* \langle w_m, L u_n \rangle &= \langle w_m, g \rangle\end{aligned}\tag{4.1.7}$$

In equation (4.1.6), we forced the residual to zero thus minimizing the error. Thus, the final representation of equation (4.1.7) is what we will use in our *method of moments* formulation. This is the same equation presented by Harrington [41]. We will use this method to solve N simultaneous equations for the N unknown coefficients a_n . This set of equations is written in matrix form (by Harrington [41]) as

$$[l_{mn}] [a_n^*] = [G_m]\tag{4.1.8}$$

where

$$\begin{aligned}[l_{mn}] &= \begin{bmatrix} \langle w_1, L u_1 \rangle & \langle w_1, L u_2 \rangle & \dots \\ \langle w_2, L u_1 \rangle & \langle w_2, L u_2 \rangle & \dots \\ \dots & \dots & \dots \end{bmatrix} \\ [a_n] &= \begin{bmatrix} a_1 \\ a_2 \\ \vdots \end{bmatrix}, \quad [G_m] = \begin{bmatrix} G_1 \\ G_2 \\ \vdots \end{bmatrix} = \begin{bmatrix} \langle w_1, g \rangle \\ \langle w_2, g \rangle \\ \vdots \end{bmatrix}\end{aligned}\tag{4.1.9}$$

If the matrix $[l_{mn}]$ is nonsingular, its inverse exists and the unknown coefficients a_n are given by

$$[a_n] = [l_{mn}]^{-1} [g_m] \quad (4.1.10)$$

The matrix equation in (4.1.10) is the fundamental equation solved by the method of moments

To implement this method the weighting functions w_m must be properly chosen. There are predefined methods for choosing the weighting function when using the weighted residual method. The first is *collocation*, also known as *point-matching* [40]. In this method, the weighting functions are Dirac delta functions. Computationally, this is the simplest weighted residual method because the inner product of the weighting function with the residual is equal to the residual evaluated at the center of the Dirac delta function. However, the validity of collocation depends on the choice of the collocation points [40]. While original MoM codes applied this method successfully, it can be difficult to know where the appropriate points are *a priori*. Therefore, collocation will not be used.

The next type is the subdomain method where subdomain basis functions are chosen as weighting functions. Commonly used functions include piecewise uniform (pulse), piecewise linear (triangular) and piecewise sinusoidal [40]. In general, these subdomain basis functions may be chosen independently of the expansion basis function u_n . A special case of the subdomain method is *Galerkin's* method. In Galerkin's method the weighting functions are chosen to be the same as the expansion functions. The advantage of this method is that you only have to choose one basis function as long as that basis function spans both the domain and range of the operator L [40]. We will be using Galerkin's method for the solution of the rectangular microstrip patch.

4.1.1.2 *Basis Functions*

As discussed in the previous section, the choice of basis function with which to expand the current is critical in the accuracy of Galerkin's method. Specifically, the choice of basis function directly affects the stability, efficiency and convergence of a moment method solution [22]. Basis functions come in two varieties: entire domain basis functions and subdomain basis functions. A single entire domain basis function is defined over a large section of the structure, and a set of these functions forms an efficient basis. However, they cannot approximate arbitrary current distributions and are only useful for unloaded patches [22]. Subdomain basis functions require more basis functions to cover the entire patch, making them less efficient. They are, however, capable of modeling any arbitrary current distribution and any arbitrary patch shape. Subdomain basis functions are used in this analysis to maintain maximum generality of the basis function given the complexity of the medium.

The most common subdomain basis functions are: pulse basis functions, piecewise sinusoidal basis functions and rooftop (triangular) basis functions. In much of his work, Pozar uses piecewise sinusoidal basis functions. However, we will use piecewise constant "pulse" and "rooftop" basis functions. This choice provides a more general solution as orientation is not assumed and is consistent with the formulation Pettis [1] used in his work.

In this chapter, we will derive the general reaction equations for a rectangular microstrip antenna with currents flowing in two dimensions. The general two-dimensional current formulation requires x -directed and y -directed currents. Each of these currents will have a component that varies in x and a component that varies in y . Therefore, we have four

expansion functions to define. We can write these four expansion functions as the single expression:

$$\bar{J}(\bar{r}') = \hat{x} \sum_m a_m J_x^m(x') J_x^m(y') + \hat{y} \sum_n b_n J_y^n(x') J_y^n(y') \quad (4.1.11)$$

4.2 Reaction Formulation

4.2.1 Reaction Equation Derivation

The printed microstrip antenna problem is described by the reaction equation. Fundamentally, we are trying to compute the currents induced on a conductor given some source current. The currents generate electric fields in the surrounding region. The reaction equation is based on satisfying the boundary conditions for these fields along the conducting antenna. On a conductor, the total tangential electric field is zero, therefore,

$$\bar{E}_{c \tan} + \bar{E}_{i \tan} = 0 \quad (4.2.1)$$

The electric field due to the impressed (or source) current (\bar{J}_i) is \bar{E}_i (impressed) and the electric field due to the induced conduction current (\bar{J}_c) is \bar{E}_c . In this problem the conduction current is unknown so we approximate it using known expansion currents. We then apply the weighting functions and take the inner product as shown in (4.1.5). In this section, we will derive a general reaction equation for a rectangular microstrip antenna printed on an arbitrarily oriented biaxial substrate. We start by rewriting (4.2.1) as

$$\bar{E}_{c \tan} = -\bar{E}_{i \tan} \quad (4.2.2)$$

and expand this simple equation to formulate the reaction equation. We know that the dyadic Green's function can be used to calculate the electric field generated by an electric current [2] using

$$\bar{E} = i\omega\mu \iiint_{V'} \bar{G}(\bar{r}, \bar{r}') \cdot \bar{J}(\bar{r}') dv' \quad (4.2.3)$$

Where G is the dyadic Green's function and J is the current source. Applying (4.2.3) to both sides of (4.2.2), we obtain

$$i\omega\mu \iiint_{V'} \bar{G}_{\tan}(\bar{r}, \bar{r}') \cdot \bar{J}_c^V(\bar{r}') dv' = -i\omega\mu \iiint_{V'} \bar{G}_{\tan}(\bar{r}, \bar{r}') \cdot \bar{J}_i^V(\bar{r}') dv' \quad (4.2.4)$$

The volume integral is taken over the source region, in this case the region over which the currents exist. In the general case of (4.2.4) the current could be a volume current, however, in the case of the microstrip antenna the conduction current is a surface current density. Therefore, we change this volume current density to a surface current density that exists over the entire surface of the antenna. We keep the impressed current as a volume current density.

$$i\omega\mu \iint_{S_c'} \bar{G}_{\tan}^{(0,0)}(\bar{r}, \bar{r}') \cdot \bar{J}_c(\bar{r}') ds' = -i\omega\mu \iiint_{V'} \bar{G}_{\tan}^{(0,1)}(\bar{r}, \bar{r}') \cdot \bar{J}_i(\bar{r}') dv' \quad (4.2.5)$$

In equation (4.2.5) we are using $\bar{G}^{(0,0)}$ on the conduction side of the equation and $\bar{G}^{(0,1)}$ on the source side. As was shown in Chapter 3, if a current is placed at the boundary, in region 0 (at $z = 0^+$), $\bar{G}^{(0,0)}$ and $\bar{G}^{(1,0)}$ produce the same tangential electric fields along the boundary. We choose $\bar{G}^{(0,0)}$ to calculate the electric field in region 0 so that when we apply the weighting function (which must be in the same region as the conduction current), it is in the same region as the field.

The fields on either side of the reaction equation (4.2.2) should be in the same region so we need to compute the electric field in region 0 on the source side as well. $\overline{\overline{G}}^{(0,1)}$ is used since we assume the source is in region 1 as would be consistent with a coaxial probe. This E-DGF was derived using the symmetrical property of the dyadic Green's function in Chapter 3.

Equation (4.2.5) expresses the boundary condition governing the tangential electric fields along the antenna. Now, we wish to apply the method described in Section 4.1.1. The Method of Moments requires that we compute the inner product of a weighting function with both sides of the governing equation (as shown in equation (4.1.7)). To do this we pre-multiply the fields by a testing, or weighting, function and integrate over that function. The testing function will be a current function equivalent to the expansion functions. We call this current the test current \overline{J}_t . The test current integration must be applied over both sides of equation (4.2.5) which, in general, results in

$$\iiint_V dv \overline{J}_t(\vec{r}) \cdot \overline{E}_{c \tan} = -\iiint_V dv \overline{J}_t(\vec{r}) \cdot \overline{E}_{i \tan} \quad (4.2.6)$$

Equation (4.2.6) is a general form for any test current. We already know our induced (conduction) current will be a surface current distribution. Therefore, the expansion functions and testing functions will also be surface currents. Applying this integral dimension reduction and the field expression to (4.2.6) results in

$$i\omega\mu \iint_S ds \overline{J}_t(\vec{r}) \cdot \iint_{S'} \overline{\overline{G}}_{\tan}^{(0,0)}(\vec{r}, \vec{r}') \cdot \overline{J}_c(\vec{r}') ds' = -i\omega\mu \iint_S ds \overline{J}_t(\vec{r}) \cdot \iiint_{V'} \overline{\overline{G}}_{\tan}^{(0,1)}(\vec{r}, \vec{r}') \cdot \overline{J}_i(\vec{r}') dv' \quad (4.2.7)$$

In the following sections, we will expand the terms of (4.2.7) further, concentrating on one side of the equation at a time. We begin by defining the current functions we will use.

4.2.1.1 Currents

The expansion function in any variational method should approximate the unknown induced current. One must use some knowledge about how the surface current should behave to choose an appropriate expansion function. The expansion function should model this known behavior (for example, the current goes to zero at the end of a dipole antenna). When using Galerkin's method, the testing function is the same as the expansion function. Therefore, in this problem, we define three currents, the impressed (or source) current \bar{J}_i , the induced conduction current \bar{J}_c , and the test current \bar{J}_t . The basis functions used to expand the conduction current and the test current are the same by Galerkin's method, however they will be evaluated at different locations so are treated separately.

4.2.1.1.1 Expansion and Weighting Functions

As previously stated, the choice of basis functions is important. We are choosing the same basis functions used by Pettis [1] in his analysis. For the basis function that describes the x variation in the x -directed current we will use overlapping triangular subdomain basis functions as defined by [1]:

$$J_x(x) = \begin{cases} \frac{1}{a}(x - (x_c - a)); & (x_c - a) < x < x_c \\ \frac{1}{a}((x_c + a) - x); & x_c < x < (x_c + a) \\ 0 & ; \text{ elsewhere} \end{cases} \quad (4.2.8)$$

where $a = L/N$, L is the length of the antenna and N is the number of subsections in the x -dimension. We will use the same function to describe the y variation in the y -directed current.

$$J_y(y) = \begin{cases} \frac{1}{b}(y - (y_c - b)); & (y_c - b) < y < y_c \\ \frac{1}{b}((y_c + b) - y); & y_c < y < (y_c + b) \\ 0 & \text{; elsewhere} \end{cases} \quad (4.2.9)$$

where $b = W/M$, W is the width of the antenna and M is the number of subsections in the y -dimension. Next, we define the y variation in the x -directed current. We will use the simple square pulse function given by

$$J_x(y) = \begin{cases} \frac{M}{W}; & |(y - y_c)| < \frac{W}{2M} \\ 0 & \text{; elsewhere} \end{cases} \quad (4.2.10)$$

Similarly, the x variation in the y -directed current is a square pulse defined by:

$$J_y(x) = \begin{cases} \frac{N}{L}; & |(x - x_c)| < \frac{L}{2N} \\ 0 & \text{; elsewhere} \end{cases} \quad (4.2.11)$$

The centers of each basis function are x_c and y_c respectively.

We note that the width of each triangular basis function is two segments (where a segment is either a or b wide for the x -directed and y -directed function, respectively). Therefore, the total number of triangular basis functions is one less than the number of divisions (i.e. $N-1$ or $M-1$ for the x -directed and y -directed function, respectively). The rectangular pulse basis functions, however, are only one segment wide (a or b), so the number of basis functions is equal to the number of divisions (N or M). The basis surface functions must cover the entire conducting patch.

In the formulation of the reaction equation, we will need the Fourier transform of the current distribution to evaluate the electric field integral. The x -oriented dipole antenna will consider only x -directed currents. The spectral domain functions were derived and the x -directed currents for the x -oriented dipole are given by:

$$\begin{aligned}\tilde{J}_x(k_x) &= ae^{-ik_x x_c} \left(\frac{\sin^2(\frac{1}{2}k_x a)}{(\frac{1}{2}k_x a)^2} \right) \\ \tilde{J}_x(k_y) &= e^{-ik_y y_c} \frac{\sin(\frac{1}{2}k_y b)}{(\frac{1}{2}k_y b)}\end{aligned}\tag{4.2.12}$$

In the patch antenna problem, we consider both x and y directed currents resulting in four basis functions. The spectral domain basis functions for the patch antenna are given by

$$\begin{aligned}\tilde{J}_y(k_y) &= be^{-ik_y y_c} \left(\frac{\sin^2(\frac{1}{2}k_y b)}{(\frac{1}{2}k_y b)^2} \right) \\ \tilde{J}_y(k_x) &= e^{-ik_x x_c} \left(\frac{\sin(\frac{1}{2}k_x a)}{(\frac{1}{2}k_x a)} \right)\end{aligned}\tag{4.2.13}$$

$$\begin{aligned}\tilde{J}_x(k_x) &= ae^{-ik_x x_c} \left(\frac{\sin^2(\frac{1}{2}k_x a)}{(\frac{1}{2}k_x a)^2} \right) \\ \tilde{J}_x(k_y) &= e^{-ik_y y_c} \left(\frac{\sin(\frac{1}{2}k_y b)}{(\frac{1}{2}k_y b)} \right)\end{aligned}\tag{4.2.14}$$

We can write the combined spectral domain current density as

$$\tilde{J}(k_x, k_y) = \hat{x} \sum_{m=1}^{M \times (N-1)} a_m \tilde{J}_x^m(k_x) \tilde{J}_x^m(k_y) + \hat{y} \sum_{n=1}^{N \times (M-1)} b_n \tilde{J}_y^n(k_y) \tilde{J}_y^n(k_x)\tag{4.2.15}$$

This expression will be used in the reaction formulation. Note that as we develop the reaction equation, we will be integrating with respect to k_x and k_y , so these current functions are for all values of k_x and k_y in a plane wave expansion.

4.2.1.1.2 Probe Model

Application of Galerkin's method also assumes we know the excitation described by the function g . Many options are available for exciting the microstrip patch antenna. In his previous work, Pozar [25] discussed the feeding of the microstrip patch noting "the most difficult aspect of the patch radiator problem is the modeling of the feed. For one thing many different types of feeds are possible." Among the feed types are: probes, coplanar microstrip feeds, proximity coupling to the microstrip patch by a line underneath the patch and aperture coupling [22]. While not always the most practical in actual antennas, probe feeds are most often used in full-wave modeling as they are computationally the simplest to model.

The probe is based on a coaxial line feed. In practice, the center conductor is fed through the substrate and attached to the patch antenna at some point exciting the antenna to radiate. The outer conductor is then attached to the ground plane below. In the literature, probe feeds are treated in two ways; the idealized model and the rigorous model. The idealized model is used extensively by Pozar [19, 25 and 26] notably in his analysis of radiation from a microstrip patch on a uniaxial substrate.

However, this idealized model ignores the probe self-impedance and the rapidly varying patch current in the vicinity of the feed. To account for this, Pozar adds a term for the probe self-inductance to the computed input impedance of the patch. This self-inductance term is based on the inductance of a short-circuited transmission line [43]. For a more accurate answer, Pozar also modifies his excitation by a term to account for the edge effects of the microstrip line as derived by Carver and Mink [16]. This still does not account for current variation on the patch in the vicinity of the probe. To accurately account for the effect of the

probe, the probe inside the substrate must be modeled [39]. In a rigorous model of the probe feed, the probe is treated as a wire with finite diameter, rather than a filament. The interaction of the probe with the patch at the feed point is then modeled in detail.

In this work, we will model the probe-feed excitation of the patch antenna with the idealized probe feed model. The entire length of the probe will be modeled through the biaxial substrate; however the real diameter of the coaxial line will be ignored, using the delta functions at the feed point as used by Pozar. This model is sufficient to evaluate the resonant length, impedance bandwidth and far field patterns of the antenna. Our analysis focuses on these key performance parameters so the idealized model is sufficient. This model would not be sufficient, however to fully characterize the probe behavior, specifically the probe self impedance term. A proper treatment of probe impedance calls for modeling fields within the substrate due to sources within the substrate. That model is outside the scope of this work, but offers an area of future work. This model does take full advantage of the generality of the E-DFG. Therefore impressed current source for the probe fed antennas modeled in this work is given by:

$$\vec{J}_i = \begin{cases} \hat{z}\delta(x-x_s)\delta(y-y_s), & -h \leq z \leq 0 \\ 0, & \text{elsewhere} \end{cases} \quad (4.2.16)$$

where (x_s, y_s) is the point at which the probe is attached to the microstrip patch (the source point) and h is the height of the substrate. Essentially, this is a rectangular pulse in the z -direction, centered at $-h/2$ with width h . Again, we will need the Fourier transform of this current function to evaluate the reaction equation. The Fourier transform of this type of rectangular pulse is given by

$$\tilde{J}_i = e^{-i(k_x x_s + k_y y_s)} e^{-ik_z h/2} \frac{\sin(k_z h/2)}{k_z h/2} \quad (4.2.17)$$

4.2.1.2 Induced Field Integral

The left hand side of the reaction equation (4.2.7) is an integral describing the interaction between the test current and the electric field due to the induced current. We are interested in the general reaction formulation for a rectangular microstrip antenna, therefore, we will assume the test and induced currents have both x and y directed components. We want to develop a more specific relationship than the one described by (4.2.7) so we need to expand that expression and simplify wherever possible.

We begin expanding (4.2.7) by substituting the expression for $\overline{\overline{G}}^{(0,0)}$ as presented in equation (3.1.1) and repeated here for convenience

$$\overline{\overline{G}}_e^{(0,0)}(\bar{r}, \bar{r}') = \frac{i}{8\pi^2} \int_{-\infty}^{\infty} d^2 \bar{k}_\rho \frac{1}{k_{0z}} e^{-i\bar{k}_0 \cdot \bar{r}'} \left\{ \begin{aligned} & \left[\hat{h}_0^- e^{i\bar{k}_0 \cdot \bar{r}} + R_{hh} \hat{h}_0^+ e^{i\bar{k}_0 \cdot \bar{r}} + R_{hv} \hat{v}_0^+ e^{i\bar{k}_0 \cdot \bar{r}} \right] \hat{h}_0^- \\ & + \left[\hat{v}_0^- e^{i\bar{k}_0 \cdot \bar{r}} + R_{vh} \hat{h}_0^+ e^{i\bar{k}_0 \cdot \bar{r}} + R_{vv} \hat{v}_0^+ e^{i\bar{k}_0 \cdot \bar{r}} \right] \hat{v}_0^- \end{aligned} \right\} \quad (3.1.1)$$

If we substitute this expression into the left hand side of equation (4.2.7), we obtain

$$i\omega\mu_o \iint_S ds \bar{J}_t(\bar{r}) \cdot \iint_{S'} \frac{i}{8\pi^2} \int_{-\infty}^{\infty} d^2 \bar{k}_\rho \frac{1}{k_{0z}} e^{-i\bar{k}_0 \cdot \bar{r}'} \left\{ \begin{aligned} & \left[\hat{h}_0^- e^{i\bar{k}_0 \cdot \bar{r}} + R_{hh} \hat{h}_0^+ e^{i\bar{k}_0 \cdot \bar{r}} + R_{hv} \hat{v}_0^+ e^{i\bar{k}_0 \cdot \bar{r}} \right] \hat{h}_0^- \\ & + \left[\hat{v}_0^- e^{i\bar{k}_0 \cdot \bar{r}} + R_{vh} \hat{h}_0^+ e^{i\bar{k}_0 \cdot \bar{r}} + R_{vv} \hat{v}_0^+ e^{i\bar{k}_0 \cdot \bar{r}} \right] \hat{v}_0^- \end{aligned} \right\} \cdot \bar{J}_c(\bar{r}') ds' \quad (4.2.18)$$

We can expand the exponents to factor out common terms. The propagation vectors are given by

$$\begin{aligned}\bar{k}_0 &= \hat{x}k_x + \hat{y}k_y - \hat{z}k_{0z} \\ \bar{k}_0 &= \hat{x}k_x + \hat{y}k_y + \hat{z}k_{0z}\end{aligned}\tag{4.2.19}$$

Our reaction equation is based on the tangential electric field boundary condition along the conducting antenna. The induced conduction current is located at the boundary between region 0 and region 1 as shown in Figure 4-1. This interface is at z' equal to zero so we can substitute zero for z' into the expression for \bar{r}' . By expanding the \bar{r}' exponents and making the z' substitution, we obtain

$$\begin{aligned}i\omega\mu_o \iint_S ds \bar{J}_t(\bar{r}) \cdot \iint_{S'} \frac{i}{8\pi^2} \int_{-\infty}^{\infty} d^2\bar{k}_\rho \frac{1}{k_{0z}} e^{-i(k_x x' + k_y y' - k_{0z} 0)} \\ \left\{ \left[\hat{h}_0^- e^{i\bar{k}_0 \cdot \bar{r}} + R_{hh} \hat{h}_0^+ e^{i\bar{k}_0 \cdot \bar{r}} + R_{hv} \hat{v}_0^+ e^{i\bar{k}_0 \cdot \bar{r}} \right] \hat{h}_0^- \right. \\ \left. + \left[\hat{v}_0^- e^{i\bar{k}_0 \cdot \bar{r}} + R_{vh} \hat{h}_0^+ e^{i\bar{k}_0 \cdot \bar{r}} + R_{vv} \hat{v}_0^+ e^{i\bar{k}_0 \cdot \bar{r}} \right] \hat{v}_0^- \right\} \cdot \bar{J}_c(x', y') ds'\end{aligned}\tag{4.2.20}$$

We can move the surface integral inside the spectral integral. The terms that do not depend on any primed position variables stay outside of the surface integral, while the exponent with primed x and y must stay inside the surface integral along with the induced current term.

$$\begin{aligned}\iint_S ds \bar{J}_t(\bar{r}) \cdot \frac{i}{8\pi^2} \int_{-\infty}^{\infty} d^2\bar{k}_\rho \frac{1}{k_{0z}} \left\{ \left[\hat{h}_0^- e^{i\bar{k}_0 \cdot \bar{r}} + R_{hh} \hat{h}_0^+ e^{i\bar{k}_0 \cdot \bar{r}} + R_{hv} \hat{v}_0^+ e^{i\bar{k}_0 \cdot \bar{r}} \right] \hat{h}_0^- \right. \\ \left. + \left[\hat{v}_0^- e^{i\bar{k}_0 \cdot \bar{r}} + R_{vh} \hat{h}_0^+ e^{i\bar{k}_0 \cdot \bar{r}} + R_{vv} \hat{v}_0^+ e^{i\bar{k}_0 \cdot \bar{r}} \right] \hat{v}_0^- \right\} \\ \iint_{S'} e^{-i(k_x x' + k_y y')} \bar{J}_c(x', y') ds'\end{aligned}\tag{4.2.21}$$

We recognize the surface integral over the primed region as the Fourier transform of the conduction current. Therefore, we replace the surface integral with $\tilde{\bar{J}}_c(k_x, k_y)$, the Fourier transform of the conduction current $\bar{J}_c(x', y')$ (note, the bar indicates that the current is a vector and the tilde indicates the Fourier transform).

$$\iint_S ds \bar{J}_t(\bar{r}) \cdot \frac{-\omega\mu_o}{8\pi^2} \int_{-\infty}^{\infty} d^2\bar{k}_\rho \frac{1}{k_{0z}} \left\{ \begin{aligned} & \left[\hat{h}_0^- e^{i\bar{k}_0 \cdot \bar{r}} + R_{hh} \hat{h}_0^+ e^{i\bar{k}_0 \cdot \bar{r}} + R_{hv} \hat{v}_0^+ e^{i\bar{k}_0 \cdot \bar{r}} \right] \hat{h}_0^- \\ & + \left[\hat{v}_0^- e^{i\bar{k}_0 \cdot \bar{r}} + R_{vh} \hat{h}_0^+ e^{i\bar{k}_0 \cdot \bar{r}} + R_{vv} \hat{v}_0^+ e^{i\bar{k}_0 \cdot \bar{r}} \right] \hat{v}_0^- \end{aligned} \right\} \cdot \tilde{J}_c(k_x, k_y) \quad (4.2.22)$$

The exponents of equation (4.2.22) can be expanded as shown previously. We can simplify the exponentials again because the fields we are interested in are again along the boundary making the z-component of the field-vector \bar{r} zero ($z=0$). Equation (4.2.22) simplifies to

$$\frac{-\omega\mu_o}{8\pi^2} \int_{-\infty}^{\infty} d^2\bar{k}_\rho \frac{1}{k_{0z}} \iint_S ds e^{i(k_x x + k_y y)} \bar{J}_t(x, y) \cdot \left\{ \begin{aligned} & \left[\hat{h}_0^- + R_{hh} \hat{h}_0^+ + R_{hv} \hat{v}_0^+ \right] \hat{h}_0^- \\ & + \left[\hat{v}_0^- + R_{vh} \hat{h}_0^+ + R_{vv} \hat{v}_0^+ \right] \hat{v}_0^- \end{aligned} \right\} \cdot \tilde{J}_c(k_x, k_y) \quad (4.2.23)$$

The surface integral in equation (4.2.23) is the complex conjugate of the Fourier transform of the test current.

$$\frac{-\omega\mu_o}{8\pi^2} \int_{-\infty}^{\infty} d^2\bar{k}_\rho \frac{1}{k_{0z}} \tilde{J}_t(-k_x, -k_y) \cdot \left\{ \begin{aligned} & \left[\hat{h}_0^- + R_{hh} \hat{h}_0^+ + R_{hv} \hat{v}_0^+ \right] \hat{h}_0^- \\ & + \left[\hat{v}_0^- + R_{vh} \hat{h}_0^+ + R_{vv} \hat{v}_0^+ \right] \hat{v}_0^- \end{aligned} \right\} \cdot \tilde{J}_c(k_x, k_y) \quad (4.2.24)$$

We can now substitute the expression for the spectral domain test currents and expansion currents from equation (4.1.11) to obtain

$$\begin{aligned}
& \frac{-\omega\mu_o}{8\pi^2} \int_{-\infty-\infty}^{\infty} \int_{-\infty-\infty}^{\infty} dk_x dk_y \frac{1}{k_{0z}} \left\{ \hat{x} \sum_{p=1}^{M \times (N-1)} \tilde{\mathcal{J}}_x^p(-k_x) \tilde{\mathcal{J}}_x^p(-k_y) \right\} \\
& \cdot \left\{ \begin{aligned} & \left[\hat{h}_0^- + R_{hh} \hat{h}_0^+ + R_{hv} \hat{v}_0^+ \right] \hat{h}_0^- \\ & + \left[\hat{v}_0^- + R_{vh} \hat{h}_0^+ + R_{vv} \hat{v}_0^+ \right] \hat{v}_0^- \end{aligned} \right\} \cdot \left\{ \begin{aligned} & \hat{x} \sum_{n=1}^{M \times (N-1)} a_n \tilde{\mathcal{J}}_x^n(k_x) \tilde{\mathcal{J}}_x^n(k_y) \\ & + \hat{y} \sum_{m=1}^{N \times (M-1)} b_m \tilde{\mathcal{J}}_y^m(k_x) \tilde{\mathcal{J}}_y^m(k_y) \end{aligned} \right\} \\
& + \frac{-\omega\mu_o}{8\pi^2} \int_{-\infty-\infty}^{\infty} \int_{-\infty-\infty}^{\infty} dk_x dk_y \frac{1}{k_{0z}} \left\{ \hat{y} \sum_{q=1}^{N \times (M-1)} \tilde{\mathcal{J}}_y^q(-k_x) \tilde{\mathcal{J}}_y^q(-k_y) \right\} \\
& \cdot \left\{ \begin{aligned} & \left[\hat{h}_0^- + R_{hh} \hat{h}_0^+ + R_{hv} \hat{v}_0^+ \right] \hat{h}_0^- \\ & + \left[\hat{v}_0^- + R_{vh} \hat{h}_0^+ + R_{vv} \hat{v}_0^+ \right] \hat{v}_0^- \end{aligned} \right\} \cdot \left\{ \begin{aligned} & \hat{x} \sum_{n=1}^{M \times (N-1)} a_n \tilde{\mathcal{J}}_x^n(k_x) \tilde{\mathcal{J}}_x^n(k_y) \\ & + \hat{y} \sum_{m=1}^{N \times (M-1)} b_m \tilde{\mathcal{J}}_y^m(k_x) \tilde{\mathcal{J}}_y^m(k_y) \end{aligned} \right\}
\end{aligned} \tag{4.2.25}$$

We can first evaluate the dot products of the Green's function dyad with the current distributions.

We can then write the two integrals in (4.2.25) as four integrals by separating the x and y components of the expansion currents. Finally, we can pull out the unknown constants a_n and b_m . We are left with the four integrals (we are calling Z)

$$\begin{aligned}
Z_{p,n} &= \frac{-\omega\mu_o}{8\pi^2} \int_{-\infty-\infty}^{\infty} \int_{-\infty-\infty}^{\infty} dk_x dk_y \frac{1}{k_{0z}} \tilde{\mathcal{J}}_x^p(-k_x) \tilde{\mathcal{J}}_x^p(-k_y) \left\{ \begin{aligned} & \left[h_{0x}^- + R_{hh} h_{0x}^+ + R_{hv} v_{0x}^+ \right] h_{0x}^- \\ & + \left[v_{0x}^- + R_{vh} h_{0x}^+ + R_{vv} v_{0x}^+ \right] v_{0x}^- \end{aligned} \right\} \tilde{\mathcal{J}}_x^n(k_x) \tilde{\mathcal{J}}_x^n(k_y) \\
Z_{p,(N'+m)} &= \frac{-\omega\mu_o}{8\pi^2} \int_{-\infty-\infty}^{\infty} \int_{-\infty-\infty}^{\infty} dk_x dk_y \frac{1}{k_{0z}} \tilde{\mathcal{J}}_x^p(-k_x) \tilde{\mathcal{J}}_x^p(-k_y) \left\{ \begin{aligned} & \left[h_{0x}^- + R_{hh} h_{0x}^+ + R_{hv} v_{0x}^+ \right] h_{0y}^- \\ & + \left[v_{0x}^- + R_{vh} h_{0x}^+ + R_{vv} v_{0x}^+ \right] v_{0y}^- \end{aligned} \right\} \tilde{\mathcal{J}}_y^m(k_x) \tilde{\mathcal{J}}_y^m(k_y) \\
Z_{(N'+q),n} &= \frac{-\omega\mu_o}{8\pi^2} \int_{-\infty-\infty}^{\infty} \int_{-\infty-\infty}^{\infty} dk_x dk_y \frac{1}{k_{0z}} \tilde{\mathcal{J}}_y^q(-k_x) \tilde{\mathcal{J}}_y^q(-k_y) \left\{ \begin{aligned} & \left[h_{0y}^- + R_{hh} h_{0y}^+ + R_{hv} v_{0y}^+ \right] h_{0x}^- \\ & + \left[v_{0y}^- + R_{vh} h_{0y}^+ + R_{vv} v_{0y}^+ \right] v_{0x}^- \end{aligned} \right\} \tilde{\mathcal{J}}_x^n(k_x) \tilde{\mathcal{J}}_x^n(k_y) \\
Z_{(N'+q),(N'+m)} &= \frac{-\omega\mu_o}{8\pi^2} \int_{-\infty-\infty}^{\infty} \int_{-\infty-\infty}^{\infty} dk_x dk_y \frac{1}{k_{0z}} \tilde{\mathcal{J}}_y^q(-k_x) \tilde{\mathcal{J}}_y^q(-k_y) \left\{ \begin{aligned} & \left[h_{0y}^- + R_{hh} h_{0y}^+ + R_{hv} v_{0y}^+ \right] h_{0y}^- \\ & + \left[v_{0y}^- + R_{vh} h_{0y}^+ + R_{vv} v_{0y}^+ \right] v_{0y}^- \end{aligned} \right\} \tilde{\mathcal{J}}_y^m(k_x) \tilde{\mathcal{J}}_y^m(k_y)
\end{aligned} \tag{4.2.26}$$

where h_{0x}^\pm is the x-component of the upward (+) and downward (-) propagating, horizontally polarized wave, h_{0y}^\pm is the y-component, v_{0x}^\pm is the x-component of the upward (+) and

downward (–) propagating, vertically polarized wave, and $v_{0,y}^{\pm}$ is the y -component. The subscripts represent the location of the basis functions along the antenna and are given by

$$\begin{aligned}
 N' &= M \times (N - 1) \\
 M' &= N \times (M - 1) \\
 p &= 1 \dots N' \\
 n &= 1 \dots N' \\
 q &= 1 \dots M' \\
 m &= 1 \dots M'
 \end{aligned} \tag{4.2.27}$$

Finally, we write the left hand side of the reaction equation in the following matrix form

$$\begin{bmatrix}
 Z_{1,1} & Z_{1,2} & \dots & Z_{1,N'} & Z_{1,(N'+1)} & \dots & Z_{1,(N'+M')} \\
 \vdots & \vdots & \ddots & \vdots & \vdots & \ddots & \vdots \\
 Z_{N',1} & Z_{N',2} & \dots & Z_{N',N'} & Z_{N',(N'+1)} & \dots & Z_{N',(N'+M')} \\
 Z_{(N'+1),1} & Z_{(N'+1),2} & \dots & Z_{(N'+1),N'} & Z_{(N'+1),(N'+1)} & \dots & Z_{(N'+1),(N'+M')} \\
 \vdots & \vdots & \ddots & \vdots & \vdots & \ddots & \vdots \\
 Z_{(N'+M'),1} & Z_{(N'+M'),2} & \dots & Z_{(N'+M'),N'} & Z_{(N'+M'),(N'+1)} & \dots & Z_{(N'+M'),(N'+M')}
 \end{bmatrix}
 \begin{bmatrix}
 a_1 \\
 \vdots \\
 a_{N'} \\
 b_1 \\
 \vdots \\
 b_{M'}
 \end{bmatrix} \tag{4.2.28}$$

where the Z matrix is filled in by the appropriate Z integral and the vector of unknown coefficients will be solved in our method of moments routine.

4.2.1.3 Excitation Integral

The right hand side of the reaction equation (4.2.7) is an integral describing the interaction between the test current (weighting function) and the electric field due to the impressed (source) current. We must use the same test current that we did for the induced field integral. We will be using both a delta gap and probe source to evaluate the rectangular microstrip antennas. The gap source is a simple, well known source function commonly used in dipole antenna problems. The details will not be presented here but can be found in Pettis'

dissertation [1, Chapter7]. Therefore, we will derive the excitation integral using the probe source. We will follow the same fundamental steps as described in Section 4.2.1.2 to get the right hand side of equation (4.2.7) in a form similar to (4.2.26).

We begin expanding the right hand side of equation (4.2.7) by substituting the expression for the Green's function into the integral. This Green's function was derived in Chapter 3 using the symmetrical property of the dyadic Green's function. We repeat the equation here for convenience.

$$\begin{aligned} \overline{\overline{G}}_e^{(0,1)}(\vec{r}, \vec{r}') = & \frac{i}{8\pi^2} \int_{-\infty}^{\infty} d^2\vec{k}_\rho \frac{1}{k_{0z}} e^{-i\vec{k}_0 \cdot \vec{r}} \\ & \left\{ \hat{h}_0^- \left[A_{ha} \hat{a}^- e^{i\vec{k}_1^a \cdot \vec{r}'} + B_{ha} \hat{a}^+ e^{i\vec{k}_1^a \cdot \vec{r}'} + A_{hb} \hat{b}^- e^{i\vec{k}_1^b \cdot \vec{r}'} + B_{hb} \hat{b}^+ e^{i\vec{k}_1^b \cdot \vec{r}'} \right] \right. \\ & \left. + \hat{v}_0^- \left[A_{va} \hat{a}^- e^{i\vec{k}_1^a \cdot \vec{r}'} + B_{va} \hat{a}^+ e^{i\vec{k}_1^a \cdot \vec{r}'} + A_{vb} \hat{b}^- e^{i\vec{k}_1^b \cdot \vec{r}'} + B_{vb} \hat{b}^+ e^{i\vec{k}_1^b \cdot \vec{r}'} \right] \right\} \end{aligned} \quad (3.2.16)$$

Note this is not the final form derived in Chapter 3, it is still mathematically correct. If we substitute this expression into the left had side of equation (4.2.7), we obtain

$$\begin{aligned} i\omega\mu_0 \iint_S ds \bar{J}_i(\vec{r}) \cdot \iiint_{V'} dv' \frac{i}{8\pi^2} \int_{-\infty}^{\infty} d^2\vec{k}_\rho \frac{1}{k_{0z}} e^{-i\vec{k}_0 \cdot \vec{r}} \\ \left\{ \hat{h}_0^- \left[A_{ha} \hat{a}^- e^{i\vec{k}_1^a \cdot \vec{r}'} + B_{ha} \hat{a}^+ e^{i\vec{k}_1^a \cdot \vec{r}'} + A_{hb} \hat{b}^- e^{i\vec{k}_1^b \cdot \vec{r}'} + B_{hb} \hat{b}^+ e^{i\vec{k}_1^b \cdot \vec{r}'} \right] \right. \\ \left. + \hat{v}_0^- \left[A_{va} \hat{a}^- e^{i\vec{k}_1^a \cdot \vec{r}'} + B_{va} \hat{a}^+ e^{i\vec{k}_1^a \cdot \vec{r}'} + A_{vb} \hat{b}^- e^{i\vec{k}_1^b \cdot \vec{r}'} + B_{vb} \hat{b}^+ e^{i\vec{k}_1^b \cdot \vec{r}'} \right] \right\} \cdot \bar{J}_i(\vec{r}') \end{aligned} \quad (4.2.29)$$

We can expand the exponents to factor out common terms. The propagation vectors are given by equations (2.1.1) through (2.1.4). Our reaction equation is based on the tangential electric field boundary condition along the conducting antenna. The antenna is located at the boundary between region 0 and region 1 as shown in Figure 4-1. The source is a coaxial probe with volume current distribution described by equation (4.2.16). First, we manipulate the source

terms (associated with the primed position vector). If we factor out the common exponential terms we obtain

$$i\omega\mu_o \iint_S ds \bar{J}_i(\bar{r}) \cdot \left. \iint_{V'} dv' \left\{ \frac{i}{8\pi^2} \int_{-\infty}^{\infty} d^2 \bar{k}_\rho \frac{e^{-i\bar{k}_0 \cdot \bar{r}}}{k_{0z}} \left[\hat{h}_0^- \left[A_{ha} \hat{a}^- e^{ik_z^{ad}z'} + B_{ha} \hat{a}^+ e^{ik_z^{au}z'} + A_{hb} \hat{b}^- e^{ik_z^{bd}z'} + B_{hb} \hat{b}^+ e^{ik_z^{bu}z'} \right] \right. \right. \right. \left. \left. \left. + \hat{v}_0^- \left[A_{va} \hat{a}^- e^{ik_z^{ad}z'} + B_{va} \hat{a}^+ e^{ik_z^{au}z'} + A_{vb} \hat{b}^- e^{ik_z^{bd}z'} + B_{vb} \hat{b}^+ e^{ik_z^{bu}z'} \right] \right] \right\} e^{i(k_x x' + k_y y')} \cdot \bar{J}_i(\bar{r}') \right\} \quad (4.2.30)$$

The primed terms are grouped together. The unprimed (field point) terms are not dependent on the primed terms. While the primed terms do depend on the values of k_x and k_y , we can change the order of integration. We move the volume integral over V' inside the spectral integral resulting in

$$\iint_S ds \bar{J}_i(\bar{r}) \cdot \frac{-\omega\mu_o}{8\pi^2} \int_{-\infty}^{\infty} d^2 \bar{k}_\rho \frac{e^{-i\bar{k}_0 \cdot \bar{r}}}{k_{0z}} \left. \iint_{V'} dv' \left\{ \hat{h}_0^- \left[A_{ha} \hat{a}^- e^{ik_z^{ad}z'} + B_{ha} \hat{a}^+ e^{ik_z^{au}z'} + A_{hb} \hat{b}^- e^{ik_z^{bd}z'} + B_{hb} \hat{b}^+ e^{ik_z^{bu}z'} \right] \right. \right. \left. \left. + \hat{v}_0^- \left[A_{va} \hat{a}^- e^{ik_z^{ad}z'} + B_{va} \hat{a}^+ e^{ik_z^{au}z'} + A_{vb} \hat{b}^- e^{ik_z^{bd}z'} + B_{vb} \hat{b}^+ e^{ik_z^{bu}z'} \right] \right\} e^{i(k_x x' + k_y y')} \cdot \bar{J}_i(\bar{r}') \right\} \quad (4.2.31)$$

Unlike the induced field integral, the source here has a z variation. Previously, the field was evaluated only at the patch surface ($z=0$) so the k_z terms fell out after the substitution. We must keep the k_z terms and, in the biaxial medium, k_z is polarization dependent. While this does complicate the integration, each term has the same form so we can consider one and apply the result to all. The downward propagating a -wave term in (4.2.31) is given by

$$\iiint_{V'} dv' \hat{h}_0^- A_{ha} \hat{a}^- e^{ik_z^{ad}z'} e^{i(k_x x' + k_y y')} \cdot \bar{J}_i(\bar{r}') \quad (4.2.32)$$

The field polarization \hat{h}_0^- does not depend on source position, so it acts as a constant in this integral. The term A_{ha} enforces that the boundary conditions are satisfied between regions 0 and 1, so this term is a constant with respect to \bar{r}' as well. The remaining terms in (4.2.32) represent the complex conjugate of the Fourier transform of the impressed current. The downward propagating *a-wave* term reduces to

$$\hat{h}_0^- A_{ha} a_z^- \tilde{J}_i(-k_x, -k_y, -k_z^{ad}) \quad (4.2.33)$$

where a_z^- is the z -component of the downward propagating *a-wave* and the Fourier transform of the impressed (excitation) current is given in (4.2.17). Each term in (4.2.31) can be decomposed in a similar manner resulting in

$$\iint_S ds \bar{J}_i(\bar{r}) \cdot \frac{-\omega \mu_o}{8\pi^2} \int_{-\infty}^{\infty} d^2 \bar{k}_\rho \frac{e^{-i\bar{k}_0 \cdot \bar{r}}}{k_{0z}} \left\{ \begin{aligned} & \hat{h}_0^- \left[A_{ha} a_z^- \tilde{J}_i(-k_x, -k_y, -k_z^{ad}) + B_{ha} a_z^+ \tilde{J}_i(-k_x, -k_y, -k_z^{au}) \right. \\ & \quad \left. + A_{hb} b_z^- \tilde{J}_i(-k_x, -k_y, -k_z^{bd}) + B_{hb} b_z^+ \tilde{J}_i(-k_x, -k_y, -k_z^{bu}) \right] \\ & + \hat{v}_0^- \left[A_{va} a_z^- \tilde{J}_i(-k_x, -k_y, -k_z^{ad}) + B_{va} a_z^+ \tilde{J}_i(-k_x, -k_y, -k_z^{au}) \right. \\ & \quad \left. + A_{vb} b_z^- \tilde{J}_i(-k_x, -k_y, -k_z^{bd}) + B_{vb} b_z^+ \tilde{J}_i(-k_x, -k_y, -k_z^{bu}) \right] \end{aligned} \right\} \quad (4.2.34)$$

Now we manipulate the field terms (unprimed components). First, we expand the exponents then simplify the z -component because the fields we are interested in are along the $z = 0$ boundary; the z -component of the field-vector \bar{r} zero. To further simplify equation (4.2.34), we can move the surface integral inside the spectral integral because:

1. The volume integral becomes a surface integral with respect to x and y because the test current is a surface current density in the x - y plane

2. With the exception of the exponential term, the integrand of the spectral integral does not depend on x or y .

When we make these simplifications, we obtain

$$\begin{aligned} & \frac{-\omega\mu_o}{8\pi^2} \int_{-\infty}^{\infty} d^2\bar{k}_\rho \frac{1}{k_{0z}} \iint_S ds e^{-i(k_x x + k_y y)} \bar{J}_t(x, y) \cdot \\ & \left\{ \begin{aligned} & \hat{h}_0^- \left[A_{ha} a_z^- \tilde{J}_i(-k_x, -k_y, -k_z^{ad}) + B_{ha} a_z^+ \tilde{J}_i(-k_x, -k_y, -k_z^{au}) \right] \\ & + A_{hb} b_z^- \tilde{J}_i(-k_x, -k_y, -k_z^{bd}) + B_{hb} b_z^+ \tilde{J}_i(-k_x, -k_y, -k_z^{bu}) \end{aligned} \right\} \\ & \left\{ \begin{aligned} & + \hat{v}_0^- \left[A_{va} a_z^- \tilde{J}_i(-k_x, -k_y, -k_z^{ad}) + B_{va} a_z^+ \tilde{J}_i(-k_x, -k_y, -k_z^{au}) \right] \\ & + A_{vb} b_z^- \tilde{J}_i(-k_x, -k_y, -k_z^{bd}) + B_{vb} b_z^+ \tilde{J}_i(-k_x, -k_y, -k_z^{bu}) \end{aligned} \right\} \end{aligned} \quad (4.2.35)$$

The surface integral in equation (4.2.35) is the Fourier transform of the test current, thus

$$\begin{aligned} & \frac{-\omega\mu_o}{8\pi^2} \int_{-\infty}^{\infty} d^2\bar{k}_\rho \frac{1}{k_{0z}} \tilde{J}_t(k_x, k_y) \cdot \\ & \left\{ \begin{aligned} & \hat{h}_0^- \left[A_{ha} a_z^- \tilde{J}_i(-k_x, -k_y, -k_z^{ad}) + B_{ha} a_z^+ \tilde{J}_i(-k_x, -k_y, -k_z^{au}) \right] \\ & + A_{hb} b_z^- \tilde{J}_i(-k_x, -k_y, -k_z^{bd}) + B_{hb} b_z^+ \tilde{J}_i(-k_x, -k_y, -k_z^{bu}) \end{aligned} \right\} \\ & \left\{ \begin{aligned} & + \hat{v}_0^- \left[A_{va} a_z^- \tilde{J}_i(-k_x, -k_y, -k_z^{ad}) + B_{va} a_z^+ \tilde{J}_i(-k_x, -k_y, -k_z^{au}) \right] \\ & + A_{vb} b_z^- \tilde{J}_i(-k_x, -k_y, -k_z^{bd}) + B_{vb} b_z^+ \tilde{J}_i(-k_x, -k_y, -k_z^{bu}) \end{aligned} \right\} \end{aligned} \quad (4.2.36)$$

We can now substitute the expression for the spectral domain test currents from equation (4.2.15) into our field integral as we did for the induced field integral. We call the vector comprised of each test current term V . Each component of V is computed using the integral above and is defined by

$$\begin{aligned}
V_p &= \frac{-\omega\mu_o}{8\pi^2} \int_{-\infty}^{\infty} \int_{-\infty}^{\infty} dk_x dk_y \frac{1}{k_{0z}} \left\{ \hat{x} \sum_{p=1}^{M \times (N-1)} \tilde{J}_x^p(k_x) \tilde{J}_x^p(k_y) \right\} \cdot \left\{ \begin{array}{l} \hat{h}_0^- [R1_{terms}] \\ + \hat{v}_0^- [R1_{terms}] \end{array} \right\} \\
V_{N'+q} &= \frac{-\omega\mu_o}{8\pi^2} \int_{-\infty}^{\infty} \int_{-\infty}^{\infty} dk_x dk_y \frac{1}{k_{0z}} \left\{ \hat{y} \sum_{q=1}^{N \times (M-1)} \tilde{J}_y^q(-k_x) \tilde{J}_y^q(-k_y) \right\} \cdot \left\{ \begin{array}{l} \hat{h}_0^- [R1_{terms}] \\ + \hat{v}_0^- [R1_{terms}] \end{array} \right\}
\end{aligned} \tag{4.2.37}$$

where $N' = M \times (N-1)$ and $R1_{terms}$ represents the region 1 terms within the square brackets in equation (4.2.36). Combining equations (4.2.28) and (4.2.37), the entire reaction equation can now be written in the matrix form

$$\begin{bmatrix} Z_{1,1} & Z_{1,2} & \cdots & Z_{1,N'} & Z_{1,(N'+1)} & \cdots & Z_{1,(N'+M')} \\ \vdots & \vdots & \ddots & \vdots & \vdots & \ddots & \vdots \\ Z_{N',1} & Z_{N',2} & \cdots & Z_{N',N'} & Z_{N',(N'+1)} & \cdots & Z_{N',(N'+M')} \\ Z_{(N'+1),1} & Z_{(N'+1),2} & \cdots & Z_{(N'+1),N'} & Z_{(N'+1),(N'+1)} & \cdots & Z_{(N'+1),(N'+M')} \\ \vdots & \vdots & \ddots & \vdots & \vdots & \ddots & \vdots \\ Z_{(N'+M'),1} & Z_{(N'+M'),2} & \cdots & Z_{(N'+M'),N'} & Z_{(N'+M'),(N'+1)} & \cdots & Z_{(N'+M'),(N'+M')} \end{bmatrix} \begin{bmatrix} a_1 \\ \vdots \\ a_{N'} \\ b_1 \\ \vdots \\ b_{M'} \end{bmatrix} = \begin{bmatrix} V_1 \\ \vdots \\ V_{N'} \\ V_{N'+1} \\ \vdots \\ V_{N'+M'} \end{bmatrix} \tag{4.2.38}$$

where the Z matrix is filled in by the appropriate Z integral and the vector of unknown coefficients will be solved in our method of moments routine.

4.2.2 Numerical Integration

The induced field integral and the excitation integral are both solved numerically using trapezoidal integration. The step size was determined in a 2 step process. We begin with the minimum sampling rates in k_x and k_y as derived by Pettis [1, Chapter 7]. These sampling rates are given by

$$f_{kx}^{\min} = 10 \frac{L}{N} \left(\frac{N-1}{\pi} \right) \tag{4.2.39}$$

$$f_{k_y}^{\min} = 10 \frac{W}{M} \left(\frac{2M+1}{2\pi} \right) \quad (4.2.40)$$

We then refine these sampling rates by observing convergence of the integral. We choose the minimum frequency (or maximum step size) for which the integration has converged. We also need to choose the limits of the doubly infinite integral. To do this, we observe the integrands and choose limits in k_x and k_y for which the integrand has converged to zero. Figure 4-2 shows an example integrand. We choose for this case to limit k_y at $150k_o$ and k_x at $500k_o$.

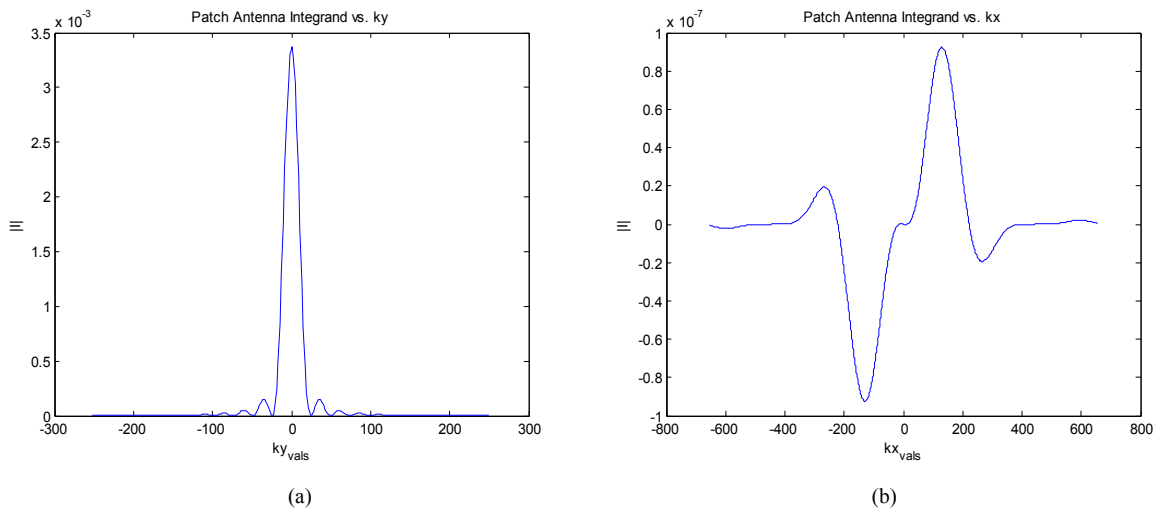


Figure 4-2: Patch antenna integrand example (a) vs. k_y , (b) vs. k_x

Singularities are important to consider in the numerical integration. If they are not handled properly, the integration will not converge. Integrals such as these can have pole singularities and branch point singularities. A pole singularity exists within the integrand when the direction of propagation is parallel to one of the optic axes. In this case, the denominator of the electric field vectors in the biaxial medium becomes zero. However, we know that if the direction of propagation is parallel to one of the optic axes, the wave will behave as if it were in an isotropic medium with vertical and horizontal polarization. This special case can be handled analytically by making the field vectors consistent with vertical and horizontal polarization when

the pole singularity is reached. Branch point singularities, however, do not pose an issue with the form of the Green's function we are using. We are using the layered Green's function. In bounded regions the integrand of the Green's function be single valued [44]. This would not be true for a single layered problem or unbounded problems, but it does hold for the layered case we are considering.

4.3 Microstrip Dipole Antennas

We begin our study of microstrip antennas with the analysis of microstrip dipole antennas. We will treat the dipole fed by a delta gap source. The delta gap source is an adequate theoretical model and in fact Pettis used this source in his dipole analysis [1]. For a real dipole antenna, usually microstrip feed lines lead to the "arms" of the dipole. The arms are equivalent to the strip we are modeling. The feed lines mimic the voltage gap source. This model is the most widely used for excitation for dipole antennas.

4.3.1 Dipole with Delta Gap Source

The series voltage gap generator is one of a few sources whose excitation fields are known directly [22]. This known electric field is given in [1] as

$$\bar{E}_i = \hat{x}\delta(x - x_s) \left[u\left(y - \left(y_s - \frac{W}{2}\right)\right) - u\left(y - \left(y_s + \frac{W}{2}\right)\right) \right] \quad (4.3.1)$$

where the location of the feed point is (x_s, y_s) and $u(y)$ is the Heaviside step function defined as unity for $y \geq 0$ and zero for $y < 0$. Given this well known electric field, we can construct the V -vector for a delta gap. We have a value of 1 at the point of the source and zero elsewhere. We are placing the source at $x_s=0$, so our V -vector looks like

$$V = \begin{bmatrix} 0 \\ \vdots \\ 1 \\ \vdots \\ 0 \end{bmatrix} \quad (4.3.2)$$

We will use the vector in (4.3.2) for the right hand side excitation vector in our reaction formulation of the gap-fed dipole.

4.3.1.1 Modified Reaction Equation

The microstrip dipole has a length (L) in the x -direction and a width (W) in the y -direction with $W \ll \lambda$. The dipole will have only x -directed currents. Therefore, of the four Z integrals defined by equation (4.2.26), only the first one will be used. Further, we need only the x -directed basis functions as defined in section 4.1.1.2. This simplifies the Z -matrix from equation (4.2.28). For convenience, we repeat this reduced form of equation (4.2.26) here

$$Z_{p,n} = \frac{-\omega\mu_o}{8\pi^2} \int_{-\infty}^{\infty} \int_{-\infty}^{\infty} dk_x dk_y \frac{1}{k_{0z}} \tilde{J}_x^p(-k_x) \tilde{J}_x^p(-k_y) \left\{ \begin{array}{l} [A_{ha}a_x^- + B_{ha}a_x^+ + A_{hb}b_x^- + B_{hb}b_x^+] h_{0x}^- \\ + [A_{va}a_x^- + B_{va}a_x^+ + A_{vb}b_x^- + B_{vb}b_x^+] v_{0x}^- \end{array} \right\} \tilde{J}_x^n(k_x) \tilde{J}_x^n(k_y) \quad (4.2.26)$$

This reduces the size of the Z -matrix to one fourth the size of the generic matrix. We can rewrite our governing matrix equation as

$$\begin{bmatrix} Z_{1,1} & Z_{1,2} & \cdots & Z_{1,N'} \\ \vdots & \vdots & \ddots & \vdots \\ Z_{N',1} & Z_{N',2} & \cdots & Z_{N',N'} \end{bmatrix} \begin{bmatrix} a_1 \\ \vdots \\ a_{N'} \end{bmatrix} = \begin{bmatrix} V_1 \\ \vdots \\ V_{N'} \end{bmatrix} \quad (4.3.3)$$

The method of moments solution to the matrix equation in (4.3.3) will give us the coefficients for the induced current basis functions.

In the method of moments solution for the dipole problem, we used the Green's function for the field in region 0 given a source in region 0. This means that the source and field points are essentially on the same plane (z and z' both equal zero). In general, the field is not well defined at the source point and a singularity may be observed when computing fields at this point. Therefore, when formulating the Green's function, this point is often avoided.

When using the method of moments, we are, in general, interested in field and source points in the same plane. When using Galerkin's method, we choose the expansion functions and weighting functions to be in the same region. In the reaction integral, we compute the reaction of the field with the weighting function at the location of the weighting function. Therefore, the field and source points will be in the same location at least with respect to z .

If we choose the Green's function for the field in region 1 with the source in region 0 (G^{10}), the field and source points may both be located at $z = 0$, but the physics of the Green's function formulation essentially means that the field point in region 1 is at $z = 0^-$ while the source point is at $z' = 0^+$. When using G^{00} this is not true. For the gap fed dipole on a biaxially anisotropic substrate, we compute the currents using the method of moments with G^{10} and G^{00} respectively to show that in this numerical solution, G^{00} may be used. Our results showed that the two Green's functions agreed with each other and with published results, indicating that in this numerical solution, the restriction on $z \neq z'$ is unnecessary.

4.3.1.2 Analysis

While computing the current coefficients from (4.3.3) is the most computationally complex portion of the antenna analysis, it tells us little about how the antenna performs.

Common metrics for antenna performance are input impedance, resonant length, impedance bandwidth and directivity. In our analysis of the gap-fed microstrip dipoles, we will compute the current distribution on the dipole, the input impedance, resonant length, directivity and directive gain. Impedance bandwidth is treated in detail for the patch antenna. We compare our results to those presented in published works including Pettis [1, Chapter 7], and then observe antenna behavior as we change the permittivity tensor and rotation angles.

4.3.1.2.1 Current Distributions

The first parameter we analyze is the current distribution along the dipole. We use the current coefficients computed using the moment method. The current distribution is the sum of the current expansion functions each multiplied by the appropriate coefficient. As the number of expansion functions increases, the approximation to the actual current distribution should improve. We are primarily interested in how the current distribution converges as number of expansion functions increases. We consider the case of an unrotated biaxial substrate shown in Figure 4-3. This case was run with 6, 12, 18 and 24 basis functions. The conduction currents for all three cases are plotted. Note that the currents are very close for both 6 and 12 basis functions and change even less as the number of basis functions increase. Therefore, we use 12 basis functions for the remaining dipoles. Also note that for the unrotated case, the current peaks at the center (as expected with the delta gap source) and that the current is symmetric about the source ($x = 0$). As a final note, Pettis [1] also concluded that 12 basis functions were sufficient for modeling the biaxial dipole using a different biaxial substrate.

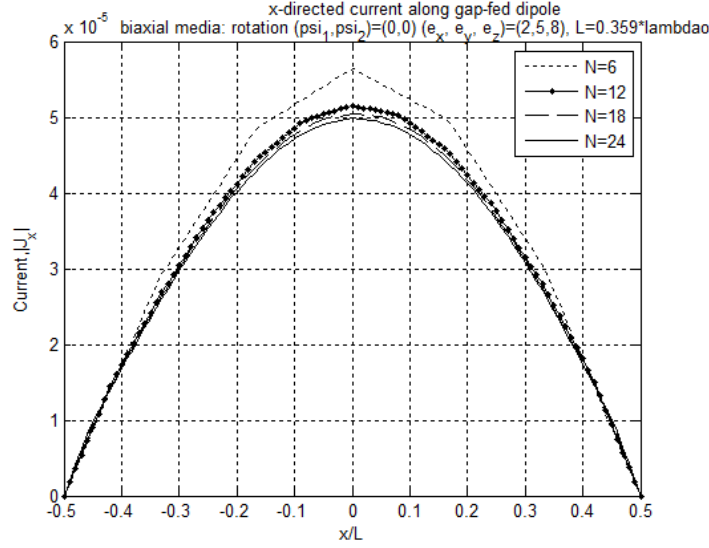


Figure 4-3: Current distribution for half wave gap-fed dipole: $N = 6, 12, 18$ and 24 expansion functions with biaxial permittivity $(\epsilon_x, \epsilon_y, \epsilon_z) = (2, 5, 8)$ and no rotation

4.3.1.2.2 Input Impedance

Input impedance is itself an important performance metric in evaluating any antenna. However, a more important metric may be the resonant length. We can use input impedance to determine resonant length as the resonant length of an antenna is the length for which it has zero reactance (imaginary impedance). We will compute input impedance for all of the dipoles we consider. Further, we will determine the resonant length of several dipoles and compare our results to those computed by Pettis [1]. We note that Pettis used the transition matrix dyadic Green's function while we use the eigenvector dyadic Green's function

The input impedance of a network can be calculated using [1]

$$Z_{in} = \frac{P_s}{I_{in} I_{in}^*} \quad (4.3.4)$$

where P_s is the input power and I_{in} is the total input current. Harrington [41] defines the complex input power delivered to an antenna as

$$P_s = -\iint_{S'} \bar{E}_s \cdot \bar{J}_s^* ds' \quad (4.3.5)$$

where \bar{E}_s is the tangential electric field produced by the induced (conduction) current (\bar{J}_s). As shown in equation (4.2.2), the tangential electric field induced on the antenna is equal to the negative of the tangential impressed electric field. This is due to the boundary condition along the perfectly conducting antenna. Making this substitution into (4.3.5) results in

$$P_s = \iint_{S'} \bar{E}_{i,\tan} \cdot \bar{J}_c^* ds' \quad (4.3.6)$$

We can write the induced conduction current as the sum of the basis functions multiplied by the coefficient we computed by the method of moments. In the introduction to this section, we discussed the electric field produced by the voltage gap source. Substituting the expression for induced current and the impressed electric field (given in equation (4.3.1)) into the power equation results in

$$P_s = \iint_{S'} \left[\hat{x} \delta(x' - x_s) \left[u\left(y' - \left(y_s - \frac{W}{2}\right)\right) - u\left(y' - \left(y_s + \frac{W}{2}\right)\right) \right] \cdot \hat{x} \sum_{m=1}^{M \times (N-1)} a_m^* J_x^{m*}(x') J_x^{m*}(y') \right] ds' \quad (4.3.7)$$

When we integrate with respect to x' , only the basis function containing x_s is non-zero. We have selected x_s to be the center of the dipole. Therefore, the only x -varying basis functions remaining after integration occur when $p = N/2$. With this understanding, the result of integrating (4.3.7) is

$$\begin{aligned}
P_s &= \sum_{q=1}^M \left[a_{[(q-1)(N-1)+\frac{N}{2}]} J_x^{[(q-1)(N-1)+\frac{N}{2}]}(x_s) \right]^* \int_{y_o^q - \frac{W}{2M}}^{y_o^q + \frac{W}{2M}} dy \frac{M}{W} \\
&= \sum_{q=1}^M \left[a_{[(q-1)(N-1)+\frac{N}{2}]} J_x^{[(q-1)(N-1)+\frac{N}{2}]}(x_s) \right]^*
\end{aligned} \tag{4.3.8}$$

Because we are using the triangular basis function, $J_x(x_s)$ is unity. With this final substitution we obtain

$$P_s = \sum_{q=1}^M a_{[(q-1)(N-1)+\frac{N}{2}]}^* \tag{4.3.9}$$

for the total power delivered by the source.

Input impedance also depends on total current. The total current, I_{in} , is given by the integral of the surface current at $x = x_s$ [1] or

$$I_{in} = \int_{-\frac{W}{2}}^{\frac{W}{2}} dy J_x(x_s) J_x(y) = \sum_{q=1}^M \left[a_{[(q-1)(N-1)+\frac{N}{2}]} \right] \int_{y_o^q - \frac{W}{2M}}^{y_o^q + \frac{W}{2M}} dy \frac{M}{W} = \sum_{q=1}^M a_{[(q-1)(N-1)+\frac{N}{2}]} \tag{4.3.10}$$

Substituting the results in equations (4.3.9) and (4.3.10) into equation (4.3.4) results in

$$Z_{in} = \frac{P_s}{I_{in} I_{in}^*} = \frac{\sum_{q=1}^M a_{[(q-1)(N-1)+\frac{N}{2}]}^*}{\sum_{q=1}^M a_{[(q-1)(N-1)+\frac{N}{2}]} \sum_{q=1}^M a_{[(q-1)(N-1)+\frac{N}{2}]}^*} = \frac{1}{\sum_{q=1}^M a_{[(q-1)(N-1)+\frac{N}{2}]}^*} \tag{4.3.11}$$

For the dipole problem where $M=1$, the input impedance reduces to

$$Z_{in,M=1} = \frac{1}{a_{\frac{N}{2}}} \tag{4.3.12}$$

To verify our results, we first consider a gap-fed dipole printed on an isotropic substrate. James and Hall [45, p.290] plots the input reactance and resistance versus antenna length for a center fed strip dipole printed on a substrate with relative permittivity 2.45 and height $0.2\lambda_0$. The results in James and Hall show antennas of varying widths and we have chosen to recreate the case with a width of $0.001\lambda_0$. Our results are shown in Figure 4-4.

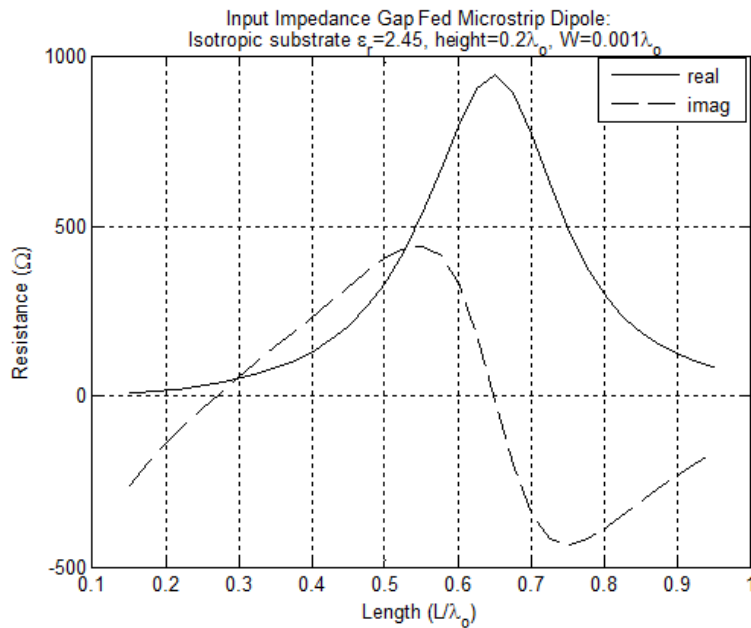


Figure 4-4: Input impedance for gap-fed dipole with width of $0.001\lambda_0$ printed on an isotropic substrate with $\epsilon_r = 2.45$, height = $0.2\lambda_0$

Our results for the isotropic comparison very closely match the published results with a resonant length between $0.6\lambda_0$ and $0.7\lambda_0$, and peak input reactance close to 500Ω . Our peak resistance is slightly lower than the published result which looks to be just over 1000Ω whereas ours is just under 1000Ω , but the overall agreement is very good given differences in computational accuracies.

Proving that the moment method routine is arriving at the correct input impedance for the isotropic substrate, we want to compute the input impedance of the dipole when the substrate

is biaxial. We can then use this information to determine resonant length dipoles by finding the length where the reactance goes to zero. The computed input impedance for an unrotated and a rotated example are shown in Figure 4-5 and Figure 4-6.

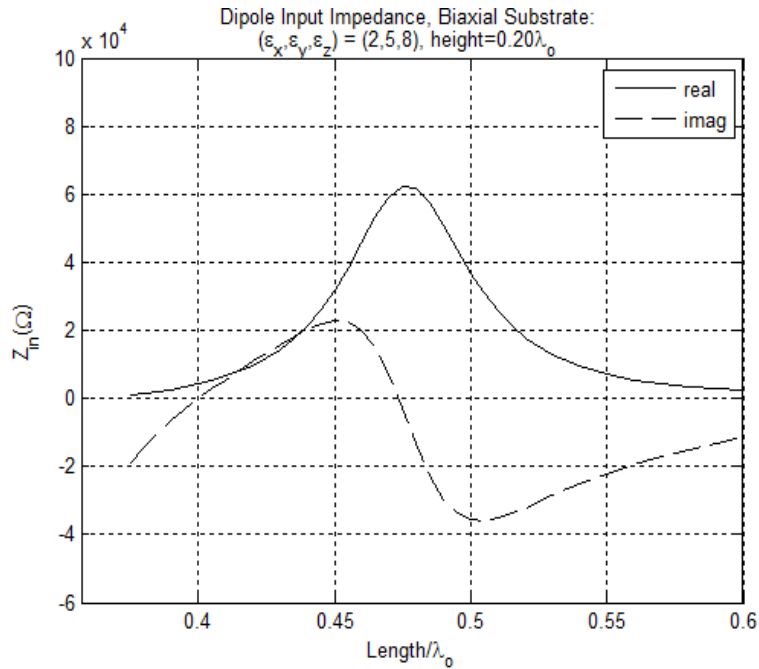


Figure 4-5: Input impedance for gap-fed dipole printed on a biaxial substrate with permittivity $(\epsilon_x, \epsilon_y, \epsilon_z) = (2, 5, 8)$ and no rotation and height $0.2\lambda_0$

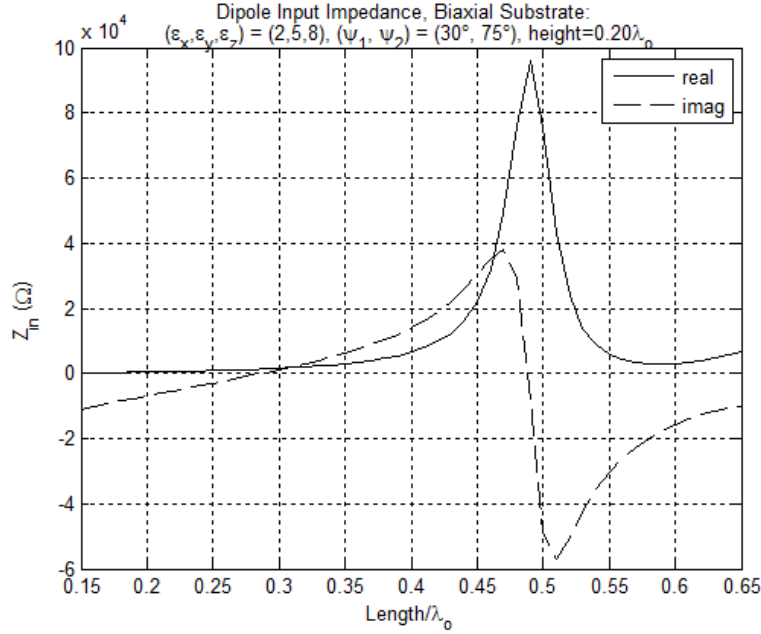


Figure 4-6: Input impedance for gap-fed dipole printed on a biaxial substrate with permittivity $(\epsilon_x, \epsilon_y, \epsilon_z) = (2, 5, 8)$ rotated by $\psi_1 = 30^\circ$ $\psi_2 = 75^\circ$ and height $0.2\lambda_0$

From the plots of input impedance, we can find the resonant length of the dipole. The antenna is resonant when the reactance is zero. We observe in Figure 4-5 and Figure 4-6 that the reactance goes to zero twice. For comparison purposes, we are choosing the length where the reactance is zero and the resistance is a maximum. The resulting resonant lengths for unrotated and rotated, strongly and weakly biaxial substrates are shown in Table 4-1. The results show that in both cases rotating the medium results in a longer resonant antenna.

Table 4-1: Resonant Lengths for Microstrip Dipoles Printed on Biaxial Substrates ($W=0.001\lambda_0$)

Permittivity $(\epsilon_x, \epsilon_y, \epsilon_z)$	Rotation (ψ_1, ψ_2)	Height	Resonant Length
(2, 5, 8)	$0^\circ, 0^\circ$	$0.2\lambda_0$	$0.4736 \lambda_0$
(2, 5, 8)	$30^\circ, 75^\circ$	$0.2\lambda_0$	$0.4878 \lambda_0$
PTFE (2.45, 2.89, 2.95)	$0^\circ, 0^\circ$	$0.2\lambda_0$	$0.5637 \lambda_0$

PTFE (2.45, 2.89, 2.95)	30°, 75°	0.2λ ₀	0.6035 λ ₀
-------------------------	----------	-------------------	-----------------------

4.3.1.2.3 Radiation Behavior

The radiation behavior of the dipole antenna can be understood by analyzing the directive gain. In this section we analyze the directive gain for dipoles printed on biaxial substrates with two different permittivity tensors and two different rotations.

Before we can compute the radiation parameters of interest, we must formulate the radiated field. In our reaction formulation, we place the expansion current in the isotropic region (region 0). To compute the electric field in region 0 generated by this source, we need the dyadic Green's function for a field in region 0 given the source in region 0. This Green's function was given in Chapter 3 and is repeated here for convenience

$$\overline{\overline{G}}_e^{(0,0)}(\vec{r}, \vec{r}') = \frac{i}{8\pi^2} \int_{-\infty}^{\infty} d^2\vec{k}_\rho \frac{1}{k_{0z}} e^{-i\vec{k}_0 \cdot \vec{r}'} \left\{ \begin{aligned} & \left[\hat{h}_0^- e^{i\vec{k}_0 \cdot \vec{r}} + R_{hh} \hat{h}_0^+ e^{i\vec{k}_0 \cdot \vec{r}} + R_{hv} \hat{v}_0^+ e^{i\vec{k}_0 \cdot \vec{r}} \right] \hat{h}_0^- \\ & + \left[\hat{v}_0^- e^{i\vec{k}_0 \cdot \vec{r}} + R_{vh} \hat{h}_0^+ e^{i\vec{k}_0 \cdot \vec{r}} + R_{vv} \hat{v}_0^+ e^{i\vec{k}_0 \cdot \vec{r}} \right] \hat{v}_0^- \end{aligned} \right\}, \quad 0 < z < z' \quad (3.1.1)$$

The Green's function in equation 3.1.1 can be used to compute the field below the source point. However, for the far field, we are interested in the field above the field point. We can use the symmetrical property of the DGF to change the Green's function we have into the Green's function we need. Using this property we obtained

$$\overline{\overline{G}}_e^{(0,0)}(\vec{r}, \vec{r}') = \frac{i}{8\pi^2} \int_{-\infty}^{\infty} d^2\vec{k}_\rho \frac{1}{k_{0z}} e^{i\vec{k}_0 \cdot \vec{r}} \left\{ \begin{aligned} & \left[\hat{h}_0^+ \left[\hat{h}_0^+ e^{-i\vec{k}_0 \cdot \vec{r}'} + R_{hh} \hat{h}_0^- e^{-i\vec{k}_0 \cdot \vec{r}'} + R_{vh} \hat{v}_0^- e^{-i\vec{k}_0 \cdot \vec{r}'} \right] \right] \\ & + \hat{v}_0^+ \left[\hat{v}_0^+ e^{-i\vec{k}_0 \cdot \vec{r}'} + R_{hv} \hat{h}_0^- e^{-i\vec{k}_0 \cdot \vec{r}'} + R_{vv} \hat{v}_0^- e^{-i\vec{k}_0 \cdot \vec{r}'} \right] \end{aligned} \right\}, \quad z > z' \quad (4.3.13)$$

for the field in region 0 at points above a source in region 0. Note that in the derivation of (4.3.13), the order of the subscripts on the reflection coefficients is reversed. Now, by applying the property shown in equation (4.2.3), the electric field is given by

$$\bar{E}_0(\bar{r}) = \frac{-\omega\mu_o}{8\pi^2} \iint_{S'} ds' \int_{-\infty}^{\infty} d^2\bar{k}_\rho \frac{1}{k_{0z}} e^{i\bar{k}_0 \cdot \bar{r}} \left\{ \begin{aligned} &\hat{h}_0^+ \left[\hat{h}_0^+ e^{-i\bar{k}_0 \cdot \bar{r}'} + R_{hh} \hat{h}_0^- e^{-i\bar{k}_0 \cdot \bar{r}'} + R_{vh} \hat{v}_0^- e^{-i\bar{k}_0 \cdot \bar{r}'} \right] \\ &+ \hat{v}_0^+ \left[\hat{v}_0^+ e^{i\bar{k}_0 \cdot \bar{r}'} + R_{hv} \hat{h}_0^- e^{-i\bar{k}_0 \cdot \bar{r}'} + R_{vv} \hat{v}_0^- e^{-i\bar{k}_0 \cdot \bar{r}'} \right] \end{aligned} \right\} \cdot \bar{J}_c(\bar{r}') \quad (4.3.14)$$

We expand the source vector exponentials resulting in

$$\bar{E}_0(\bar{r}) = \frac{-\omega\mu_o}{8\pi^2} \iint_{S'} ds' \int_{-\infty}^{\infty} d^2\bar{k}_\rho \frac{1}{k_{0z}} e^{i\bar{k}_0 \cdot \bar{r}} \left\{ \begin{aligned} &\hat{h}_0^+ \left[\hat{h}_0^+ e^{-i(k_x x' + k_y y' + k_{0z} z')} + R_{hh} \hat{h}_0^- e^{-i(k_x x' + k_y y' - k_{0z} z')} + R_{vh} \hat{v}_0^- e^{-i(k_x x' + k_y y' - k_{0z} z')} \right] \\ &+ \hat{v}_0^+ \left[\hat{v}_0^+ e^{i(k_x x' + k_y y' + k_{0z} z')} + R_{hv} \hat{h}_0^- e^{-i(k_x x' + k_y y' - k_{0z} z')} + R_{vv} \hat{v}_0^- e^{-i(k_x x' + k_y y' - k_{0z} z')} \right] \end{aligned} \right\} \cdot \bar{J}_c(\bar{r}') \quad (4.3.15)$$

We note that the source current is located at the boundary between region 0 and region 1 making z' zero. After this substitution, the source terms only contain x and y components, the same components of the surface integral. We can move the surface integral inside the spectral integral. The result of these manipulations is

$$\bar{E}_0(\bar{r}) = \frac{-\omega\mu_o}{8\pi^2} \int_{-\infty}^{\infty} d^2\bar{k}_\rho \frac{1}{k_{0z}} e^{i\bar{k}_0 \cdot \bar{r}} \left\{ \begin{aligned} &\hat{h}_0^+ \left[\hat{h}_0^+ + R_{hh} \hat{h}_0^- + R_{vh} \hat{v}_0^- \right] \\ &+ \hat{v}_0^+ \left[\hat{v}_0^+ + R_{hv} \hat{h}_0^- + R_{vv} \hat{v}_0^- \right] \end{aligned} \right\} \cdot \iint_{S'} ds' e^{-i(k_x x' + k_y y')} \sum_m^{M(N-1)} \hat{x} a_m J_x^m(x') J_x^m(y') \quad (4.3.16)$$

Next, we change the order of the summation and integration of the source term. The coefficient can be pulled out of the integral as it does not directly depend on position. We see then that the integral is simply the Fourier transform of the x -directed basis functions. The field can thus be expressed by

$$\begin{aligned}
\bar{E}_0(\bar{r}) &= \frac{-\omega\mu_o}{8\pi^2} \int_{-\infty}^{\infty} d^2\bar{k}_\rho \frac{1}{k_{0z}} e^{i\bar{k}_0 \cdot \bar{r}} \left\{ \hat{h}_0^+ \left[\hat{h}_0^+ + R_{hh} \hat{h}_0^- + R_{vh} \hat{v}_0^- \right] \right. \\
&\quad \left. + \hat{v}_0^+ \left[\hat{v}_0^+ + R_{hv} \hat{h}_0^- + R_{vv} \hat{v}_0^- \right] \right\} \\
&\quad \hat{x} \sum_{m=1}^{M(N-1)} a_m \iint_{S'} ds' e^{-i(k_x x' + k_y y')} J_x^m(x') J_x^m(y') \quad (4.3.17) \\
&= \frac{-\omega\mu_o}{8\pi^2} \int_{-\infty}^{\infty} d^2\bar{k}_\rho \frac{1}{k_{0z}} e^{i\bar{k}_0 \cdot \bar{r}} \left\{ \hat{h}_0^+ \left[\hat{h}_0^+ + R_{hh} \hat{h}_0^- + R_{vh} \hat{v}_0^- \right] \right. \\
&\quad \left. + \hat{v}_0^+ \left[\hat{v}_0^+ + R_{hv} \hat{h}_0^- + R_{vv} \hat{v}_0^- \right] \right\} \cdot \hat{x} \sum_{m=1}^{M(N-1)} a_m \tilde{J}_x^m(k_x) \tilde{J}_x^m(k_y)
\end{aligned}$$

In the far field we assume $\bar{r} \gg \bar{r}'$ so the $e^{i\bar{k}_0 \cdot \bar{r}}$ terms will be rapidly varying such that integral contributions are zero on average. This allows us to apply the method of stationary phase. When the field is written in the form of (4.3.17) we can obtain the stationary phase approximation in two steps as derived by Pettis [1, Appendix L]. First, we extract the slowly varying terms from the integrand which yields

$$E_0(\bar{r}) = \frac{-\omega\mu_o}{8\pi^2} \left[\int_{-\infty}^{\infty} d^2\bar{k}_\rho \frac{1}{k_{0z}} e^{i\bar{k}_0 \cdot \bar{r}} \right] \left\{ \left[\hat{h}_0^+ \hat{h}_0^+ + R_{hh} \hat{h}_0^+ \hat{h}_0^- + R_{vh} \hat{h}_0^+ \hat{v}_0^- \right] \right. \\
\left. + \left[\hat{v}_0^+ \hat{v}_0^+ + R_{hv} \hat{v}_0^+ \hat{h}_0^- + R_{vv} \hat{v}_0^+ \hat{v}_0^- \right] \right\} \cdot \hat{x} \sum_{m=1}^{M(N-1)} a_m \tilde{J}_x^m(k_x) \tilde{J}_x^m(k_y) \quad (4.3.18)$$

Then we replace the remaining integral over k_x and k_y with $-k_{0z} \frac{i2\pi}{r} e^{ik_0 r}$. This gives us the final radiated electric field

$$\bar{E}_0(\bar{r}) = \frac{i\omega\mu_o}{4\pi} \frac{e^{ik_0 r}}{r} \left\{ \left[\hat{h}_0^+ \hat{h}_0^+ + R_{hh} \hat{h}_0^+ \hat{h}_0^- + R_{vh} \hat{h}_0^+ \hat{v}_0^- \right] \right. \\
\left. + \left[\hat{v}_0^+ \hat{v}_0^+ + R_{hv} \hat{v}_0^+ \hat{h}_0^- + R_{vv} \hat{v}_0^+ \hat{v}_0^- \right] \right\} \cdot \hat{x} \sum_{m=1}^{M(N-1)} a_m \tilde{J}_x^m(k_x) \tilde{J}_x^m(k_y) \quad (4.3.19)$$

When we consider far field radiation patterns we usually consider the θ and ϕ directed fields. Furthermore, we want to evaluate \hat{h} , \hat{v} , and R at $k_x = k_0 \cos\theta \cos\phi$ and $k_y = k_0 \sin\theta \sin\phi$ where θ and ϕ are the observation angles. Therefore, we want to convert from Cartesian to spherical coordinates. Pettis [1, Appendix Q] showed that

$$\begin{aligned}\hat{h}^\pm &= -\hat{a}_\phi \\ \hat{v}^\pm &= -\hat{a}_\theta\end{aligned}\quad (4.3.20)$$

So, we can write

$$\bar{E}_0(\bar{r}) = -\frac{i\omega\mu_0}{4\pi} \frac{e^{ik_0r}}{r} \left\{ \begin{aligned} &\hat{a}_\phi \left[\hat{h}_0^+ + R_{hh}\hat{h}_0^- + R_{vh}\hat{v}_0^- \right] \\ &+ \hat{a}_\theta \left[\hat{v}_0^+ + R_{hv}\hat{h}_0^- + R_{vv}\hat{v}_0^- \right] \end{aligned} \right\} \cdot \hat{x} \sum_{m=1}^{M(N-1)} a_m \tilde{J}_x^m(k_x) \tilde{J}_x^m(k_y) \quad (4.3.21)$$

The θ -directed field (E_θ) and phi-directed field (E_ϕ) can be expressed by

$$E_\theta = k_0 \left[v_{0x}^+ + R_{hv}h_{0x}^- + R_{vv}v_{0x}^- \right] \sum_{m=1}^{M(N-1)} a_m \tilde{J}_x^p(k_x) \tilde{J}_x^p(k_y) \quad (4.3.22)$$

$$E_\phi = k_0 \left[h_{0x}^+ + R_{hh}h_{0x}^- + R_{vh}v_{0x}^- \right] \sum_{m=1}^{M(N-1)} a_m \tilde{J}_x^p(k_x) \tilde{J}_x^p(k_y) \quad (4.3.23)$$

which gives us the final electric field formulation

$$\bar{E}_0(\bar{r}) = -i\eta_0 \frac{e^{ik_0r}}{4\pi r} \left[\hat{a}_\theta E_\theta + \hat{a}_\phi E_\phi \right] \quad (4.3.24)$$

First, we want to use these results to compute directive gain. According to Balanis [46] directive gain is the ratio of radiation strength in a specific direction to the radiation strength of a reference antenna. This ratio is given by [46]

$$D(\theta, \phi) = 4\pi \frac{U(\theta, \phi)}{\int_0^{2\pi} \int_0^\pi U(\theta, \phi) \sin \theta d\theta d\phi} \quad (4.3.25)$$

where

$$U(\theta, \phi) = r^2 \left[\frac{1}{2} \text{Re}(\bar{E} \times \bar{H}^*) \cdot \hat{a}_r \right] = r^2 \left\{ \frac{1}{2} \frac{\eta_0}{(4\pi r)^2} \left[|E_\theta|^2 + |E_\phi|^2 \right] \right\} = \frac{1}{2} \frac{\eta_0}{(4\pi)^2} \left[|E_\theta|^2 + |E_\phi|^2 \right] \quad (4.3.26)$$

Substituting (4.3.26) into (4.3.25) we obtain

$$D(\theta, \phi) = 4\pi \frac{|E_\theta|^2 + |E_\phi|^2}{\int_0^{2\pi} \int_0^\pi [|E_\theta|^2 + |E_\phi|^2] \sin \theta d\theta d\phi} \quad (4.3.27)$$

for the directive gain of the antenna. Directivity is the peak directive gain in the given direction.

Directivity is computed using

$$D(\theta, \phi) = 4\pi \frac{\left(|E_\theta|^2 + |E_\phi|^2 \right)_{\max}}{\int_0^{2\pi} \int_0^\pi [|E_\theta|^2 + |E_\phi|^2] \sin \theta d\theta d\phi} \quad (4.3.28)$$

Katehi and Alexopoulos [47] considered the effect of substrate thickness for a printed dipole on an isotropic substrate with ϵ_r of 2.35. They modeled resonant length half-wave wire dipoles with radius $10^{-4}\lambda_0$. According to Stutzman and Thiele [23], a wire dipole of radius r can be approximated by a flat printed dipole of width $4r$. We will consider the same dipole lengths and substrate thicknesses but we will model the flat printed dipole with a width of $4 \times 10^{-4}\lambda_0$.

The first case is the thinnest substrate with thickness of $0.2\lambda_0$. Katehi and Alexopoulos give the exact length of this dipole as $0.369345\lambda_0$. Our result, shown in Figure 4-7, agrees with the published result in [47].

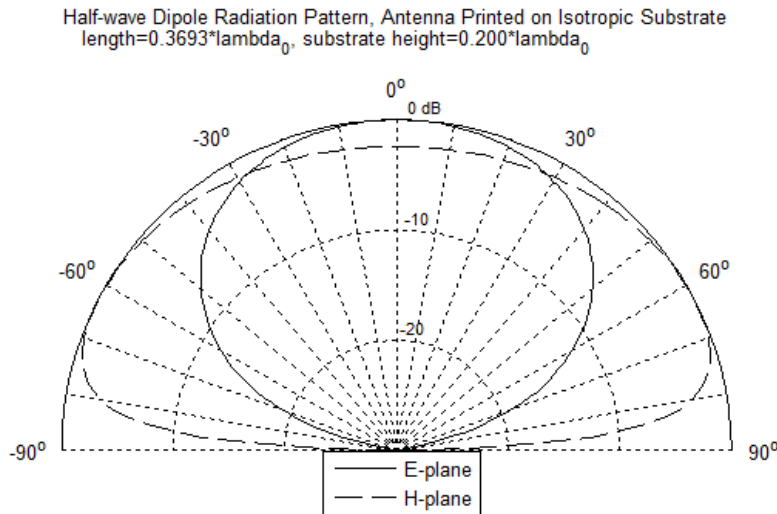


Figure 4-7: Radiation pattern of half-wave dipole printed on isotropic substrate of height $0.2\lambda_0$ ($\epsilon_r=2.35$)

Katehi and Alexopoulos were interested in the effect of substrate thickness (or height) on the antenna behavior. Specifically, they analyzed the lobing effect of increasing substrate thickness. When the substrate is increased to $0.975\lambda_0$, Katehi and Alexopoulos show two lobes in the radiation pattern. We also show two lobes (Figure 4-8) for this substrate thickness. In this case, the actual length is not specified in paper. Using the published figure of resonant length versus substrate height, we modeled the dipole with length $0.38\lambda_0$. Clearly, this is not as precise a value as what was published for the previous case, but it is a good enough approximation to recreate the radiation patterns published by Katehi and Alexopoulos, as shown in Figure 4-8. Finally the substrate thickness is increased to $1.05\lambda_0$ resulting in three lobes in the radiation pattern. The simulated dipole had a length of $0.375\lambda_0$ and again the input reactance is on the

order of 10^{-10} . Our result shows three lobes (Figure 4-9) and again agrees with the published result.

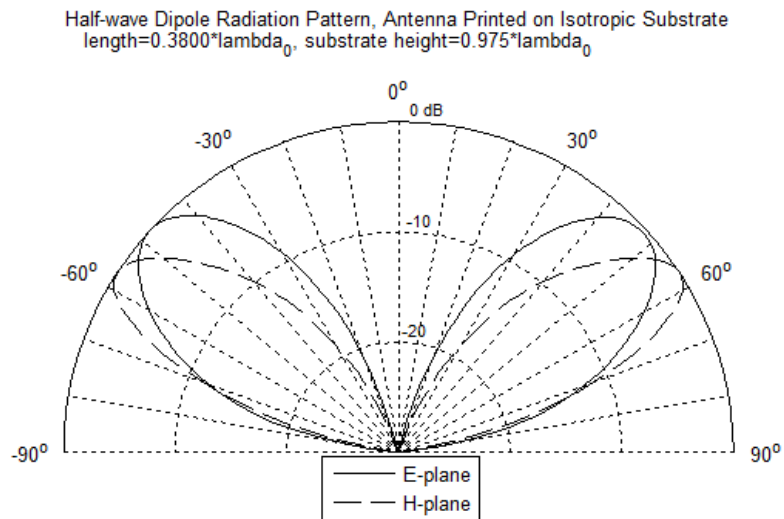


Figure 4-8: Radiation pattern of half-wave dipole printed on isotropic substrate of height $0.975\lambda_0$ ($\epsilon_r=2.35$)

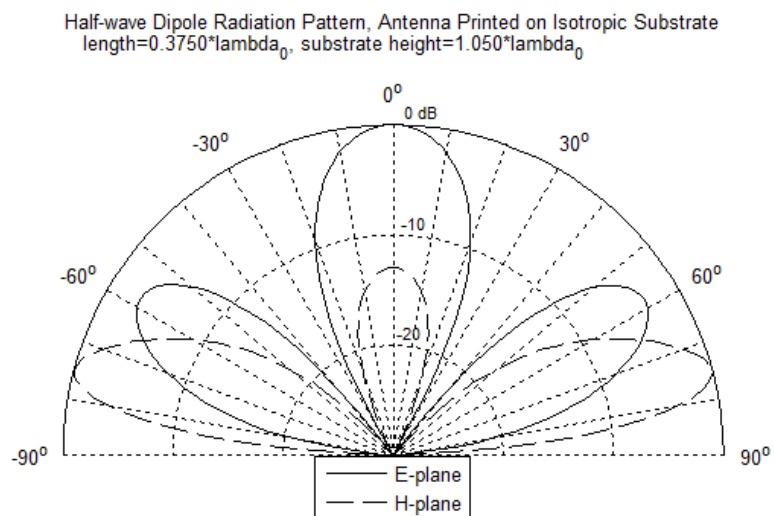


Figure 4-9: Radiation pattern of half-wave dipole printed on isotropic substrate of height $1.05\lambda_0$ ($\epsilon_r = 2.35$)

We also present the published results in Figure 4-10 for comparison. The substrate heights are $0.2\lambda_0$, $0.975\lambda_0$ and $1.05\lambda_0$ for plots (b), (c) and (d), respectively.

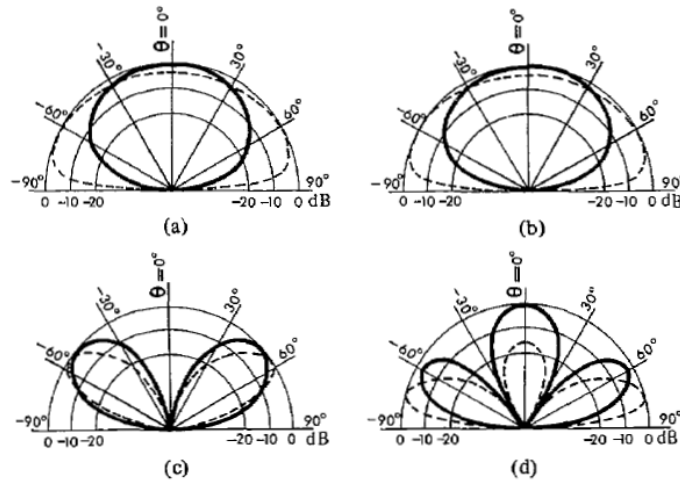


Fig. 6. Printed dipole radiation patterns. — E -plane. --- H -plane.

Figure 4-10: Patterns for dipole printed on isotropic substrates of varying heights – from [47] P. B. Katehi and N. G. Alexopoulos, “On the effect of substrate thickness and permittivity on printed circuit dipole properties”, *IEEE Trans. Ant. Prop.* vol. 31, no. 1, pp. 34-39, January 1983.

This analysis verifies our code against dipoles printed on isotropic substrates. We will now focus on dipoles printed on biaxial substrates. First, we again verify our code against existing results. In his dissertation, Pettis [1] studied gap-fed microstrip dipoles printed on a biaxial substrate. He presented directive gain patterns for dipoles printed on an unrotated biaxial substrate with permittivity tensor $(\epsilon_x, \epsilon_y, \epsilon_z) = (5, 3, 4)$. Pettis presented patterns for resonant

length dipoles on substrates of three thicknesses. We repeated his analysis and found that our results agree. Our directive gain patterns are shown in Figure 4-11.

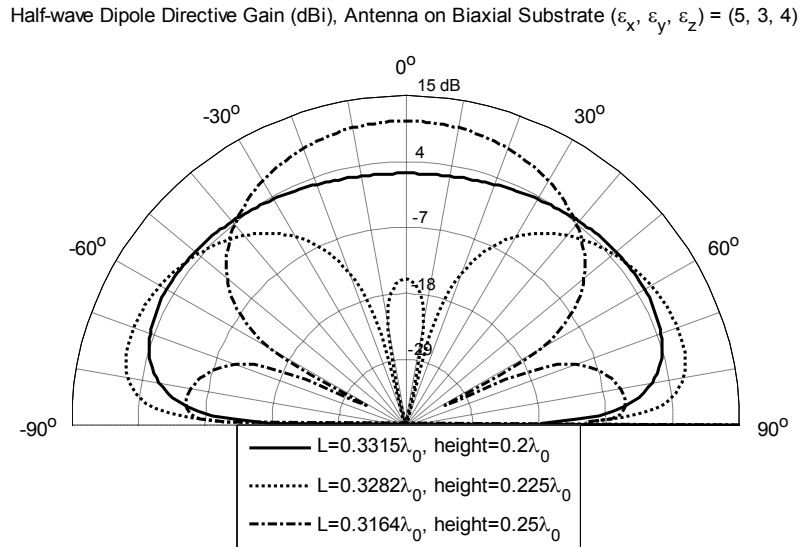


Figure 4-11: Directive gain for gap-fed dipole with biaxial permittivity $(\epsilon_x, \epsilon_y, \epsilon_z) = (5, 3, 4)$ as height is varied

The biaxial substrate considered by Pettis is somewhat weakly biaxial. We consider a strongly biaxial medium with permittivity tensor $(\epsilon_x, \epsilon_y, \epsilon_z) = (2, 5, 8)$ and the very weakly biaxial PTFE cloth. In Figure 4-12 we present the directivity patterns for resonant dipoles printed on both unrotated and rotated strongly biaxial substrates (thickness $0.20\lambda_0$) and Figure 4-13 we present the same results using PTFE cloth. We note that upon rotation, the directive gain of the antenna on the strongly biaxial substrate becomes considerably wider. However, on the weakly biaxial substrate, the difference is negligible. We observed a similar behavior with PTFE when studying the resonant length. We can then conclude that the orientation of the biaxial medium is increasingly important as the strength of the biaxial anisotropy increases.

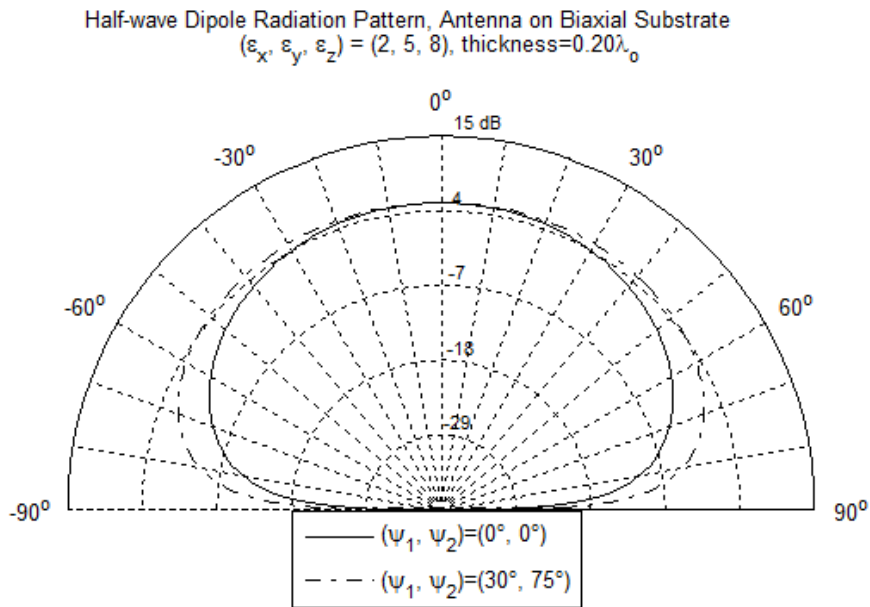


Figure 4-12: Directive gain for resonant half wavelength gap-fed dipole printed on a biaxial substrate with permittivity $(\epsilon_x, \epsilon_y, \epsilon_z) = (2, 5, 8)$

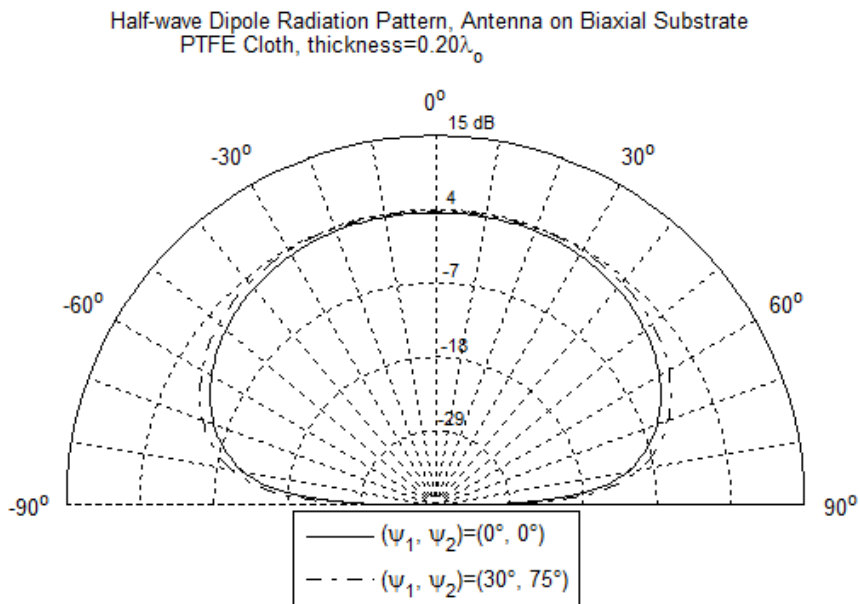


Figure 4-13: Directive gain for resonant half wavelength gap-fed dipole printed on PTFE cloth

4.4 Rectangular Microstrip Patch Antenna

We now focus on the more general rectangular microstrip patch antenna fed by a coaxial probe. A diagram of the geometry is shown in Figure 4-14. In the case of the patch, the width (W) can be much larger than that of the dipole. This additional size makes the problem more complex. We will consider currents directed in both x and y . Therefore, we will need the entire matrix described by equation (4.2.38). The complexity of the solution will increase as there will be four complex integrals to solve instead of one. Additionally, the patch antenna will be fed by a coaxial probe as described in Section 4.2.1.1.2. The probe feed is a more complex excitation than the delta gap source. Modeling the probe feed requires a different Green's function and normal field components in additions to the tangential components.

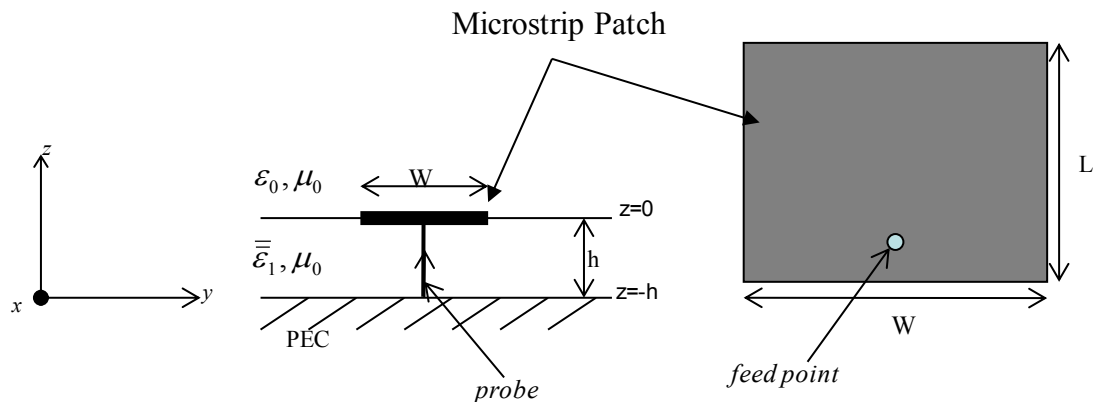


Figure 4-14: Rectangular Microstrip Patch Antenna Geometry

The analysis of the microstrip patch antenna focuses primarily on the effects of varying patch parameters on the input impedance and resonant length of the patch. We also consider the radiation behavior of the patch antenna, as we did for the dipole. A majority of references surveyed analyzed patch antennas with a 1.5 width-to-length ratio so we also consider patches with these dimensions. Two approaches to resonance analysis were represented in the

literature. In the first, a given physical patch dimension is set and the frequency is varied until the resonant frequency can be determined. In the second, the width-to-length ratio is fixed and the electrical length of the antenna is varied to determine the resonant length. The later approach was used in the input impedance analysis of the dipole antenna in the previous section and will be used again for the patch antenna analysis. This provides a general design solution that could be applied to any frequency of operation.

4.4.1 Reaction Equation

The microstrip patch antenna currents are computed using the method of moments. The governing reaction equation was derived in Section 4.2.1. To compute the patch antenna currents, we use all four integrals in the Z -matrix as described by equation (4.2.26) and the V -vector is computed using the integral described by equation (4.2.36). The resulting currents are used in our analysis of the patch antenna.

4.4.2 Basis Function Convergence

Determining the proper number of basis functions required to accurately model the rectangular patch antenna is necessary to know that we are arriving at accurate solutions. The number of basis functions is deemed sufficient if there is convergence in the solution. In the dipole section, we showed that the current coefficients converged as we increased the number of basis functions. Current coefficient convergence is more difficult to show in the patch antenna case as the currents are two dimensional. A more straight forward metric to monitor is the input resistance. As will be derived in this section, the input impedance uses the current coefficients

and the voltage vector elements. It then follows that if the impedance is converging, these elements will be converging as well.

We primarily consider a rotated $((\Psi_1, \Psi_2) = (30^\circ, 75^\circ))$ biaxial medium of length $.175\lambda_0$, width $W=1.5L$, and height $0.02\lambda_0$. In this case the width is larger than the length and we have the most general type of a permittivity tensor (full matrix due to the rotation). We investigate this antenna in rigorous detail to understand the basis function convergence. First, we observe the effect of increasing the number of basis function on the current coefficients when $M=1$ as shown in Figure 4-15. We observe that the current is converging as N increases to 18 basis functions ($N=18$), but with 20 basis functions, the solution becomes unstable. A triangular current basis function gives rise to a step discontinuity in the charge (charge being the derivative of current). As the basis functions become very small, this charge discontinuity becomes a larger portion of the basis function, making the solution unstable. We do not want our solution to be dominated by this discontinuity, so ideally we want to back off of $N=18$ and use $N=12$. Also note that, in this instance, the probe is positioned at $x = 0.25\lambda_0$. The real part of the current coefficients, in Figure 4-15(a), shows a discontinuity at $0.25\lambda_0$. This is to account for the continuity of current from the probe. We do not see this discontinuity in the imaginary part of the current because we assumed the current on the probe was real (1A).

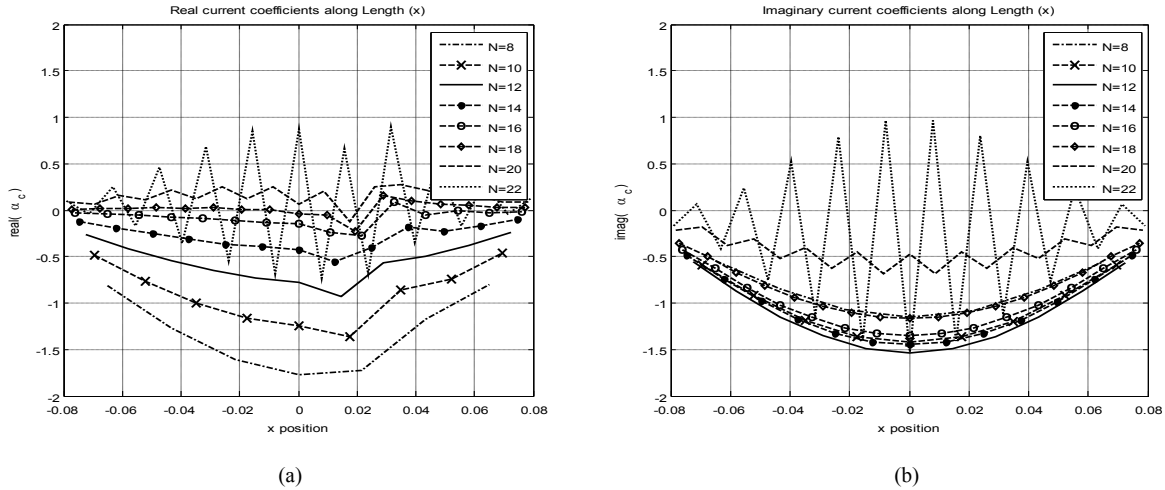


Figure 4-15: Current coefficients along the length of a rectangular microstrip antenna ($W/L=1.5$) on rotated biaxial substrate (a) real, (b) imaginary

Next, we modeled the input impedance versus electrical length for $N=10, 12$ and 14 . The results are shown in Figure 4-16. Note, we normalized the x -axis to a length of $0.1733\lambda_0$ to demonstrate the relative electrical lengths (frequency shifts). The figure shows that the resonance is shifting slightly as the number of basis functions change. However, this change is less than 0.5%. Also, we see that the peak impedance values also change only slightly (by less than 5Ω). We conclude then that with 12 basis functions the solution is adequately converged (which is the same thing concluded for the dipole).

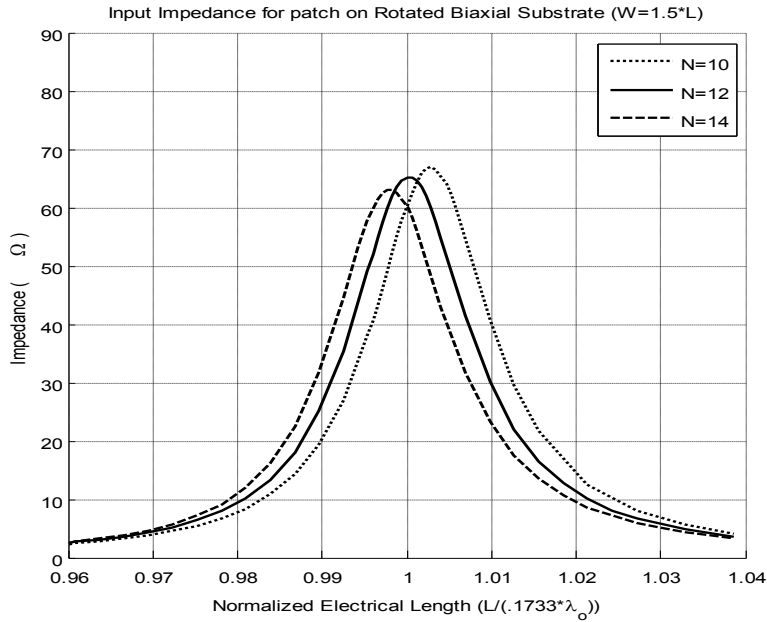


Figure 4-16: Input impedance behavior for $M=1$ and N is increased from 10 to 14

Up to this point our analysis has concentrated on the number of basis functions along the length (in the x -direction). We also need to know how many basis functions are necessary along the width. Figure 4-17 shows the input impedance behavior as M (the number of basis functions along the width) is increased. Here we see that for $M=1, 3$ and 4 there is even less variation than there was when we changed N from 10 to 14. This implies that there is little variation in the current along the width. This most likely is due to the fact that the probe is centered along the width and the dominant cavity mode excited has uniform H-field in the y -direction. The result is a nearly uniform current distribution along the width of the antenna. Future work, as will be discussed in Chapter 5, could investigate further the modal behavior of resonant structures in biaxial media.

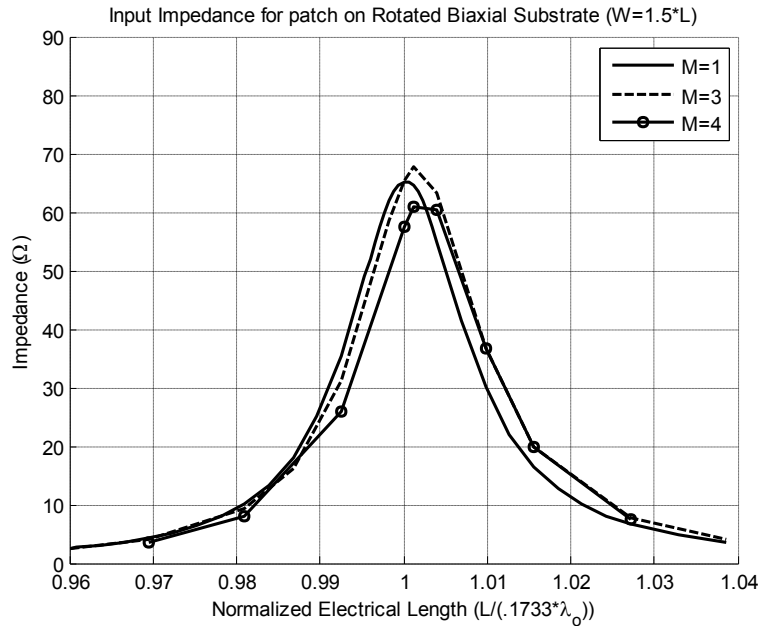


Figure 4-17: Input impedance behavior for $N=12$ and M is increased from 1 to 4

We performed the same analysis with a patch on an isotropic substrate (the same antenna in reference [48]), and an unrotated biaxial substrate with a narrow patch antenna. These analyses reached the same conclusion; very little change in input impedance was observed as M increased and $N=12$ was sufficiently converged. Therefore, for our purposes, we conclude that 12 basis functions along the length of the antenna and 1 basis function along the width will be adequate for modeling the input impedance behavior of a patch antenna. As previously discussed, the x -directed currents will have a triangular variation in the x -direction and a uniform (rectangular pulse) variation in the y -direction. Note that the uniform y -dependence is required. This is not the same as saying there is no y -dependence. If there were no y -dependence, we would not be bounding the antenna in the y -direction. The single uniform pulse is necessary to define the width of the antenna.

We also analyze the radiation patterns of the patch antennas. We want to be sure that the patterns are converging as we increase the number of basis functions as well. Figure 4-18(a) shows that as the number of basis functions in y (M) increases from 1 to 4, the principal polarized radiation pattern does not change. This would be expected if the dominant current is along the x -dimension as was concluded in our investigation of the input impedance convergence. Figure 4-18(b) shows the cross-polarized radiation field. We observe that the magnitude is small and peak magnitude varies little as M increases. However, there is a change in the shape of the cross-pol pattern when increasing M from 1 to 2; the shape remains the same as M is increased beyond two. Therefore, when computing currents for radiation analysis we will use $N=12$ and $M=2$.

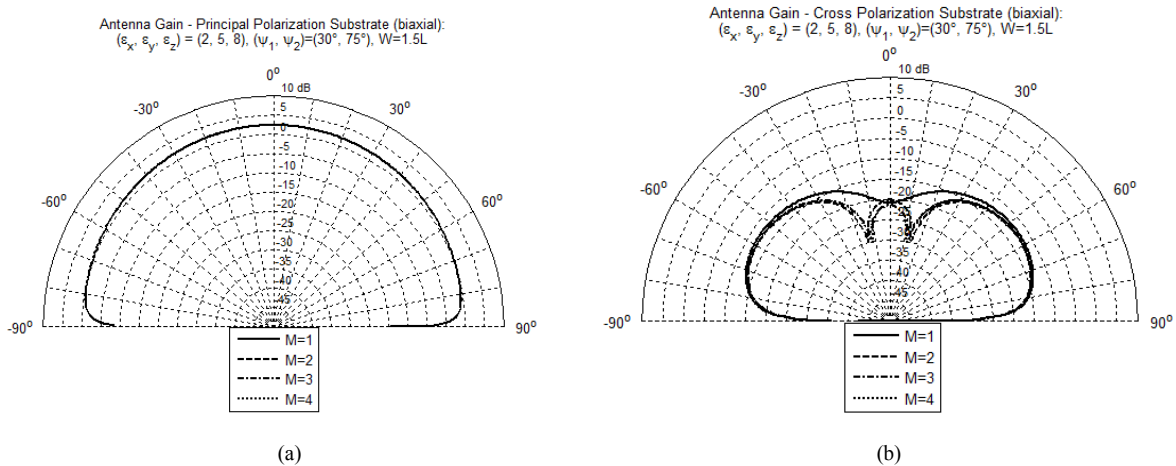


Figure 4-18: Radiation patterns for $N=12$ and M is increased from 1 to 4 (a) principal polarization (b) cross polarization

4.4.3 Performance Analysis

The analysis of the rectangular microstrip patch antenna primarily focuses on input impedance and resonant length. We also analyze the radiation behavior considering both the principal polarized fields and the cross-polarized fields. Cases of varying substrate thicknesses

(heights), patch widths and substrate permittivities are computed and discussed to better understand the behavior of antennas printed on biaxially anisotropic substrates.

4.4.3.1 Input Impedance, Resonant Length and Impedance Bandwidth

The focus of the patch antenna analysis is input impedance, resonant length and impedance bandwidth. All of these parameters will be computed from the input impedance of the antenna. The delta gap source model we applied to the dipole antenna is not applicable to the patch antenna. Therefore, we must derive a new expression, beginning again from [1]

$$Z_{in} = \frac{P_s}{I_{in} I_{in}^*} \quad (4.4.1)$$

where P_s is the input power and I_{in} is still the total input current and, again, the complex input power delivered to the antenna is given by [41]

$$P_s = \iint_{S'} \bar{E}_{i,tan} \cdot \bar{J}_c^* ds' \quad (4.4.2)$$

$\bar{E}_{i,tan}$ is the impressed tangential electric field along the conductor (antenna) due to the vertical probe current (impressed current) while \bar{J}_c^* is the complex conjugate of the induced conduction current along the antenna. The impressed tangential field is not known, as it was for the gap feed. As discussed in Section 4.2.1.3, this field can be computed using the DGF presented in (2.2.16). The electric field is computed using

$$\bar{E}_i = i\omega\mu_o \iiint_{V'} dv' \frac{i}{8\pi^2} \int_{-\infty}^{\infty} d^2\bar{k}_\rho \frac{1}{k_{0z}} e^{-i\bar{k}_0 \cdot \bar{r}} \left\{ \hat{h}_0^- \left[A_{ha} \hat{a}^- e^{i\bar{k}_1^a \cdot \bar{r}'} + B_{ha} \hat{a}^+ e^{i\bar{k}_1^a \cdot \bar{r}'} + A_{hb} \hat{b}^- e^{i\bar{k}_1^b \cdot \bar{r}'} + B_{hb} \hat{b}^+ e^{i\bar{k}_1^b \cdot \bar{r}'} \right] \right. \\ \left. + \hat{v}_0^- \left[A_{va} \hat{a}^- e^{i\bar{k}_1^a \cdot \bar{r}'} + B_{va} \hat{a}^+ e^{i\bar{k}_1^a \cdot \bar{r}'} + A_{vb} \hat{b}^- e^{i\bar{k}_1^b \cdot \bar{r}'} + B_{vb} \hat{b}^+ e^{i\bar{k}_1^b \cdot \bar{r}'} \right] \right\} \cdot \bar{J}_i(\bar{r}') \quad (4.4.3)$$

Note that the primed (source) terms are grouped together. The unprimed (field) terms are not dependent on the primed terms. While the primed terms do depend on the values of k_x and k_y , we can change the order of integration. We move the volume integral over V' inside the spectral integral resulting in

$$\begin{aligned} \bar{E}_i = & \frac{-\omega\mu_o}{8\pi^2} \int_{-\infty}^{\infty} d^2\bar{k}_\rho \frac{e^{-i\bar{k}_0 \cdot \bar{r}}}{k_{0z}} \\ & \iiint_{V'} dv' \left\{ \hat{h}_0^- \left[A_{ha} \hat{a}^- e^{ik_z^{ad}z'} + B_{ha} \hat{a}^+ e^{ik_z^{au}z'} + A_{hb} \hat{b}^- e^{ik_z^{bd}z'} + B_{hb} \hat{b}^+ e^{ik_z^{bu}z'} \right] \right. \\ & \left. + \hat{v}_0^- \left[A_{va} \hat{a}^- e^{ik_z^{ad}z'} + B_{va} \hat{a}^+ e^{ik_z^{au}z'} + A_{vb} \hat{b}^- e^{ik_z^{bd}z'} + B_{vb} \hat{b}^+ e^{ik_z^{bu}z'} \right] \right\} e^{i(k_x x' + k_y y')} \cdot \bar{J}_i(\bar{r}') \end{aligned} \quad (4.4.4)$$

The volume integral is the same integral we manipulated in the excitation integral of the reaction equation. In Section 4.2.1.3 the volume integral reduced to the complex conjugate of the Fourier transform of the impressed current for the spectral expansion of each biaxial wave. Following the same steps as outlined in Section 4.2.1.3 we can rewrite equation (4.4.4) in the form

$$\begin{aligned} \bar{E}_i = & \frac{-\omega\mu_o}{8\pi^2} \int_{-\infty}^{\infty} d^2\bar{k}_\rho \frac{e^{-i\bar{k}_0 \cdot \bar{r}}}{k_{0z}} \\ & \left\{ \hat{h}_0^- \left[A_{ha} \hat{a}_z^- \tilde{J}_i(-k_x, -k_y, -k_z^{ad}) + B_{ha} \hat{a}_z^+ \tilde{J}_i(-k_x, -k_y, -k_z^{au}) + A_{hb} \hat{b}_z^- \tilde{J}_i(-k_x, -k_y, -k_z^{bd}) + B_{hb} \hat{b}_z^+ \tilde{J}_i(-k_x, -k_y, -k_z^{bu}) \right] \right\} \\ & \left\{ + \hat{v}_0^- \left[A_{va} \hat{a}_z^- \tilde{J}_i(-k_x, -k_y, -k_z^{ad}) + B_{va} \hat{a}_z^+ \tilde{J}_i(-k_x, -k_y, -k_z^{au}) + A_{vb} \hat{b}_z^- \tilde{J}_i(-k_x, -k_y, -k_z^{bd}) + B_{vb} \hat{b}_z^+ \tilde{J}_i(-k_x, -k_y, -k_z^{bu}) \right] \right\} \end{aligned} \quad (4.4.5)$$

Now we substitute the expression in equation (4.4.5) into the power equation (4.4.2) which yields

$$\begin{aligned} P_s = & \iint_{S'} ds' \frac{-\omega\mu_o}{8\pi^2} \int_{-\infty}^{\infty} d^2\bar{k}_\rho \frac{e^{-i\bar{k}_0 \cdot \bar{r}'}}{k_{0z}} \\ & \left\{ \hat{h}_0^- \left[A_{ha} \hat{a}_z^- \tilde{J}_i(-k_x, -k_y, -k_z^{ad}) + B_{ha} \hat{a}_z^+ \tilde{J}_i(-k_x, -k_y, -k_z^{au}) + A_{hb} \hat{b}_z^- \tilde{J}_i(-k_x, -k_y, -k_z^{bd}) + B_{hb} \hat{b}_z^+ \tilde{J}_i(-k_x, -k_y, -k_z^{bu}) \right] \right\} \\ & \left\{ + \hat{v}_0^- \left[A_{va} \hat{a}_z^- \tilde{J}_i(-k_x, -k_y, -k_z^{ad}) + B_{va} \hat{a}_z^+ \tilde{J}_i(-k_x, -k_y, -k_z^{au}) + A_{vb} \hat{b}_z^- \tilde{J}_i(-k_x, -k_y, -k_z^{bd}) + B_{vb} \hat{b}_z^+ \tilde{J}_i(-k_x, -k_y, -k_z^{bu}) \right] \right\} \cdot \bar{J}_c^*(\bar{r}') \end{aligned}$$

(4.4.6)

The induced conduction current is known after the method of moments solution is complete.

This current is given by

$$\bar{J}_c^*(\bar{r}') = \hat{x} \sum_m a_m^* J_x^{m*}(x') J_x^{m*}(y') + \hat{y} \sum_n b_n^* J_y^{n*}(x') J_y^{n*}(y') \quad (4.4.7)$$

Since we are using Galerkin's method the expansion and test functions have the same form. The expansion functions in (4.4.7) are given by J_x^m and J_y^n and so the induced conduction current is the same as the test current multiplied by the current coefficients computed by the method of moments. If we let the terms inside the square brackets associated with region 1 in the integral equal $R1_{terms}$, substitute (4.4.7) into (4.4.6) and let $z'=0$ (along the antenna), we obtain

$$\begin{aligned} P_s = & \iint_{S'} ds' \frac{-\omega\mu_o}{8\pi^2} \int_{-\infty}^{\infty} d^2\bar{k}_\rho \frac{e^{-i(k_x x' + k_y y')}}{k_{0z}} \sum_m a_m^* J_x^{m*}(x') J_x^{m*}(y') \left\{ \begin{array}{l} h_{0x}^- [R1_{terms}] \\ + v_{0x}^- [R1_{terms}] \end{array} \right\} \\ & + \iint_{S'} ds' \frac{-\omega\mu_o}{8\pi^2} \int_{-\infty}^{\infty} d^2\bar{k}_\rho \frac{e^{-i(k_x x' + k_y y')}}{k_{0z}} \sum_n b_n^* J_y^{n*}(x') J_y^{n*}(y') \left\{ \begin{array}{l} h_{0y}^- [R1_{terms}] \\ + v_{0y}^- [R1_{terms}] \end{array} \right\} \end{aligned} \quad (4.4.8)$$

where h_{0x}^- is the x -component of the downward propagating, horizontally polarized wave, h_{0y}^- is the y -component, v_{0x}^- is the x -component of the downward propagating, vertically polarized wave, and v_{0y}^- is the y -component. The current coefficients are constants that do not depend on any of the integration parameters. Removing these coefficients from the integral and integrating over x' and y' yields

$$\begin{aligned}
P_s = & \sum_m a_m^* \frac{-\omega\mu_o}{8\pi^2} \int_{-\infty}^{\infty} d^2\bar{k}_\rho \frac{1}{k_{0z}} \tilde{J}_x^{m*}(k_x) \tilde{J}_x^{m*}(k_y) \left\{ \begin{array}{l} h_{0x}^- [R1_{terms}] \\ + v_{0x}^- [R1_{terms}] \end{array} \right\} \\
& + \sum_n b_n^* \frac{-\omega\mu_o}{8\pi^2} \int_{-\infty}^{\infty} d^2\bar{k}_\rho \frac{1}{k_{0z}} \tilde{J}_y^{n*}(k_x) \tilde{J}_y^{n*}(k_y) \left\{ \begin{array}{l} h_{0y}^- [R1_{terms}] \\ + v_{0y}^- [R1_{terms}] \end{array} \right\}
\end{aligned} \tag{4.4.9}$$

The resulting integral is exactly the integral we computed for the V -vector in the method of moments solution (see equation (4.2.37)). The power then can be written as the sum of the product of each term in the current coefficient vector and voltage vector (or dot product)

$$P_s = \sum_m a_m^* V_m + \sum_n b_n^* V_n \tag{4.4.10}$$

The current on the probe is assumed to be 1 A, therefore the input impedance of a probe-fed microstrip patch antenna is given by

$$Z_{in} = \frac{P_s}{I_{in}^* I_{in}} = \sum_m a_m^* V_m + \sum_n b_n^* V_n \tag{4.4.11}$$

This is the same equation presented by Pozar in [19] and will be used in our input impedance analysis.

4.4.3.1.1 Isotropic and Uniaxial Substrates

The first antennas modeled are reference antennas used to verify our results against published results. We have chosen two reference patch antennas, one on an isotropic substrate and one on a uniaxial substrate. The chosen isotropic reference is a rectangular microstrip patch antenna by W. F. Richards [48]. In his section on microstrip antennas, Richards uses the reference antenna to demonstrate an empirical method of determining the probe self reactance.

We use this method in our analysis to help determine resonant length. The probe reactance can be approximated using a simple equation presented by Pozar [19] for isotropic substrates. However, this expression is not applicable in complex media. In fact, in Pozar's paper on microstrip antennas printed on uniaxial substrates, he ignores probe reactance when computing input impedance. As discussed previously, our idealized model does not lend itself to analyzing the probe self impedance term in detail.

The isotropic reference used is a rectangular patch with length of 7.62 cm and width of 11.43 cm. The substrate has permittivity of $2.62\epsilon_0$ and height of 0.16 cm. The frequency is varied in the 1200 MHz region. Our results are shown in Figure 4-19(a). Observe the sharp drop in the imaginary part of the input impedance around 1205 MHz. While this is a resonant type of behavior, the reactance does not actually pass through zero. According to Richards [48], this offset is due to the probe self impedance (which is ignored in Figure 4-19(a)) and the probe reactance can be determined by finding the center of this drop off. After subtracting the probe reactance from the computed input reactance, the input impedance plot changes to a more recognizable resonant behavior (as shown in Figure 4-19(b)).

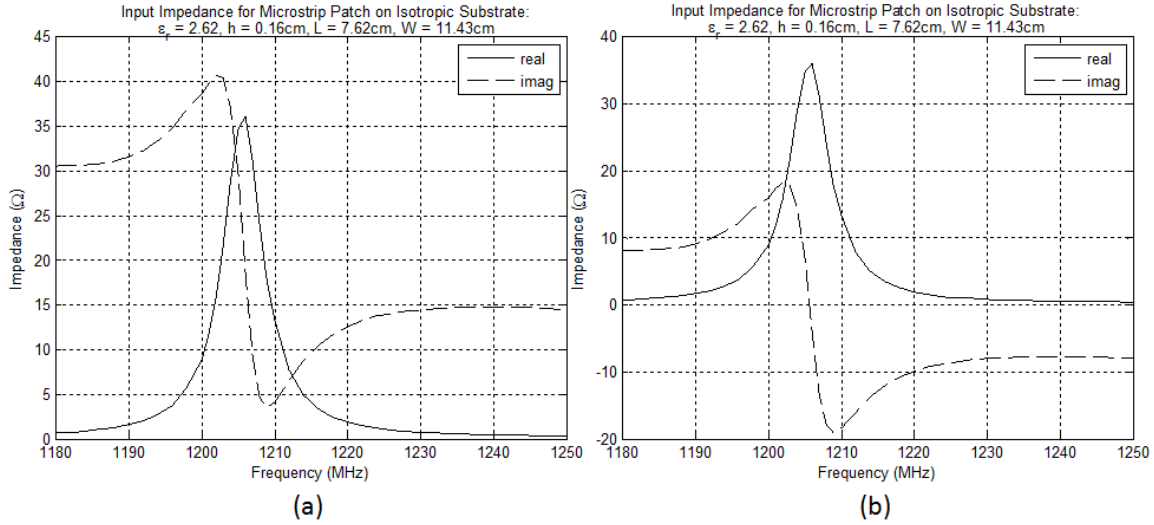


Figure 4-19: Input impedance for isotropic microstrip antenna (a) prior to probe reactance compensation, (b) with probe reactance compensation

We do note a few deviations in our result from Richard's published result [48]. First, the resonant frequency here is approximately 1205MHz whereas in the published result it is 1225MHz. This is a 25MHz or 2% difference. This may be attributed to several sources. First, the medium permittivity is not explicitly described as lossless and there is no loss tangent attributed to it. We assumed it to be lossless, but there may have been a loss that could account for some deviation. Also, an altogether different model was used, which could account for some additional deviations. Finally, in all of the patch modeling, our substrates are very weakly isotropic. While this is likely to be a smaller contribution, all together these sources could account for the 2% difference. The other deviation is in the approximated probe reactance. The reference shows a probe reactance of approximately 7.5Ω while we arrive at 22.5Ω . However, the reference does not describe the model used for the probe. If their probe diameter is larger

(less inductance) than our idealized model, this would account for the difference in probe reactance.

We also consider the patch antenna printed on a uniaxial substrate as investigated by Pozar [26]. The material of interest is “Epsilam-10”, which is known to be a negative uniaxial material with $(\epsilon_x, \epsilon_y, \epsilon_z) = (13, 13, 10.2)$. Pozar considered three media, all with ϵ_z of 10.2. He considered a positive uniaxial medium with ϵ_x of 6, an isotropic medium with ϵ of 10.2 and the negative uniaxial Epsilam-10. He plots the resonant length of all three versus substrate height. We consider a subset of his analysis. We compute the resonant length for three heights of Epsilam-10, then compare the other two media at a height of $0.02\lambda_0$. We have chosen these points to show that our code provides similar resonant length results and the same trends demonstrated by Pozar.

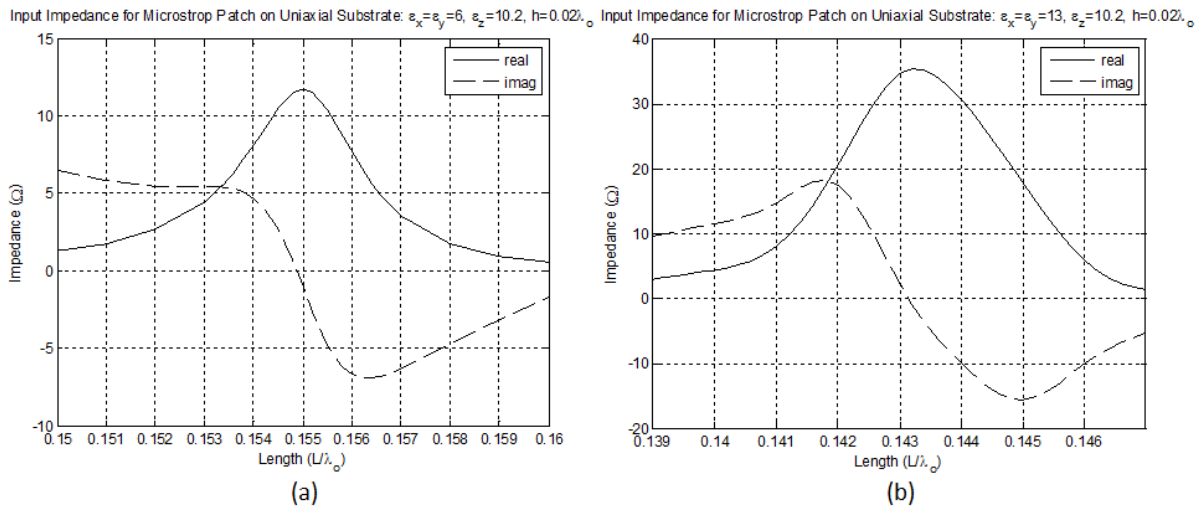


Figure 4-20: Input impedance for microstrip patch antenna with width of $0.23\lambda_0$ printed on uniaxial substrate with height of $0.02\lambda_0$. (a) positive uniaxial: $(\epsilon_x, \epsilon_y, \epsilon_z) = (6, 6, 10.2)$, (b) negative uniaxial: $(\epsilon_x, \epsilon_y, \epsilon_z) = (13, 13, 10.2)$

Figure 4-20 shows the input impedance for the two uniaxial substrates at height $0.02\lambda_0$. Note that the scales for impedance for the two cases are different. Also note that the

“probe reactance” approximation proposed by Richards [48] has been used here; a reactance term has been subtracted out of the computed reactance at the resonant point. Figure 4-21 shows the summary of the 5 patch antennas considered. We observe the same trend as demonstrated by Pozar. As height increases, resonant length decreases. We also see that as ϵ_x decreases, resonant length increases. The isotropic medium resonant length is closer to the resonant length of Epsilam-10 than to the uniaxial medium with ϵ_x of 6. These are the same behaviors published in Pozar’s paper [26] and the lengths themselves appear to match as closely as can be discerned from the figure provided. However, a more important note of comparison is with measured results. Pozar published a chart with measured results from an antenna printed on Epsilam-10 (substrate height of $0.02\lambda_0$) and used this measured result to verify his computation. The measured resonant length is $.1423\lambda_0$ and Pozar’s computed resonant length is $.1431\lambda_0$. Our computed resonant length is $.1429\lambda_0$ which compares very well with Pozar’s computed result and is actually slightly closer to the measured result than Pozar’s.

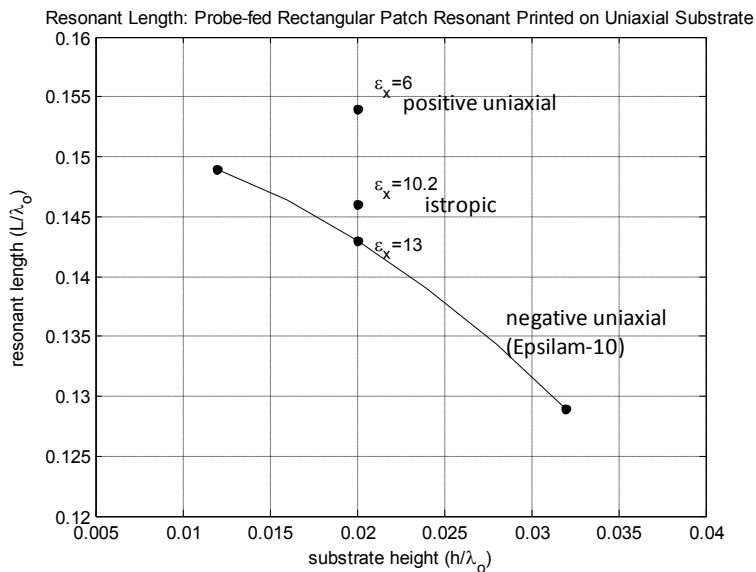


Figure 4-21: Resonant length of probe fed patch antennas on uniaxial (one isotropic) substrates of varying heights

This verifies our results against simulated and measured data. It also confirms that Richards' method for subtracting out a probe reactance, or "residual reactance", term at resonance is an adequate method for determining resonant length. In effect, Richards' method is defining resonant length as the point of peak resistance and a discontinuity in reactance then forcing the input reactance to zero at that point. We have chosen to ignore probe impedance (as Pozar did as well) with the idealized probe model. Therefore, we will not verify whether or not this term is equal to the probe reactance. We continue to use this method in our analyses as it proved useful in the uniaxial case, but we call this term *residual reactance* so as not to confuse it with the probe reactance that may be computed with a rigorous probe model.

4.4.3.1.2 Biaxial Substrates

The isotropic and uniaxial results verified our methodology for modeling a microstrip patch antenna. This method is used to model patch antennas printed on biaxial substrates. The substrates considered have biaxial permittivities of $(\epsilon_x, \epsilon_y, \epsilon_z) = (2, 5, 8)$ and are either unrotated or rotated by $\psi_1 = 30^\circ$ and $\psi_2 = 75^\circ$. The substrate height varies for different cases. For most cases, the typical width-to-length ratio of 1.5 was used. We also consider two special cases of the square antenna where the width is equal to the length and a narrow patch antenna where the width-to-length ratio is 0.55. This width is larger than a dipole, but still smaller than the length.

We are primarily interested in the resonant length and impedance bandwidth of the antennas. We have already defined resonant length. The impedance bandwidth is determined from the return loss. Return loss is computed from the voltage reflection coefficient [49] given by

$$\Gamma = \frac{Z_{in} - Z_o}{Z_{in} + Z_o} \quad (4.4.12)$$

where Γ is the reflection coefficient, Z_{in} is the input impedance and Z_o is the characteristic impedance (we are using 50Ω , a common standard). Then the return loss (RL) in dB is computed using

$$RL = 20 \log_{10} |\Gamma| \quad (4.4.13)$$

For each antenna we first determined the resonant length with the probe at some arbitrary location. Next, the antenna length was fixed at resonance and the probe was moved until we located the point where the input resistance was approximately 50Ω . We then ran these parameters across electrical lengths. We determined the 10dB impedance bandwidth of the antenna from the -10dB points on the return loss figure. Figure 4-22 through Figure 4-25 are representative of the input impedance and return loss results obtained for the antennas modeled. In these representative cases the thickness of all four substrates is $0.02\lambda_o$ and the width-to-length ratio is 1.5. A total of 16 cases have been considered. Table 4-2 summarizes the behaviors of all of the antennas modeled. Note that we have included the residual reactance term (X_{res}) as previously discussed.

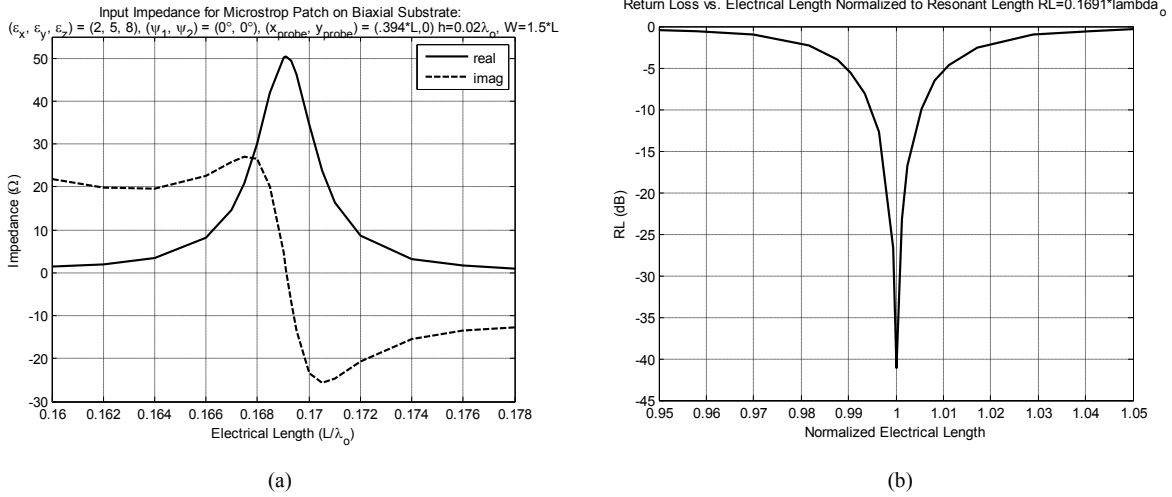


Figure 4-22: Input impedance (a) and return loss (b) of rectangular patch printed on unrotated biaxial substrate (2, 5, 8) of height $0.02\lambda_0$

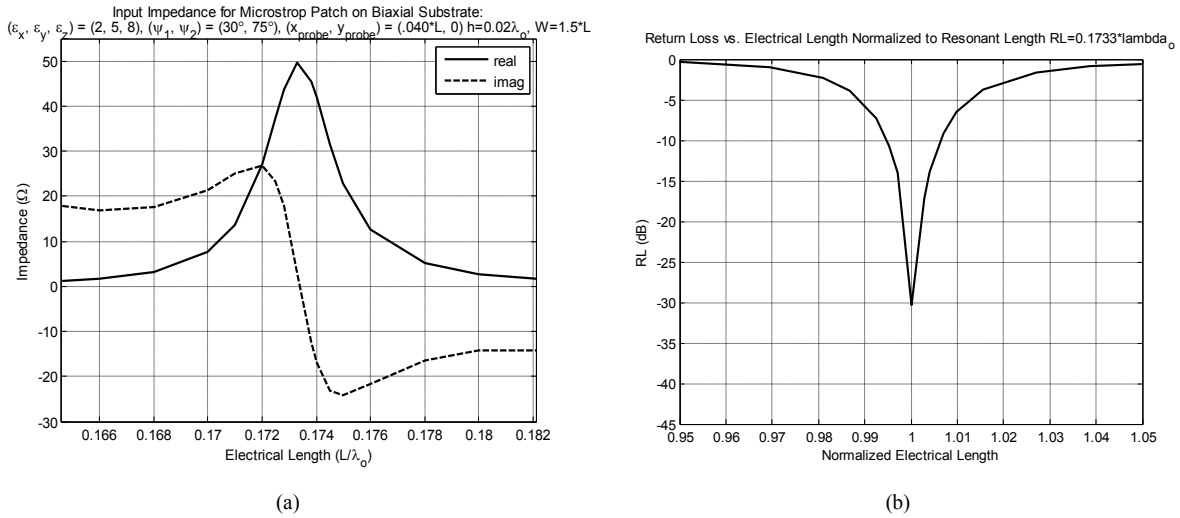


Figure 4-23: Input impedance (a) and return loss (b) of rectangular patch printed on rotated ($\psi_1 = 30^\circ$ $\psi_2 = 75^\circ$) biaxial substrate of height $0.02\lambda_0$

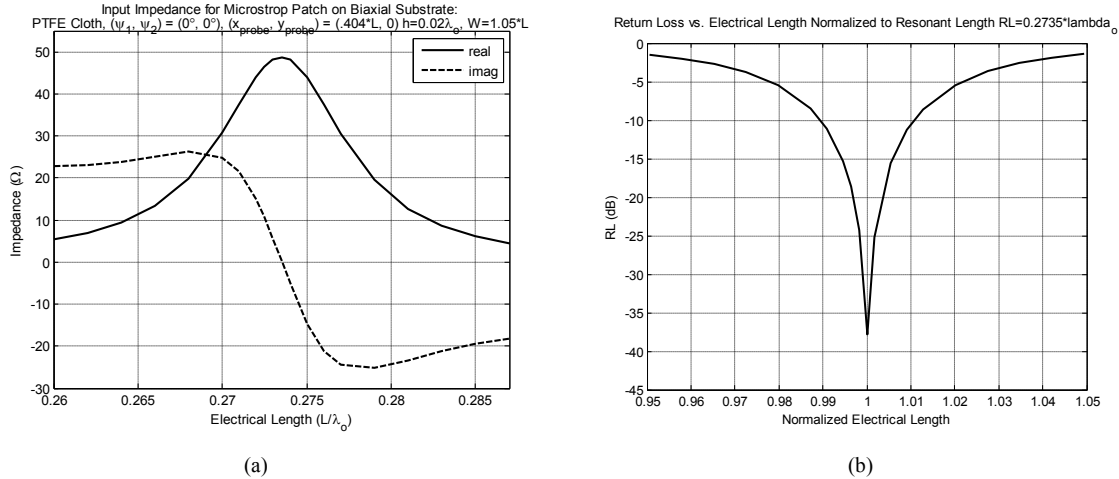


Figure 4-24: Input impedance (a) and return loss (b) of rectangular patch printed on PTFE cloth of height $0.02\lambda_0$

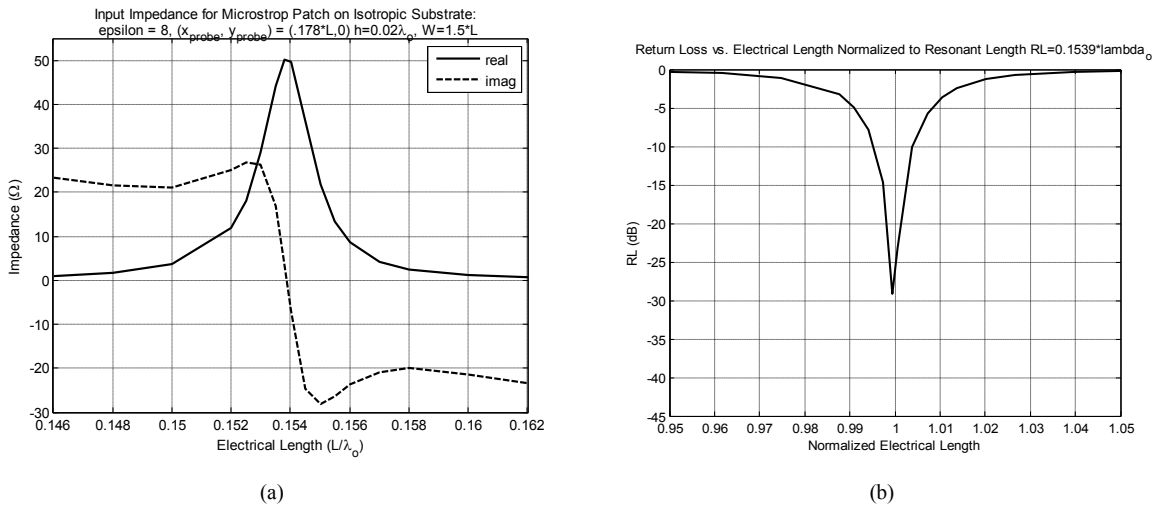


Figure 4-25: Input impedance (a) and return loss (b) of rectangular patch printed on isotropic substrate ($\epsilon_r = 8$) of height $0.02\lambda_0$

Table 4-2: Half-Wave Resonant Lengths of Rectangular Microstrip Patch Antennas

Case	Permittivity ($\epsilon_x, \epsilon_y, \epsilon_z$)	Rotation (Ψ_1, Ψ_2)	W/L	height/ λ_0	x_s/L probe pos.	X_{res} (Ω)	Res. Length (L/λ_0)	BW (%)
1	(2, 5, 8)	($0^\circ, 0^\circ$)	1.5	0.02	0.394	80	0.169	1.06
2	(2, 5, 8)	($0^\circ, 0^\circ$)	1.5	0.01	0.405	35	0.175	0.65
3	(2, 5, 8)	($0^\circ, 0^\circ$)	1.5	0.03	0.392	70	0.168	1.75

4	(2, 5, 8)	(0°, 0°)	1.5	0.10	0.430	17	0.142	7.20
5	(2, 5, 8)	(0°, 0°)	1	0.02	0.390	184	0.174	0.80
6	(2, 5, 8)	(0°, 0°)	0.55	0.02	0.126	285	0.182	0.55
7	(2, 5, 8)	(30°, 75°)	1.5	0.02	0.040	160	0.173	1.16
8	(2, 5, 8)	(30°, 75°)	1.5	0.10	0.407	18	0.142	9.70
9	(8, 5, 2)	(0°, 0°)	1.5	0.02	0.359	20	0.217	0.50
10	(2.45, 2.89, 2.95) [PTFE]	(0°, 0°)	1.5	0.02	0.404	50	0.274	2.17
11	(2.45, 2.89, 2.95) [PTFE]	(30°, 75°)	1.5	0.02	0.402	58	0.274	2.19
12	8 [isotropic]	-	1.5	0.02	0.178	107	0.154	0.87
13	8 [isotropic]	-	1.5	0.01	0.283	235	0.172	0.58
14	8 [isotropic]	-	1.5	0.03	0.244	64	0.156	1.70
15	2 [isotropic]	-	1.5	0.02	0.412	30	0.330	2.70
16	5 [isotropic]	-	1.5	0.02	0.350	86	0.208	1.65

The first parameter we investigated was the height of the substrate. We modeled patch antennas on unrotated biaxial substrates with heights $0.01\lambda_0$, $0.02\lambda_0$, $0.03\lambda_0$, and $0.10\lambda_0$ (Cases 1 through 4). First, we observe that increasing the thickness of the substrate decreases the resonant length and increases the bandwidth. The same is true when the medium is rotated (Cases 7 and 8); the thinner substrate (Case 7) has a longer resonant length and narrower bandwidth. This resonant length behavior as a function of substrate thickness is the same behavior shown for the uniaxial substrate (in Figure 4-21).

The next investigation was on the effect of the width on the resonant length. We varied the width of the antenna printed on the unrotated biaxial substrate with a fixed height of $0.02\lambda_0$ (Case 1, Case 5 and Case 6). As width increases from $0.55L$ to $1.5L$, the resonant length decreased. If we consider the case of the dipole antenna as a special case of the rectangular patch, this trend is further verified as the resonant length of the very thin dipole is considerably greater than the patch.

The third parameter investigated is rotation. When the strongly biaxial medium is rotated, the resonant length changed very little but the bandwidth increased by 2% (see Cases 1 and 7). This behavior is not observed when the medium is PTFE (Teflon cloth), which is weakly biaxial (Cases 10 and 11). This behavior upon rotation raises the question of what controls the resonant length of the antenna on a biaxial substrate.

Several additional antennas were investigated in an attempt to correlate the resonant behaviors of patches with biaxial substrates to those with isotropic substrates and answer the question of what is controlling the resonant length. First, we ran isotropic antennas with permittivities equal to the individual permittivities in the unrotated biaxial tensor. Observe for Cases 12, 15 and 16 in Table 4-2 that the resonant length of the patch on the unrotated biaxial substrate has a resonant length between the resonant lengths of the isotropic antennas with ϵ_r of 5 and 8, but is closer to ϵ_r of 8 (Case 12). We might have expected to observe a resonant length similar to an isotropic antenna with permittivity close to the average of the biaxial values, but this is not the case.

The question is then “is the resonant length governed by the largest value in the tensor, the z -directed permittivity or some combination?” To answer this question, we changed the biaxial medium from “positive” biaxial (increasing permittivity from ϵ_x to ϵ_z) to “negative” biaxial such that the maximum permittivity is ϵ_x and the minimum is ϵ_z as in Case 9 shown in Table 4-2. If the resonant length is governed by the z -directed permittivity we expect the resonant length of this antenna to be closest to the resonant length of the antenna printed on the isotropic medium with $\epsilon_r=2$. The resonant length of this antenna is greater than the case where the permittivities are in the opposite order, it is closer to the $\epsilon_r=5$ case. While this change did

increase the resonant length significantly, it is not clear that the z -directed permittivity is dominating the resonant length. It does however show that if you are looking for a shorter resonance, the z -component should be larger than the x -component.

4.4.3.2 Radiation Behavior

The radiation behavior of the patch antennas is also of interest. We compute the far fields the same way we did in Section 4.3.1.2.3, using the method of stationary phase. However, for the patch antenna we are interested in both the principal polarization pattern and the cross polarization pattern. There are several definitions of cross polarization. In his paper, Ludwig [50] proposes three definitions of reference (or primary) polarization and cross polarization:

1. “In a rectangular coordinate system, one unit vector is taken as the direction of the reference polarization, and another as the direction of cross polarization”
2. “In a spherical coordinate system the same thing is done using the unit vectors tangent to a spherical surface”
3. “Reference and cross polarization are defined to be what one measures when antenna patterns are taken in the usual manner”

Definitions one and two are antenna-centric while definition three is receiver-centric. For example, the rectangular unit vector in definition one is taken such that a transmitting antenna is at the center of an x - y - z coordinate system. In the third definition, the coordinate system is centered at some receiving antenna position. Schuman [51] provides a straightforward way of computing the principal and cross polarization by defining the polarization vectors as

$$\hat{p} = \cos(\phi_r - \phi_0)\hat{a}_\theta - \sin(\phi_r - \phi_0)\hat{a}_\phi \quad (4.4.14)$$

$$\hat{c} = \sin(\phi_r - \phi_0)\hat{a}_\theta - \cos(\phi_r - \phi_0)\hat{a}_\phi \quad (4.4.15)$$

where ϕ_0 is angle for the dominant electric current, chosen to align with the antenna orientation and ϕ_r is the angle to the far field point (or the receiver). If the far-field electric field is given by

$$\bar{E} = \hat{a}_\theta E_\theta + \hat{a}_\phi E_\phi \quad (4.4.16)$$

then the principal and cross polarization electric fields are given by

$$E_p = \bar{E} \cdot \hat{p} = \cos(\phi_r - \phi_0)E_\theta - \sin(\phi_r - \phi_0)E_\phi \quad (4.4.17)$$

$$E_c = \bar{E} \cdot \hat{c} = \sin(\phi_r - \phi_0)E_\theta - \cos(\phi_r - \phi_0)E_\phi \quad (4.4.18)$$

respectively. This is a general formulation for principal and cross polarized fields of a reference antenna. In our analysis, we assume ϕ_0 and ϕ_r are equal. For this case the principal-pol reduces to E_θ and the cross-pol reduces to E_ϕ . The principal and cross polarization fields are normalized by reference field as was done for the total directive gain shown in equation (4.3.25). For all cases, we modeled the resonant length, 50Ω antennas from Table 4-2.

The first set of radiation patterns are for the patches printed on unrotated biaxial substrates with permittivity $(\epsilon_x, \epsilon_y, \epsilon_z) = (2, 5, 8)$. The antenna width-to-length ratio is fixed at 1.5 and the height (thickness) is varied with respect to wavelength. Figure 4-26(a) shows the resulting principal polarization field and Figure 4-26(b) shows the cross polarized field. We note that when the substrate is very thin ($0.01\lambda_0$), the cross-pol field is very small (approximately -35 dBi). When the substrate is thicker, the cross-pol is larger. For all three heights, the principal polarization pattern is essentially unchanged.

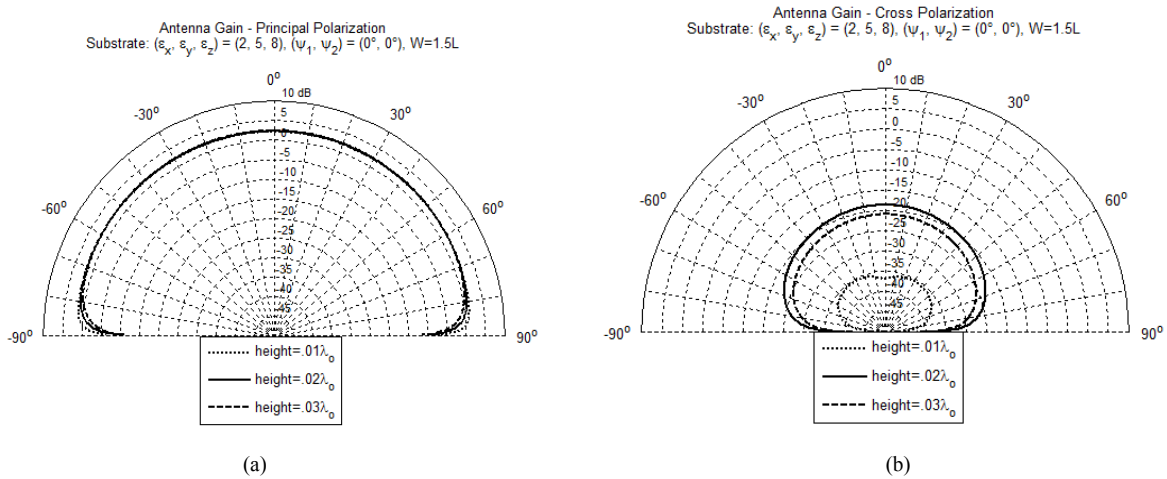


Figure 4-26: Radiation patterns, unrotated biaxial substrate with permittivity $(\epsilon_x, \epsilon_y, \epsilon_z) = (2, 5, 8)$ and varied height (a) principal polarization, (b) cross polarization

The patterns generated by the patch on the biaxial substrate can best be understood within the context of similar antennas on isotropic substrates. Patterns generated by patches printed on isotropic substrates with $\epsilon_r = 8$ and the same heights are shown in Figure 4-27 (a) and (b). First, we observe that the principal polarization field (a) is again unchanged by changing the height. We also note that these fields are approximately equal to the principal-pol fields generated by the biaxial patch. The cross-polarized fields (b) however are different. For a height of $0.02\lambda_0$ the cross-polarized field when the substrate is biaxial is approximately 7 dB smaller than when the substrate is isotropic. When the height is increased to $0.03\lambda_0$, the cross-pol is again larger than it was when the substrate is biaxial, but the difference is smaller (2 dB). Again, we observe that when the height is $0.01\lambda_0$ the cross-pol is very small and approximately the same as in the biaxial case. We can say then, the cross polarized field of the patch on the biaxial substrate is less than the cross polarized field of the patch on the isotropic substrate with relative permittivity of 8. Another point of comparison is isotropic substrates of varying relative

permittivities (Figure 4-28 (a) and (b)). Close inspection of the cross-polarized fields show that when the isotropic relative permittivity is 5, the cross-pol field most closely matches the patch on the biaxial substrate. This indicates that, with respect to the cross-polarized far field, the biaxial patch is acting most like it is an isotropic substrate of permittivity 5. This indicates some interesting complex behavior of the patch printed on the biaxial medium. We noted previously that the input impedance behavior more closely resembled the isotropic medium with permittivity 8. Here we observe the radiated fields more closely resemble the isotropic medium with permittivity 5.

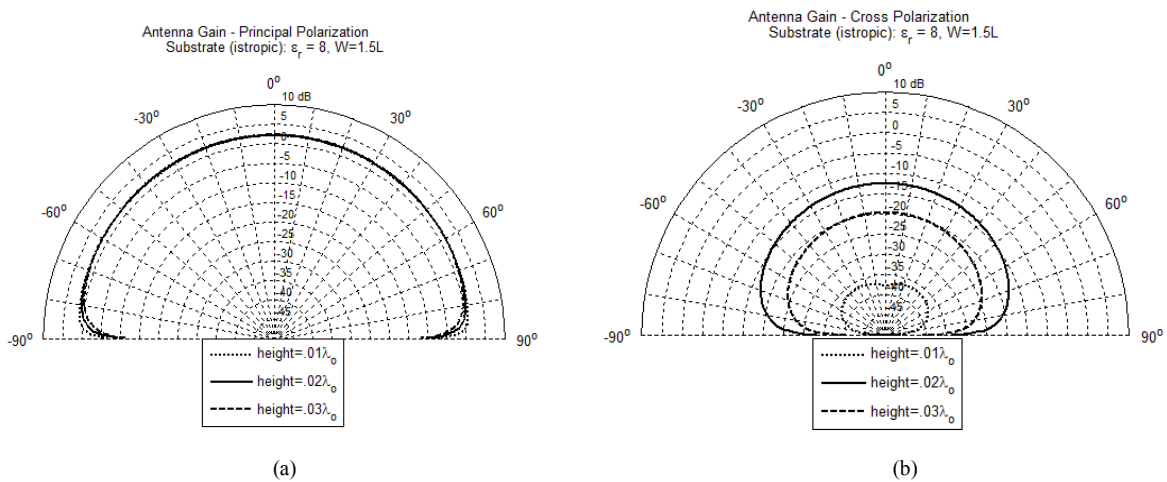


Figure 4-27: Radiation patterns, substrate with isotropic permittivity $\epsilon_r = 8$ and varied height (a) principal polarization, (b) cross polarization

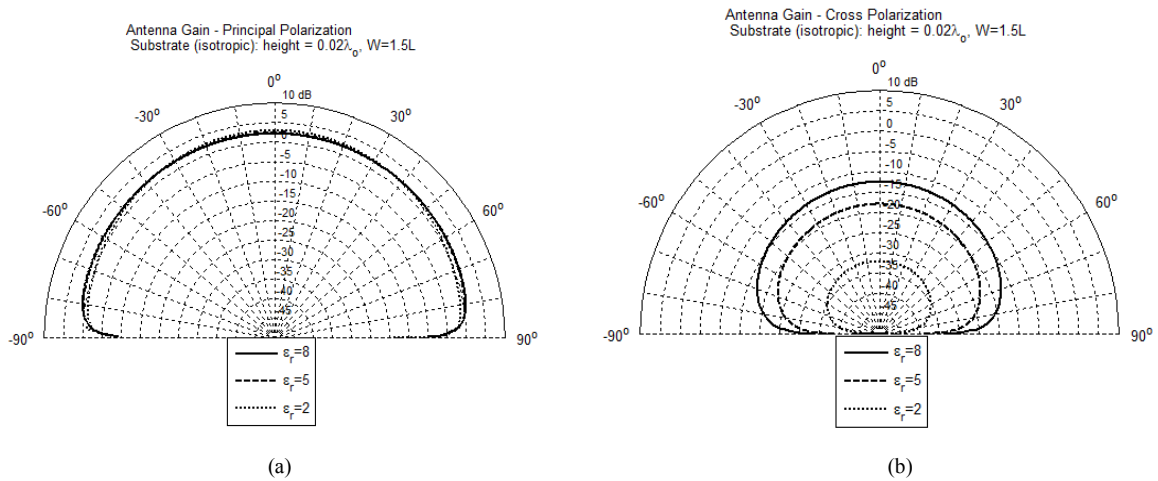


Figure 4-28: Radiation patterns, substrate thickness $0.02\lambda_0$ varied isotropic permittivity (a) principal polarization, (b) cross polarization

The orientation of the biaxial substrate is also of interest. In Figure 4-29 the principal (a) and cross (b) polarization patterns are plotted for the rotated and unrotated biaxial substrate with permittivity $(\epsilon_x, \epsilon_y, \epsilon_z) = (2, 5, 8)$ and height $0.02\lambda_0$. The cross-pol behavior of the antenna on the rotated case is significantly different than any of the other patterns. There are two wide lobes off boresight and nulls in the patterns at approximately $\pm 10^\circ$. There may be some applications in which suppressing the cross polarized field at some angle is important. The orientation of a biaxial substrate could be modified to achieve this.

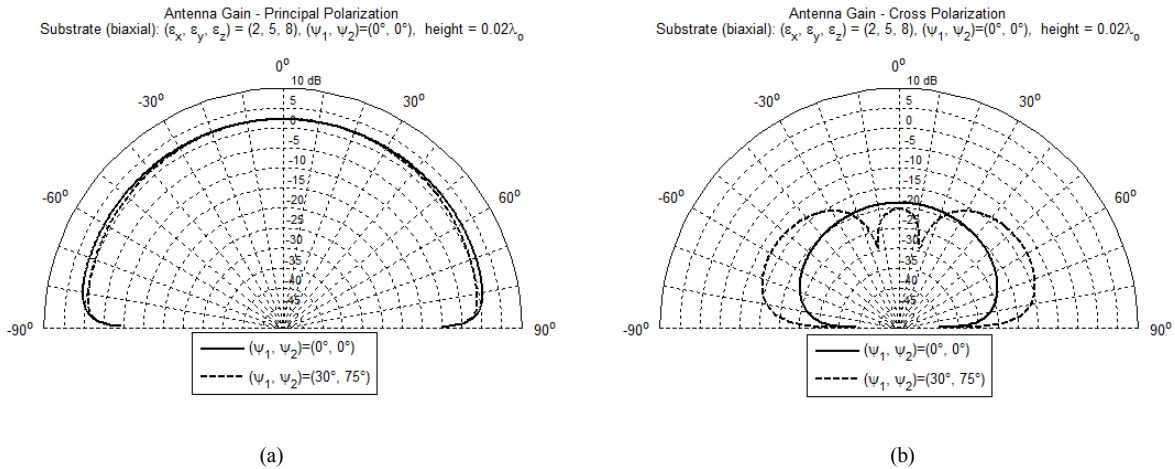
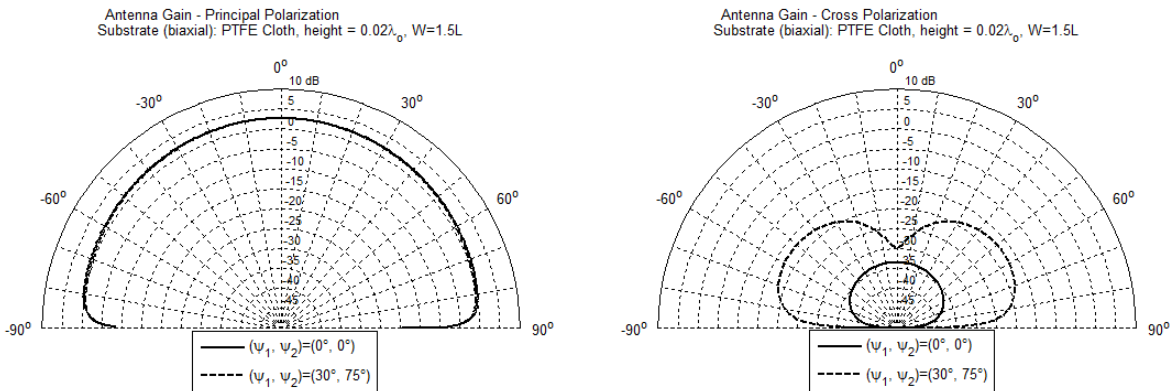


Figure 4-29: Radiation patterns, biaxial substrate with permittivity $(\epsilon_x, \epsilon_y, \epsilon_z) = (2, 5, 8)$ and two rotations (a) principal polarization, (b) cross polarization

Again when the medium is PTFE cloth, a weakly biaxial medium, we observe a change in the shape of the cross polarized field as shown in Figure 4-30(b). The figure shows a small dip or null in the cross-pol pattern at boresight and two wide lobes. Also of interest is that the overall cross-pol pattern is much larger when the medium is rotated. In our previous analyses, rotation of PTFE resulted in little change in antenna performance, however, here we observe that the cross-pol pattern is sensitive to medium rotation even when it is weakly biaxial.



(a)

(b)

Figure 4-30: Radiation patterns, biaxial PTFE cloth substrate with two rotations (a) principal polarization, (b) cross polarization

We conclude our analysis of microstrip patch antennas printed on biaxially anisotropic substrates. We have observed that the behavior of these antennas is quite complex. They cannot be simply predicted based on the individual permittivities that make up the substrate tensor. Conclusions drawn from this work and future extensions of this work are discussed in Chapter 5.

5 CONCLUSIONS AND FUTURE WORK

This research had two primary objectives. The first was to provide a better understanding of the behavior of electromagnetic waves at interfaces with biaxially anisotropic materials. The second was to understand the behavior of microstrip antennas printed on biaxially anisotropic substrates. The first objective provided the framework for all subsequent analyses. In this chapter we summarize the primary contributions of this research and provide suggestions for future research in this area.

In Chapter 2, we studied the reflection and transmission behaviors of electromagnetic waves at isotropic-biaxial interfaces. We considered half-space cases with waves impinging from either medium type and consider the two-layer case. We showed that if a wave is incident from an isotropic region to a biaxial region, the wave which is more strongly reflected can change. At small angles of incidence the vertically polarized wave may be more strongly reflected; as the angle of incidence increases, the horizontally polarized wave may be more strongly reflected. Although the vertically polarized wave may be more strongly reflected at small angles of incidence, it can still experience the Brewster angle effect and reach an angle of total transmission. This is completely different from anything observed at an isotropic-isotropic boundary. At these boundaries the horizontally polarized wave is always more strongly reflected than the vertically polarized wave. We also showed that when there are two layers (a biaxially anisotropic layer bounded by two isotropic layers), the vertically polarized wave can experience total transmission at more than one angle of incidence. This multiple Brewster angle effect was observed primarily due to the layer thickness.

In Chapter 3 we introduced the eigenvector dyadic Green's function (E-DGF). We also applied the symmetric property of the dyadic Green's function (DGF) to obtain the Green's function for the electric field in region 0 generated by a source in region 1. We also discussed the benefits of using this Green's function. This work was the first to use this Green's function to model microstrip antennas. Pettis [1] used the same Green's function to model Hertzian dipoles, but this work takes the E-DGF a step further in using it in a method of moments solution.

In Chapter 4 we presented our results for microstrip antennas printed on biaxially anisotropic substrates. First, we modeled gap-fed dipole antennas. We showed that our results agreed with many published results including Pettis's [1] results for the same type of dipoles. Pettis used a transition matrix dyadic Green's function to model his dipole. The agreement shown between the two is verification of the two methods. We also showed that rotating the medium with respect to the reference coordinate system had little effect on the medium with weak anisotropy (PTFE cloth) but did have a significant effect on the medium with strong anisotropy.

The largest contribution of this work is the study of the patch antenna on biaxially anisotropic substrates. This antenna had never been modeled before. First, we showed that increasing the number of basis functions along the width of the antenna had little effect on input impedance and radiation performance. This is revealing of the fundamental behavior of the medium as will be discussed later. Next, we analyzed the input impedance behaviors as medium properties changed. The results revealed that the resonant dimensions of a patch printed on a biaxial substrate are smaller than when the substrate is isotropic with the average permittivity of

the three biaxial values. Similar to antennas printed on isotropic and uniaxial substrates, when the height of a biaxial substrate increases, the resonant length decreases and the impedance bandwidth increases. Changing the orientation of the substrates with respect to the principal axes also changes the resonant length and bandwidth; for the cases we investigated, the rotation decreased the resonant length and increased the bandwidth. These behaviors could be very valuable when designing individual microstrip antennas or even microstrip arrays.

Antenna modeling also requires analysis of radiation patterns. In Chapter 4, the principal and cross polarization patterns of the resonant patch antennas were analyzed. The principal polarization pattern changed little for all of the cases we considered. This is likely due to the fact that the currents along a half-wave resonant structure generally have the same behavior. The cross polarization patterns, however, did vary considerably. The orientation of the biaxial medium had a major impact on the shape of the cross-polarization patterns and the thickness of the substrate had a major impact on the magnitude. The patterns also revealed that the cross-pol pattern of the antennas with a biaxial substrate did behave similarly to those of an antenna on an isotropic substrate whose permittivity is the average of the biaxial permittivities. The patch antenna analyses suggest that the biaxial substrate acts like a high permittivity substrate in some ways and a lower permittivity substrate in others. This feature could offer benefits to antenna designers. In the future, substrates could be engineered so that patch antennas would have specific cross-pol properties.

Future work could further solidify the potential benefits of biaxially anisotropic material. As discussed the resonant length of the patch antenna imitates that of an isotropic material with the largest value in the biaxial permittivity tensor. This is valuable in that it

translates into a smaller resonant structure. One drawback to using isotropic materials with large permittivities is that, in an array, mutual coupling increases with permittivity. An extension of this work would be to consider two antenna systems (first two dipoles; then two patches) on biaxial substrates and analyze the mutual coupling between them. The two antenna analysis could then be extended to arrays of antennas printed on biaxially anisotropic substrates. The hope would be that biaxial media would suppress surface modes and other phenomena that limit the scan range of microstrip phased array antennas.

Another application of biaxial materials with respect to microstrip antennas is using them as a superstrate. The E-DGF could be modified to include a fourth layer. The third layer could then be an isotropic substrate and the fourth layer ground. With this structure, an antenna element could then be placed between an isotropic substrate and biaxial superstrate. There could be some beam shaping properties of a biaxial superstrate that would be advantageous in antenna design.

Another area of future work would be the rigorous modeling of the coaxial probe. This would require modeling the currents and the fields inside the biaxial medium. It could also include modeling the fields at the probe-antenna junction. This may require new basis functions that provide for better modeling of the discontinuity of current at the feed point. All of this modeling effort would provide information about the probe self impedance, which was ignored in our study of the patch antenna.

In our analysis of basis function convergence to model a patch antenna, we concluded that one basis function along the width was sufficient to compute input impedance of the patch antenna. This suggests that the mode set up in the cavity is somewhat uniform along the width.

This behavior warrants further investigation. To determine how the modes are set up, one would set up a cavity using equivalent currents on the boundaries and the equivalence principle used to determine the fields within the cavity. This procedure could be extended to a moment methods solution for a microstrip antenna printed on a finite biaxial substrate. This work would be an excellent area for future research.

This dissertation has extended research in the area of biaxially anisotropic materials. As metamaterials become increasingly popular, materials we can only imagine today may be available in the near future. When these materials mature, material properties will be one additional parameter in the antenna designer's arsenal. Understanding how to model these types of materials and being able to predict their behavior will be increasingly important.

We have used a new, versatile Green's function to develop electric field formulation and model microstrip antennas with the method of moments. Research such as this provides the groundwork for this new and exciting area of antenna design. This powerful algorithm provides the framework for future research in the area of biaxially anisotropic materials and their use in antenna applications.

BIBLIOGRAPHY

- [1] G. F. Pettis, *Hertzian Dipoles and Microstrip Circuits on Arbitrarily Oriented Biaxially Anisotropic Media*, PhD Dissertation, Syracuse University, Syracuse, NY. December 2008.
- [2] J. A. Kong, *Electromagnetic Wave Theory*, EMW publishing, Cambridge, Massachusetts, 2000.
- [3] J. L. Tsalamengas, "Interaction of electromagnetic waves with general bianisotropic slabs," *IEEE Transactions on Microwave Theory and Techniques*, vol. 40, no. 10, pp. 1870-1878, October 1992.
- [4] I. V. Semchenko, and S. A. Khakhomov, "Artificial uniaxial bianisotropic media at oblique incidence of electromagnetic waves," *Electromagnetics*, vol. 22, no. 1, pp. 71-84, January 2002.
- [5] Y. H. Lee, *Microwave Remote Sensing of Multi-Layered Anisotropic Random Media*, PhD Dissertation, Syracuse University, Syracuse, NY, December 1993.
- [6] S. Rikte, G. Kristensson, and M. Andersson, "Propagation in bianisotropic media – reflection and transmission", *IEE proceedings: Microwaves, Antennas and Propagation*, vol. 148, no. 1, pp. 29-36, February 2001.
- [7] S. He, Y. Hu and S. Ström, "Electromagnetic reflection and transmission for a stratified bianisotropic slab," *IEEE Transactions on Antennas and Propagation*, vol. 42, no. 6, pp. 856-858, June 1994.
- [8] T. M. Grzegorzcyk, M. Nikku, X. Chen, B.-I. Wu, and J. A. Kong, "Refraction laws for anisotropic media and their application to left-handed metamaterials," *IEEE Transactions on Microwave Theory and Techniques*, vol. 53, no. 4, pp.1443-1450, April 2005.
- [9] T. M. Grzegorzcyk, X. Chen, X., J. Pacheco, J. Chen, B.-I. Wu, and J. A. Kong, "Reflection coefficients and Goos-Hänchen shifts in anisotropic and bianisotropic left-handed metamaterials," *Progress in Electromagnetics Research*, PIER 51, pp. 83-113, 2005.
- [10] J. J. Stannnes, and G. S. Sithambaranathan, "Reflection and refraction of an arbitrary electromagnetic wave at a plane interface separating an isotropic and a biaxial medium," *J. Opt. Soc. Am., A*, vol. 18, no. 12, pp. 3119-3129, December 2001.
- [11] I. Abdulhalim, "Exact 2x2 matrix method for the transmission and reflection at the interface between two arbitrarily oriented biaxial crystals," *Journal of Optics A.: Pure and Applied Optics*, vol. 1, no.6 pp. 655-661, November 1999.
- [12] G. D. Landry, *Transmission and Reflection Characteristics of Biaxial Interfaces in Single and Multilayer Structures*, Masters Thesis, The University of Texas at Arlington, December 1993.

- [13] G. D. Landry, and T. A. Maldonado, "Complete method to determine transmission and reflection characteristics at a planar interface between arbitrarily oriented biaxial media," *J. Opt. Soc. Am., A*, vol. 12, no. 9, pp. 2048-2063, September 1995.
- [14] N. G. Alexopoulos, "Integrated-circuit structures on anisotropic substrates," *IEEE Transactions on Microwave Theory and Techniques*, vol. 33, no. 10, pp. 847-881, October 1985.
- [15] J. L. Tsalamengas, N. K. Uzunoglu, and N. G. Alexopoulos, "Propagation characteristics of a microstrip line printed on a general anisotropic substrate," *IEEE Transactions on Microwave Theory and Techniques*, vol. 33, no. 10, pp. 941-945, October 1985.
- [16] K. R. Carver, and J. W. Mink, "Microstrip antenna technology," *IEEE Transactions on Antennas and Propagation*, vol. 29, no. 1, pp. 2-24, January 1981.
- [17] N. K. Uzunoglu, N. G. Alexopoulos, and J. G. Fikioris, "Radiation properties of microstrip dipoles," *IEEE Transactions on Antennas and Propagation*, vol. 27, no. 6, pp. 853-858, November 1979.
- [18] N. G. Alexopoulos, and I. E. Rana, "Mutual impedance computation between printed dipoles," *IEEE Transactions on Antennas and Propagation*, vol. 29, no. 1, pp. 106-111, January 1981.
- [19] D. M. Pozar, "Input impedance and mutual coupling of rectangular microstrip antennas," *IEEE Transactions on Antennas and Propagation*, vol. 30, no. 6, pp. 1191-1196, November 1982.
- [20] M. C. Bailey, and M. D. Deshpande, "Resonant frequency of rectangular microstrip antennas," in *IEEE 1981 AP-S International Symposium (digest)*, Los Angeles, CA, pp. 3-6, June 1981.
- [21] M. Kara, "A simple technique for the calculation of the bandwidth of rectangular microstrip antenna elements with various substrate thicknesses," *Microwave and Optical Technology Letters*, vol. 12, no. 1, pp. 16-20, May 1996.
- [22] R. Garg, P. Bhartia, I. Bahl and A. Ittipiboon, *Microstrip Antenna Design Handbook*, Artech House Inc., Norwood, MA, 2001.
- [23] W. L. Stutzman and G. A. Thiele, *Antenna Theory and Design, 2nd Ed.*, John Wiley & Sons Inc., New York, 1998.
- [24] J. P. Damiano and A. Papiernik, "Survey of analytical and numerical models for probe-fed microstrip antennas," *IEE Proc. - Microw., Antennas Propag.*, Vol. 141, no. 1, pp. 15-22, February 1994.
- [25] D. M. Pozar and D. H. Schaubert, "Analysis of an infinite array of rectangular microstrip patches with idealized probe feeds," *IEEE Trans. Ant. Prop.*, vol. 32, no. 10, Oct. 1984.

- [26] D. M. Pozar, "Radiation and scattering from a microstrip patch on a uniaxial substrate," *IEEE Trans. Ant. Prop.*, vol. 35, no. 6, pp. 613-621, June 1987.
- [27] K.-L. Wong, J.-S. Row, C.-W. Kuo, and K.-C. Huang, "Resonance of a rectangular microstrip patch on a uniaxial substrate," *IEEE Trans. Micro. Theory Tech.*, vol. 41, no. 4, pp. 698-701, April 1993.
- [28] M. R. M. L. Albuquerque, A. G. d'Assuncao, and S. G. da Silva, "Broadband microstrip patch antennas on anisotropic substrates," *IEE 11th Intern. Conf. Ant. Prop.*, pp. 49-52, April 2001.
- [29] J. de R. S. Oliveira and A. G. d'Assuncao, "Input impedance of microstrip patch antennas on anisotropic dielectric substrates," *IEEE Ant. Prop. Intern. Sym.*, vol. 2, pp. 1066-1069, July 1996.
- [30] R. M. Nelson, D. A. Rogers, and A. G. d'Assuncao, "Resonant frequency of a rectangular microstrip patch on several uniaxial substrates," *IEEE Trans. Ant. Prop.*, vol. 38, no. 7, pp. 973-981, July 1990.
- [31] T. Q. Ho and B. Beker, "Spectral-domain analysis of shielded microstrip lines on biaxially anisotropic substrates," *IEEE Trans. Microwave Theory and Tech.*, vol. 39, no. 6, pp. 1017-1021, June 1991.
- [32] G. Elert, "Refraction: the physics hypertextbook," *Wikipedia: Birefringence*, retrieved 2007.
- [33] J. K. Lee and J. A. Kong, "Dyadic Green's functions for layered anisotropic medium," *Electromagnetics*, Vol. 3, pp.111-130, 1983.
- [34] S. Mudaliar, and J. K. Lee, "Dyadic Green's functions for a two-layer biaxially anisotropic medium," *Journal of Electromagnetic Waves and Applications*, vol. 10, pp. 909-923, 1996.
- [35] M. Born and E. Wolf, *Principles of Optics: Electromagnetic Theory of Propagation, Interference and Diffraction of Light*, 7th ed., Cambridge University Press, 1999.
- [36] H. C. Chen, *Theory of Electromagnetic Waves: A Coordinate-Free Approach*, McGraw-Hill Book Company, New York, 1983.
- [37] C. T. Tai., *Dyadic Green Functions in Electromagnetic Theory*, 2nd Ed., IEEE Press, NY, 1994.
- [38] J. K. Lee, *Electromagnetic Wave Propagation and Scattering in Layered Anisotropic Random Medium*, PhD Dissertation, Massachusetts Institute of Technology, Cambridge, MA, February 1985.
- [39] J. T. Aberle, *Analysis of Probe-Fed Circular Microstrip Antennas*, PhD Dissertation, University of Massachusetts, May 1989.

- [40] M. N. O. Sadiku, *Numerical Techniques in Electromagnetics*, 2nd ed., CRC Press LLC, Boca Raton, FL, 2001.
- [41] R. F. Harrington, *Field Computation by Moment Methods*, Robert E. Krieger Publishing Inc., Malabar, Florida, 1968.
- [42] R. F. Harrington, *Time-Harmonic Electromagnetic Fields*, McGraw Hill, 1961; Reissued by IEEE Press, John Wiley and Sons, New York, 2001.
- [43] D. K. Cheng, *Field and Wave Electromagnetics*, 2nd Ed., Addison-Wesley, Reading MA, 1992.
- [44] E. Arbel and L. B. Felsen, "Theory of radiation from sources in anisotropic media. Part I. General sources in stratified media. Part II. Point source in infinite homogeneous media," *International Series of Monographs on Electromagnetic waves, vol. 6: Electromagnetic Theory and Antennas Part I.*, ed. E. C. Jordan, pp. 391-459, Pergamon Press, New York, 1963.
- [45] J. R. James and P. S. Hall (ed.), *Handbook of Microstrip Antennas Volume 1*, Peter Peregrinus Ltd., London, UK, 1989.
- [46] C. A. Balanis, *Antenna Theory: Analysis and Design*, 2nd Edition, John Wiley and Sons, Inc, 1997.
- [47] P. B. Katehi and N. G. Alexopoulos, "On the effect of substrate thickness and permittivity on printed circuit dipole properties", *IEEE Trans. Ant. Prop.* vol. 31, no. 1, pp. 34-39, January 1983.
- [48] W. F. Richards, "Chapter 10: Microstrip Antennas," *Antenna Handbook: Theory, Applications and Design Vol. II (Y.T. Lo and S. W. Lee, eds.)*, Van Nostrand Reinhold Co., NY 1988.
- [49] D. M. Pozar, *Microwave Engineering*, 2nd ed., Wiley, New York, NY, 1998.
- [50] A. C. Ludwig, "The definition of cross polarization," *IEEE Transactions on Antennas and Propagation*, vol. 21, no. 1, pp.116-119, January 1973.
- [51] H. K. Schuman, "Polarization of antenna far radiated fields," *Atlantic Research Services Corporation*, December 1988.

VITA

Jennifer W. Graham graduated Summa Cum Laude from Syracuse University with a B.S. in Electrical Engineering in 2000. She continued her academic career at Syracuse University graduating with an M.S. in Electrical Engineering in 2004 and being awarded the “Outstanding Graduate Student in Electrical Engineering” Award. In 2007 Jennifer was awarded a Syracuse University Fellowship to pursue a doctorate in electrical and computer engineering. As a University Fellow, Jennifer spent a year as a teaching assistant for undergraduate electromagnetics course. Jennifer participated in the Future Professoriate Program (FPP) earning the Certificate in University Teaching and also served as a guest lecturer for graduate-level electromagnetics course.

Jennifer Graham currently works at SRC Inc. in North Syracuse, NY as a systems engineer where she has been an employee since 2004. While working at SRC Jennifer has been a lead systems engineer. Her work has involved detailed antenna modeling, antenna calibration, system architecture analysis and integration test planning and execution. Prior to working at SRC Inc. Jennifer worked at Lockheed Martin Corp. MS2 in Syracuse, NY from 2001 to 2004. While at Lockheed Martin, Jennifer was a participant in the Engineering Leadership Development Program which provided rotation assignments for broad technical background, in depth on-site radar classes and training in program management, technical writing and effective presentation.

